HIPERWIND

HIghly advanced Probabilistic design and Enhanced Reliability methods for high-value, cost-efficient offshore WIND

Atmospheric-Wave Multi-Scale Flow Modelling

Deliverable no: D2.1

Delivery date: 31 May 2022

Lead beneficiary: University of Bergen

Dissemination level: Public

This project has received funding from the European Union's Horizon 2020 Research and Innovation Program under Grant Agreement No. 101006689

Author information (alphabetical):		
Name	Organization	Email
Mostafa Bakhoday-Paskyabi	UiB	Mostafa.Bakhoday-Paskyabi@uib.no
Hai Bui	UiB	hai.bui@uib.no
Mohammadreza Mohammadpour Penchah	UiB	Mohammadreza.Penchah@uib.no

Acknowledgements/Contributions::		
Name	Name	Name

Document information:					
Version	Date	Description	Prepared by	Reviewed by	Approved by
1.0	31 May 2022	First official version	Authors listed above	Mark Kelly, DTU Pierre-Antoine Joulin, IFPEN Maria Laura Mayol, IFPEN	Nikolay Dimitrov, DTU

Definition:	

Contents

List of Figures

List of Tables

List of Abbreviations

ADM	Actuator Disc Model
ABL	Atmospheric Boundary Layer
ARW	Advanced Research WRF
COAWST	Coupled Ocean-Atmosphere-Wave-Sediment Transport
DA	Data Assimilation
ECMWF	European Centre for Medium-Range Weather Forecasts
EMODnet	European Marine Observation and Data Network
ERA5	ECMWF Reanalysis v5
FDDA	four-dimensional data assimilation
GEBCO	General Bathymetric Chart of the Oceans
IO	Inertial Oscillation
LES	Large Eddy Simulation
LLJ	Low-Level Jet
LiDAR	Light Detection and Ranging
MABL	Marine Atmospheric Boundary Layer
MAE	Mean Absolute Error
MBE	Mean Bias Error
NORA3	The 3 km Norwegian reanalysis
NWP	Numerical Weather Prediction
OCC	Open Cellular Convection
OSTIA	Operational Sea Surface Temperature and Sea Ice Analysis
PBL	Planetary Boundary Layer
Radar	Radio Detection and Ranging
RMSE	Root Mean Square Error
SCADA	Supervisory Control And Data Acquisition
SWAN	Simulating WAve Nearshore
WBLM	Wave Boundary Layer Model
WRF	Weather Research and Forecast
WFP	Wind-Farm Parameterizations

1 Executive Summary

To achieve a better understanding of the uncertainty sources and their management, one of the challenges, that HIPERWIND project addresses, is to improve the representation of environmental conditions and flow variability in the area of offshore wind parks. This is performed by improving the overall performance (accuracy and spatial resolution) of met-ocean models with different levels of fidelity, and by improving further the representation of key environmental physical processes that strongly affect the design and operation of offshore wind turbines/farms such as wind turbulence, surface gravity waves, wind-wave-turbulence interactions, and joint probability distributions of wind and waves.

The first three tasks in WP2 aim to develop a multiscale and observation-informed model chain to improve understanding key physical processes that are relevant for the offshore wind energy industry (see Fig. 2.1). We use a fully coupled ocean-atmosphere-wave-sediment transport (COAWST) modelling system and further develop a one-way coupled system (offline wind-wave nesting system) to identify and quantify the complex air-sea interactions, particularly during transient atmospheric and sea-state episodes. In this report (in accord with Tasks 2.1-2.3), the developed multiscale modelling framework contains the following components:

- WRF: The Weather Research and Forecasting model that downscales the synoptic-scale from a global reanalysis, simulates realistically mesoscale features and variations of the atmospheric flow fields and provides also the lateral forcing and nesting boundary information for other high-fidelity models.
- SWAN: A wave spectral model that focuses on understanding the wave dynamics, wave evolution, wave-wave, and wind-wave-turbulence interactions.
- The Coupled Ocean-Atmosphere-Wave-Sediment-Transport (COAWST) modeling system: In this coupled system, we only use the atmosphere model (WRF) and the wave spectral model SWAN are fully coupled.
- An offline, one-way wave-wind coupled system: The wave bulk information in this model is provided to the WRF model as offline input.
- WRF-LES: A high-fidelity Large Eddy Simulation (LES) coupled online within the WRF model to enable the model chain for resolving large turbulent eddies and parameterizing the smaller eddies.
- PALM: The simulation tool PArallelised Large-eddy simulation Model (PALM) that is run and is coupled offline with the WRF model. PALM provides even higher resolutions compared to the WRF-LES and the wakes from individual wind turbines can be resolved. PALM can also be applied for simulations of both atmospheric and oceanic boundary layers.
- WBLM: A Wave boundary Layer Model (WBLM) is used within the SWAN spectral wave model to address better the complex interactions between the wind and waves (Rogers et al., 2012; Zieger et al., 2015; Hara and Belcher, 2004).
- WRFDA: The WRF Data Assimilation (WRFDA) tools are used to provide more accurate and realistic model predictions, based on the integration of available observational data into the modelling system, particularly during the transient atmospheric events that the performance of models may significantly decline.

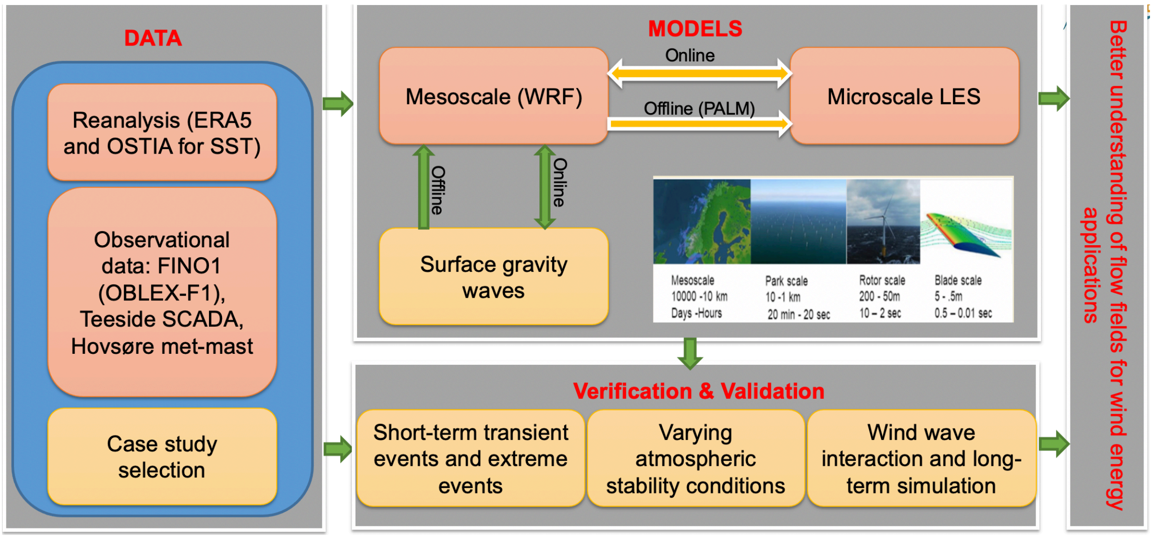

Figure 2.1: Multiscale framwork consisting of model components, input data, and outputs.

Based on our suggested multiscale model chain, we can:

- Assess the added value of simulations with the multiscale framework.
- Improve the understanding of the effects of (thermally- and mechanically-driven) flows on wake evolution and the turbine load behaviour over a wide range of atmospheric forcing and stability conditions.

2 Introduction

2.1 Motivations

In recent years, the rapid growth of the Earth's population has resulted in a huge increase in energy demand worldwide. The fact that fossil fuels are limited in nature and can cause catastrophic global climate change (i.e. through greenhouse gas emissions) motivated continuous/fast developments toward renewable energy resources such as wind energy. The wind over land is however an intermittent and non-persistent energy resource that makes it difficult to effectively accommodate such growing electricity demand. The need for access to higher and more consistent wind energy resources has dramatically exciting interests in offshore wind energy towards deep oceans where very large wind turbines will operate under very harsh environmental conditions for the years to come. While 16% of Europe's electricity demand is currently supplied by wind energy (mainly onshore), several emerging offshore wind projects are establishing the offshore wind industry as a key player in the global energy market (Walsh, 2020). In this regard, the global offshore wind market experienced about 30% growth between 2010 and 2018. Europe increased the wind power capacity by $14,7$ GW with a plan to install 105 GW for the next five years. Furthermore, the global installed capacity has approached to 35 GW in 2020 aiming to reach 300 GW of offshore wind installations by 2050 (IEA-report, 2021).

Several engineering and scientific studies are focusing on improving the overall efficiency of wind energy converters to meet the aforementioned growing electricity demand (Trust, 2015; Musial, 2020). Because the wind is the driving force of wind power plants, it is crucial to precisely evaluate the wind energy potential and understand its local and non-local conditions as the first steps in the reliable development of wind park projects and wind turbine technology (Archer et al., 2017). For example, a better understanding of large-scale weather systems (that control the wind speed and direction on the farm scale), inflow conditions to each wind turbine, local wind shear and veer, as well as turbulence are important for estimating the dynamic loading on different components of wind turbines and for enhancing the overall performance of power generation system (Hahmann et al., 2015; Imberger et al., 2021; Pettas et al., 2021).

Wind energy analyses rely generally on observational data within or in the close vicinity of offshore wind energy sites. Offshore meteorological masts are equipped with various meteorological and oceanic sensors, and oceanic surface buoys are designed to record wind and waves in the lower part of the atmosphere (Peña et al., 2008). These in-situ measuring techniques, however, suffer from limited spatial and temporal coverage that can be somewhat alleviated by the use of Light Detection and Ranging (LiDAR) measuring techniques. It is noted that the LiDAR devices are not able to measure high-frequency fluctuations of wind due to insufficient operating temporal resolution, but they can provide a reliable estimate of turbulence intensity for lower altitudes when there is enough aerosol density. While some of the above techniques provide coarse resolution information about wind (both in time and space), the space-born measurements can generate high-resolution wind data, particularly in space (Sommerfeld et al., 2019).

Measurements are, however, expensive, sparse in space and time, and time-consuming. To obtain a more comprehensive data coverage than those provided by the in-situ or remote sensing observations, Numerical Weather Prediction (NWP) models combined with available measurements are used for offshore wind energy applications (Arthur et al., 2020). The NWP models with a spatial resolution ranging from 1 km to tens of kilometers with temporal resolutions in the order of minutes to hours can adequately assess the mesoscale characteristics of the Atmospheric Boundary Layer (ABL). However, the mesoscale NWP models working at such grid spacing, are unable to resolve the fine-scale turbulences and other subgrid-scale details of flow variations which are keys to studying the structural mechanics of offshore wind turbines (Krüger et al., 2022). This motivates the development of a multiscale framework in which a wide range of scales and processes, relevant to the wind park design and control, can be properly captured through a series of coupled models (Wise et al., 2021).

Just recently, Large-Eddy Simulation (LES) has been used to study non-idealized setups and processes within the ABL through a grid nesting approach (Lin et al., 2021; Arthur et al., 2020). This nesting approach enables the modelling framework to simulate details of flow fields within and around the offshore wind park regions to explicitly capture the complex interactions between wind turbines and ambient flow as well as the turbine-induced wakes and their meandering. The nesting technique employs a number of LES model domains with different horizontal grid spacing where the outermost domain (with the coarsest resolution) obtains its boundary information from mesoscale NWP models (Hellsten et al., 2021). The child domains receive the boundary forcing information (one-way or two-way coupled nesting) from their respective parent domains. In the boundaries of the outermost LES domain, the nesting variables are horizontally/vertically interpolated from the NWP model onto the lateral boundaries at each time step. While the grid nesting approach enables the model chain to capture a wide range of spatiotemporal scales, whether such a multiscale system can resolve an almost full range of important physical processes within the marine atmospheric boundary layer (MABL) is still a question.

Many physical processes in the MABL rely on characteristics of the air-sea interface and its variability in time and space such as the heat and momentum exchanges. This adds even more complexity when compared to the terrestrial environment because: (1) the MABL possesses a shallower depths than the ABL over the land, thus the MABL 'feels' more effects from the wavy air-sea interface; (2) the upward momentum flux from the waves to the MABL depends on the atmospheric stability conditions; and (3) waves contribute in both aerodynamic and hydrodynamic loading on floating offshore wind turbines. The coupling between the spectral wave models and atmospheric NWP models may then provide better characterization of the wind power density through (a near-optimal) determination of the interfacial stress between the ocean and atmosphere (Porchetta et al., 2021a). Will this helps to better understand how do the wind and turbulence change and interact with wavy air-sea interface very close to the sea surface? This is a key question which roots in the parameterizations of air-sea fluxes of momentum and heat. In general, better models for the atmosphere-ocean-wave coupled systems can play a key role in reducing the uncertainties in the modelling of offshore wind energy systems.

Although the multiscale system integrated with ocean wave spectral models is meant to significantly reduce the model errors, there are still several sources of errors in the model chain (Haupt et al., 2019). While the accuracy of a modelling system can be improved by optimizing the physics and dynamics options (using sensitivity analysis of physics and dynamics options), further model uncertainty reduction can be achieved through the implementation of Data Assimilation (DA) approaches (Bakhoday-Paskyabi and Flügge, 2021; Sommerfeld et al., 2019) and using good quality initial and boundary information, and high-resolution terrain data. The DA combines the available high-quality observations (e.g. surface temperature and wind) into the model simulations to improve the performance of the multiscale framework in simulating the offshore wind. In the Southern North Sea, the local atmospheric conditions can be affected by the clusters of offshore wind parks and the model results might have biases without appropriate corrections to the modelling framework.

The motivation of this work is to test the effects of using a multiscale (mesoscale-to-microscale) framework for wind simulations and to address its limitations (see Fig. 2.1). This includes the study of the qualities of simulations under different atmospheric stability and forcing conditions. Furthermore, we present a methodology on how to provide meteorological boundary forcing information for high-fidelity microscale LES models. Special interest is given to investigating the model performance during transient atmospheric events.

2.2 Objectives

The primary objective of this report is to develop and use sophisticated methodologies for improving wind prediction for offshore wind applications under varying sea states, atmospheric forcing, and stability conditions. Specifically, we develop a mesoscale-to-microscale framework that enables downscaling of the regional mesoscale wind to turbine scales turbulent winds. Another objective is to study uncertainties of the coupled multiscale system, particularly during extreme weather phenomena such as Low-Level Jet (LLJ), Open Cellular

Convection (OCC), and storms.

The objectives of Tasks 2.1, 2.2, and 2.3 in WP2 are, therefore, briefly listed as follows:

- Identify and improve the representation of important (non-well-resolved) processes in the mesoscale ABL modelling that influence the accurate prediction of air-wave-sea interactions.
- Improve multiscale flow modeling of the ABL (from mesoscale to microscale) using available observational data and modelling tools to efficiently understand and simulate key physical processes relevant for offshore wind energy design and operation.
- Verification of wind simulation during transient and extreme events to be used in other WPs.

2.3 Challenges in offshore wind energy

Three important challenges need to be tackled to improve/enhance innovations in both technology and research mainstreams (read more in Veers and et al. (2019)): (i) urgent needs for a more comprehensive understanding and identification of atmospheric flow variability under varying forcing conditions in connection with wave field and ocean variability; (ii) the technological and engineering advancements in constructing large mechanical rotating (floating) energy devices operating under harsh environmental conditions; and (iii) development of sophisticated control and optimization systems for the wind turbines/farm to be operationally connected with the electricity grids (by maintaining a stable and reliable grid system). Any growth in each of the aforementioned challenges, governed by research and technological developments, can decrease the Levelized Cost of Energy (LOCE). Furthermore, these challenges are interconnected such that future innovations in the wind technology direction rely, to a large extent, on the progress in the understanding of complex physical processes. Such highly coupled phenomena and physical processes act on a broad range of spatial and temporal scales which are relevant directly/indirectly to wind energy. For example, the impact of changes in the wind field on the cost of wind energy needs the development of an accurate multiscale model-observation (numerical/statistical) framework to assess changes from flow distributions toward energy output and LCOE.

2.4 Multi-scale flow modelling

The reanalysis and forecast data are available globally with a resolution of a few dozen kilometers and frequencies of hours. For example, the ERA5 reanalysis data (Hersbach et al., 2020) can be downloaded hourly with a horizontal resolution of $0.25° \times 0.25°$ degrees (roughly 28 km grid size with an effective resolution of $8 \times \Delta x$ of about 220 km Bolgiani et al., 2022). Mesoscale numerical models are useful tools to downscale the synoptic conditions to a smaller scale of a few kilometers, where many atmospheric processes that are important in wind energy applications such as low-level jet (LLJ), open cellular convection (OCC), etc., can be resolved.

On the other hand, the engineering applications have much finer resolutions in both space and time, for example, a large eddy simulation (Witha et al., 2014) that can simulate the wake effect explicitly has a typical spatial resolution of meters and time step of milliseconds. Many engineering application assumes a stationary state of the environmental conditions of wind and thermal dynamics. These assumptions are useful for the model as they simplify the initial conditions—which normally take the form of vertical profiles and boundary conditions, and the periodic conditions that allow the turbulence within the model a long enough time to spin up.

Thus, there is a gap in the spatial-temporal scale between the operational atmospheric numerical models and the engineering applications, typical of the scale between tens of kilometers to under a kilometer. This scale is often referred to as *terra incognita* (Wyngaard, 2004). There is a need to close such a gap because the mesoscale model has difficulties to capture properly the micro-scale features, while the engineer-type models have difficulty capturing the abrupt changes during the transient events such as the passages of fronts, LLJ., and OCCs. Knowledge and understanding of local and non-local environmental met-ocean conditions are needed to bridge the gap between wind engineering applications and atmospheric science and to improve the performance of offshore/onshore wind parks.

Several atmospheric physical processes have potentially high impacts on offshore wind energy such as atmospheric heating and cooling, weather events on different spatiotemporal scales (e.g. cold front and storm passage), and mesoscale systems (e.g. convective cells, low-level jets, and wind ramps). Existing Numerical Weather Prediction (NWP) models used for wind energy production and forecast remain, however, inaccurate to capture properly the unexpected variability of the flow field of various scales, particularly during transient events. This constraint needs the improvement in the predictive skills of model forecasts through incorporating the effects of the aforementioned physical processes and developing a multiscale framework to account for the diverse meteorological processes. Developing such a multiscale framework would be extremely challenging to capture mesoscale information down-scaled to fine-scale (turbulent flow phenomena from seconds to hours with spatial scales expanding between 10^{-2} m and 10^{3} m).

2.5 Wind-wave interaction

Several mesoscale atmospheric models (e.g. MM5 and WRF) provide wind forcing for the wave spectral models either through offline or online coupled modelling systems. These models reproduce the 10-m wind fields in a good agreement with observations that can be used to estimate the momentum fluxes by solving the wind stress coefficients. While earlier studies suggested a linear dependence between wind stress and wind speed, such representation cannot be applied to a wide range of air-sea interactions and sea-state conditions. Several empirical relations based on best fit with observations were emerged to estimate the wind stresses by accounting for the effects of wave-induced stresses in the momentum and energy equations of the turbulent stress (i.e. the Wave Boundary Layer Model, WBLM, see Fig. 2.2) under very diverse sea-state or extreme wind conditions. For instance, Fan et al. (2009) applied the WBLM to the Wave-Watch III (WWIII) model. The results showed an improvement in the prediction of significant wave height, H_s, and an underestimation in the prediction of the dominant wavelength.

Waves have direct effects on the exchange of humidity, momentum, and energy between air and sea. When the wind blows over the sea, the momentum flux from the atmosphere acts to generate the surface waves (Smedman et al., 1999). In turn, the waves increase the ocean surface's roughness, which then influences back the atmospheric flow fields. When the wave grows, its slopes increase to the point where the waves cannot maintain such slopes and start to break. The wave breaking over a wide range of spatiotemporal scales

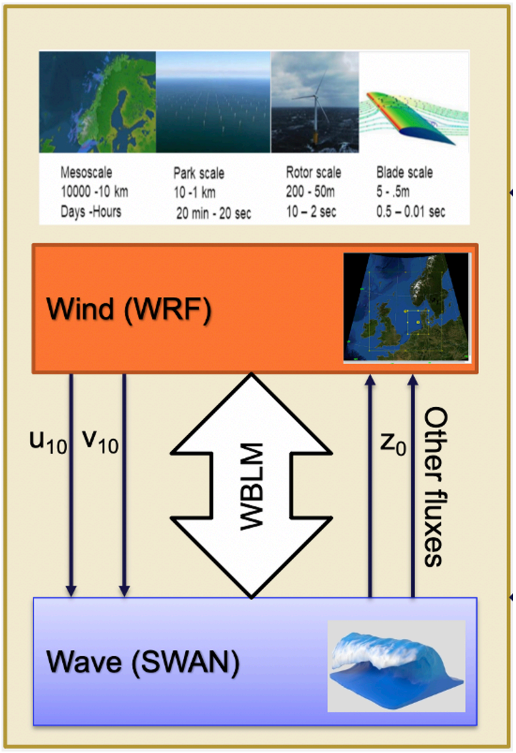

Figure 2.2: Schematic of wave boundary layer model implemented in the SWAN wave model.

will further complicate the estimations of momentum fluxes near the sea surface (Drennan et al., 1999).

For the generated waves as a result of the work done by the wind stress on the air-sea interface, the total stress, τ_{tot}, close to the surface can be represented by (Du et al., 2017)

$$\tau_{tot} = \tau_\nu + \tau_t + \tau_w, \tag{2.1}$$

where τ_ν , τ_t, and τ_w are the viscous stress, the turbulence stress, and the wave-induced stress, respectively. The total stress and wind speed can be empirically formulated by

$$\tau_{tot} = \rho_a C_D U_{10}^2 = \rho_a u_{*a}^2, \tag{2.2}$$

where ρ_a is the air density, C_D is the drag coefficient, and u_{*a} denotes the air-side friction velocity. The viscous stress is expressed as $\tau_\nu = \rho_a C_\nu U_{10}^2$, where C_ν denotes the viscous drag coefficient.

Very close to the sea's surface, the turbulence vanishes, and therefore τ_t approaches zero. In such circumstances, the total wind stress is a combination of the viscous and wave-induced stresses (Janssen et al., 1989). On the other hand, for the heights above the ocean surface, τ_{tot} is expressed by the sum of the turbulent stress and the wave-induced stress because the viscous stress is negligible (Wu et al., 2017). The wave-induced stress is usually calculated in wave models by considering the wave evolution represented by the spectral energy balance equation. The ocean wave spectrum, $E(f, \theta)$, is described in terms of ω, wavenumber k (or frequency f) and the propagation direction θ. The energy balance equation is:

$$\frac{\partial E}{\partial t} + c_g \, . \, \nabla E = S_{in} + S_{ds} + S_{nl}, \tag{2.3}$$

where E is the wave energy density, c_g denotes the wave group velocity, and the right-hand side of the equation contains different source terms including S_{in}, the energy input by the wind; S_{ds}, the dissipation of wave energy; and S_{nl}, the energy transfer between wave components due to the non-linear wave-wave interaction. There are several wave models which use different methods that solve the above equation (such as SWAN, WAM, and WWIII). Equation (2.3) can be rewritten in terms of the action density $(N = E/\sigma)$ as

$$\frac{\partial N}{\partial t} + \frac{\partial c_x N}{\partial x} + \frac{\partial c_y N}{\partial y} + \frac{\partial c_\sigma N}{\partial \sigma} + \frac{\partial c_\theta N}{\partial \theta} = \frac{S_{tot}}{\sigma} \tag{2.4}$$

where σ is the intrinsic circular frequency (in the absence of ocean current, $\sigma = 2\pi f$), and $\boldsymbol{c} = (c_x, c_y)$ is the group velocity vector at the geographical location of (x, y). The c_σ and c_θ are the propagation speeds in frequency and direction. S_{tot} denotes the combination of source and sink terms.

Source terms in Janssen et al. (1989)

In Janssen et al. (1989), the wind energy input is expressed by an exponential growth term β as

$$S_{in}(\sigma, \theta) = \beta E(\sigma, \theta), \tag{2.5}$$

where

$$\beta(\sigma, \theta) = C_\beta \sigma \frac{\rho_a}{\rho_w} \left(\frac{u_{*a}}{c}\right)^2 \cos^2(\theta - \theta_w), \tag{2.6}$$

in which ρ_w and ρ_a are the water and air density, respectively. C_β is the Miles parameter that can be determined from the non-dimensional critical height λ:

$$C_\beta = \frac{J}{\kappa^2} \lambda^{ln4} \lambda, \qquad \lambda \leq 1. \tag{2.7}$$

The dimensionless critical height is given by

$$\lambda = \frac{g z_e}{c^2} \exp(\kappa / x), \qquad x = \max\left[0, (u_{*a}/c) \cos(\theta - \theta_w)\right], \tag{2.8}$$

where c represents the wave phase speed, and θ and θ_w denote the wave and the wind directions, respectively. g denotes the gravitational acceleration, $J = 1.2$, and $\kappa = 0.41$ is the von Kármán constant. The effective roughness length is calculated as follows:

$$z_e = \frac{z_0}{\sqrt{1 - \frac{\tau_w}{\tau_{tot}}}}, \tag{2.9}$$

where z_0 is the roughness length, τ_{tot} is the total surface stress, and the wave-induced stress τ_w is defined as:

$$\tau_w = \rho_w \int_0^\infty \int_{-\pi}^{\pi} \sigma^2 \, S_{in}(\sigma, \theta) \frac{\vec{k}}{k} \, d\theta \, d\sigma. \tag{2.10}$$

Here k denotes the wavenumber. The wind speed profile in Janssen (1991) model is assumed to be logarithmic:

$$U(z) = \frac{u_{*a}}{\kappa} \ln\left[\frac{z + z_e - z_0}{z_e}\right], \tag{2.11}$$

where z is height. In SWAN, the default white-capping dissipation source term S_{ds} is formulated by Komen et al. (1984) as:

$$S_{ds}(\sigma,\theta) = -C_{ds}\left[(1-\delta) + \delta\frac{k}{\bar{k}}\right]\left(\frac{\bar{S}}{\bar{S}_{PM}}\right)^p \bar{\sigma}\frac{k}{\bar{k}}E(\sigma,\theta), \tag{2.12}$$

where E_{tot} is the total energy, $\bar{S} = \bar{k}\sqrt{E_{tot}}$ is the mean spectral steepness, and C_{ds}, δ, and p are tunable parameters (with default values of 0.24×10^{-4}, 1, and 4 respectively). The $\bar{\sigma}$ and $\bar{k}$ are the mean circular frequency and the mean wavenumber. The $\bar{S}_{PM}$ is the mean spectral steepness for the Pierson–Moskowitz spectrum.

Source term ST6 in SWAN model

The ST6 package in SWAN provides an observation-based representation for S_{in} and S_{ds} including positive and negative wind input, wave-turbulence interaction (swell decay), and two-phase white-capping dissipation (Rogers et al., 2012; Zieger et al., 2015).

The wind energy input source term in this package is written as

$$S_{in}(\sigma,\theta) = \frac{\rho_a}{\rho_w}\sigma G\sqrt{B_n}WE(\sigma,\theta), \tag{2.13}$$

where $B_n = A(\sigma)E(\sigma)k^3c_g$ denotes the normalized spectral saturation, A indicates the directional spreading function defined as follows:

$$A^{-1}(\sigma) = \int_0^{2\pi}\frac{E(\sigma,\theta)}{E_{max}(\sigma)}d\theta,$$

where $E_{max}(\sigma)$ represents the maximum density over all directions, and G is the sheltering coefficient to account for the effect of flow separation on wave growth:

$$G = 2.8 - [1 + \tanh(10\sqrt{B_n}W - 11)]. \tag{2.14}$$

The negative values of the wind input in ST6 is formulated through definition of W (for the opposed stress) as

$$W(\sigma,\theta) = W_1(\sigma,\theta) - a_0W_2(\sigma,\theta), \tag{2.15}$$

where a_0 is a tuning parameter, and the positive wind input W_1 and the the negative wind input, W_2, are defined as

$$W_1(\sigma,\theta) = \max{}^2\left\{0, s_{ws}\frac{u_{*a}}{c}\cos(\theta-\theta_w)\right\}, \tag{2.16}$$

$$W_2(\sigma,\theta) = \min{}^2\left\{0, s_{ws}\frac{u_{*a}}{c}\cos(\theta-\theta_w)\right\}, \tag{2.17}$$

where c indicates the wave phase speed and s_{ws} is a scaling parameter (with default value of 32 in SWAN), and the air-side friction velocity is calculated using Eq.(2.2), (Zieger et al., 2015).

The estimated wind input is then used to calculate the wave-induced stress. This stress can be decomposed into the high-frequency, τ_w^{HF}, and the low-frequency, τ_w^{LF}, terms as $\tau_w = \tau_w^{HF} + \tau_w^{LF}$. If we calculate the τ_w^{LF} stress for all frequencies less than a maximum frequency of σ_{max}, it results in a larger value compared to the calculation with a non-directional energy spectrum in Eq. (2.10). For the calculation of non-resolved (tail) part of the spectrum for frequencies beyond σ_{max}, we use a σ^{-5} diagnostic up to 10 Hz. In order to avoid the total wave stress to not exceed the total wind stress, a wavenumber frequency-dependent correction factor, $L(k)$, is applied to the wind input (i.e. $S_{in} \leftarrow LS_{in}$) as $L(k) = \min[1, \exp(\delta[1 - 28u_{*a}/c])]$, where δ is a parameter that controls the strength of the wavenumber reduction with strong impact on high frequencies and is calculated iteratively (see also (Bakhoday-Paskyabi et al., 2012; Tsagareli et al., 2010)).

The dissipation source term in ST6 is estimated by the sum of two components of T_1 (breaking related to instabilities in the wave) and T_2 (dissipation of shorter waves by longer breaking waves) (Rogers et al., 2012; Zieger et al., 2015):

$$S_{ds}(\sigma,\theta) = [T_1(\sigma) + T_2(\sigma)]E(\sigma,\theta), \tag{2.18}$$

where

$$T_1(\sigma) = a_1 A(\sigma)\frac{\sigma}{2\pi}\left[\frac{E(\sigma) - E_T(\sigma)}{E_T(\sigma)}\right], \tag{2.19}$$

$$T_2(\sigma) = a_2 \int_{\sigma_1}^{\sigma_2} \frac{A(\sigma')}{2\pi}\left[\frac{E(\sigma') - E_T(\sigma')}{E_T(\sigma')}\right] d\sigma', \tag{2.20}$$

where the threshold spectral density is defined as

$$E_T(\sigma) = \frac{B_{nt}}{A(\sigma)c_g k^3},$$

in which a_1, a_2, and B_{nt} are constants, and σ_1 is a prognostic frequency. According to the definition of this source term, the breaking happens if the energy spectrum at the frequency of σ exceeds the corresponding threshold value of $E_T(\sigma)$.

Sea surface roughness length parameterizations

Appropriate parameterization of roughness length is crucial to better compute the sea surface fluxes (Porchetta et al., 2019; He et al., 2021). Most atmospheric models use the Charnock (1955) relation to calculate the roughness length over the sea:

$$z_0 = \alpha\frac{u_{*a}^2}{g}, \tag{2.21}$$

where α is the Charnock parameter (with a default value of 0.018 in the WRF model).

Several field measurements have confirmed the dependence of z_0 and C_D to the sea-state, wave age, steepness, and fetch (e.g. Donelan, 1982; Smith et al., 1992; Oost et al., 2002; Hwang and Shemdin, 1988; Johnson et al., 1998; Taylor and Yelland, 2001; Lange et al., 2004; Jiménez and Dudhia, 2018).

Hsu (1974) calculated the roughness length using the significant wave height H_s and the wave length L from laboratory measurements as follows:

$$z_0 = aH_s \left(\frac{u_{*a}}{c_p}\right)^2 \tag{2.22}$$

where $c_p = \sqrt{gL/2\pi}$ is the peak phase velocity. Donelan (1990) improved the above representation by considering the fact that z_0 does not always depend on the square of (u_{*a}/c_p):

$$z_0 = a_1 H_s \left(\frac{u_{*a}}{c_p}\right)^{b_1}. \tag{2.23}$$

Here a_1 and b_1 are two constraint values. Drennan et al. (2003) combined several observational data from field experiments under a variety of atmospheric and sea-state conditions, and estimated $a_1 = 3.35$ and $b_1 = 3.4$.

Taylor and Yelland (2001) developed an alternative relation for z_0 based on wave steepness. They used wavelength at the peak of the wave spectrum L_p and H_s.

$$\frac{z_0}{H_s} = 1200 \left(\frac{H_s}{L_p}\right)^{4.5}. \tag{2.24}$$

Jiménez and Dudhia (2018) proposed a relationship for z_0 for the shallow water using measurements at FINO1 based on bathymetry and friction velocity:

$$\ln\left(\frac{z_0}{z_{1m}}\right) = \frac{2.7u_{*a} - 1.8/b}{u_{*a} - 0.17/b}, \tag{2.25}$$

where $b = (1/30)\ln(1260/d)$ and d indicates the water depth. They showed that above formulation is able to reduce the wind speed bias in the NWP models

Recently, Porchetta et al. (2019) developed a parameterization scheme for z_0 to account for the wind-wave misalignment based on wind and wave information at the FINO1 and ASIT offshore sites:

$$\frac{z_0}{H_s} = 20\cos(0.45\theta)\left(\frac{u_*}{c_p}\right)^{3.8\cos(-0.32\theta)}, \tag{2.26}$$

where θ denotes the difference between the wind and wave directions. They showed that the roughness length increases with increasing misalignment

What these studies all show is that the exchange of momentum and energy is extremely governed by the ocean waves, and wave-wind interaction is very important to simulate and forecast the wind fields over the oceans in the NWP models.

3 Data and tools

In this section, we describe the data used in this report. The data are categorized into two sections: Observed and reanalysis data. The observed data include the available measurements at the two stations: Teesside and FINO1.

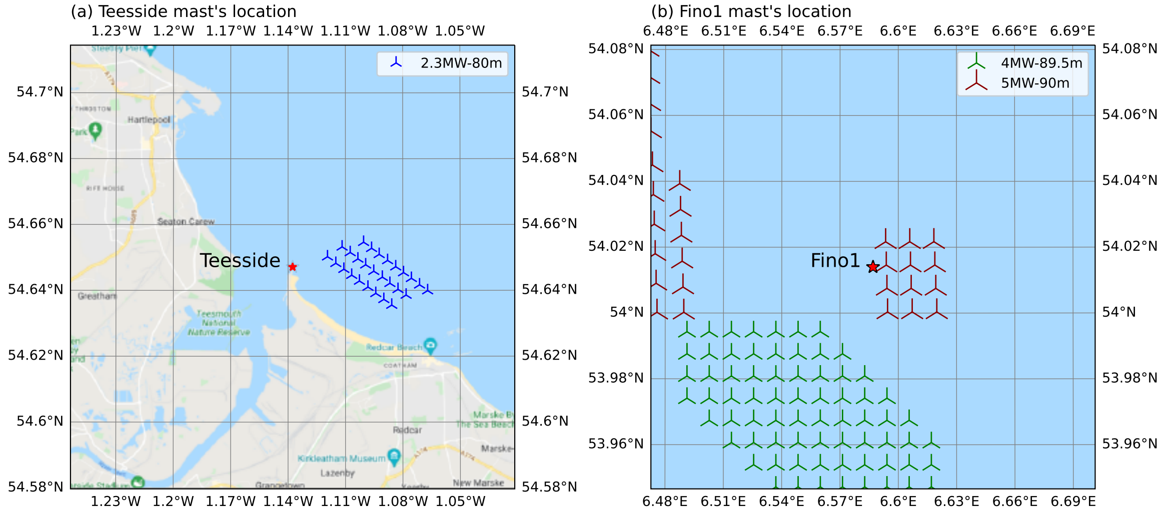

Figure 3.1: The Teesside (a) and FINO1 (b) mast stations and the nearby wind farms. The plotting region sizes are 15x15 km.

3.1 Observed data

Teesside

- Teesside's meteorological mast with 10-min sampling frequency data includes: (1) wind speed average and standard deviation at 10 m, 30 m, 50 m, and 80 m; (2) wind direction average and standard deviation at 8 m, 28 m, and 48 m; and (3) temperature, relative humidity, and atmospheric pressure at 10 m and 50 m. The data coverage is from 10 Sep. 2015 to 2 Feb. 2018.
- Bouy's wave data ranges from 12 Sep 2015 to 28 May 2019 including sea surface temperature, wave's peak period, peak direction, peak spread, significant wave height, the height of the highest wave, and the zero up-crossing period.
- SCADA data of 27 turbines of the Teesside offshore wind farm about 2 km to the east of the Teesside meteorological mast station. The data includes 10 minute average of ambient wind and standard deviation, nacelle angle which can be used to estimate the ambient wind direction, wind power production, and many other technical data of turbines.

Figure 3.2 shows the SCADA and mast data for two days (21–23 Nov 2015). The SCADA mean wind speed is averaged using two methods: using all turbine data (SCADA total averaged) or using only the turbines on the front rows that face the headwind (SCADA headwind averaged). Overall, the SCADA and the mast data are quite close to each other but some small differences exist. Those differences might result from several possible causes. The first reason is the distance between the Teesside mast and the wind farms, which is about 1.4 km, although small, but still can cause some significant differences in wind speed and direction in some situations, especially because the wind park is very close to the shore (about 1.5 km). The differences seem to depend on the directions (Fig. 3.2d), which is likely affected by the surrounding topography as the mast station is located right on the shore. The second reason might come from the wake effect between the turbines (Sun et al., 2020), where the wind speed at a downstream wind turbine is reduced because of an upstream one. For this reason, the SCADA headwind averaged wind speed is closer

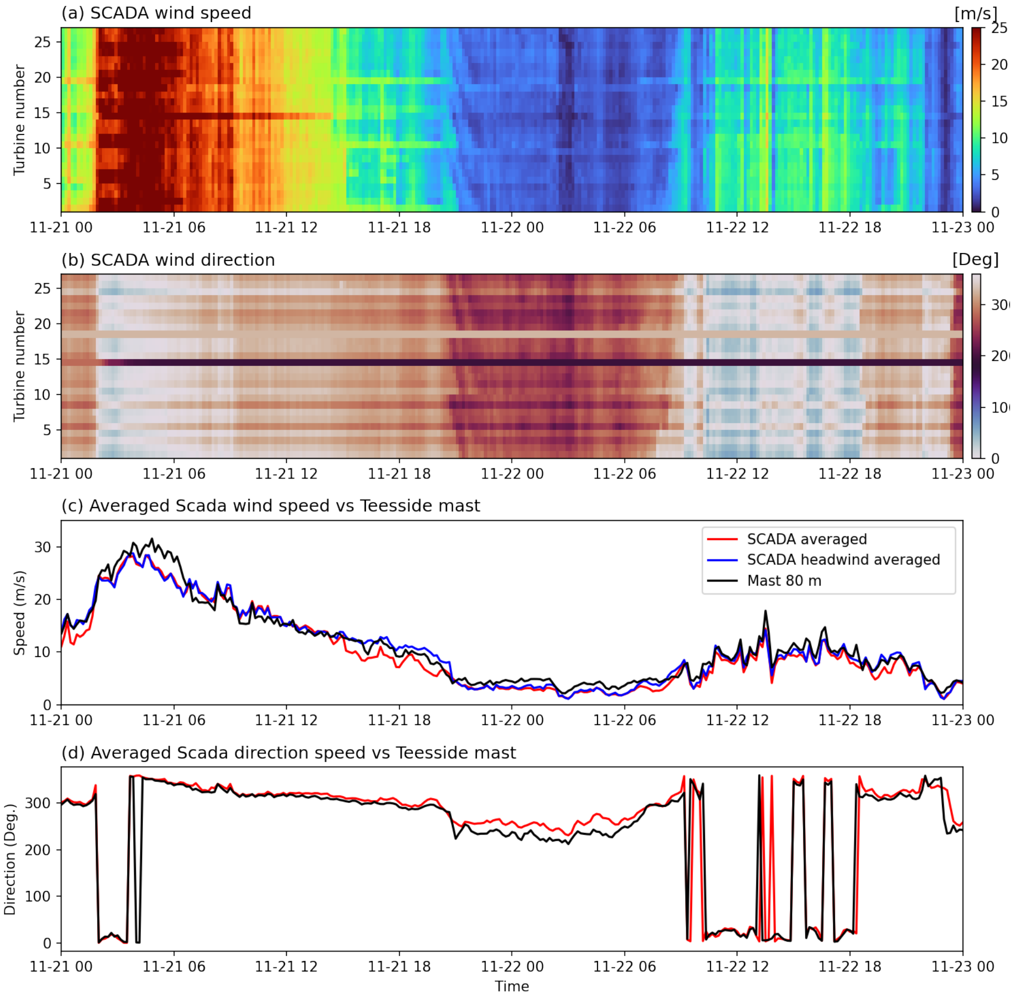

Figure 3.2: An example of the Teesside mast and SCADA data from 21 Nov. to 23 Nov. 2015: (a) SCADA wind speed; (b) SCADA wind direction (c) Averaged SCADA wind speed vs mast; and (c) Averaged SCADA wind direction vs mast.

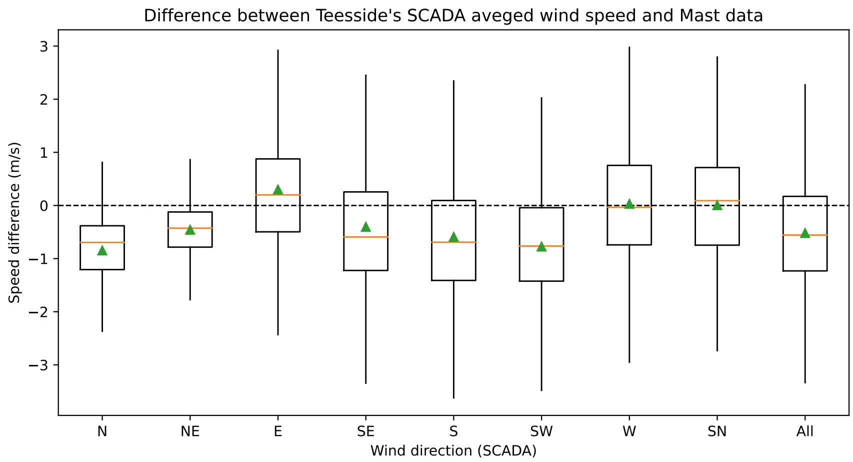

Figure 3.3: Speed difference between the Teesside's SCADA vs mast data relative to the wind direction. The data ranges for the analysis from 10 Sep 2015 to 31 Dec 2015.

Table 3.1: Wind speed errors (see section 3.11) between Teesside's SCADA vs mast data, assumed that the mast data represents the ground truth.

-	N	NE	E	SE	S	SW	W	NW	All direc.
MBE	−0.85	−0.46	−0.3	−0.4	−0.59	−0.77	0.03	0.01	−0.52
MAE	0.94	0.67	0.91	1.1	1.18	1.08	0.87	0.8	1.03
RMSE	1.24	0.93	1.22	1.43	1.58	1.36	1.1	0.98	1.34

to the mast's observation and larger than the SCADA total averaged in most cases. The third possible reason comes from the turbine blockage effect (Medici et al., 2011), where the wind reduction in front of each turbine can result in a lower measured wind speed than the far-field ambient wind. This effect may be more noticeable during the high-wind speed periods, for example around 06Z 21 Nov. 2015 (Fig. 3.2c).

Figure 3.3 and Table 3.1 illustrates the distribution of the difference between the head-wind averaged SCADA data and the mast data from Sep to Dec 215. Overall, the SCADA wind speed is weaker than about 0.5 m/s than the mast data. The MAE and RMSE are about 1 m/s and 1.3 m/s, respectively. The negative bias of the SCADA over the mast is largest for the north direction and from the southeast to southwest directions.

FINO1

The FINO1 offshore research platform (Fischer, 2006) is the first platform of the research project FINO (Forschungsplattformen In Nord und Ostsee—Research Platforms in the North Sea and Baltic). Data for FINO1 are listed as follows:

- The FINO1's meteorological mast has the cup anemometers that measure the 10-min average standard deviation of wind speed at 33 m, 40 m, 50 m, 60 m, 70 m, and 90 m. Notice that the cup anemometers are located to the southeast of the mast's pole (Fig. 3.4), thus the pole can affect the wind from the northwest. The met mast is

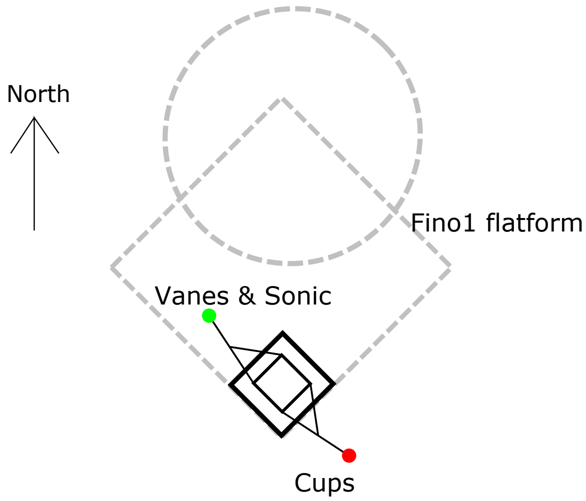

Figure 3.4: A top-view sketch of the FINO1 meteorological mast.

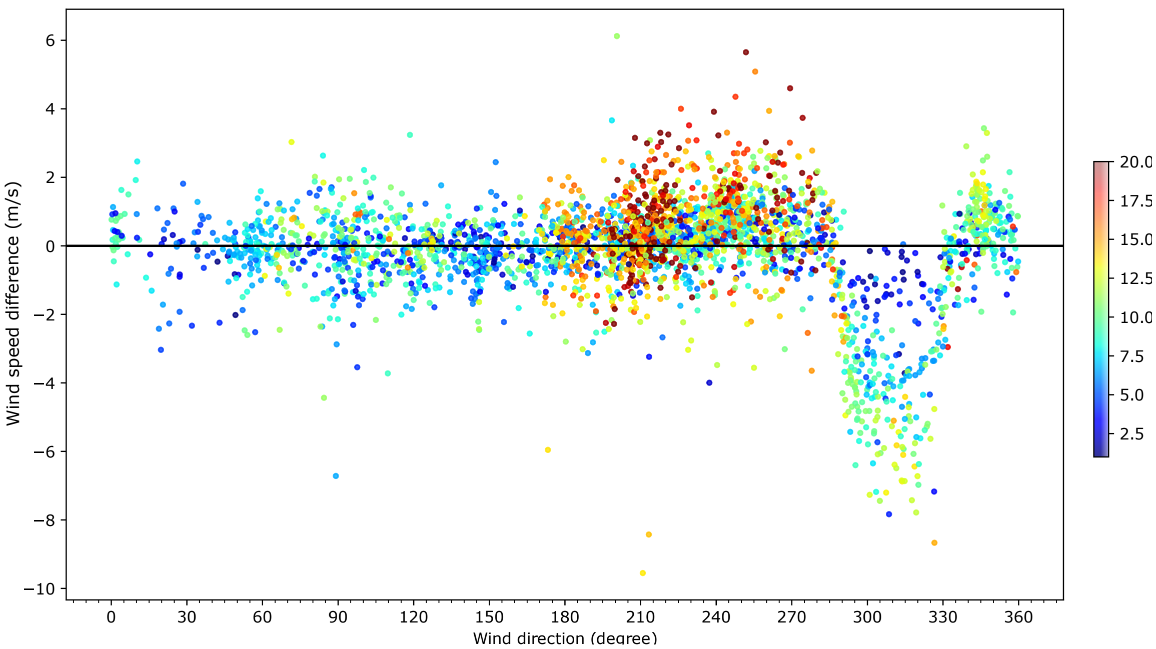

Figure 3.5: Wind speed differences between the FINO1's cup anemometer at 90m and the LiDAR from 22 May 2015 to 31 Dec 2015.

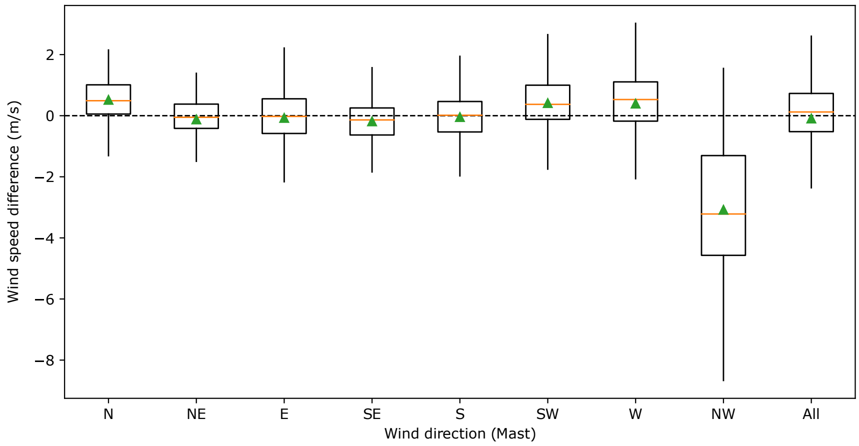

Figure 3.6: Wind speed differences between the FINO1's cup anemometer vs LiDAR data relative to the wind direction. The data ranges for the analysis from 10 Sep 2015 to 31 Dec 2015.

Table 3.2: Wind speed errors (see section 3.11) between FINO1's cup anemometer vs LiDAR data at 90 m, assumed that the LiDAR data represents the ground truth.

-	N	NE	E	SE	S	SW	W	NW	All direc.
MBE	0.52	-0.12	-0.07	-0.19	-0.05	0.41	0.39	-3.08	-0.09
MAE	1.82	0.58	0.79	0.58	0.68	0.81	1.06	3.14	1.01
RMSE	1.04	0.82	1.11	0.78	0.96	1.14	1.41	3.73	1.54

also located in a region surrounded by a couple of off-shore wind parks nearby, and their wake effect may significantly affects the wind at the met mast, especially the Alpha Ventus wind park locates just about 400 m to the east (Fig. 3.1). We have data coverage from 1 May 2015 to 31 Dec. 2015.

- LIDAR data includes 10-min averaged wind speed and direction up to 3126 m. Note that there may be missing data in time and at different heights. Data coverage is from 1 Aug 2015 to 1 Sep 2016.
- Sonic high-frequency data with sample frequency of 25 Hz for June, July, and September 2015. Data contains 3-dimensional wind components and temperature.

From the positions of the cup anemometers relative to the mast's pole (Fig. 3.4), we can expect the shadow effect occurs for the wind blows from the northwest. Figure 3.5 quantifies this shadow effect by comparing the cup anemometers and the LiDAR's observation in different wind direction angles. There is a bias mismatch with the wind direction between 285 ° and 345 ° with the largest difference at 315° (North-West direction).

Figure 3.6 and Table 3.6 show the distribution of the errors between the FINO1's mast wind speed versus the LiDAR data, assuming that the LiDAR represents the ground truth. As expected, when taking an average of all the directions, the mast and the LiDAR data are quite close to each other with almost zero bias and MAE and RMSE are approximately

1 m/s and 1.5 m/s respectively. However, the shadow direction of NW suffers a heavy negative bias of 3 m/s with MAE and RMSE of 3.1 and 3.7 m/s, respectively. Interestingly, the directions adjacent to the shadow zone suffer a slight positive bias of about 0.5 m/s.

3.2 Reanalysis gridded data

- We use the fifth-generation ECMWF hourly reanalysis (ERA5, Hersbach et al., 2020) on surface and pressure levels for WRF input and lateral boundary conditions. The data have a resolution of 0.25° (roughly 27 km) on 37 pressure levels from 1000 hPa to 1 hPa and provides hourly data for a large number of atmospheric, ocean-wave, and land-surface quantities. The ERA5 reanalysis on pressure levels can be downloaded from https://cds.climate.copernicus.eu/cdsapp#!/dataset/reanalysis-era5-pressure-levels.
- For the lower boundary condition, we replace the ERA5 SST with the Operational Sea Surface Temperature and Sea Ice Analysis (OSTIA, Stark et al., 2007; Donlon et al., 2012), with a daily temporal frequency and a 0.05° horizontal resolution.
- The CORINE (Coordination of Information on the Environment) Land Cover (CLC) 2018 version data can be downloaded from https://land.copernicus.eu/pan-european/corine-land-cover/clc2018. We downloaded the data in raster format with a resolution of 100 m and converted it to WPS's geogrid format with a resolution of 0.001° for creating the WRF's a higher resolution with lower boundary conditions.
- The Digital Elevation Model over Europe (EU-DEM) v1.1 data is downloaded from https://land.copernicus.eu/imagery-in-situ/eu-dem/eu-dem-v1.1/view for some specific sites, for example, the Teesside region. The data is downloaded in a raster format with a resolution of about 30m, then converted to WPS's geogrid format for WRF-LES simulation.
- Some simulations are compared with the the 3-km Norwegian Reanalysis (NORA3, Haakenstad et al., 2021) data. The NORA3 wind and wave 3-km hindcast data can be downloaded from https://thredds.met.no/.
- General Bathymetric Chart of the Oceans (GEBCO) bathymetric data set for coarse WRF domains (resolution of 3km and over), GEBCO is a global elevation data with a resolution of 15 arc-second and is available on the website: www.gebco.net/data_and_products/gridded_bathymetry_data.
- EMODnet bathymetry for finer domains (smaller than 3 km). EMODnet is the bathymetry data produced by the European Marine Observation and Data Network for Europe's sea basins with a grid resolution of 1/16 × 1/16 arc minute (about 115 × 115 meters) (www.emodnet-bathymetry.eu).

3.3 The WRF model

The Weather Research and Forecasting (WRF) Model (Skamarock et al., 2019) is an open-source mesoscale numerical weather prediction system designed for both atmospheric research and operational forecasting applications. The advanced research WRF (ARW) dynamical core serves a wide range of multi-scale applications, from the synoptic scale of thousands of kilometers down to microscale of tens of meters to thousands of kilometers. The WRF-ARW modeling system is community-maintained on Github's repository at https:

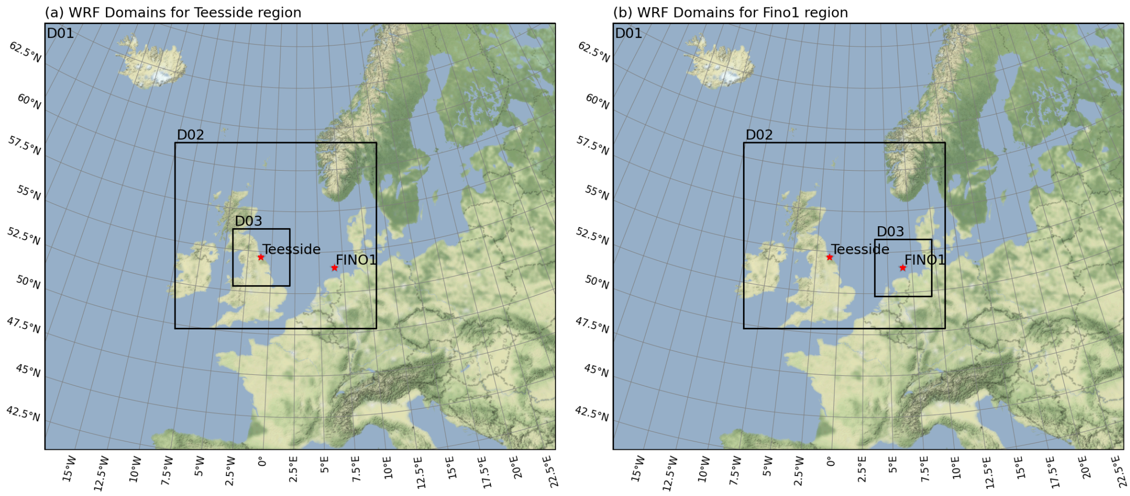

Figure 3.7: WRF nested domains for Teesside (a) and FINO1 (b) regions.

//github.com/wrf-model/WRF/ with the latest version of 4.3.3 (by 10 March 2022).

We used the latest version of WRF-ARW with the main input data from the hourly ERA5 reanalysis (Hersbach et al., 2020). Because of the importance of the Sea Surface Temperature (SST) and the land-sea distribution, we use the OSTIA high-resolution SST reanalysis with a resolution of 0.054 degrees (or roughly 6 km) (Stark et al., 2007), which is linearly interpolated from a daily basis to hourly basis to accommodate with the ERA5 data.

For the mesoscale's experiments, we use three-level nesting domains (Fig. 3.7): the first domain (D01) has a resolution of 9 km and covers a part of north-west Europe and a part of North Atlantic to downscale the large scale feature from the reanalysis data; the second domain (D02) has a resolution of 3 km and covers the North Sea regions; and finally, the third domain (D03) centered around the target interested region Teesside (Fig. 3.7a) or FINO1 (Fig. 3.7b) with a resolution of 1 km and domain size of 384 km $\times$ 384 km. We use 60 stretched vertical levels with the highest resolution near the surface of about 10 m and 21 levels below the height of 500 m.

In all the studies in this report, the control (CTRL) experiment for the WRF uses the built-in CONUS physics suite (Wang et al., 2021), with the planetary boundary layer and surface layer schemes replaced by the MYNN schemes because of their popularity among wind energy applications. Table 3.3 summarizes the physics and dynamics options of the CTRL experiments. Note that the cumulus option is only used for the outermost 9-km domain. The inner domains have grid sizes that are fine enough to enable the explicit convection and thus the scheme is turned off.

3.4 The COAWST model: WRF-SWAN

COAWST (Coupled Ocean-Atmosphere-Wave-Sediment-Transport) modeling system (Warner et al., 2010) is an open-source tool that includes a Regional Ocean Modeling System (ROMS) for the ocean; WRF, hydrology model (WRF-Hydro) for the atmosphere; Simulating Waves Nearshore (SWAN), WAVEWATCHIII, and InWave model for waves;— the USGS Community Sediment Models for sediment transport; and a sea ice model. The

Table 3.3: The physics and dynamics options for the WRF's control (CTRL) experiment design.

Option type	Option name	Namelist group	Namelist value
Micro physics	Thompson (Thompson et al., 2008)	mp_physics	8
Cumulus parameterization	Tiedtke scheme (Zhang et al., 2011)	cu_physics	6
Planetary boundary Layer	Mellor–Yamada Nakanishi Niino Level 2.5 (MYNN2) (Nakanishi and Niino, 2006)	bl_pbl_physics	5
Surface layer	MYNN	sf_sfclay_physics	5
Shortwave radiation	RRTMG (Iacono et al., 2008)	ra_sw_physics	4
Longwave radiation	RRTMG	ra_lw_physics	4
Land Surface	Unified Noah Land Surface Model	sf_surface_physics	2

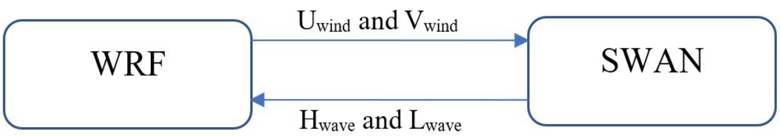

Figure 3.8: Exchangeable parameters between WRF and SWAN in the COAWST system.

COAWST system can be very useful for offshore studies because it can consider/model the complex interactions between the ocean, waves, and the atmosphere (e.g. see (Benetazzo et al., 2013; Olabarrieta et al., 2012; Bai et al., 2020; Calvino et al., 2021)). In this study, the atmosphere model (WRF) and a wave spectral model (SWAN) are used for the mesoscale modeling of WP2 multiscale framework. SWAN is a third-generation spectral wave model that solves the evolution of wave action by accounting for wave propagation, shoaling, wave refraction over bathymetry, and the effects of ocean currents. This model incorporates further the effects of the nonlinear triad and quadruplet wave-wave interactions, and wind-wave growth, as well as the dissipation due to the white capping, bottom friction, and depth-limited breaking. There is a coupler in the COAWST model (the Model Coupling Toolkit (MCT) that enables the exchange of data between different model components (Warner et al., 2010). The parameters that are transferred between WRF and SWAN models are illustrated in Fig. 3.8. To account for the effects of wind-wave interaction in the COAWST model, there are three different formulations based on Taylor and Yelland (2001), Eq. (2.24), Drennan et al. (2003), and Oost et al. (2002). In the online approach, the WRF model provides the horizontal wind data (at 10 m height) for the SWAN model, and the significant wave height, H_s, and the peak wavelength are transformed from SWAN to the WRF model.

3.5 WRF offline wind-wave interaction

To consider the wind-wave interactions, we develop/apply two (Offline and Online) methods and compare them against available observational data. The online method was explained briefly above. In the offline method, we develop modules and modify some scripts in the WRF model to read wave parameters (significant wave height, wave period, and wave direction) from ERA5 data and interpolate them in time and space to the WRF grid to calculate the roughness length based on formulations by Porchetta et al. (2019), Taylor and Yelland (2001), Oost et al. (2002) and Drennan et al. (2003). Hence, this method is called offline wave-wind coupling. The offline wave-wind coupling has several advantages: it can run stand-alone with the WRF; is relatively easy to implement; and costs less computational resources compared to online wave-wind coupling models. In this report, we evaluate the performance and accuracy of both online and offline wind-wave coupling systems in simulating wind and energy production.

Previous studies showed that differences in wind-wave direction can affect roughness length over the sea (see Patton et al., 2015; Porchetta et al., 2019). So, in this study, we choose two different periods to evaluate the models based on misalignment and alignment between wind and wave directions. Based on Porchetta et al. (2021b), we classify the wind-wave alignment into three categories. When the difference between the wind and wave directions is more than 120^o (less than 60^o), it is considered misalignment (alignment). Figure 3.9 shows the differences between the wind and wave directions during the entire 2015. As can be seen, the frequency of misalignment cases is very low in September and there are lots of alignment cases during September. Therefore, we select some days during September (i.e. between $03-17$) containing a reasonable number of alignment cases. For the misalignment, we select a period containing some misalignment episodes in July 2015 (i.e. $10-12$ and $20-26$ July 2015). Figure 3.10 shows the selected study periods used in our analyses.

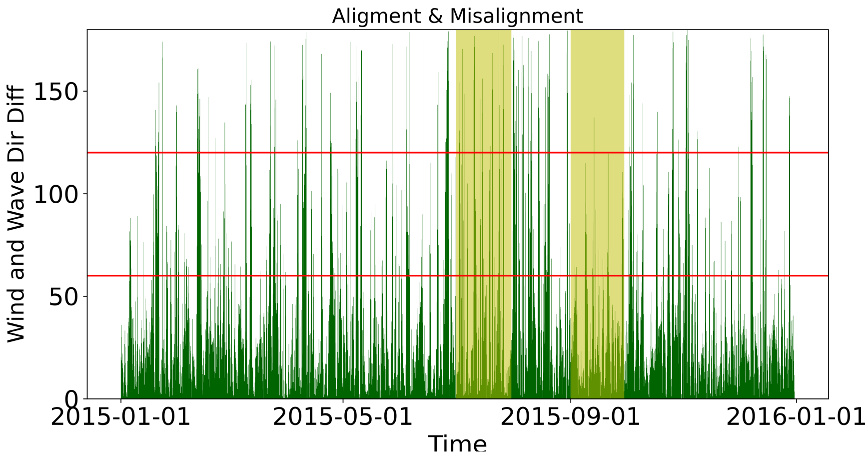

Figure 3.9: differences between wind and wave direction using NORA3 hourly data during the whole of 2015. A difference of more than 120° indicates misalignment and a difference of less than 60° indicates an alignment.

The results are compared with wind measurements at the FINO1 station. The COAWST V3.7 is used for the online coupling of the WRF and the SWAN models. Three domains in both models with the same sizes are defined (see Fig. 3.7b). The initial and boundary

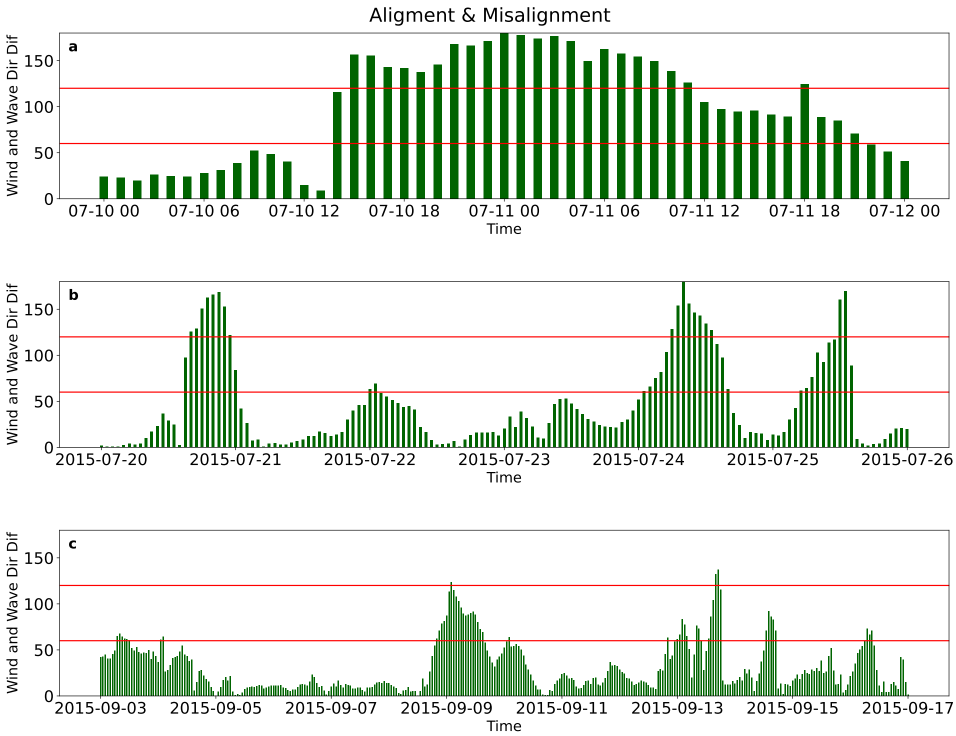

Figure 3.10: Differences between wind and wave directions using NORA3 hourly data during: a) $10-12$ July 2015 (a misalignment period); (b) $20-26$ July 2015 (a misalignment period); and (C) $3-17$ September 2015 (an alignment period). An angular difference of more than 120^{o} indicates a misalignment case and a difference of less than 60^{o} indicates an alignment event. These two thresholds are indicated by the two horizontal red lines

conditions for the WRF and SWAN models are obtained from ECMWF ERA5 data. We use significant wave height, wave period, and wave direction to generate the boundary forcing information of the SWAN model. Some atmospheric parameters (like air temperature, pressure, humidity, geopotential and etc) are also extracted to create the initial and boundary conditions for the WRF model.

In order to examine the effects of shallow water in an offline coupled system, bathymetry data is also ingested into the WRF model. Bathymetry data is provided from two data resources. We use GEBCO bathymetric data set for coarse domains (i.e. domains D01 and D02), and EMODnet bathymetry for the finer domain (i.e. domain D03).

Shallow water in the offline coupling system is defined as the water depth being less than half a wavelength, which is calculated by:

$$\lambda = \frac{g}{2\pi}T^2, \tag{3.1}$$

where g is the gravitational acceleration, λ denotes the wavelength, and T is the wave period. In the deep water, the phase velocity c_p is calculated from:

$$c_p = \sqrt{\frac{g\lambda}{2\pi}} = \frac{g}{2\pi}T \tag{3.2}$$

But in shallow water c_p depends on the water depth, h (see Stockdon and Holman (2000)):

$$c_p = \sqrt{gh} \tag{3.3}$$

In the offline wave-wind coupling simulations, we linearly interpolate the ERA5 hourly data to 30 minutes (any user-defined coupling timestep). In this study, we test 5 different experiments including: CTRL, offline_wave, online_wave, (Mis)Alignmen, com1_offline. The CTRL experiment uses the WRF model without any wave coupling method and it utilizes the default WRF formula to calculate the roughness length over the ocean. offline_wave, online_wave, and (Mis)Alignmen experiments use the same physics configurations but with different formulations for calculating the roughness length. Experiment com1_offline utilizes physics configurations of com1 (see Table 5.2) and it uses the roughness length formula similar to the Offline_wave experiment. For the offline_wave, online_wave and com1_offline experiments, we use Drennan et al. (2003) and for the (Mis)Alignmen run, we used Porchetta et al. (2019) formulation, i.e. Eq. (2.26). Experiment com1_wave uses a different physics configuration compared with other experiments (which is one of the optimal setups obtained in our sensitivity studies for an OCC event, see Table 5.2).

The online_wave simulations are carried out with WRF-SWAN coupled system. We define, the same as offline case, 3 domains with the same sizes for the WRF and the SWAN models with a horizontal resolution of 9 km, 3 km, and 1 km. Boundary conditions for the SWAN model extracted from the NORA3 data. The GEBCO bathymetry datasets are used for the domains D01 and D02, and the EMODne data is used for the domain D03. We set 25 frequency bands from 0.04 Hz to 1 Hz, and 36 directional bins for the SWAN model.

Table 3.4: Physics configurations for different wind-wave interaction experiments.

Experiment	PBL	Surf. layer	Sh.wave rad.	Lo.wave rad.	roughness length
CTRL	MYNN2	MYNN	RRTMG	RRTMG	Charnock
Offline_wave	MYNN2	MYNN	RRTMG	RRTMG	Drennan Offline
Online_wave	MYNN2	MYNN	RRTMG	RRTMG	Drennan Online
Porchetta	MYNN2	MYNN	RRTMG	RRTMG	Porchetta Offline
com1_wave	BouLac	Eta	Dudhia	RRTM	Drennan Offline

3.6 WRF large eddy simulation: WRF-LES

3.6.1 WRF-LES online nesting

In this section, we use the online nesting technique for the WRF-LES simulation. The advantage of this method is that the LES domain can get the environmental information from the mesoscale model at every time step instead of at a coarse time interval as in the offline nesting technique. The simulations include four or five domains with the first three domains being the WRF domains for solving the Reynolds averaged Navier Stokes equations (RANS) and domains 4 and 5 are the LES domains. The first 3 domains have the resolutions of 9 km, 3 km, and 1 km (similar to Fig. 3.7), and the same configuration as the WRF experiments. The two LES domains have the resolutions of 200 m and 40 m with the target site in the center (for example, see Fig. 7.1). For the LES domains, the boundary layer parameterization is turned off. The diffusion mixing is evaluated using stress form (diff_opt=2). The eddy coefficient can be estimated using either the 1.5 TKE closure (km_opt=2) or Smagorinsky's first order closure (km_opt=3). The TKE closure and Smagorinsky can also be used with the option of nonlinear backscatter anisotropic (NBA, sfs_opt=1). We also examined another experiment using the Weighted Essentially Non-Oscillatory (WENO Shu, 1998), by changing the advection options *_adv_opt, see 3.5 for detail). Table 3.5 summarizes the experiments and the WRF namelist options that we used for this study.

Table 3.5: WRF namelist option for the LES experiments

-	LES_CTR	LES_Smag	LES_NBA	LES_NBA_Smag	LES_Weno
km_opt	2	3	2	3	2
sfs_opt	0	0	1	1	0
km_opt	2	3	2	3	2
moist_adv_opt	1	1	1	1	4
scalar_adv_opt	1	1	1	1	3
momentum_adv_opt	1	1	1	1	3

For the LES simulation around the Teesside region, because of its coastal location, the influence of the land-sea contrast as well as topography may play an important role. However, the finest topography and landuse resolution provided with the WRF distribution has the finest resolution of roughly 1 km, which is not fine enough for the LES simulation. For the terrain height, we converted the Digital Elevation Model over Europe (EU-DEM), with the original resolution of 25m, to the WPS geogrid format with a resolution of about 50 m. For land use, we converted the CORINE Land Cover (CLC) database of 2018 to the geogrid format with a resolution of 100 m and 21 Modis categories.

3.6.2 Cell perturbation method

Traditional LES models usually use the periodic lateral boundary condition. Thus the turbulent eddies have enough time to fully develop into a pseudo-equilibrium state. However, with the nesting technique, the small-scale turbulence cannot come from the outer domain into the inner domain and the eddies may not have enough time to develop fully, especially with the small inner domain, high ambient wind speed, or under a stable boundary layer condition.

To overcome the turbulent spin-up problem, we use the cell perturbation method (Muñoz-Esparza et al., 2014, 2015), which is a simple, fast, and effective method for a more realistic turbulent representation. The method applies a uniform random perturbation within an interval [-0.5, 0.5] for three 8×8 grid point cells (thus 24 grid points are perturbed) near the inflow boundary. In our real data application, we apply the perturbation for all four lateral boundaries to account for all situations. Also, in the idealized setup of Muñoz-Esparza et al. (2014), the perturbations are introduced at every vertical grid point up to two-thirds of the inversion layer, which depth is known in the idealized setting. In our approach, the perturbations are applied with full magnitude up to 400 m, then relaxed to zero at 1000 m. We also test an option to apply the perturbation for vertical cells of 8 grid points instead of every grid point as in the original paper.

Because the cell perturbation method is not available with the distribution of WRF, we implement our own WRF modification. First, registry entries are added to WRF to include new namelist options (Table 3.6) and one 3D field, cell_perturb_th to the WRF input file. To simplify the process, we created a python script to modify the variable directly after the WRF inputs of the LES domains are generated.

During the run time, this perturbation is added to the potential temperature field. However, as pointed out by Muñoz-Esparza et al. (2014), the perturbing process should not be done at every time step, but at an interval that is at least equal to the perturbation time scale, $T_s = 2\pi k_{min}^{-1} U_g^{-1}$, where U is the characteristic velocity scale and $k_{min} = 2\pi/8\Delta x$. Thus $T_s = 8\Delta x/U$, is the needed time for the perturbation to be advected over eight grid sizes. In our coarse LES experiment, $\Delta x = 200$ m, thus a characteristic velocity 5 m/s will results in $T_s = 320$s. Finally, we provide another option, 'cell_pert_alternate', which will change the sign of the perturbation alternately, so that the perturbation will resemble a simple oscillation instead of a fixed value.

3.7 The PALM model

In the present work, we use the Large-Eddy Simulation (LES) tool PArallelized Large-eddy simulation Model (PALM, Maronga et al., 2015, 2020), developed at the Institute for Meteorology and Climatology of Leibniz University Hannover. PALM has been optimized for massively parallel architectures and has the ability to simulate atmospheric and oceanic flow fields under varying atmospheric stability and boundary forcing conditions through

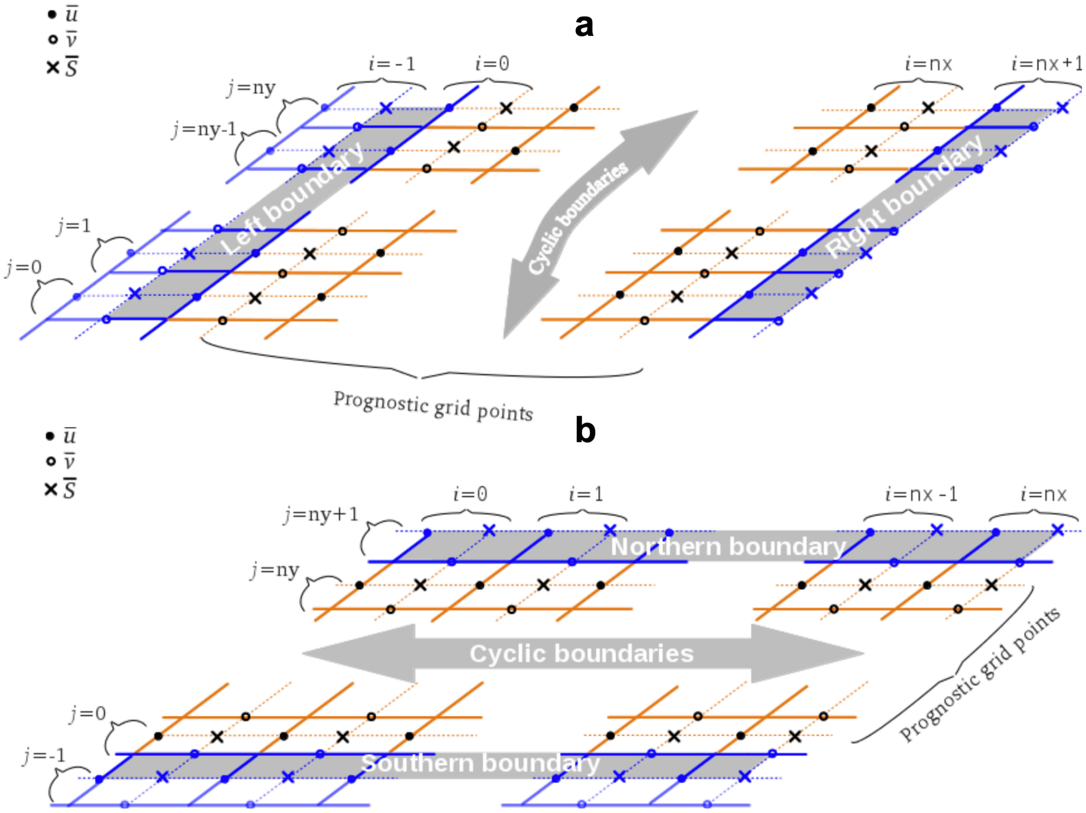

Figure 3.11: PALM grid structure at the lateral boundaries with non-cyclic lateral boundary conditions: (a) along the left-right direction; and (b) along the north-south direction. Figure is adapted from https://palm.muk.uni-hannover.de/trac/wiki/doc/tec/bc.

Table 3.6: WRF namelist options for the cell perturbation (namelist group: cpert)

Name	Default value	Description
cell_pert	0	(For each domain) =1 will turn on the cell perturbation
cell_pert_interval	320	(For each domain) Perturbation time interval in seconds
cell_pert_alternate	0	=1 will alternate the sign of the perturbation
cell_pert_magnitude	0.5	Perturbation magnitude (K)

the cooling/heating of the surface. It utilizes the central finite difference approach to spatially discretize the filtered non-hydrostatic and incompressible Boussinesq-approximated Navier–Stokes equations. This model uses a uniformly spaced Cartesian grid with Arakawa staggered C-grid type (grids are allowed for stretching in the vertical direction). Prognostic equations of PALM are solved for five quantities: the wind, the potential temperature, the water vapour mixing ratio, a passive scalar, and the subgrid-scale turbulent kinetic energy. PALM uses a third-order Runge-Kutta scheme for the time advancement and the advection terms are solved by a fifth-order Wicker-Skamarock scheme. A modified Smagorinsky methodology (following Deardorff) can be used to implicitly parameterize the subgrid-scale turbulence (Maronga et al., 2020). PALM has the ability to account for cyclic and non-cyclic boundary conditions (see Fig. 3.11), and it generates time-dependent turbulent inflow in the case of non-cyclic boundary conditions through a turbulence recycling method.

In order to create a fully developed turbulence (both in time and space) in a more idealised setting, PALM uses: (a) cyclic precursor simulation which is computationally expensive particularly for the convective stability conditions (i.e. non-stationary flow); and (b) a synthetic turbulence approach by knowing the information regarding to the turbulent length/time scales for the velocity fields and the Reynolds stresses. Therefore, the wind velocity (u_i for $i = 1, 2,$ and 3) at the inflow boundary can be decomposed as

$$u_i = \bar{u}_i + a_{ij} u_{*j},$$

where $\bar{u}_i$ represents the mean velocity component, a_{ij} is the amplitude of the Reynolds stress, and u_{*j} denotes the fluctuating velocity with a zero mean and a zero cross-correlation. The turbulent wind can be calculated based on timescale, T, and lengthcale, L, as follows (Kim et al., 2013):

$$u_{*j}(t + \Delta t) = u_{*j}(t) \exp\left(-\frac{c\Delta t}{T}\right) + \Psi_j(t, L) \left[1 - \exp\left(-\frac{2c\Delta t}{T}\right)\right]^{0.5}, \tag{3.4}$$

where c is the phase velocity to be calculated for each velocity component, and Ψ denotes a prescribed function to implement the effect of length scale along the vertical and spanwise directions. The generated turbulence is then correlated in space and time, according to the above. In this method, turbulence is added to the velocity field and not to the potential temperature and subgrid-scale turbulent kinetic energy.

Simplified turbine models have been recently implemented in the PALM in order to study the effects of wind turbine wakes on flow field variation in the areas of wind farms. Namely, two models are (Maronga et al., 2020): (a) the Actuator Disk Model (ADM); and (b) the Actuator Disk Model with Rotation (ADM-R). The latter is less representative than the actuator line model but it is much more computationally efficient. The ADM-R in the recent version of PALM contains the parameters of the NREL 5 MW research turbine (with a hub height of 90 m and a rotor diameter of 126 m. The rotor speed in the PALM ADM-R is adjusted in accord with the fluctuating inflow through a generator torque controller. For instance, in the ADM model, the wind turbines exert a thrust force into the inflow field to harness a certain amount of energy from the wind. The thrust force is given as follows:

$$F_T = \frac{1}{2}\rho_a C_T(a) A U_\infty^2, \tag{3.5}$$

where according to the 1D momentum theory, $C_T(a) = 4a(1-a)$ is the thrust coefficient as a function of axial induction factor a (one of the wind turbine control parameters which is less or equal than $1/3$ according to the Betz limit), ρ_a is the air density, A denotes the swept area of the rotor plane, and U_∞ is the upwind effective wind speed far from the rotor disc. Using a, we can define the disc-averaged wind as follows:

$$U_d = (1-a)U_\infty, \tag{3.6}$$

The thrust force for the i^{th} turbine with axial induction factor of a_i and the disc-averaged wind U_{d_i} in a wind park can be then rewritten as

$$F_{T_i} = \frac{1}{2}\rho_a C_T(a_i) A \left(\frac{U_{d_i}}{1-a_i}\right)^2, \tag{3.7}$$

Time-varying power extracted from the incoming flow at i^{th} turbine is given by

$$P_i = F_{T_i} U_{d_i}.$$

3.8 Mesoscale-microscale offline nesting: WRF-PALM model

In this mesoscale-microscale offline nesting, we first run the WRF model to downscale the global reanalysis ERA5 data to a 1-km grid and 10-min output resolution. Then the atmospheric fields from the WRF output are interpolated to the PALM model. Figure 3.12 illustrates the innermost 1-km WRF domain and the nested 270-m PALM domain around the FINO1 region.

PALM is able to account for the non-stationary and spatially heterogeneous conditions using nesting of its parent domain into the results of a mesoscale model. In this way, there are two major steps: (a) external processing to interpolate (horizontally and vertically) the forcing (mesoscale) data along the outer boundary cells of the PALM parent domain; and (b) PALM internal processing that interpolates the nesting input data in time, removes any residual divergence, and superimposes the turbulence to the velocity fields using the synthetic turbulence scheme described in the previous subsection.

In order to generate the lateral and top boundary conditions for PALM, the following WRF fields are used: (1) velocity; (2) thermodynamic fields (e.g. pressure, temperature, etc.); (3) soil information; (4) vertical grid structure; and (5) some other required geographical information. In this work, we update the PALM boundary information every 10 minutes. Non-cyclic boundary conditions are applied along all boundary cells (within the sponge layer) of the PALM parent domain.

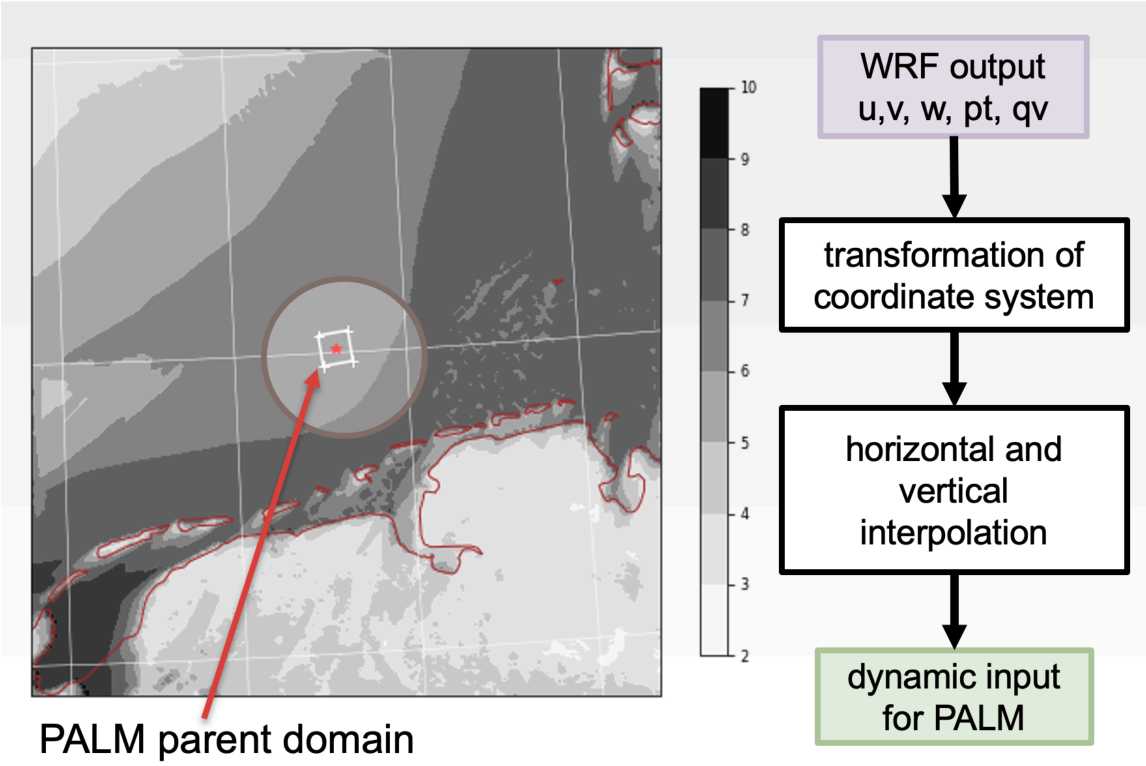

Figure 3.12: WRF fine resolution domain (i.e. D03 with 1 km horizontal resolution) and PALM outer domain with horizontal resolution of 270 m. The right-hand-side panel shows the flow chart corresponding to the offline WRF and PALM nesting.

3.9 Observation-based WRF modelling

We have shown how the coarsely resolved WRF regional simulations can be dynamically downscaled to provide spatiotemporal boundary data for the fine-scale models. The results show that such model (grid-spacing) refinements are able to enhance the performance and accuracy of modelling system. However, some more accuracy can be achieved if: (1) we nudge the model towards the available (met-mast or LiDAR) observational data that reflect the effects of local geophysical variability; or (2) use other data assimilation techniques (such as 3DVAR and 4DVAR) based on qualified available observational datasets.

3.9.1 Observation nudging

Observation nudging belongs to the Four-Dimensional Data Assimilation (FDDA) family in which each grid point is nudged towards the observation. The observation data locates a user-defined radius of influence and the nudging in time and space is performed by the use of a weighted average of differences between the observation and model. Here, we present the nudging of wind speed and direction with a time interval of 3 h for a few points between an altitude of 75 m and 1200 m (depending on the availability of the LiDAR observational data). In the nudging-based methods, nonphysical forcing terms are added, for example, in the prognostic equations of momentum as follows (see Skamarock et al. (2019)):

$$\frac{d\chi\mu}{dt}(x,y,z,t) = F_\chi(x,y,z,t) + \mu G_\chi \frac{\Sigma_{i=1}^{N} W_\chi^2(i,x,y,z,t)[\chi^o(i) - \chi^m(x_i,y_i,z_i,t)]}{\Sigma_{i=1}^{N} W_\chi(i,x,y,z,t)} \quad (3.8)$$

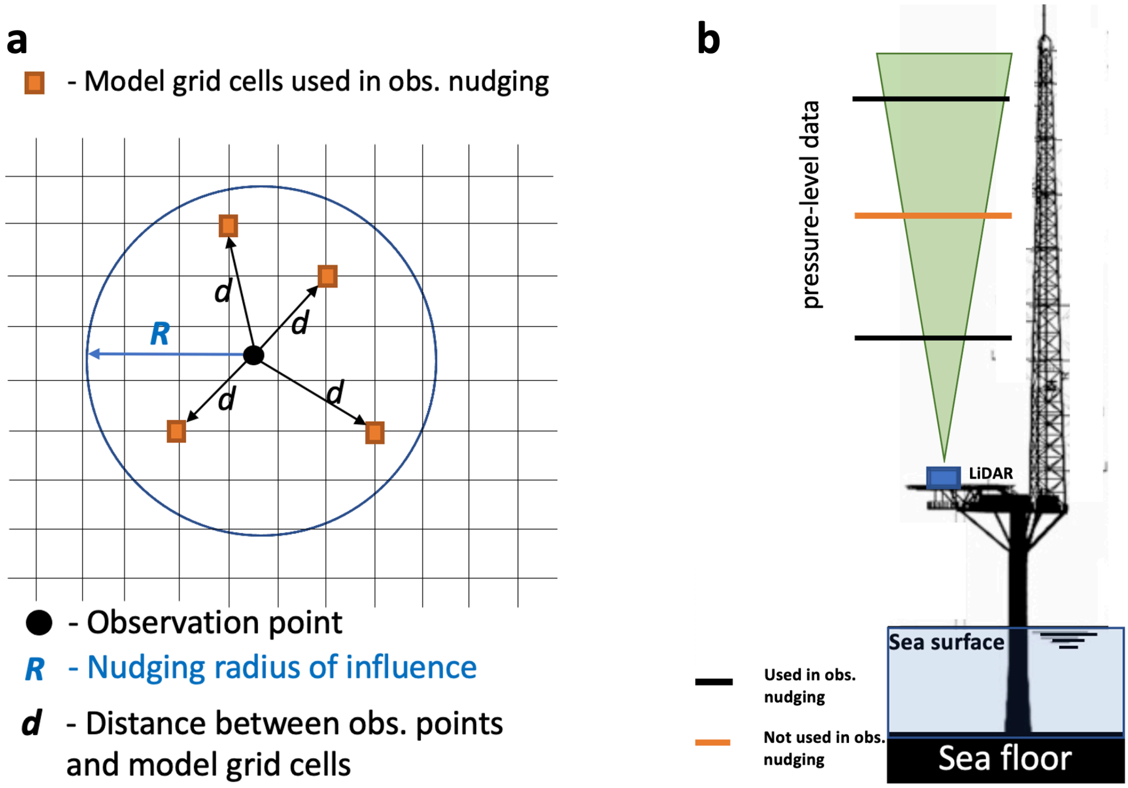

Figure 3.13: (a) Representation of radius of influence in a Cressman function scheme; and (b) schematic of the offshore FINO1 platform incorporating an upward-looking LiDAR system. Vertical lines show the pressure levels will be used in observation nudging (black horizontal lines) and the one cannot be used due to quality control constraints of nudging conversion tool (orange line).

Table 3.7: Values of nudging coefficients used in this study.

potential temperature	U and V winds	water vapour	geopotential height .
5×10^{-5}	5×10^{-5}	5×10^{-6}	–

where μ denotes the dry hydrostatic pressure, χ indicates the nudging quantity (here wind speed and wind direction), and F_χ and G_χ refer to the physical tendency and the nudging strength of variable χ respectively. For N assimilation points, W_χ shows the spatiotemporal weighting function between observations χ^o and the model results at grid cells χ^m. These weights highlight the strength of nudging in space and time, and can then be divided into two groups: the spatial nudging weights (associated with the xy horizontal nudging and the z vertical nudging); and the temporal nudging weights (varying between 0 and 1). We select nudging time windows of 1h and 3h and assure that the used observations do not overlap through a quality control process. Table 3.7 contains the values used in this study.

For the horizontal weighting function, W_h, we use the distance between the model grid cells and observation location, D, as well as the radius of influence, R based on the Cressman scheme as follows:

$$W_h = \begin{cases} \frac{R^2-D^2}{R^2+D^2} & \text{if } 0 \leq D \leq R \\ 0 & \text{otherwise} \end{cases}$$

3.9.2 WRF data assimilation

In this report, we explain the Data Assimilation (DA) system in WRF (i.e. WRFDA) that incorporates different deterministic (like 3DVAR and 4DVAR) or probabilistic assimilation techniques. We use the 3DVAR DA system by incorporating LiDAR data in the WRF modelling system. 3DVAR works by iteratively minimizing a cost function $J(x)$ for a control variable $\boldsymbol{x}$ as follows (Barker et al., 2003):

$$J(x) = \frac{1}{2}(\boldsymbol{x} - \boldsymbol{x}_b)^T B^{-1}(\boldsymbol{x} - \boldsymbol{x}_b) + \frac{1}{2}(\boldsymbol{y} - H(\boldsymbol{x}))^T R^{-1}(\boldsymbol{y} - H(\boldsymbol{x})). \tag{3.9}$$

The first term in the above equation is a background term including the analysis state vector $\boldsymbol{x}$ and a background (or first guess) vector, $\boldsymbol{x}_b$. The second term is called the observation term. This term contains the observation state vectors, y, and a function H that maps the control variable $\boldsymbol{x}$ onto the observation vector space. There are two important covariance matrices in the representation of $J(x)$: the background error B and the observation error matrix R. The covariance matrix B is a square and semi-definite and symmetric matrix (i.e. with positive eigenvalues), and its diagonal elements contain the variances of the background forecast errors. Assuming no correlation between different observations leads to a diagonal matrix representation for the error covariance matrix R.

An appropriate determination of $\boldsymbol{B}$ is key in all variational DA approaches. There are three different techniques to determine $\boldsymbol{B}$: the NMC method, the innovation statistics-based method, and the analysis ensemble method. We apply the NMC method which is a widely used method for generating $\boldsymbol{B}$ (less computationally expensive and its results look more physically acceptable). In this method, the forecast error covariance is estimated through the computation of the forecast difference statistics of, for example, 24h and 12h for a month or longer period (Bakhoday-Paskyabi and Flügge, 2021). The results of WRFDA will be explained in another article associated with HIPERWIND project and will not be explored in this report.

3.10 Case selection

Open cellular convection events

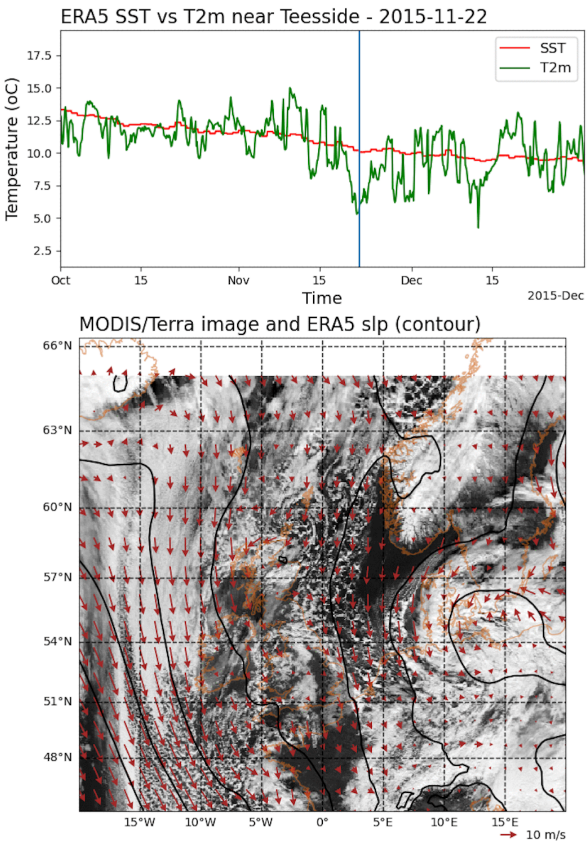

Figure 3.14: An example of the OCC event at 00Z Novemeber 2015 that occurs over both Teesside and FINO1 regions. Top panel shows the Sea Surface Temperature (SST) and T2m air temperature (T2m) from ERA5 data over the Teesside region. Bottom panel shows the sea level pressure (black contours), 10m wind vectors, and satellite cloud images.

An OCC event occurs typically when SST is consistently larger than T2m (i.e. the temperature of overlying air), which is often associated with a cold air outbreak event where the cold air from the north or from the continent during nighttime blows over a warmer sea surface. To select the OCC events, we generated a series of GIF animations of 1-day frequency within two years $2015--2016$. Each animation cover 3 month periods with each plot showing the SST and 2m air temperature, a horizontal distribution of sea level pressure, 10 m wind vectors, and satellite cloud images. The OCC events are selected manually from the visual cue of these plots by considering the availability of the observational data.

3.11 Validation method

To validate the model results against corresponding observations, we use several statistical parameters and charts. Observations of the wind data are acquired from meteorological masts, LiDAR, SCADA, etc. To evaluate the model performance, two following statistical parameters are used:

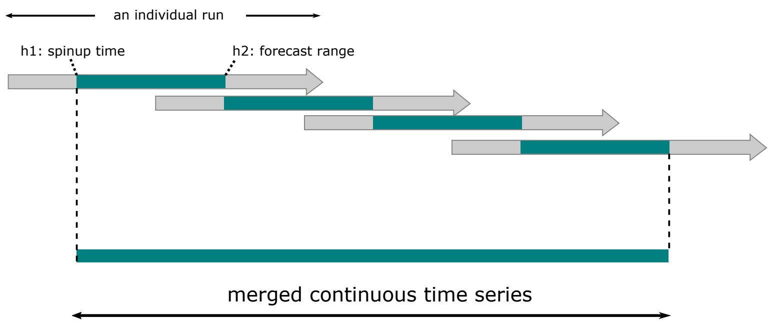

Figure 4.1: A conceptual diagram explains the processing of merging individual simulation to get a continuous time series with the forecast period from h1 to h2, where h1 is the spin-up time and h2 is the forecast range.

Mean Absolute Error (MAE) as defined through

$$MAE = \frac{1}{N}\sum_{i=1}^{N}|y_i - o_i|, \tag{3.10}$$

where y denotes the wind speed simulated by the model and o is the reference wind speed, for example, the observation in the same place and time, and N is the total number of pairs of simulation-observation.

Another statistic to measure the error is the Root Mean Square Error (RMSE), which is defined by:

$$RMSE = \left(\frac{1}{N}\sum_{i=1}^{N}(y_i - o_i)^2\right)^{1/2}. \tag{3.11}$$

The Mean Bias Error (MBE), or simply bias, is defined by,

$$MBE = \frac{1}{N}\sum_{i=1}^{N}(y_i - o_i), \tag{3.12}$$

If the bias is positive, the simulated values tend to overestimate the truth; if it is negative, the simulated values tend to underestimate the truth.

The wind speed is fitted with the Weibull distribution defined as follows

$$f(x;\lambda,k) = \begin{cases} \frac{k}{\lambda}\left(\frac{x}{\lambda}\right)^{k-1} e^{-(x/\lambda)^k}, & x \geq 0, \\ 0, & x < 0, \end{cases} \tag{3.13}$$

where $k > 0$ is the shape parameter and $\lambda > 0$ is the scale parameter of the distribution.

4 A 2-month mesoscale simulation

4.1 Experiment design

Long-period simulations are important for wind energy applications, for example, to access wind resources. Because the mesoscale processes have a limit of predictability, the simulations with a long integration time, for example, longer than 7 days are usually not reliable and the shorter range forecasts are generally considered more reliable. However, the model also needs some time for the fields to be in dynamic balance with each other. For this reason, sometimes the first few hours are considered a spin-up time and are dropped. For example, the NORA3 data (Haakenstad et al., 2021) is achieved by carrying out four 9-h simulations a day and dropping the first 2 hours as the spin-up time.

To examine the effect of the simulation length, we first carry out 2-day simulations starting at 00Z of each day, for two months from 1 July 2015 to 29 August 2015. This simulation strategy results in 31 individual simulations that can be merged into a single time series with different choices of the dropped spin-up time and forecast range. Figure 4.1 illustrates the method of merging by dropping h_1 hours at the beginning of each run and thus the effective forecast period is from h_1 to h_2, which is the maximum forecast length. We name the case as experiment h_1–h_2, for example, experiments 0–24h use the first day of each simulation for the merged series, while experiment 12–36h drops the first 12h and uses simulations from 12 h to 36 h of each run. We test 5 methods of merging for this series of 2-day simulations: 0–24h, 6–30h, 12–36h, 18–42h, and 24–48h.

On the other end of the spectrum of the predictability for mesoscale processes, we carry out 11 simulations with a range of 7 days and a run frequency every 5 days. The outputs from different runs are merged to a single time series using the mentioned method by dropping the first 2 days, thus resulting in the sixth experiment: 48–168h (i.e. the effective simulation range is from 2 to 7 days).

Because of the limitation of the computation and storage, we use only the 9 km domain (Fig. 3.7) to carry out all the experiments. The full 3-D outputs are produced every 3h, but at the locations of the Teesside and FINO1 mast, we output the time series at every model timesteps from the surface up to the height of 1500 m. These wind speed and wind direction time series are then resampled to a 10-minute frequency and merged into 2-month continuous time series using the above methods.

4.2 Simulations for FINO1 site

Figure 4.2 shows the merged time series of the WRF simulated wind speed at the height of 90 m, which is hub height of the Alpha Ventus wind turbines, with different merging methods compared with the mast's cup anemometer and LiDAR observations. In general, the WRF model at different simulation ranges can capture the magnitude of the wind speed quite well for some periods, for example from 28 Aug. to 30 Aug. However, there are some periods where the WRF's simulation systematically overestimates the wind speed compared to the observations, for example, around day 9–10 July and 23–24 Aug. These mismatched periods, however, can be grouped into two types: the first type where the WRF's speed is larger than the mast's cup's observation, but close to the LiDAR's observation, for example, the period from 9–10 July; the second type where the WRF's speed is larger than both cup's and LiDAR's observations, for example, 23–24 Aug.

The NORA3 data is supposed to be superior to our simulations because of its shorter range (9 h versus 24 h) and higher resolution (3 km versus 9 km) and it is indeed close to the observation most of the time (Fig. 4.2). However, in the periods where there is a large difference between the WRF's simulation and the observation, for example, 14 Aug. or 23-24 Aug., there is the same problem with the NORA3's simulation. Interestingly, the NORA3 data also behaves similarly to the WRF during the two types of speed differences mentioned

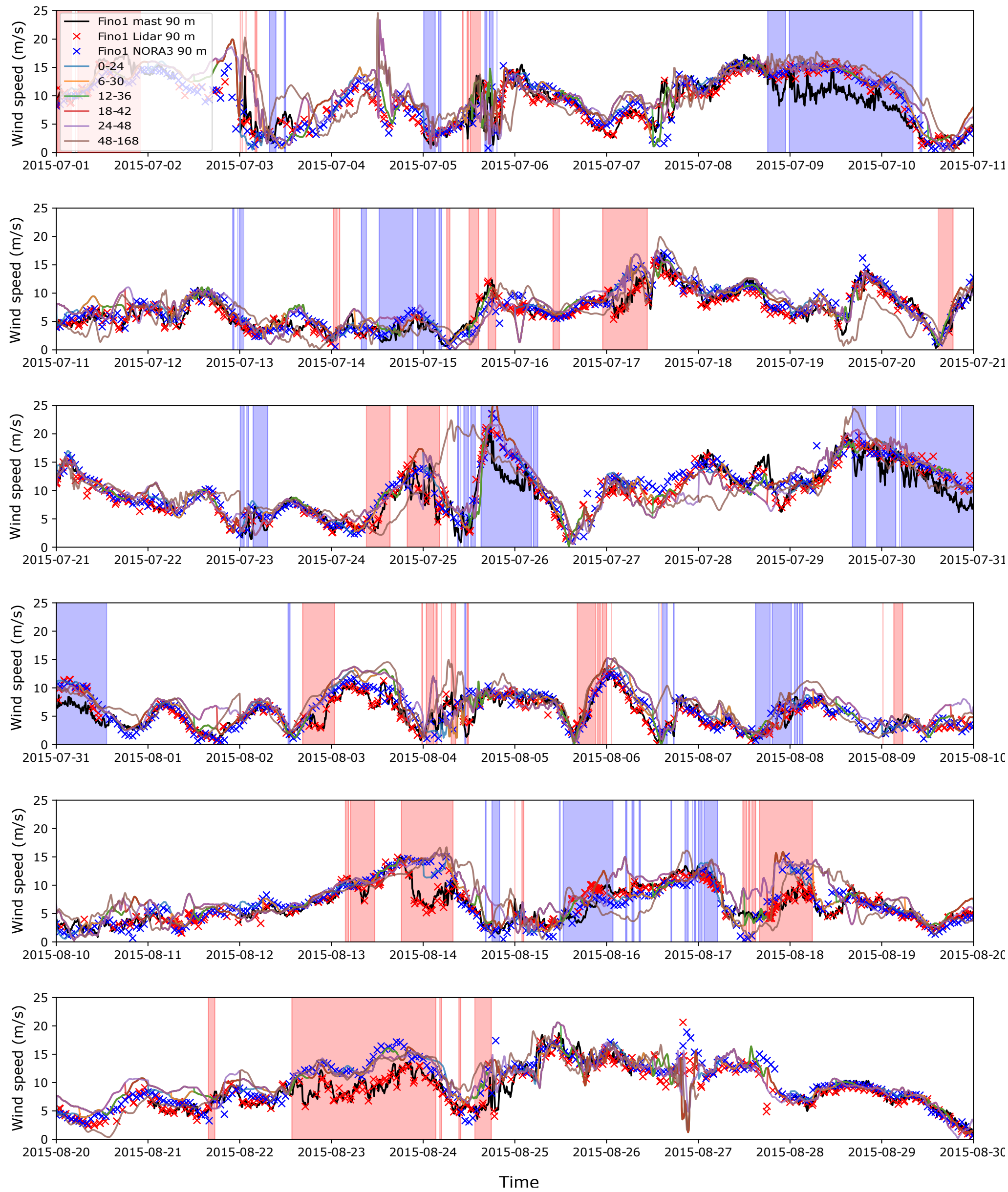

Figure 4.2: Time series of wind speed at 90 m of WRF's results with different simulation ranges compared with FINO1's cup anemometer, LiDAR data, and NORA3 data. The blue shades mark the regions with the wind direction between 285° and 345° (around the North-West direction), the red shades mark the regions with the wind direction between 70° and 110° (around the East direction).

above. If the observation is correct, then there are some fundamental processes that the mesoscale models (WRF and HARMONIE-AROME used by NORA3) cannot capture, for example, the wake effect of the wind turbines or small-scale turbulence. There is also a possibility the errors come from the initial and boundary conditions, which is ERA5 for both our simulation and ERA5. There are a few short periods where the NORA3 performs worse than the WRF, for example, around 12Z, 7 July, and 28 Aug., which may come from a coarse forcing of the lateral boundary conditions of 6h of NORA3 compared to 1h of our simulations.

The first type of mismatch between the WRF and the cup's observation can be attributed to the errors in the observation. For example, Porchetta et al. (2019) mentioned a shadow zone that affects the sonic anemometers caused by the mast when the wind direction is 60 and 200°. However, because the position of the cup anemometers relative to the mast are opposite to those of the sonic anemometers, we expect that the shadow zone for the cup anemometers is also opposite. These mismatches consistently confirm the influence of the mast pole on the observed wind speed of the cup anemometers. In Fig. 4.2, the wind direction between 285 and 345° are marked with the blue shades.

The second type of speed mismatch cannot be explained by the shadow effect because there is no systematic difference between the LiDAR and cup anemometers. From Fig. 3.1b, the FINO1 mast locates less than 500 m to the west of the closes wind turbine of the Alpha Ventus offshore wind park. Thus, the wind speed at the FINO1 mast may be influenced by the wake effects of the wind turbines when the direction is from the east. In Fig. 4.2, we marked the directions between 70–110° (easterly wind) as red shades, which well covers the second type of speed mismatch between the mesoscale simulations (WRF and NORA3) and the observations (cups and LiDAR).

Figure 4.3 shows the wind roses for the two months of the FINO1's cup anemometer observation and WRF simulations with different ranges discarded the time steps where the mast's wind directions are within the shadow or wake zones. The majority of the wind distribution comes from the west-southwest direction, which is well captured by the WRF from the simulation ranging from 0–24h to 12–36h. However, the simulated wind slightly rotated to the west direction.

4.3 Simulations for Teesside site

Contrary to the FINO1 mast station, which is quite far from land, the Teesside mast station is right at the coast (Fig. 3.1) and thus may be influenced by more complex topography-related atmospheric processes. The nearby offshore wind park is less than 2 km from the east, thus a little further away compared to the FINO1 station. However, the wind park is packed with a higher density of wind turbines and we should expect some influence from the wake effect of the wind turbines.

For the Teesside region, the simulation period is outside of the coverage of our available meteorological mast data. For this reason, we use the averaged wind speed of the SCADA data at wind turbines of Teesside's offshore wind park (Fig. 3.1a). Figure 4.4 shows the time series of the WRF's simulations and NORA3 data compared with the SCADA data. Similar to the FINO1 region, the NORA3 and the WRF agree quite well with each other and to the observation for most of the time. However, there are also some periods where both the NORA3 and WRF are diverse from the SCADA data, for example, 23–24 Aug.

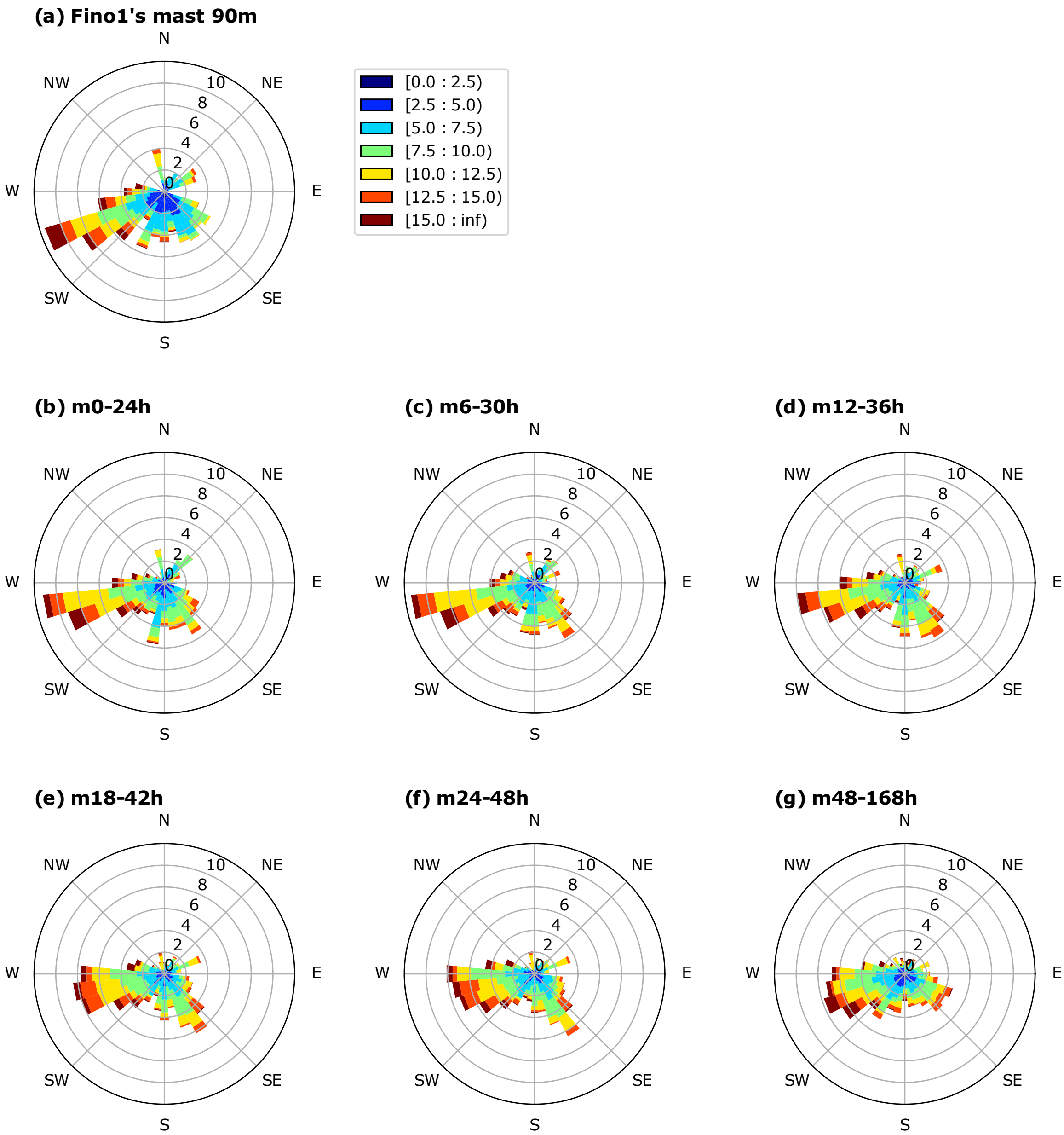

Figure 4.3: Windroses for the two-month period of FINO1's cup observation at 90 m vs. WRF's simulations

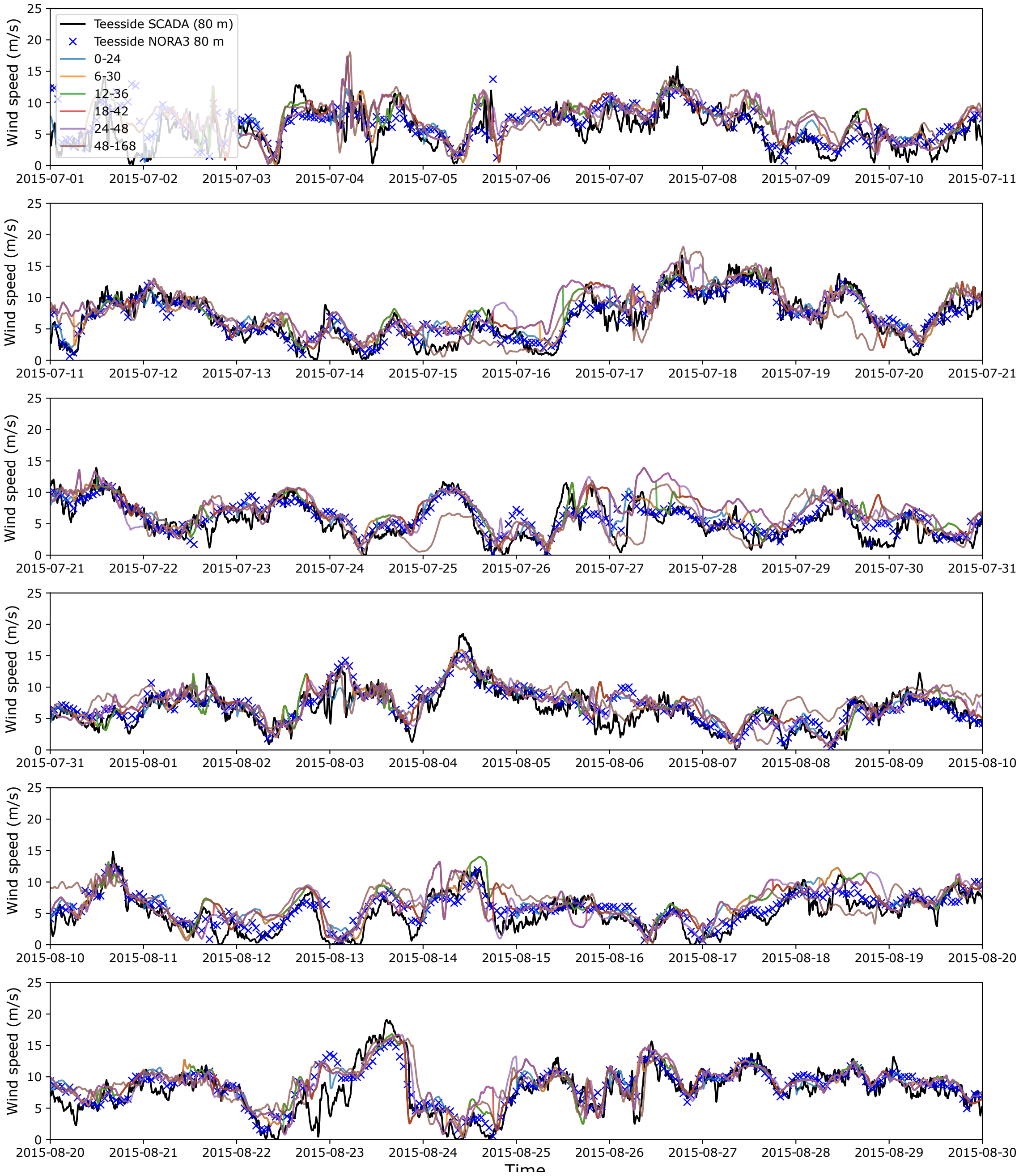

Figure 4.4: Time series of wind speed at 80 m of WRF vs SCADA's wind speed of 27 Teesside's turbines and NORA3 data.

Because we don't use the Teesside mast data, the issues of shadow effect as well as the wake effect on the mast location are excluded. However, there are also some periods where htere are large mismatches between the WRF and SCADA data, for example from 21 to 23 Aug 2015. The NORA3 data also behaves similarly to the WRF during these periods. Thus, these mismatches can result from several reasons: the wind speed difference between locations of the mast and the wind farm, or small-scale processes that the mesoscale models cannot capture.

Figure 4.5 displays the windroses for the Teesside wind farm's headwind averaged SCADA data and the WRF's simulations at the Teesside mast's locations. Similar to the simulations at the FINO1 site, the WRF's shorter-range simulations can capture the prevalent wind directions of SW, similar to the observation. The distribution of lower wind speed (under 5 m/s) is higher for the observation.

4.4 Validation

Figure 4.6 shows the Taylor diagram for the WRF's simulated wind speed versus SCADA's observation (for Teesside) and mast's anemometer (for FINO1). The diagram demonstrates that the WRF's performance decreases consistently with the simulation range, with the best performance at 0-24h. Before the exclusion of the shadow and wake direction, the simulations for the FINO1 site have a similar performance to that for the Teesside site, with a correlation of about 86% at the FINO1 and 83% at the Teesside for the range of 0-24h. However, the variation of the WRF simulation is larger than the observation for the FINO1 site and smaller than the observation for the Teesside site. After excluding the shadow and wake directions, the simulation at FINO1 performs better than at the Teesside with a correlation of nearly 90% for the 0-24h range. The variation of the WRF simulation after the direction exclusion is also closer to, although slightly smaller than the observation.

Figure 4.7 shows the fitted Weibull's distribution for the two months at Teesside and FINO1 of the observations and WRF's simulations. The shape and scale parameters are provided in Table 4.1. For the Teesside site, the model underestimates the frequency of the low-speed wind (under 5 m/s) while overestimating the frequency of the high-speed wind. The peak probability of the wind speed for the SCADA data is about 4 m/s and is higher for the simulation at about 7 m/s. For the FINO1 site, the wind speed distribution is closer to the observation. The peak wind speed for the mast's anemometer is about 6 m/s, which is higher than that for Teesside's SCADA data. On the other hand, the peak wind speed of the WRF at the FINO1 is similar to that at the Teesside's mast location.

Figure 4.8 and Table 4.2 summarize the wind speed errors of the WRF simulation compared with the observation for the 2-month period. Once again, the results show a systematic decrease in the model's performance with the longer simulation range. The longer the range is, the higher the MAE and RMSE are. For both sites, there is a positive wind speed Mean Bias Error (MBE). With the shadow and the wake directions excluded, the results for the FINO1 perform better than the Teesside. The best performance is for the range 0-24h at the FINO1 with a bias MBE of 0.64 m/s, MAE of 1.42, and RMSE of 1.85 m/s. While there is a certain bias, which may result from the fact that the WRF simulation does not take into account the wake effects of the surrounding wind farms (Fig. 3.7), the MAE and RMSE are quite close to those between the mast's anemometer and the LiDAR data (Table 3.2), which are 1.01 and 1.54 m/s respectively.

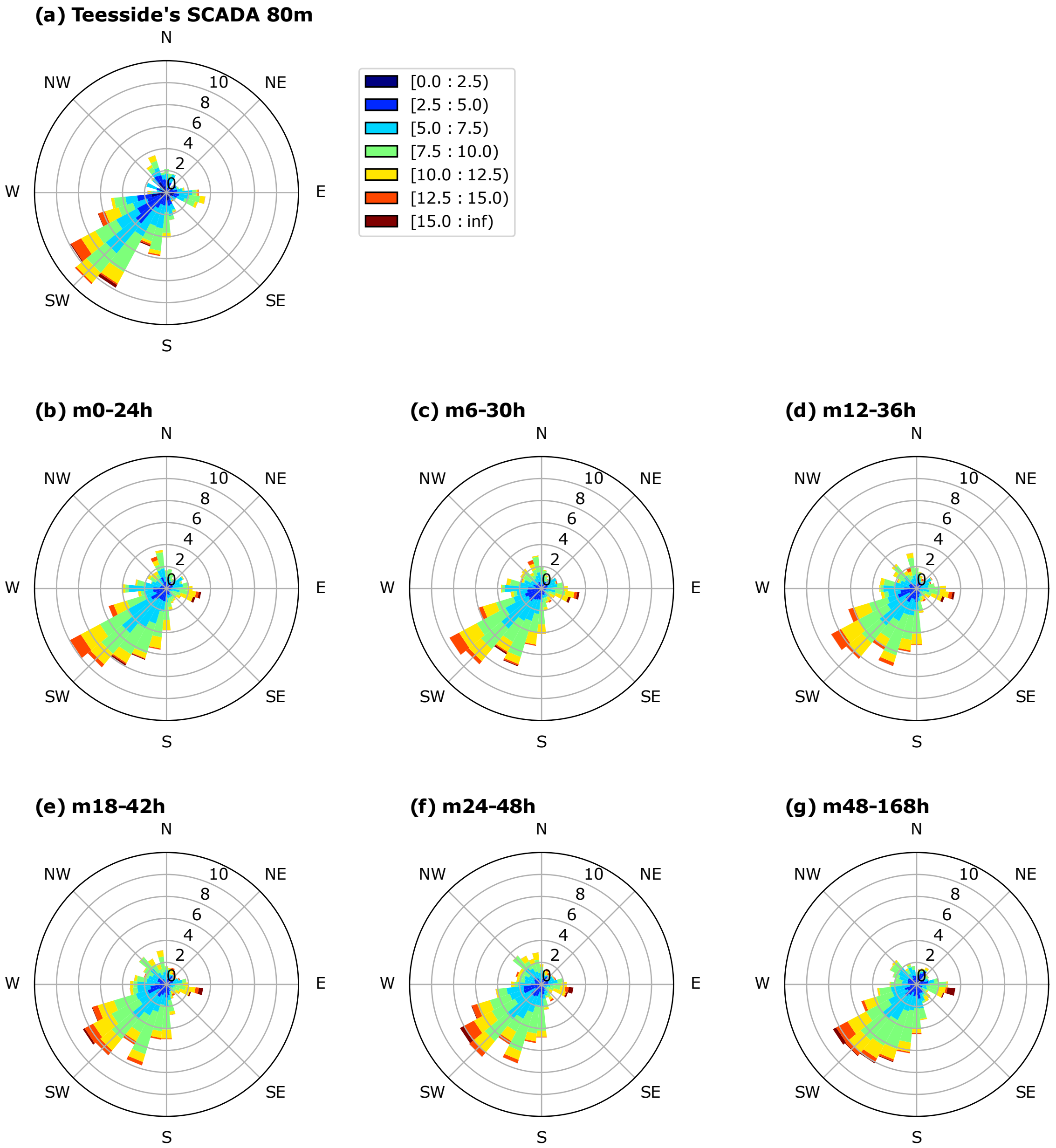

Figure 4.5: Windroses for the two-month period of Teesside's SCADA observation at 80 m vs. WRF's simulations

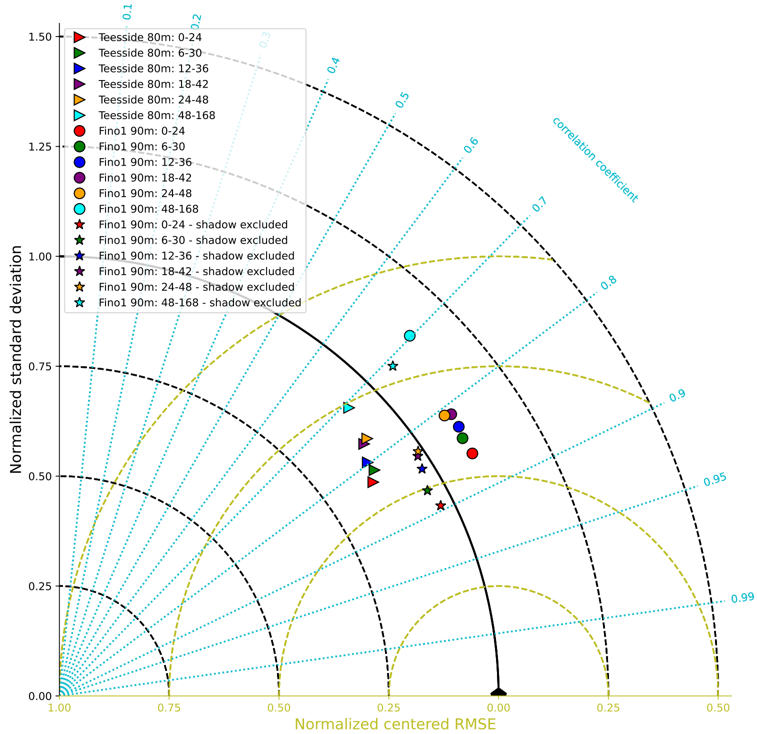

Figure 4.6: Taylor diagram for WRF's wind speed simulations vs. Teesside's SCADA data and FINO1's cup anemometer data at 90 m

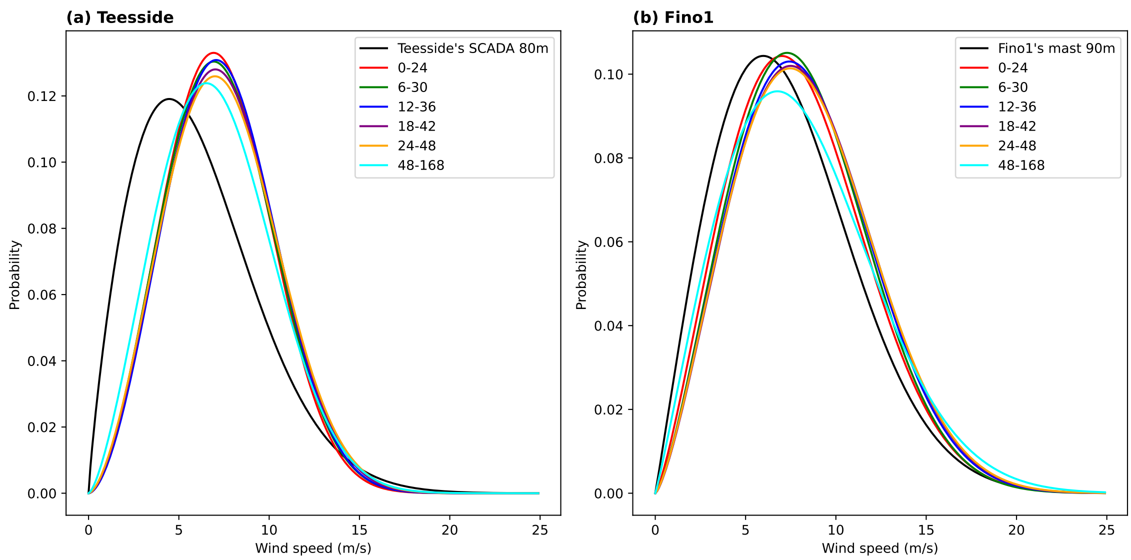

Figure 4.7: Fitted Weibull's distribution for the two-month period at Teesside and FINO1 of observations and WRF's simulations.

Case	Shape param. k	Scale param. λ
For Teesside at 90 m		
SCADA	1.84	6.84
0-24h	2.74	8.17
6-30h	2.70	8.23
12-36h	2.75	8.33
18-42h	2.68	8.35
24-48h	2.64	8.38
48-168h	2.46	8.06
For FINO1 at 90 m		
Mast	2.03	8.32
0-24h	2.28	9.02
6-30h	2.37	9.20
12-36h	2.36	9.37
18-42h	2.36	9.46
24-48h	2.34	9.47
48-168h	2.09	9.22

Table 4.1: Fitted Weibull parameters for the two-month simulations at Teesside and FINO1 vs the observations.

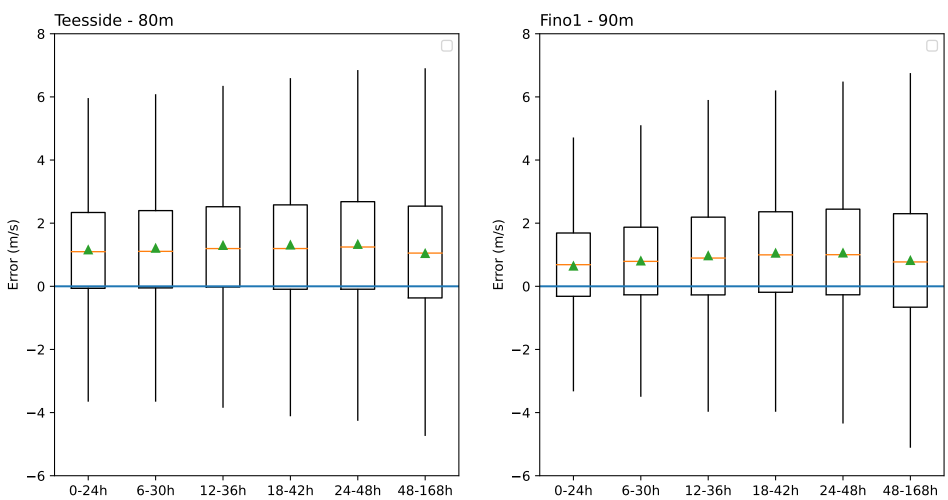

Figure 4.8: Box plots for the wind speed errors for the 2-month simulations at Teesside and FINO1. The data at FINO1 has the shadow and wake directions excluded.

Table 4.2: Wind speed errors for the 2-month simulations.

-	0-24h	6-30h	12-36h	18-42h	24-48h	48-168h
For Teesside at 80 m						
MBE	1.16	1.21	1.30	1.31	1.33	1.04
MAE	1.73	1.78	1.87	1.95	2.00	2.08
RMSE	2.20	2.29	2.40	2.53	2.56	2.67
For FINO1 with shadow/wake directions excluded						
MBE	0.64	0.81	0.97	1.05	1.06	0.82
MAE	1.42	1.56	1.76	1.87	1.91	2.25
RMSE	1.85	2.06	2.30	2.44	2.48	3.13

4.5 Discussion

We have carried out the mesoscale simulations using the WRF with the resolution of 9 km for a large region containing the North Sea (Fig. 3.7) with different simulation range from 1 day (0–24h) to a week (48–168h). The purpose of the simulation is to examine the ability of the mesoscales model to simulate the wind speed at the hub height of the wind turbines and the effect of the simulation range on the model's performance. We validate the simulation results with the observations of the Teesside and FINO1 meteorological mast at the hub height of the wind turbines located nearby.

The WRF model performs the best with the shortest range simulation of 0–24h as the errors increase systematically with the longer range. The performance of the WRF for the FINO1 site is better once we exclude the wind directions that are affected by the shadow effect of the mast pole (directions between 285° and 285°, i.e. the north-westerly wind) and the wake effect from the nearby turbines (directions between 70° and 110°, i.e. the easterly wind). The simulation for the Teesside site performs worse in our experiments, which may result from the fact that the wind farm locates close to the coast (Fig. 3.1), where the processes influenced by the topography and land-sea contrast might be more difficult to capture.

For the FINO1, even after the exclusion of the shadow effect from the mast and the wake effect from turbines to the east, the simulated wind speed still has a positive bias of nearly 1 m/s (Table 4.2), which may be attributed to the wake effect of the wind farm nearby. These differences can be alleviated by the inclusion of a wind farm parameterization, for example, the Fitch's scheme to the WRF. However, the direct wake effect of the individual turbines, as we will demonstrate in another section of this report, cannot be captured by the mesoscale WRF, even with the wind farm parameterization, which takes into account the wake effect of multiple wind turbines collectively. For this reason, the use of smaller-scale LES models with an appropriate actuator disc model to account for the wake effect of individual wind turbines is desirable.

5 WRF case studies for transient events

5.1 During an OCC event

5.1.1 Background

Open Cellular Convection (OCC) is a special type of mesoscale shallow convection that often occurs when a cold air mass moves over a warmer sea surface during a cold air outbreak event (Agee et al., 1973; Atkinson and Wu Zhang, 1996). The OCC can cause high-frequency fluctuations in the wind speed that greatly affect the operation of offshore wind farms (Atkinson and Wu Zhang, 1996; Göçmen et al., 2020). These high-frequency fluctuations have predictable timescales of only a few hours or less (Lorenz, 1969; Archer et al., 2017) and thus is a challenge for mesoscale models, where the sub-hour fluctuations are considered stochastic and the exact time and location of the convective cells are unpredictable. On another hand, the OCC is also associated with large-scale conditions, a mesoscale model is expected to be able to simulate the time-varying, or so-called the deterministic aspect, as well as the statistics of stochastic aspects of the OCC. Thus, for model validation, we propose the decomposition of the original time series data into the deterministic and stochastic components.

To resolve the small-scale convection as the OCC, a fine resolution of a few kilometers is usually needed. In such cases, the cumulus parameterization is usually turned off. Then, the choice of physics parameterizations, especially the boundary layer and microphysics schemes can greatly affect the accuracy of the simulation. There were a number of OCC studies using the WRF models (e.g. Vincent et al., 2012; Göçmen et al., 2020; Imberger et al., 2021). However, to our knowledge, no studies were done to investigate the sensitivity of the parameterizations for the OCC specifically. Several studies investigated the sensitivity of planetary boundary layer parameterizations for the wind prediction in the boundary layer in general (Draxl et al., 2014; Carvalho et al., 2014; Banks et al., 2016; Avolio et al., 2017; Gunwani and Mohan, 2017; De Lange et al., 2021) and there is no agreement on the optimal configuration in general.

In this section, we carried out a parameter sweep experiment of physics parameterization using the WRF model during an OCC event. We investigate how the wind speed in the boundary layer changes with model resolutions and physics options. Starting from a control experiment, we designed three series of experiments, each varying the parameterizations of one group out of three: the planetary boundary layer, microphysics, and radiation. The sensitivity experiment is carried out for the Teesside region because it has less affected by the surrounding wind parks compared to the FINO1. We then validate the results against Teesside's meteorological mast data and derive the optimal configuration by combining the best option in each category.

We simulate the wind field for two days from 00Z November 21 to 00Z November 23, 2015. During the period, an OCC event was associated with the cold air mass behind an extratropical cyclone and passed through the Teesside region. The time series of wind speeds at Teeside's mast location was extracted at every model time step. The WRF uses three nested domains (Fig. 3.7a), with the resolution of 9 km, 3 km, 1 km and time steps of 30 seconds, 10 seconds, and 10/3 seconds for D01, D03, and D03 respectively.

Table 5.1: Sensitivity experiments: The options denoted by "-" means they are the same as the CTRL experiment. The references for all the options can be found in https://www2.mmm.ucar.edu/wrf/users/physics/phys_references.html
.

Experiment	PBL	Surf. layer	Microphysics	Shortwave rad.	Longwave rad.
CTRL	MYNN2	MYNN	Thompson	RRTMG	RRTMG
bl01	YSU	MM5	-	-	-
bl02	MYJ	Eta	-	-	-
bl04	QNSE	QNSE	-	-	-
bl06	MYNN3	MYNN	-	-	-
bl07	ACM2	Pleim–Xiu	-	-	-
bl08	BouLac	MM5	-	-	-
bl09	UW	Eta	-	-	-
bl10	TEMF	TEMF	-	-	-
mp02	-	-	Lin	-	-
mp04	-	-	WSM5	-	-
mp06	-	-	WSM6	-	-
mp07	-	-	Goddard	-	-
mp10	-	-	Morrison	-	-
mp13	-	-	SBU–YLin	-	-
mp14	-	-	WDM5	-	-
mp16	-	-	WDM6	-	-
ra01	-	-	-	Dudhia	RRTM
ra02	-	-	-	Goddard	RRTM
ra03	-	-	-	CAM	CAM
ra05	-	-	-	New Goddard	New Goddard

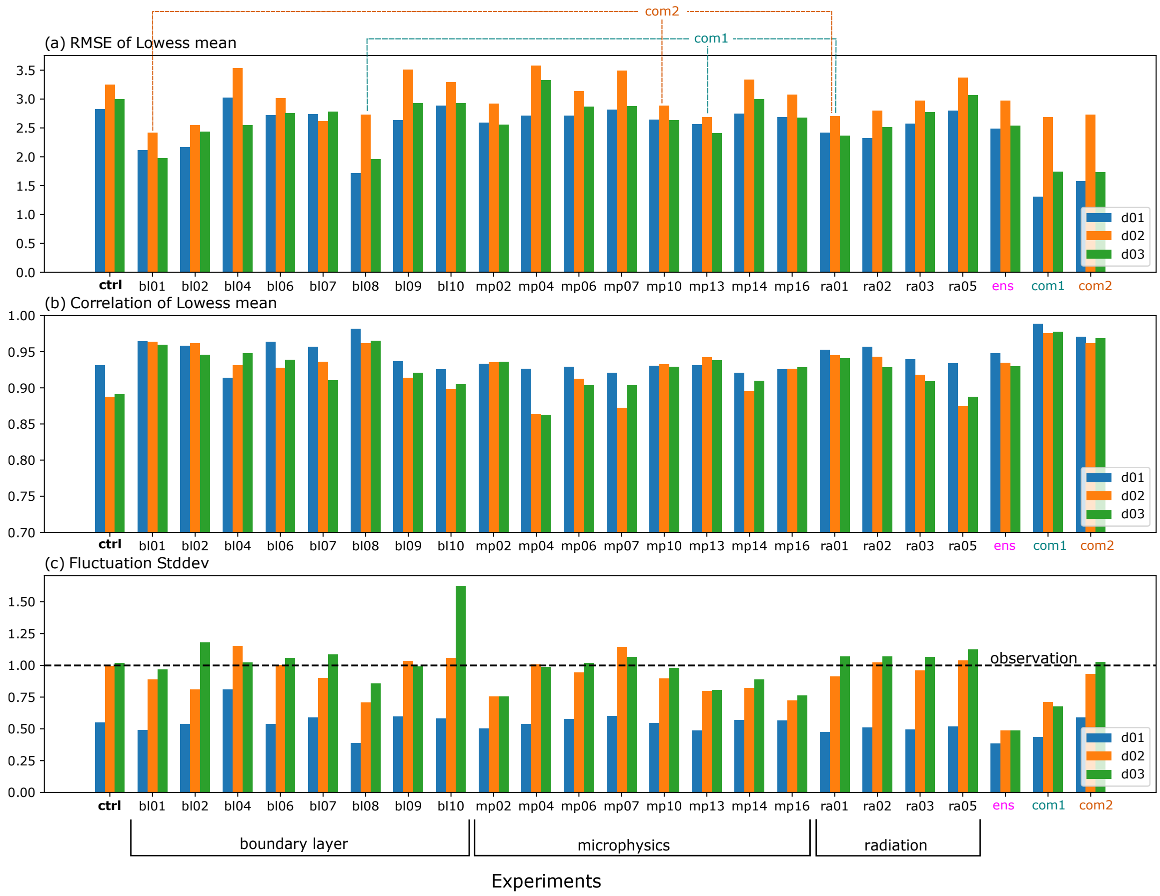

Figure 5.1: The root mean square errors of the mean (a), the correlation coefficient of the mean (b), and standard deviation of the fluctuation (c) of the 10-min averaged wind speed at 50 m for different experiments against the Teesside's mast anemometer.

5.1.2 Experiment design

The simulation results depend on the combinations of the physics parameterizations: the Planetary Boundary Layer (PBL), the surface layer, the microphysics, the cumulus convection, the short wave radiation, and the longwave radiation. It is impractical to test all the combinations as the number is very large. In our study, we reduced the number of combinations by starting from a control experiment(CTRL, Table 3.3), then changing the parameters in each of the three parameterization groups: boundary layer, microphysics, and radiation (Table 5.1). In the first group, eight experiments are designed with several PBL and surface schemes together. There are also eight experiments that vary the microphysics schemes and four that vary the radiation schemes (shortwave and longwave). As discussed, the cumulus parameterization can be turned off for the 3-km and 1-km domains, and use the Tiedtke cumulus scheme (Zhang et al., 2011) for the 9-km grid, which is the same for all the sensitivity experiments. We use the Unified Noah Land Surface Model (Mukul Tewari et al., 2004) for the land surface parameterization. The wind farm parameterization is not used because it can only be used together with the MYNN planetary boundary layer schemes.

Table 5.2: Two derived combinations of physics configurations

Experiment	Boundary layer	Surface layer	Microphysics	Shortwave rad.	Longwave rad.
com1	BouLac	MM5	SBU–YLin	Dudhia	RRTM
com2	YSU	MM5	Morrison	Dudhia	RRTM

5.1.3 Result

The RMSE and correlation of the deterministic component, as well as the standard variation of the stochastic component, are shown in Fig. 5.1. Firstly, we found that higher resolution does not lead to a better performance in terms of the deterministic aspects. For most cases, the 3-km resolution performs the worst with the highest RMSE and lowest correlation coefficient, the 9-km domain performs slightly better than the 1-km domain (Fig. 5.1a,b).

From the stochastic perspective, the variation of the fluctuation is highly sensitive to the resolution. The variation of the stochastic component is higher with smaller grid sizes (Fig. 5.1c). The 9-km domain can captures only about half of the observation's variation, while the variation of the 1-km resolution simulation is similar to the observed for most experiments.

In an attempt to improve the simulation result, we first carry out a simple ensemble mean (named ens in Fig. 5.1) by taking an average of the wind speed of all experiments. However, the result is disappointing: the statistics for the deterministic component are not the best compared to individual experiments; on the other hand, the stochastic fluctuation is heavily damped (Fig. 5.1c).

Two additional experiments in Fig 5.1, com1 and com2 (Table 5.2), are the combinations derived from choosing the options that perform well in each parameterization group. com1 is the combination of experiments bl08 (BouLac boundary layer), mp13 (SBU-YLIN microphysics), and ra01 (Dudhia and RRTM radiations). Each option is the best-in-group for the deterministic component. However, bl08 and mp13 have the lowest (worst) standard deviation of the stochastic component. Thus, the com2 is chosen as a compromise by changing the boundary layer and physics option to bl01 (YSU) and mp10 (Morrison), which are the second-best-in-group, and the stochastic standard deviation is more realistic.

Experiment com1 performs better than all other experiments for the deterministic component with the lowest RMSE and highest correlation at the 9-km and 1-km resolutions, which means the combination has an additive effect on the individual experiments. However, the stochastic variation is significantly damped and is only slightly larger than the ensemble. On the other hand, com2 also performs well for the deterministic component similar to com1. However, the fluctuation level of com2 is higher and is closer to the observation, especially for the 1-km resolution.

The 10-min averaged time series of wind speed at the height of 50 m (Fig. 5.2) show that experiments ctrl, ens, com1, and com performs much better than the forcing ERA5 reanalysis data, which heavily underestimates the wind speed. For the control experiment, the wind speed is underestimated at around 06Z on Nov 21 and overestimated around 00Z on Nov 22 by about 5 m/s for all resolutions. The ensemble means, ens, does not improve the performance compared to the ctrl and most of the fluctuation is heavily removed.

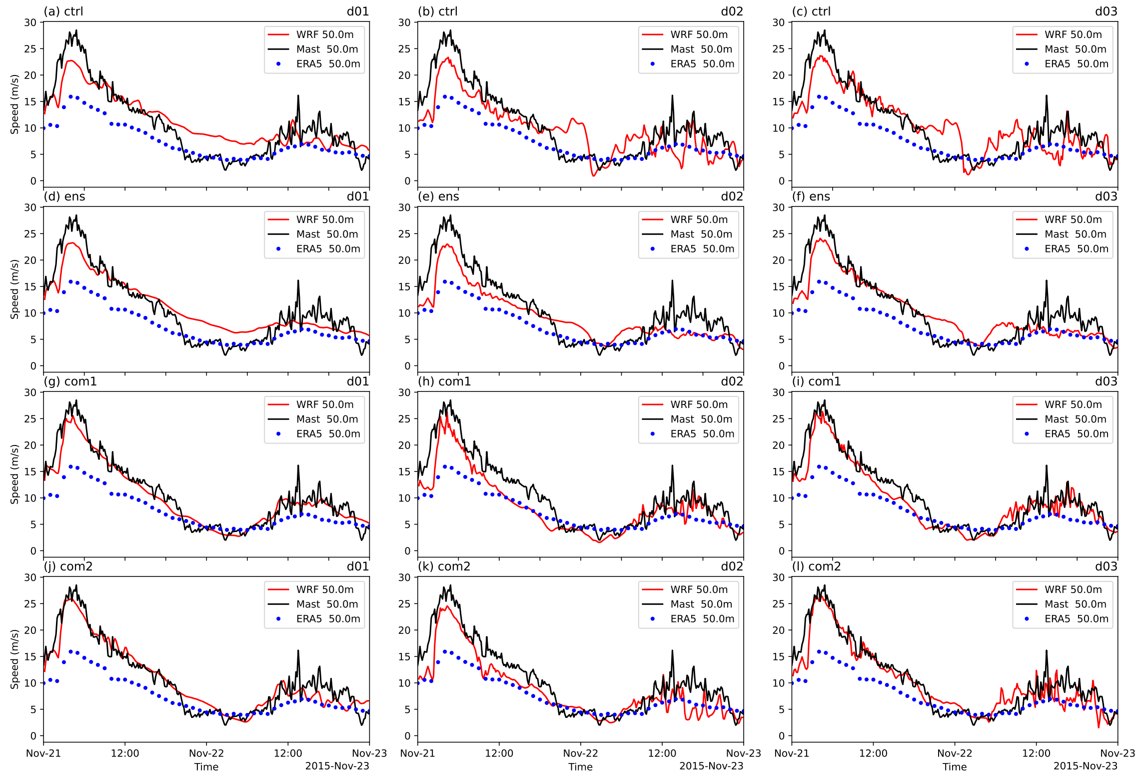

Figure 5.2: Time series of 50-m, 10-min wind speed of the Teesside mast's observation versus WRF simulations of experiments ctrl, ens, com1 and com2 at three resolutions. The ERA5 reanalysis data is also shown hourly.

Experiment com1 performs the best for the deterministic component, especially for the coarse resolution of 9 kilometers. However, it slightly underestimates the wind speed for the first day for the 3-km and 1-km grids. The high-frequency variation is also significantly reduced across the resolutions during the first day, which explains the low standard deviation in Fig. 5.1. However, com1 can still capture some of the stochastic variations on the second day, when the OCC passed through the Teesside met mast.

Experiment com2 also performs well for the deterministic component similar to com1, despite the fact the two experiments use different PBL schemes. Com2 performs better than com1 for the first day but slightly underestimates the wind speed near the end of the integration period. Unlike com1, the fluctuation level of com1 is closer to the observation.

The snapshot of the vertical velocity at the Teesside turbines' hub height (80 m) shows that all experiments cannot resolve the OCC structure and 9 km resolution (Fig. 5.3). The OCC structure starts to reveal from 3 km with upward motions at the edges and the downward motion in the center of the cells. The power spectral density shows that most of the experiments, except com1, have a realistic spatial scale ranging from 20 km to 70 km, compared with 50 km of the observation (Fig. 5.4.a). The com1 experiment has the smallest spatial scale, especially at the 1-km resolution as the spatial scale is less than one-fifth of the observation. Higher resolution can also capture fluctuation with higher frequencies as revealed by the temporal power density spectral of the wind speed (Fig. 5.4.b). The variation for CTRL and com2 peaks ranges from 2 to 3 hours, while the peak period of com1 is less than 1 hour.

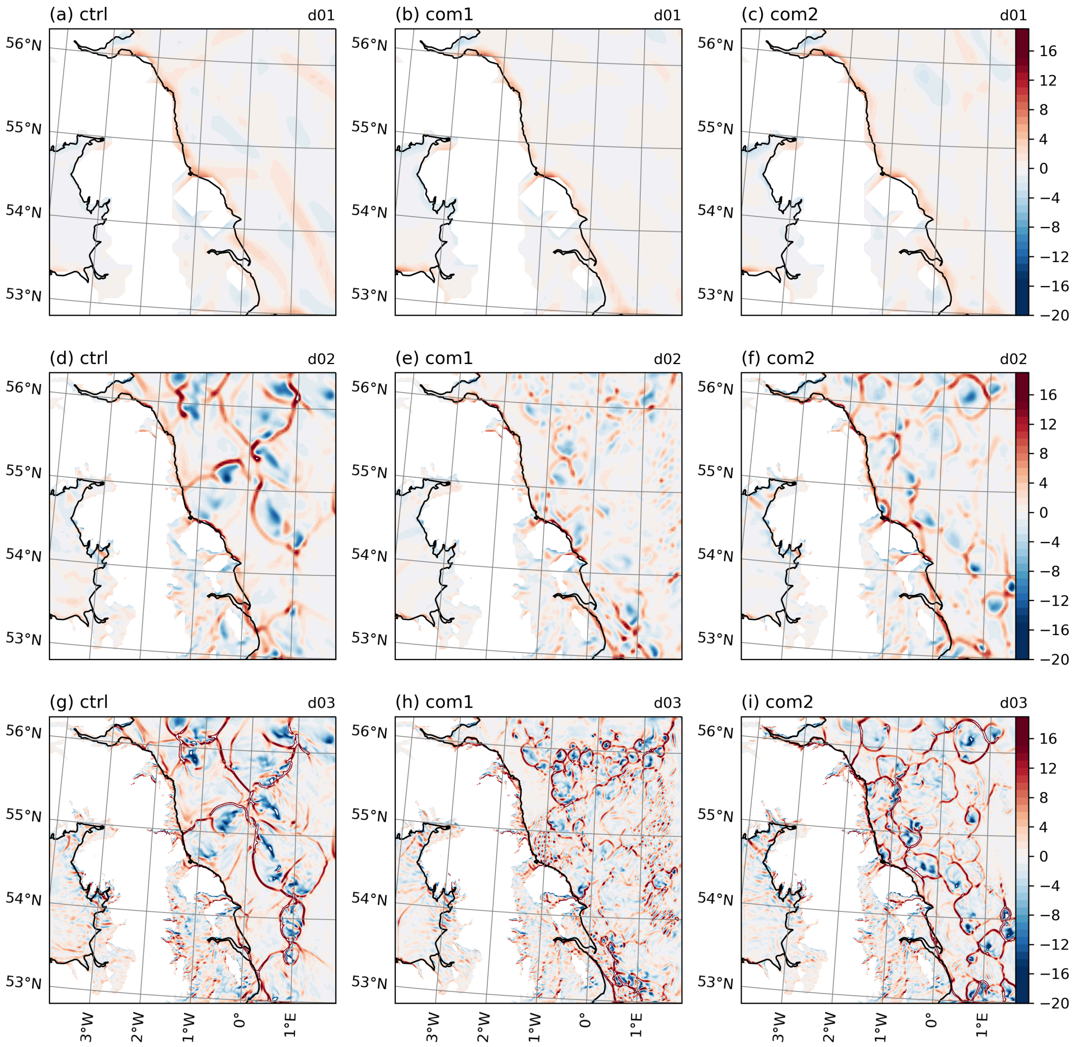

Figure 5.3: Snapshots at 12Z November 22, 2015 of vertical velocity at 80 m (Teesside turbine's hub height) in cm s^{-1} for experiments ctrl, com1, and com2. All plots are zoomed to the inner most domain (d03).

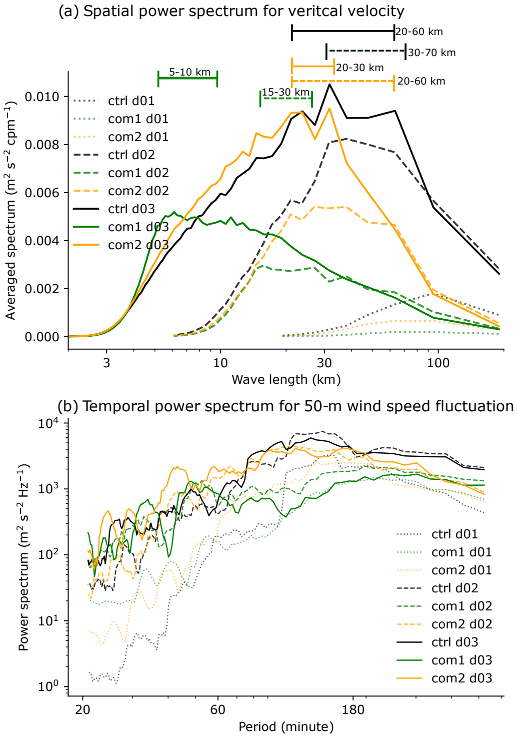

Figure 5.4: (a) Power spectrum of 80-m vertical velocity for experiments ctrl, com1, and com2; (b) Power spectrum of 10-min wind speed fluctuations.

5.1.4 Discussion

This study investigates the ability of a mesoscale numerical model to simulate an OCC event that passed through Teesside's wind park in November 2015. We use the WRF model with three nested domains to downscale the ERA5 reanalysis to a 1-km resolution. Three series of parameter-sweep sensitivity experiments are tested to select optimal configurations (Table 2) for the OCC event. To validate the model, we decompose the time series into deterministic and stochastic components. The results show that stochastic fluctuation is more sensitive to the resolution: higher resolution results in higher and more realistic fluctuation. The WRF starts to resolve the OCC structure from the resolution of 3 km and the spatial scale of the simulated OCC also strongly depends on the choices of the physics parameterization.

The MYNN schemes are popularly used in wind energy applications, partly because they can be used together with wind farm parameterization. However, in this case, study, both MYNN2, and MYNN3 do not perform well. We obtained two optimal configurations for the specific case. The first configuration performs the best in the deterministic aspect, however, the stochastic fluctuation is heavily damped. The second configuration performs well in the stochastic sense and is just slightly worse than the first configuration in the deterministic sense.

This study has an obvious caveat with only one case study, and the inaccuracy of the initial conditions and the observations are not taken into account. However, we demonstrated that an optimal configuration can be obtained by carrying out sensitivity studies of different parameters independently and by the combination of the well-performed experiments in each category. Interestingly, the combination can outperform all individual ones in an additive manner. To achieve a reliable general optimal configuration, further studies are needed by using a larger number of cases, data assimilation, and other sources of observation.

5.2 During a low-level jet event

5.2.1 Background

Low-level jet (LLJ) is the phenomenon where there is a relatively strong wind speed peak occurs within 2-3 km from the surface. In wind energy applications, LLJ noses within the boundary layer are of particular interest because the high wind speed and the fact that the LLJ-induced wind shear can affect the operation of the wind turbines.

The mechanism for the LLJ can be categorized into two groups: (a) Inertia Oscillations (IOs) and (b) baroclinicity. The IO mechanism for the LLJ is clearly explained by Blackadar (1957), where the nocturnal inversion leads to a decoupling of the atmosphere to the surface and reduces the apparent friction. The imbalance of the Coriolis and pressure gradient forces leads to an inertial oscillation with a period of $2\pi/f$, where f is the Coriolis. The original sub-geostrophic wind later becomes super-geotropic wind after a duration of less than half of the inertial period, which is about 8.5 h for the latitude of 45°N. The surface decoupling occurs where a thermal inversion exists, which does not limit to the nocturnal effect. It also occurs in some other situations, for example when the wind flows into a colder surface, with a less roughness length, or in a warm front system.

The baroclinicity mechanism is described by Holton (1967), where the LLJ occurs because of the temperature horizontal difference over sloping terrain. The direction of this temperature gradient alternates with the diurnal cycles and the diurnal oscillations provide energy for the LLJ. Burk and Thompson (1996) described a coastal LLJ that associates the baroclinicity along the coast and a capped inversion of the marine ABL. In any case, a strong temperature gradient zone near the surface results in a steep slope of the isobaric surfaces. Due to the thermal wind relation that leads to a high geostrophic wind speed maximum at the surface and decreases with height. The LLJ is a result of this decrease of geostrophic wind height above the LLJ, and the decrease of wind due to the friction below the LJJ. The horizontal temperature gradient can be formed from the differential heating of sloping topography or land-sea distribution, or when a cyclone-induced cold front swept through. Because the pure baroclinicity LLJ is weaker than the geostrophic wind, while the IO LLJ is stronger than the geostrophic wind, one can expect a more frequent occurrence of the IO type.

In reality, the LJJ can occur as a result of the combination of both mechanisms. The strong IO LLJ also requires a relatively strong geostrophic wind in the first place, thus the baroclinic effect also plays as a conditioning factor that builds up the potential environment for the IO LLJ. For the North Sea regions, Wagner et al. (2019) pointed out three mechanisms: a) Baroclinicity due to the difference of land-sea heating; b) Baroclinicity dues to fronts; and c) Inertial oscillations from the frictional decoupling at the coastline and on-land ABL stabilization.

5.2.2 A case study for the FINO1 region

We revisit an LLJ event from 13 Aug. 2015 to 12Z, 14 Aug. 2015, previously investigated by Wagner et al. (2019), which features a distinct jet profile and was well covered by the measurements. We perform the WRF simulation with 3 nested domains from 9 km to 1

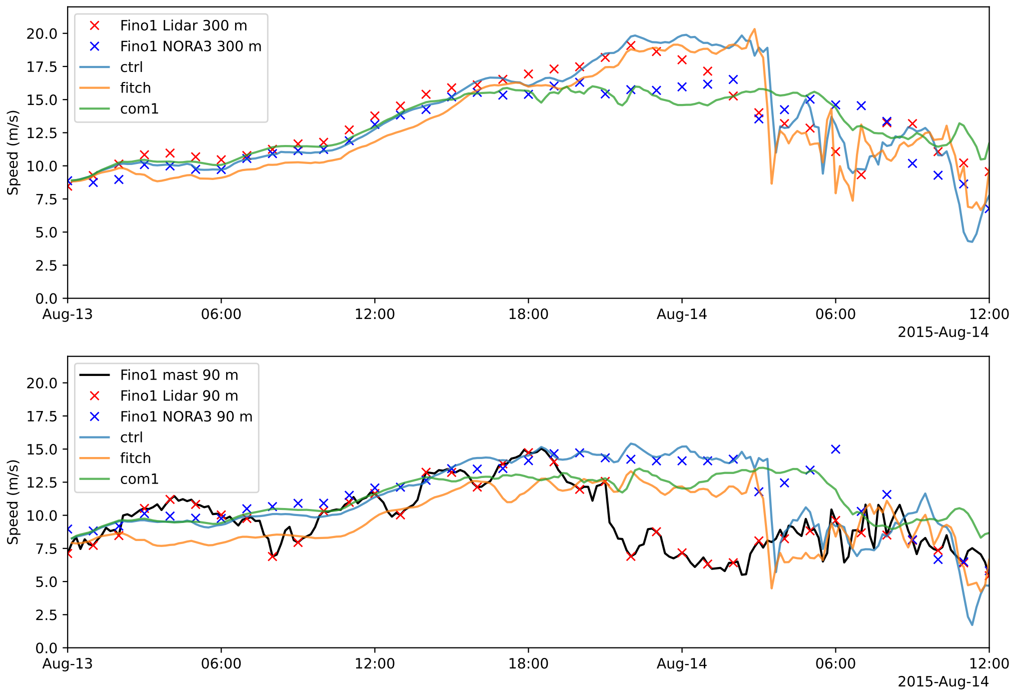

Figure 5.5: Time series of wind speed at the jet core height 300 m (a) and turbine hub height 90 m (b) of the observation (LiDAR and cup anemometer), NORA3, and three WRF's simulations from 13 Aug 2015 to 12Z, 13 Aug 2015.

km (Fig. 3.7b). Besides the control experiment CTRL (Table 3.3), we simulate the event with the same WRF's configuration with the Fitch's wind farm parameterization turned on - experiment fitch. We also performed the com1 configuration (Table 5.2), which is the optimal combination derived from the OCC sensitivity experiments.

Figure 5.5 shows the wind speed time series at the 90 m and 300 m (near the LJJ core) form WRF simulation versus the observation and the NORA3 data. For the 300 m level (Fig. 5.5a), all the WRF simulations capture closely the LiDAR data for the first 24 h until 00Z, 14 Aug. 2015. Interestingly, from 18Z, 12 Aug. 2015. the WRF experiments CTRL and Fitch perform better than NORA3 data, which is similar to the com1 experiment. After that, there is a sudden decrease in the wind speed for the CTRL and Fitch, in contrast to the gradual decrease in LiDAR data and an even smaller change for NORA3 and com1. With the wind farm effect presented, the Fitch experiment is slightly weaker than the CTRL throughout the integration period.

For the lower level at 90 m (Fig. 5.5a), the differences between the observations (mast's anemometer and LiDAR) and the mesoscale are more notable. Although the models capture the general trend of the wind speed for the first 18h, the fluctuation level of the observation is higher with some short periods of speed reduction. The most striking difference started from 18Z, 13 Aug. 2015, where the observed wind speed quickly decreases about 7 m/s over the 9 hours, while the WRF models and NORA3 data wind speed stay unchanged. Compared to the CTRL experiment, the Fitch experiment has a wind reduction of about 2 m/s, larger than that at higher levels.

As evident in Fig. 5.6a, the strong LLJ with a wind speed over 15 m/s occurs between

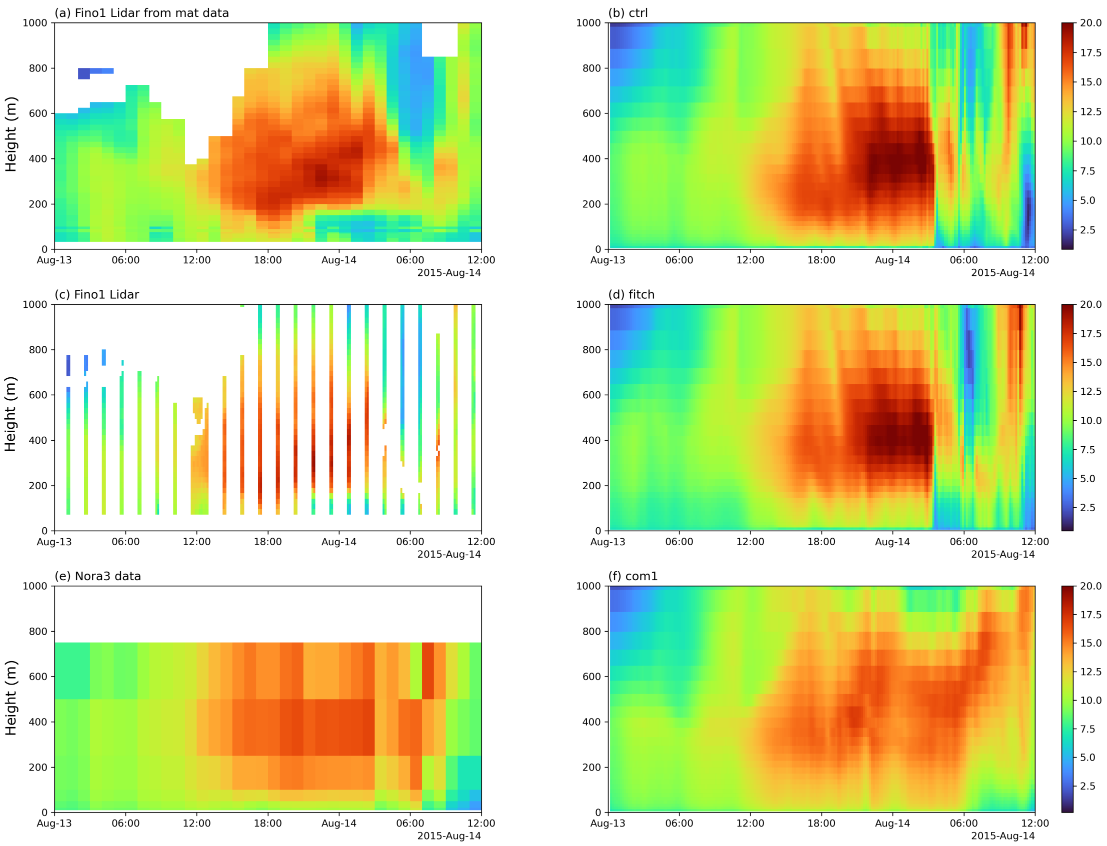

Figure 5.6: Time-height section of the LiDAR data (a,c), NORA3 data (e), and three WRF's simulations from 13 Aug 2015 to 12Z, 13 Aug 2015: ctrl (b), fitch (d), com1 (f).

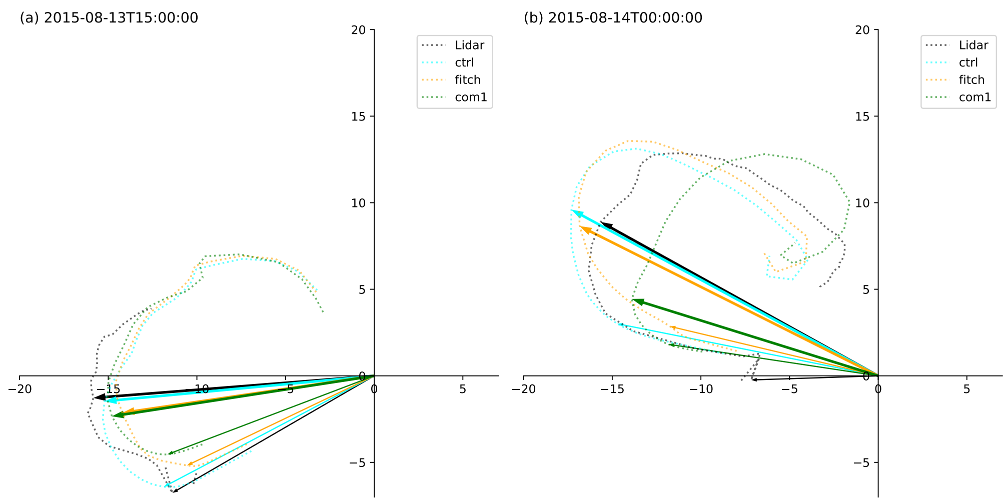

Figure 5.7: Hodographs at two timeslices at (a) 15Z, 13 Aug and (b) 00Z, 14 Aug 2015 for LiDAR data and WRF simulations. The thin arrows are wind vectors at 90m and the thick arrows are wind vectors at 300m

12Z, 13 Aug. and 06Z, 14 Aug. 2015, with the strongest intensity of about 20 m/s at the midnight 00Z, 14 Aug. 2015. The jet core lies between 200 to 400 m. In the simulation by Wagner et al. (2019), the simulated LLJ intensity is underestimated (their Fig. 17), which agrees with our com1 experiment (Fig. 5.6f). However, for our CTRL and Fitch experiments, the LLJ intensity is slightly stronger than that in the LiDAR data.

Above 200 m and around 06Z, 14 Aug., there is a large wind speed reduction present in the LiDAR. The LLJ weakens with the core height coming lower down to 200 m, then the LLJ terminates as there is no decrease of the wind speed with height. Both CTRL and Fitch can capture this evolution while com1 and NORA3 as well as the simulation by Wagner et al. (2019), cannot.

The hodographs (Fig. 5.7) show that at the onset of the LLJ in the afternoon, 15Z 13 Aug., the WRF simulations can capture well both the wind speed and direction with height, as the observed wind spiral is close to the models. However, the spirals become diverse at the peaked-intensity time for the LLJ at 00Z, 14 Aug. with an overestimation of the LLJ intensity for CTRL and Fitch, and an underestimation for com1. At the hub-height levels, all the simulations overestimate over 5 m/s or 100% to that of the LiDAR data. The hub-height WRF's wind direction is also slightly rotated clockwise compared to the observation.

The wind speed reduction from 18Z, 13 Aug., and 06Z, 14 Aug. in the LiDAR data (Fig. 5.6a) occurs rather uniformly in a thin layer of about 200 m from the surface. This suggests the wake effect of the wind turbines nearby. The wake effect is also evident in the hodograph at 00Z 14 Aug (Fig. 5.7b), the observed wind below 90 m is easterly, which is the direction to the nearest wind turbine of the Alpha Ventus wind farm (Fig. 3.1b). While the wake effect is represented using the Wind-Farm Parameterization (WFP) in the Fitch experiment, the WRF cannot resolve this strong wind speed reduction over time and space. The reason is that the WFP in the WRF model considers a collective effect of multiple turbines within a grid cell. The distance from the FINO1 platform to the nearest wind turbines is about 400 m, which is smaller than the finest grid size of D03 of 1 km.

Thus, the wake effect can be presented throughout the integration period with a weaker magnitude and regardless of the wind direction (Fig. 5.6d and Fig. 5.5a).

5.2.3 Mechanism of the low-level jet event

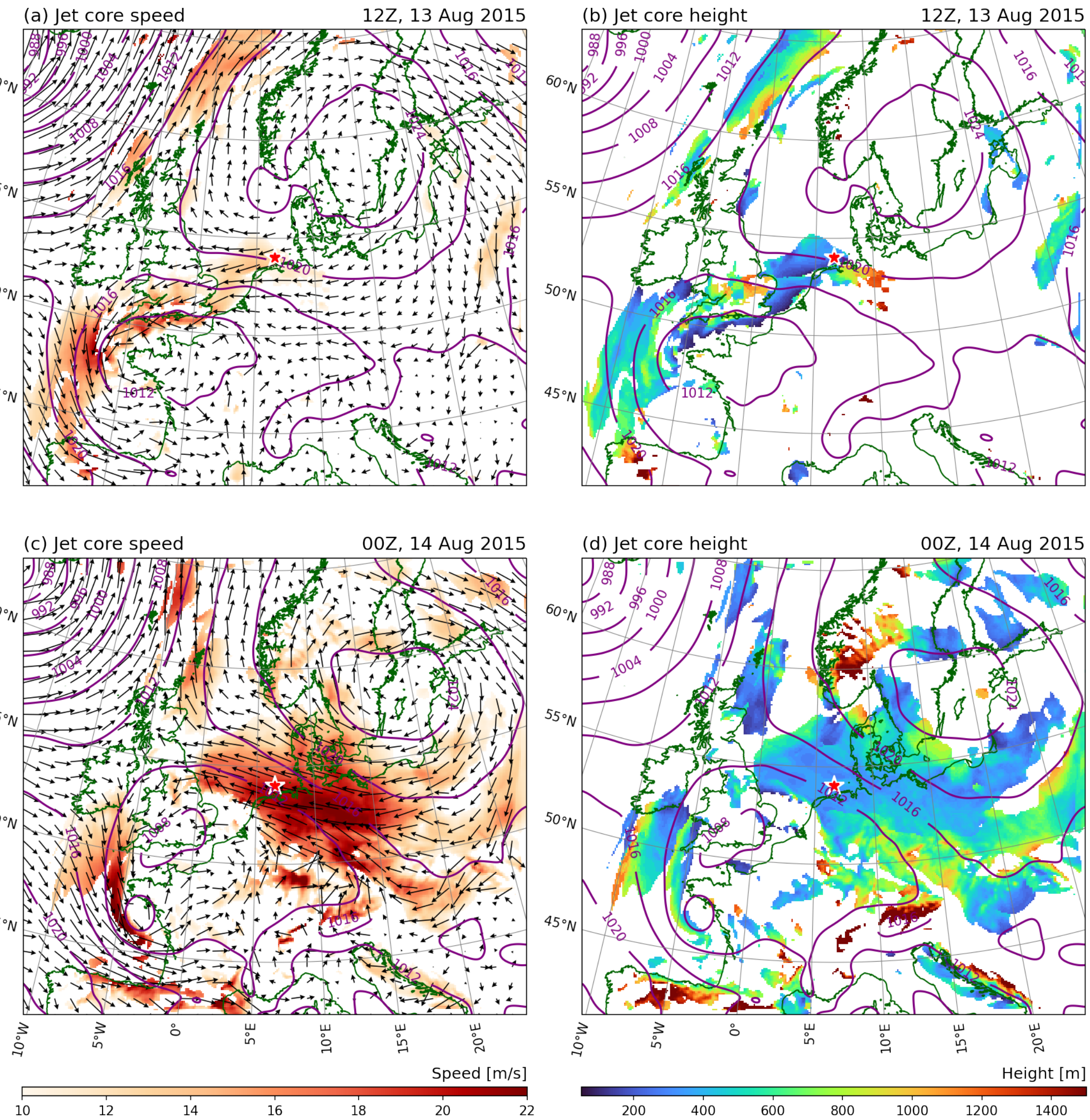

Figure 5.8: Low-level jet core speed and 300m horizontal wind vectors (a,c), core height (b,d) for 12Z, 13 Aug. (top) and 00Z, 14 Aug. 2015 (bottom) detected from the 9-km domain of the CTRL simulation. The plots are overlaid with smoothed sea level pressure.

Because the CTRL case can capture most of the features of the observed LLJ, we consider the WRF dynamics is reliable in this case and three-dimension WRF outputs can be used to understand the mechanism of the LJJ. Figure 5.8 shows the horizontal distribution of the LLJ core speed and height at the onset time (at 12Z, 13 Aug., Fig. 5.8a–b) and maximum-intensity time (00Z 14 Aug., Fig. 5.8c–d) for the 9-km domain WRF's CTRL experiment. The LLJ is detected using the detection method of Wagner et al. (2019) where under 1500 m, there must be a wind speed maximum that is at least 2 m/s and 25% greater than the maximum above it. This is a relatively relaxed condition where the LJJ intensity can be as low as 2.25 m/s. To focus on the stronger LLJ event, we added another criterion, where the wind speed maximum must be at least 10 m/s.

At the onset time, the LLJ occurs mainly offshore in the southern part of the North Sea, starts from the southern part of an anti-cyclone located over southern Sweden, and extends to the northwest part of a weak cyclone located over the coast of France. The LLJ intensity over FINO1 is just over 10 m/s. At the maximum intensity phase, the LLJ originates further from the land and blows towards the Southern North Sea. The LLJ core speed at FINO1 increases nearly two folds in 12h to over 20 m/s. The cyclone elongated and splits into two centers with a new one locates in the south of England. To the east of the combined centers, there exists a narrow northerly LLJ with strong intensity of over 20 m/s. In both times, the height of the LLJ over the south of the North Sea ranges from 200 to 400 m, whereas the LLJ to the east of the cyclones has a higher level of about 500 m.

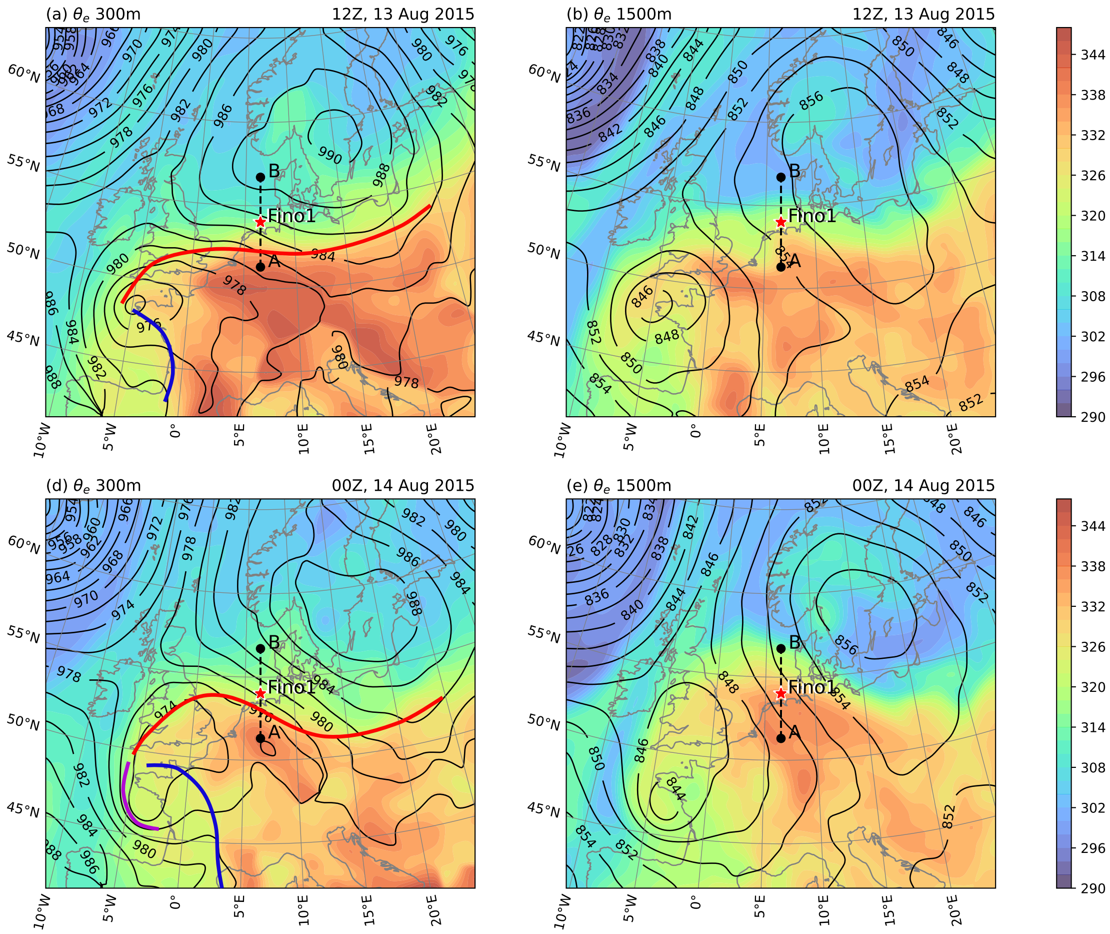

Figure 5.9: Equivalent potential temperature (shaded) and atmospheric pressure (contours) at 300 m (left) and 1500 m (right). The solid red, green, purple curves are averaged surface front lines for warm, cold and occluded fronts respectively. The dashed black line A–B is used for the cross section in Fig. 5.10.

Figure 5.9 shows the equivalent potential temperature, which is useful for identifying air masses, on 300 m and 1500 m levels for the two time-slices. During this period, the cyclone evolves into the occlusion phase, the center moves a little southward, while the warm front moves slightly closer to the FINO1 platform. The position of the LLJ to the east of the cyclone suggests that this is a sting jet. The LLJ over the southern North Sea, on the other hand, locates in front of the surface warm front associated with the cyclone. Notice that at 00Z, 14 Aug. 2015, at the level of 300 m, the warm front locates to the south of the FINO1 platform, but to the north of FINO1 at the level of 1500 m. This suggests a gentle slope of the front surface, which is typical for warm fronts.

In both time slices, the isobaric lines over FINO1 are denser on the 300-m level compared to the 1500-m level, this implies a decrease of geostrophic wind with height, consistent with the westerly thermal wind that is opposite the easterly geostrophic wind. The decrease of the geostrophic wind with height suggests the baroclinic mechanism for the LLJ, where the wind speed decreases below the LLJ core due to the surface friction.

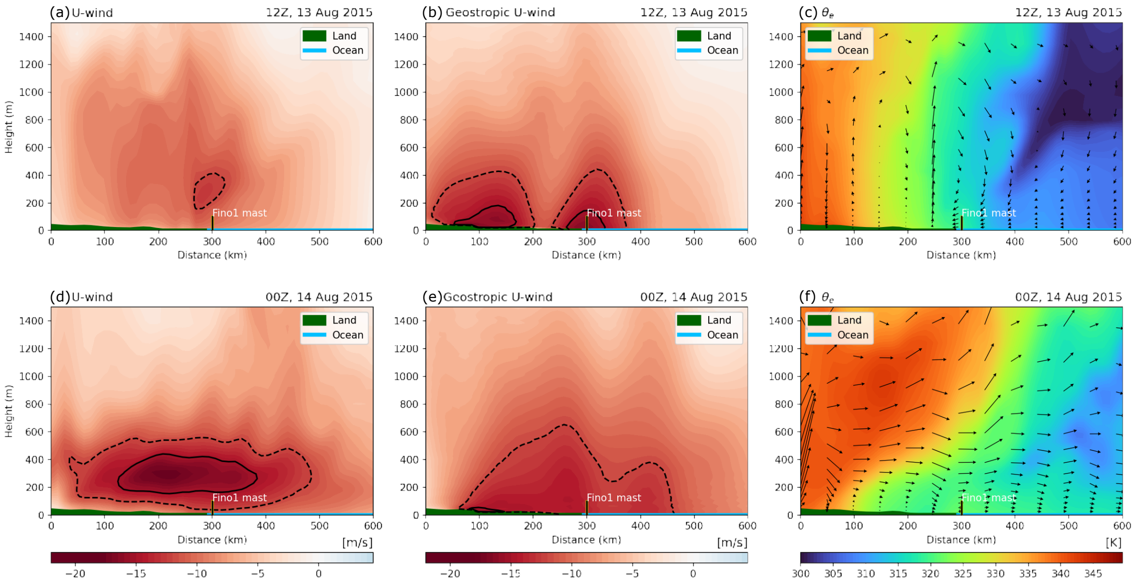

Figure 5.10: Meridional-Vertical cross section through the FINO1 mast (line A–B in Fig.5.9) of zonal wind (left, geostropic zonal wind (midle), and potential temperature (right) for 12Z, 13 Aug. (top) and 00Z, 14 Aug. 2015 (bottom). The zonal wind plots are overlayed with the isolines of 12 m/s (dashed) and 15 m/s (solid). The equivalent potential temperature plots are overlayed with meridional-vertical wind vectors.

To have further looks at the LLJ over the FINO1, we compared the south-north cross-section of zonal wind (U-component) with the geostrophic wind (Fig. 5.10). At noon 12Z, 13 Aug. 2015, the frontal zone is not well defined (i.e. Fig. 5.10c)). The geostrophic wind shows two maxima which are the largest on the surface: one over the FINO1 platform and another over land about 200 km to the south. These two maxima are associated with the meridional temperature gradients, which in turn may result from the difference in radiative heating of sloped terrain and land-sea contrast.

Over the first geostrophic wind maximum, the actual wind does not resemble the LLJ structure with a weaker wind speed and smaller vertical shear compared to the geostrophic wind (Fig. 5.10a,b). This can be attributed to the convective, well-mixing boundary layer, which is associated with the heating of the land surface during the day. Over the sea, the neutral boundary condition leads to a decrease in the geostrophic wind below the LJJ jet level, resulting in a weak LLJ over 12 m/s right above the FINO1 platform. Since the location of the LLJ co-locates with the geostrophic wind maximum but the intensity is weaker, we conclude that this LLJ is kick-started by the baroclinic mechanism from the differential land-sea heating during the day plus the cyclone-induced warm front.

At the maximum intensity phase (Figs. 5.10e–g)), which occurs at midnight, we do not observe an increase in the geostrophic U-wind speed, however, the actual U-wind speed of the LLJ core is over 20 m/s, which is near twice the geostrophic wind speed. The LLJ has a width of over 400 km and locates at a height of around 300 m. Thus we conclude that the main mechanism for the LLJ at this time is the Inertial Oscillation (IO), which associates with the fact that the warm front zone is sloped towards the north and leads to a stable boundary layer that acts to decrease the surface friction. As the LLJ extends over a large region over both land and sea, the main reason for the decoupling is not the radiative cooling of the surface that is often discussed for nocturnal LLJ, but rather the warm front-induced stabilization. However, the radiative heating over land during the daytime does produce an unstable PBL that disrupts the LLJ on land. A consistent increase of the LLJ core speed since noon (Fig. 5.5a), instead of since the sunset, supports this assessment.

Our analysis agrees with Wagner et al. (2019), where they attribute the LLJ to frictional decoupling (i.e. IO) and the baroclinicity due to land-sea contrast and warm front passage. However, they distinguished the LLJ on land due to the IO mechanism and at the coastline due to either IO or baroclinity. In our view, the LLJ development over the FINO1 is one entity that is first initiated near the coastline by the baroclinicity from both the land-sea contrast. Later the main mechanism for the LLJ both over land and sea is the IO mechanism with the warm front-induced decoupling effect.

5.2.4 Effect of nudging and data assimilation

The ability of nudging to capture the variability of flow fields in accordance with observations (here from LiDAR) depends highly on the LiDAR data availability and its quality. Several LiDAR data in time and space do not meet the expected quality and will not participate in the assimilation (such as quality constraints in terms of spatiotemporal differences between the model simulations and LiDAR measurements).

We know that the LLJ events are observed mostly under a stable atmosphere and Fig. 5.11 provides an overview of winds (Fig. 5.11a), stability (Fig. 5.11b), and turbulence intensity (Fig. 5.11c) to characterize the small-scale property during LLJ at 15 m height in August 2015. Using high frequency sonic data (i.e. with sampling frequency of 25 Hz), the Monin–Obukhov stability parameter L, is calculated as follows

$$L = -\frac{u_{*a}^3 \bar{\theta}_v}{\kappa g(\overline{w'\theta_v'})}, \tag{5.1}$$

where w' is the vertical velocity fluctuation, $\bar{\theta}_v$ denotes the mean virtual potential temperature, and $\overline{w'\theta_v'}$ is the flux of the virtual temperature. κ and g are the von Kármán constant and the gravitational acceleration, respectively. The overbar indicates a mean and the prime denotes the fluctuations. The friction velocity in the above equation is given as

$$u_{*a} = (\overline{u'w'}^2 + \overline{v'w'}^2)^{1/4}, \tag{5.2}$$

where u' and w' are horizontal and vertical wind fluctuations, respectively.

During the study period (blue coloured area), the wind speed declines from 15 m/s (at the beginning of the period) to 6 m/s (the occurrence of the first LLJ event), see Fig.

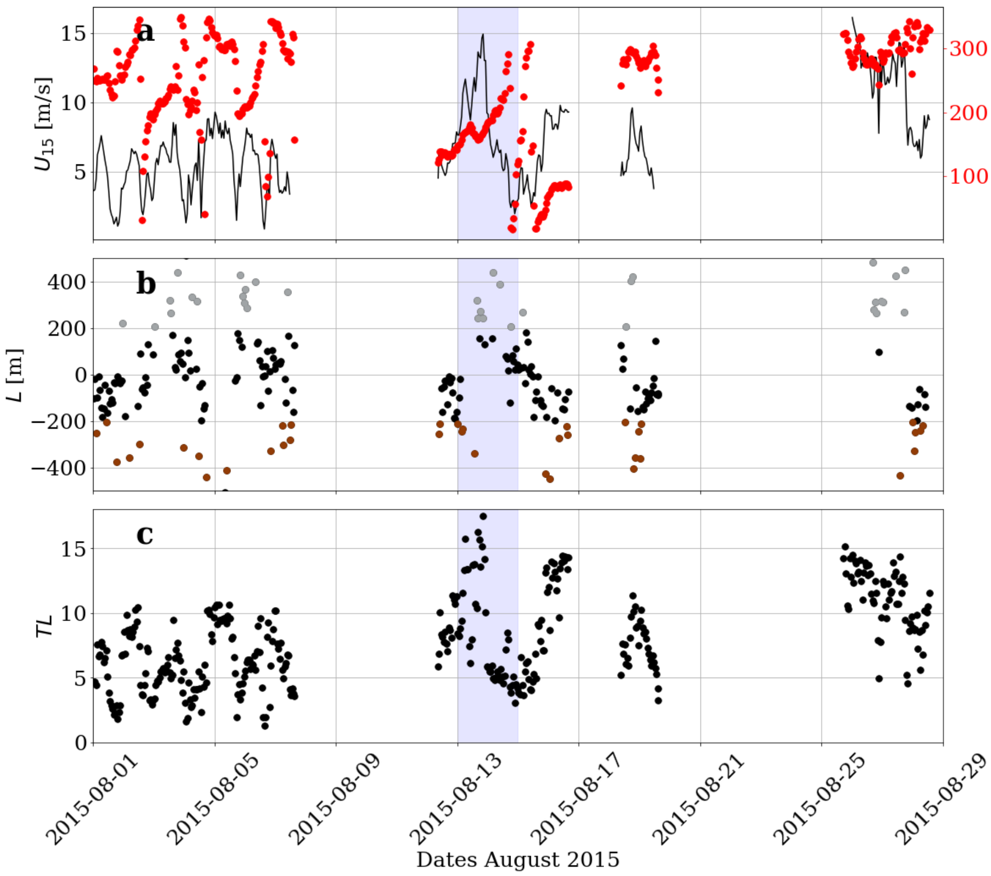

Figure 5.11: The time-evolution of (a) wind speed (black line) and wind direction (red markers); (b) stability parameter L. Stable and unstable conditions are marked by blue and orange colors; and (c) Turbulence Intensity (TI).

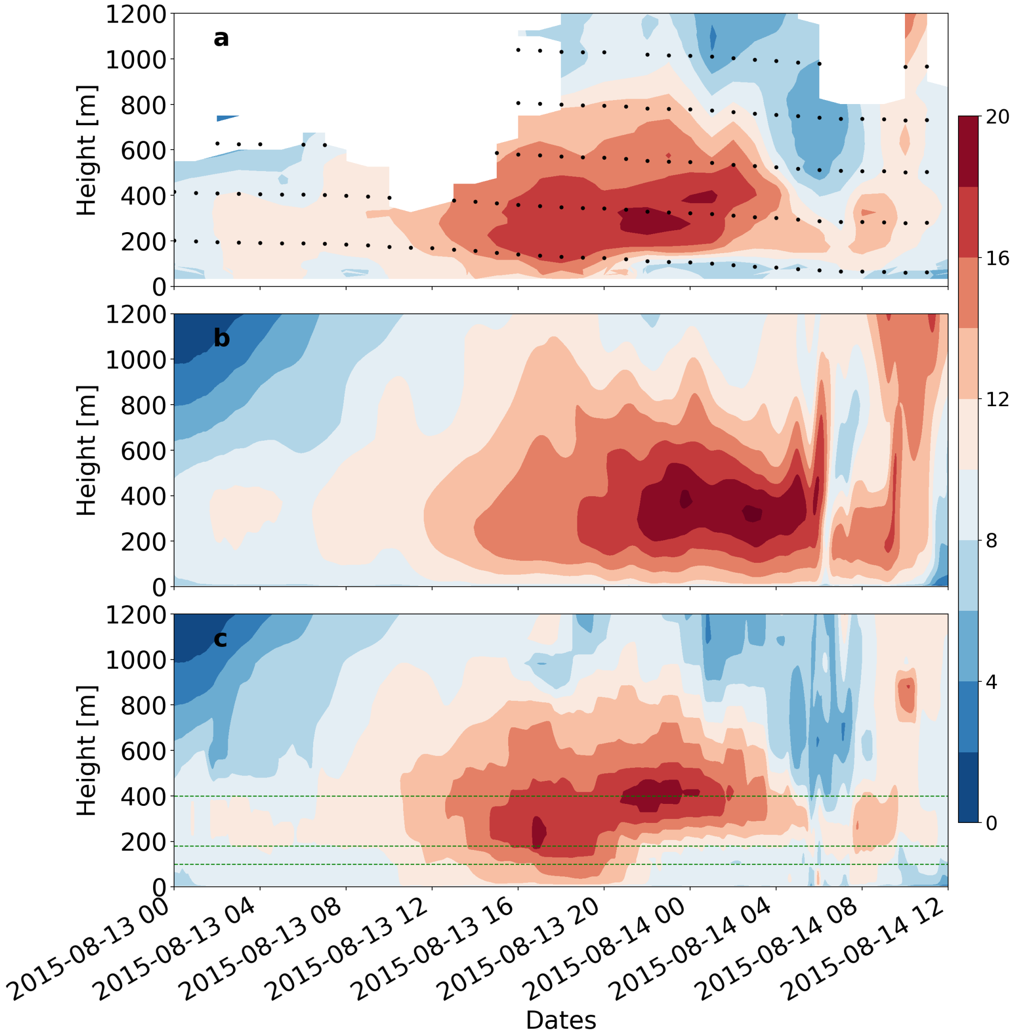

Figure 5.12: (a) Time-height plots of measured and modeled horizontal wind speeds at FINO1 over the study period of August 13–15 2015: (a) the LiDAR measurement of wind speed overlaid with the available and qualified data for the observation nudging in time and space (the dotted black); (b) WRF without Observation nudging Analysis (OA); and (c) WRF with OA. The horizontal green lines represent heights (90 m, 180 m, and 400 m) that we conduct detailed analyses in the next figures.

5.11a. Unstable conditions frequently occur during August 2015, but the stable atmospheric condition is the most frequent condition during this time (Fig. 5.11b). The TI is large before the first LLJ event and reaches approximately 20%, then is suppressed during the LLJ stable event (Fig. 5.11c).

Figure 5.12a shows the 10-min wind speed of LiDAR measurements at in time and altitudes (dotted black markers). Note that these data points have passed the required quality criteria of the observation nudging before being used in the WRFDA system. The LLJ core is observed on 13 August starting at 14:20 UTC with an approximate jet core at 290 m. This event persists for a few hours and is followed by another weak LLJ at 14 August around 08:00 UTC (during the first event, the LiDAR coverage is higher than 1.2 km, and there are, however, missing data points above 800 m for the second event).

Figure 5.12b shows the WRF simulation of wind speed at the FINO1 location for the CTRL configuration combined with the wind farm effects for the parent domain (i.e. D01 with a horizontal resolution of 9 km). In the outer domain, there are large land regions in the southern of FINO1 so that the development of LLJs will not fail due to the possibility of the development of stable atmospheric stability conditions over the study area. The maximum wind speed is predicted between 200 m and 400 m. However, the WRF overpredicts the wind speeds during both LLJ events (the jet core for the first event is expanded over a longer duration relative to what is expected from the measurement as shown in Fig. 5.12a). The simulated jet nose level is higher than the observation and the model does not simulate properly the weakening periods above 400 m between the two events.

The wind speed prediction from the observation nudging is shown in Fig. 5.12c, based on the CTRL configuration combined with the farm effects. The overall agreement with measurements is greatly improved by employing the OA. The model predicts very similar variation before/during/after the LLJ event and the remained discrepancies are explained by the fact that a limited number of measurement points in time and space have been used for the nudging (i.e. the black markers in Fig. 5.12a).

Figure 5.13 compares the time-height wind direction at FINO1 of the LiDAR measurement versus the WRF simulations. The mean wind direction at low altitudes below 100 m is mainly southerly (namely before 14 August at 14:00 UTC) that turns then gradually towards the southwesterly wind. For higher altitudes, the flow direction is southeasterly before LLJ and southwesterly during LLJ (the intensity, the strength, and duration of such transient event might be explained by the seasonal variability of the atmospheric flow which, along with its interaction with land, is one of the responsible factors in the generation of this event).

While both the nudged and unnudged simulations show an almost good agreement with the measurement, the unnudged illustrate a larger error at high altitudes, particularly after the first LLJ (around 14 August at 06:00 UTC) where we observe almost a constant large bias in the wind direction at roughly all heights. Although the observation nudging substantially reduces the wind direction bias and improves statistically the wind prediction (not shown), the accuracy of the model prediction may decline at higher altitudes due to the lack of LiDAR data availability.

Figure 5.14 shows time-series comparisons between simulated and measured wind speeds at three heights (90 m, 180 m, and 400 m respectively from top to bottom). Before the LLJ event, all simulated results are in good agreement with measurements (the unnudged

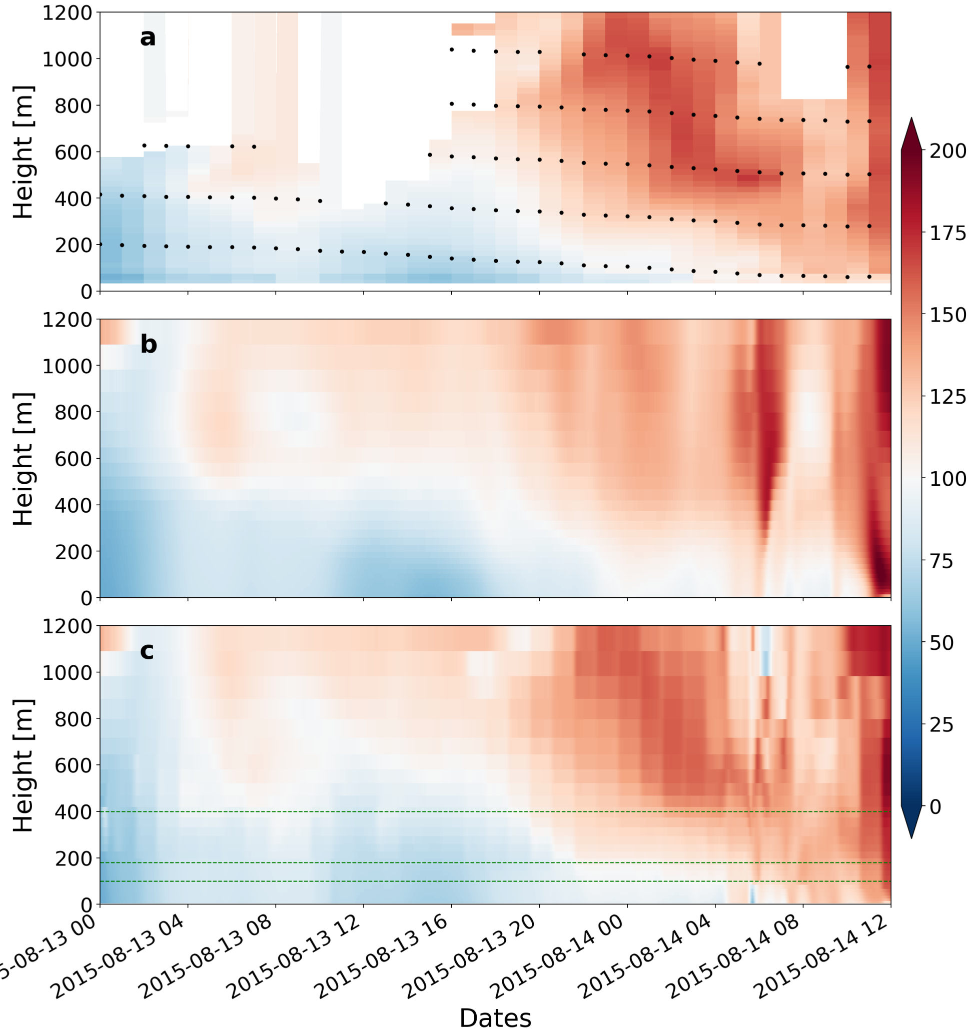

Figure 5.13: (a) Time-height plots of measured and modeled wind directions at FINO1 over the study period between August 13–15 2015: (a) LiDAR measurement (the dotted markers show the available and qualified data to be used in the observation nudging); (b) WRF without OA; and (c) WRF with OA. The horizontal green lines represent the heights (90 m, 180 m, and 400 m) that we conduct detailed analyses in coming figures.

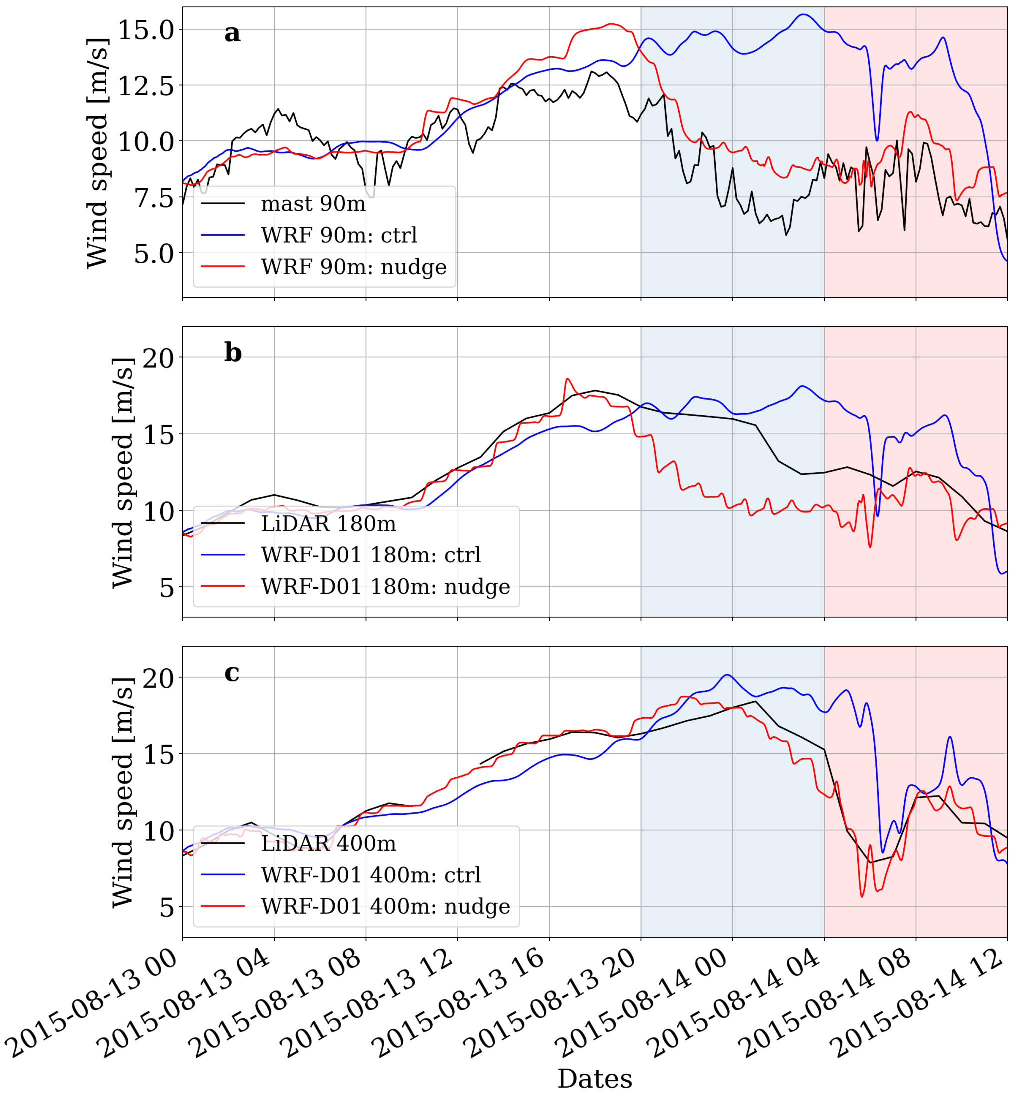

Figure 5.14: (a) Time series of measurements (black lines), nudged (red curves) and unnudged (blue lines) WRF simulations on parent domain (i.e. D01 with 9 km horizontal resolution) for the closest location to the FINO1 at different heights: (a) 90 m; (b) 180 m; and (c) 400 m. The coloured areas in this figure are study periods being analyzed in the next figure.

simulation with a slightly better match). During the first LLJ, the largest error is found by the unnudged simulation at the level height of 90 m. The observation nudging could capture fairly well the variation in the wind speed at 180 m, but its performance is low when compared with other heights.

Note that the altitude between 180 m and 300 m is where the LLJ core resides and implementation of additional measurements may improve the predictive skills of the nudged experiment. The error of the CTRL in low altitudes, as described in the previous section, is due to the wake effects from the turbines to the east of FINO1. Thus, the nudging mechanism simply adjusts the wind toward the observation at the FINO1 location without taking into account any physical processes. Therefore, we do not expect the current nudging to improve the wind presentation outside of the FINO1 region.

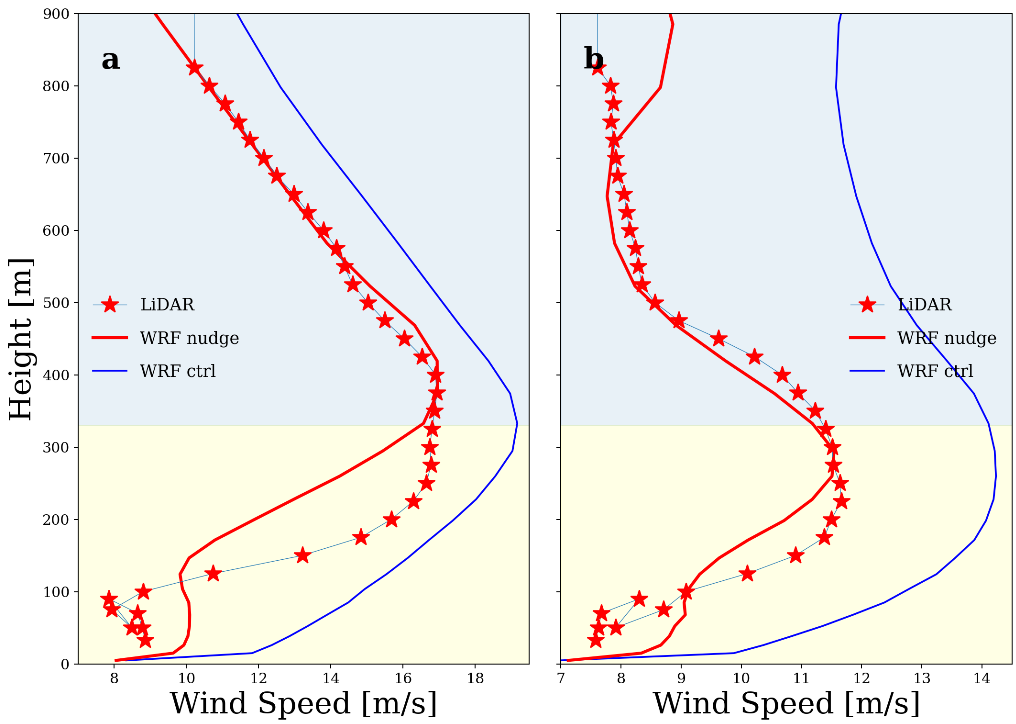

Figure 5.15: Mean wind speed profiles at the location of FINO1 during the periods identified by coloured areas in Fig. 5.14. The vertical time-averaged wind profiles: (a) during the first LLJ event (blue coloured area in Fig. 5.14); and (b) during the second LLJ (red coloured area in Fig. 5.14).

We select two time periods covering the first and the second LLJs in order to investigate the accuracy of vertical profiles of two WRF experiments in more detail against the LiDAR measurements. For the first event in Fig. 5.15a, a clear jet nose is evident when comparing the temporally-averaged WRF profile against measurement. The perfect agreement is highlighted for the altitudes above 320 m (blue coloured area). The agreement declines for the lower heights (yellow coloured area) where the error reaches approximately $2-3$ m/s. For the second event, the nudged mean profile agrees perfectly well with respect to the measurements almost in all heights (except about 1 m/s bias for the heights below 180 m). The unnudged mean profile overpredicts substantially the wind.

We have detected two intensity classes throughout the study period during (very stable) atmospheric near-surface stability conditions (a strong LLJ followed by a weak event of a different pattern). Figure 5.16 illustrates that southwesterly winds are frequent at different altitudes, particularly at the heights close to the nose of LLJ. The maximum speed is shown by the distance from the origin. At 90 m, the maximum speed is frequently observed from the southwest, and WRF with OA could predict perfectly well (i.e. Fig. 5.16b), while the unnudged simulation predicts northwesterly winds (Fig. 5.16a). Weak westerly and southerly winds are observed from the observation nudging (Fig. 5.16b) and unnudged simulation predicts wind speeds of excess of 6 m/s from the southern sector. At an altitude of 180 m, the dominant wind direction is from the northwest sector as a result of the jet intensification and development (partly from persistent weather features over the North Sea farther North). By a qualitative look, the nudged experiment (Fig. 5.16e) could better predict winds than the unnudged run (i.e. Fig. 5.16d), if we compare with measurements (i.e. Fig. 5.16f). The results of both nudged (Fig. 5.16h) and unnudged (Fig. 5.16g) are equally well in agreement with measurements (i.e. Fig. 5.16i), and both cannot capture the northeasterly winds (from 90 m that the wind turns from southeasterly to northwesterly).

In Fig. 5.17, we investigate the effects of single-point nudging (with a radius of influence of 180 km) on the surface wind (i.e. wind at 10 m height). Comparing Figs. 5.17a and c, it is obvious that the winds close to the measurement location are forced by the largest changes compared with the unnudged cells. Figures 5.17b and d similarly suggest that the cells close to the FINO1 experience the largest changes in the wind speed and its horizontal variation.

5.2.5 Discussion

We revisited an LLJ event over the FINO1 region and examined the associated generation mechanisms using the mesoscale model WRF. The atmospheric condition is simulated by downscaling from the ERA5 reanalysis data using three nested domains down to 1 km. The LLJ is a mesoscale phenomenon that can be simulated well using the WRF, even with the coarsest resolution of 9km. However, the local wake effect by the wind turbines—which not only effectively reduce the wind speed under 200 m, but also can modify the weather condition above—cannot be captured by a mesoscale model, even when the wind farm parameterization is included.

We have shown that the spatiotemporal prediction of the LLJ nose and its vertical evolution can be significantly improved by the use of appropriate observation nudging settings together with qualified LiDAR data. However, the number of nudging points, their quality, and their spatial and temporal availability/distributions may limit the accuracy of the observation nudging. The nudging method in specific or the data assimilation in general can only adjust the model to the observation in the vicinity of the available observation points and cannot improve the physical mechanism. Thus a finer resolution LES model combined with the actuator disc effect is required to properly simulate the effect.

6 Wind-wave interaction results

Here, we present the results from different WRF wind-wave interaction experiments listed in Table 3.4. We compare the online and offline wave coupling simulation results with the wind data from the FINO1 met mast. In section 6.1, the accuracy of simulated wind fields

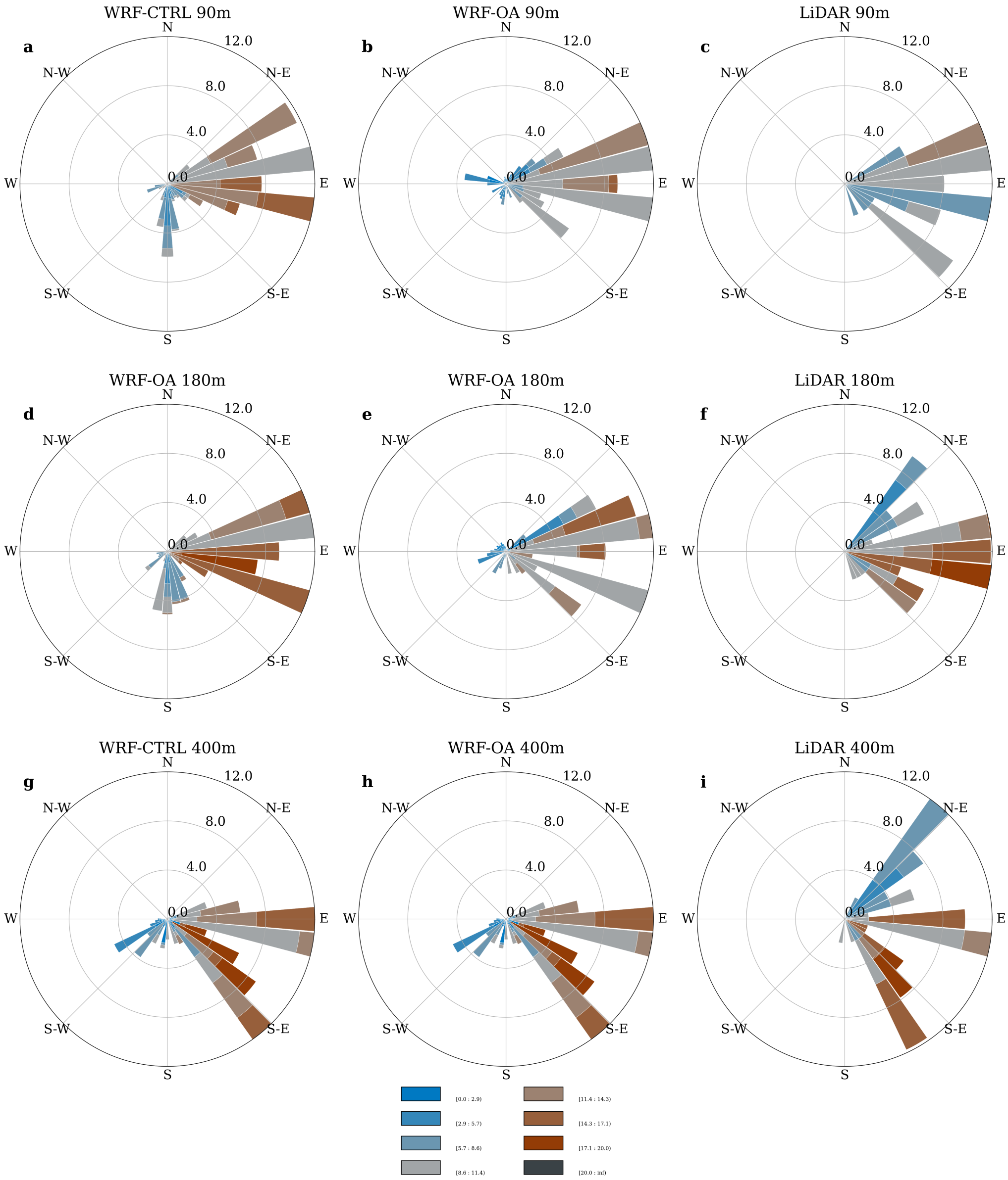

Figure 5.16: Wind roses associated with all simulated and measured wind speeds throughout the study period at heights of 90 m, 180 m, and 400 m.

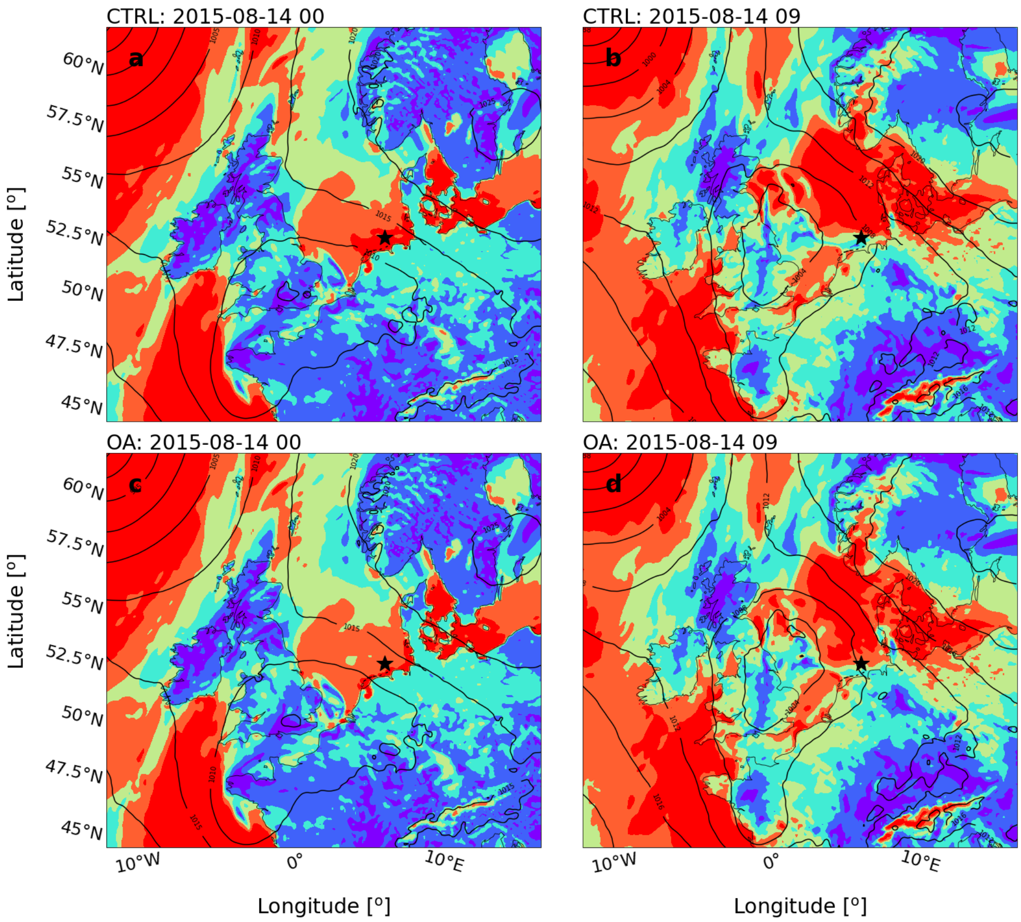

Figure 5.17: Two-dimension maps of wind speed at 10 m height from: (a,b) the control unnudged run at two different times; and (c,d) the observation nudging at two different times.

Table 6.1: Statistical parameters of the observed and simulated wind speeds at FINO1 station for the period of $03 - 17$ September 2015.

Parameter	Observation	CTRL	Online_wave	Offline_wave	(Mis)Alignment	com1_wave
Min	1.33	0.21	0.38	0.72	0.95	1.09
Max	18.7	22.28	23.69	23.28	22.61	20.54
Std	3.51	4.09	4.06	4.04	3.73	3.6
Correlation		0.80	0.80	0.76	0.80	0.86
MBA		-0.23	-0.61	**-0.04**	-0.24	0.16
MAE		1.81	1.91	1.97	1.62	**1.31**
RMSE		2.37	2.41	2.68	2.15	**1.74**

using five different experiments was assessed by comparing the results against observations during an alignment period of 03–17 September 2015. Because the numbers of detected misalignment cases are low in this period, we select another period that contains more misalignment cases in section 6.2.

6.1 Alignment Period

6.1.1 Validation of wind field

Figure 6.1 shows the time series of observed and simulated wind speeds at the FINO1 station for the period of $03 - 17$ September 2015. Because the hub heights of the wind turbines (in the Alpha Ventus wind park) are approximately 90 m, we analyze the results at 90 m in this section. As can be seen, all wind simulations (speed and direction) are in good agreement with observations. It is emphasized that we exclude hereafter all winds affected by the wind shadow zone of the measurement met mast (direction from $285^o - 345^o$). The gaps in the time series in this figure are then attributed to this shadow zone effect.

Table 6.1 contains the statistical parameters of the observed and simulated wind speeds for the period of $03 - 17$ September 2015. The minimum, maximum, and standard deviation of the observed wind speeds are 1.33, 18.7, and 3.51 m/s respectively. The best simulation results are related to the com1_wave experiment with minimum, maximum, and standard deviation of 1.09, 20.54, and 43.6 m/s respectively. The com1_wave results show positive bias suggesting an overestimation of wind speed on average. Other configurations underestimate the wind speed (with negative biases). The highest correlation and minimum MAE and RMSE are related to the com1_wave with a correlation of 0.86 and MAE and RMSE of 1.31 and 1.74, respectively. The CTRL, Online_wave, and (Mis)Alignment experiments have the same correlation roughly about 0.80 and the lowest correlation is related to the Offline_wave configuration, with a value of 0.76. After the com1_wave configuration, (Mis)Alignment is in the second rank based on the statistical parameters listed in the Table 6.1.

Figure 6.2 shows the observed and simulated wind roses. Based on the observed wind rose, the wind direction for the study period is from the east to the southwest. There are two predominant directions: the E-SE for the medium wind speed under 12.5 m/s, and the

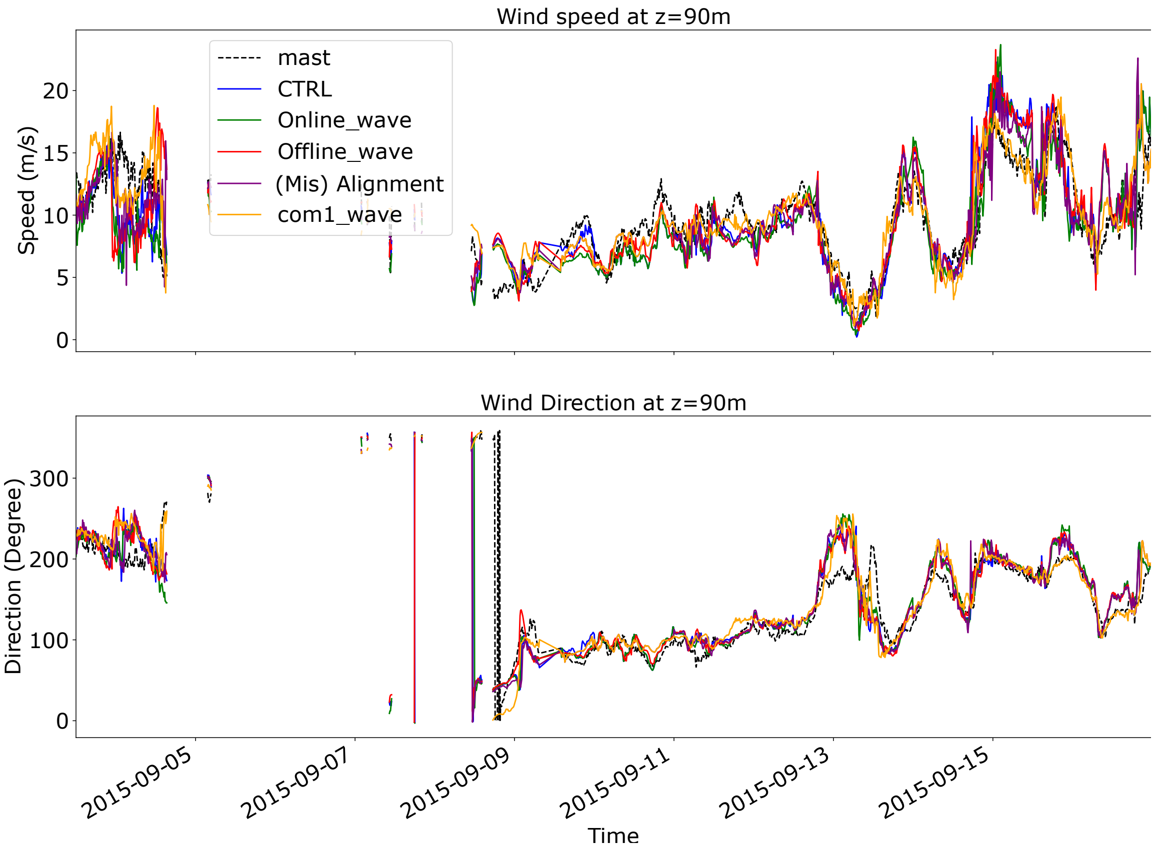

Figure 6.1: Time series of wind speed (top panel) and direction (bottom panel) at height of 90 m for FINO1 station during $03 - 17$ September 2015.

Table 6.2: Comparing Weibull distribution parameters of the observation and simulation results.

Parameter	Observation	CTRL	Online_wave	Offline_wave	(Mis)Alignment	com1_wave
Shape	3.02	2.48	2.40	2.49	2.73	2.91
Scale	10.74	10.55	10.11	10.77	10.50	10.93

S-SW for the high wind speed over 15 m/s. All model simulations can reproduce these two predominant wind directions to some extent, although slightly rotated (clockwise or counterclockwise) compared to the measurements.

To better assess the quality of simulation results, the Weibull distributions are plotted in Fig. 6.3. It can be seen that the highest frequency of the wind speeds for observation data is in the range of $9-10$ m/s. The Weibull distributions corresponding to the com1_wave and the (Mis)Alignment simulations are in better agreement compared to other simulations. The shapes of the Weibull distribution curves for Online_wave, the Offline_wave, and the CTRL runs show a shift to the left, which means they underestimate the highest frequency of wind speed. The Weibull parameters (shape and scale) are shown in Table 6.2. The shape and scale parameters of the observed distribution are 2.9916 and 10.3715 respectively, and the minimum differences (versus observation) are related to the com1_wave simulation.

Figure 6.4 shows a Taylor diagram of the simulated wind speeds from five different experiments. In this diagram, the radial (along-axis) distance from the origin is assigned to the standard deviation, and the radial dashed lines correspond to the correlation coefficients, while the dashed lines represent the RMSE (which is higher when the radius of the sector becomes larger). In other words, each point in the Taylor diagram simultaneously shows the standard deviation, correlation coefficient, and RMSE of the simulated time series against observations. As can be seen in Fig. 6.4, the com1_wave simulation shows better performance than other experiments, with a higher correlation and lower RMSE.

Figure 6.5 shows changes of the percentiles (for scores from 1% to 99%) of the wind speed errors at FINO1 station. For the low wind speeds (lower than 4 m/s), most of the simulations underestimate the wind speed (negative error). For the wind speed between $4-7$ m/s, most of the simulations show positive bias. When the wind speed is between $7-14$ m/s, most of the experiments show negative bias, and for wind speeds more than 14 m/s, the errors grow significantly in most of the simulations. The com1_wave results show, however, the lowest error compared to other experiments.

6.1.2 Wind shear and Veer

Figure 6.6 shows time-height plot of the wind speed at FINO1 station for the period of $03-17$ September 2015. Given that the wind and wave alignment could be observed at higher wind speeds, during this period, wind speeds over 8 m/s are the most frequently observed events. On September 6, the simulation results show a high wind speed, but unfortunately, suitable wind mast data is not available. We alternatively conduct a comparison between simulation results and NORA3 reanalysis data that shows a very good match on this day. On September 15, we can also see a high wind speed pattern and all the simulations provide good performance in producing the wind patterns on this day. In low wind speed conditions,

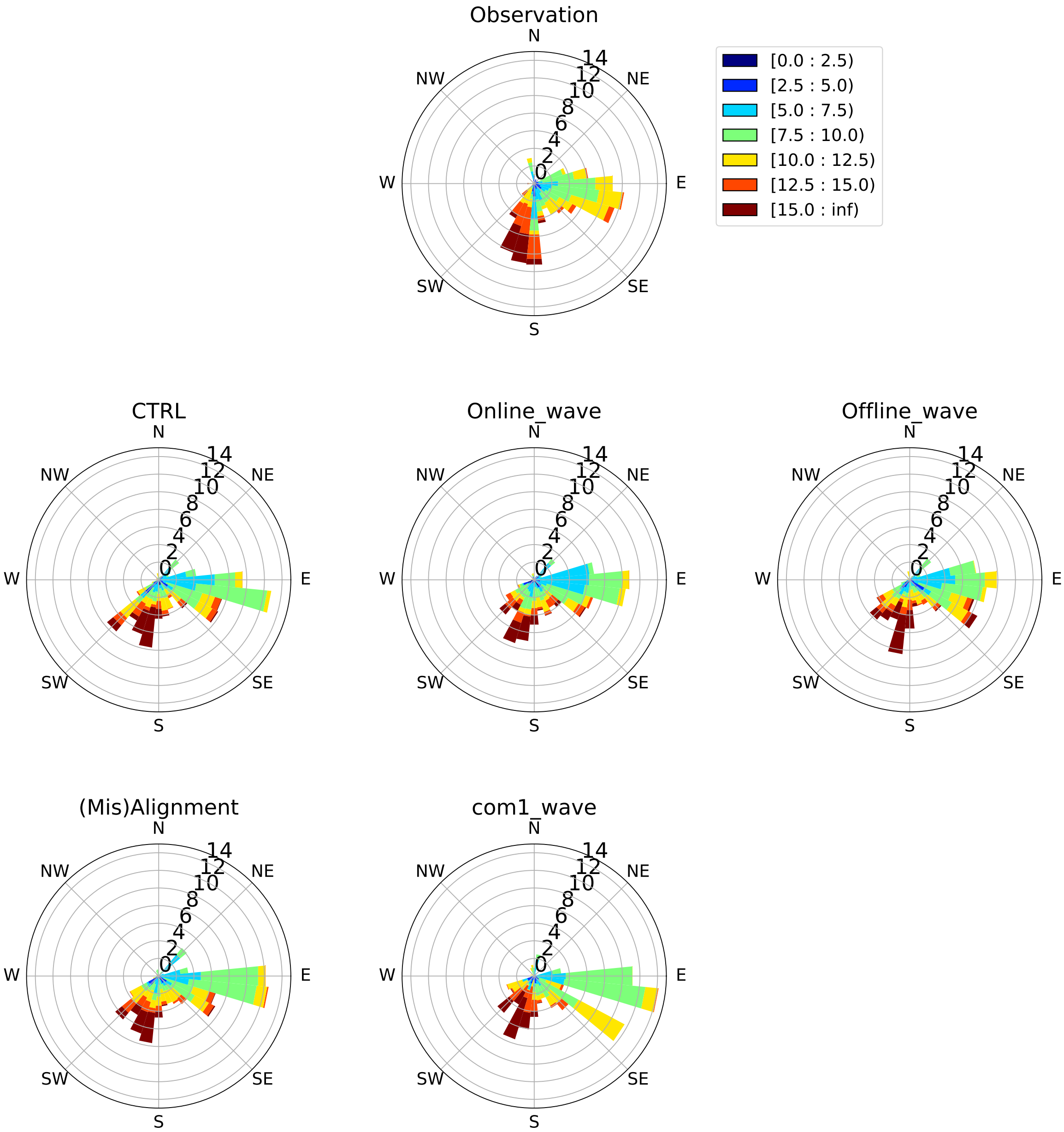

Figure 6.2: Wind Rose at FINO1 station; comparison between the observed (top) and the simulated wind fields during $03 - 17$ September 2015.

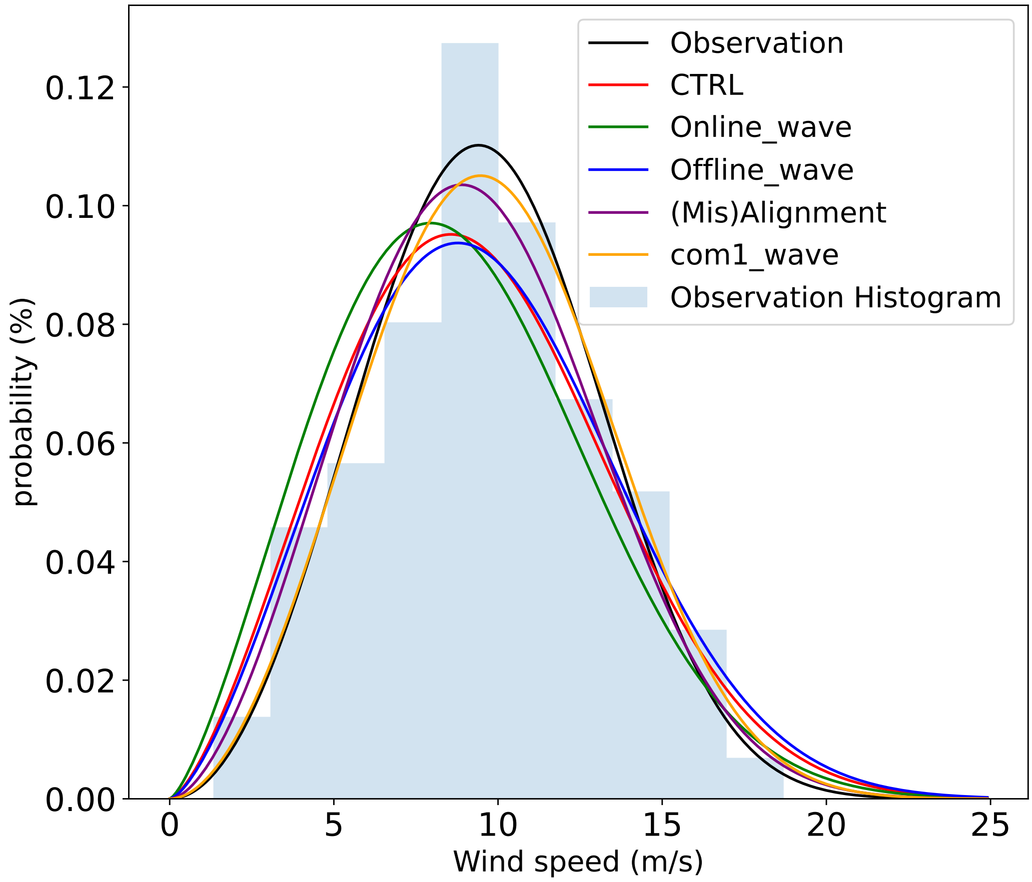

Figure 6.3: Comparing Weibull distribution of the observation and simulated time series during $03-17$ September 2015.

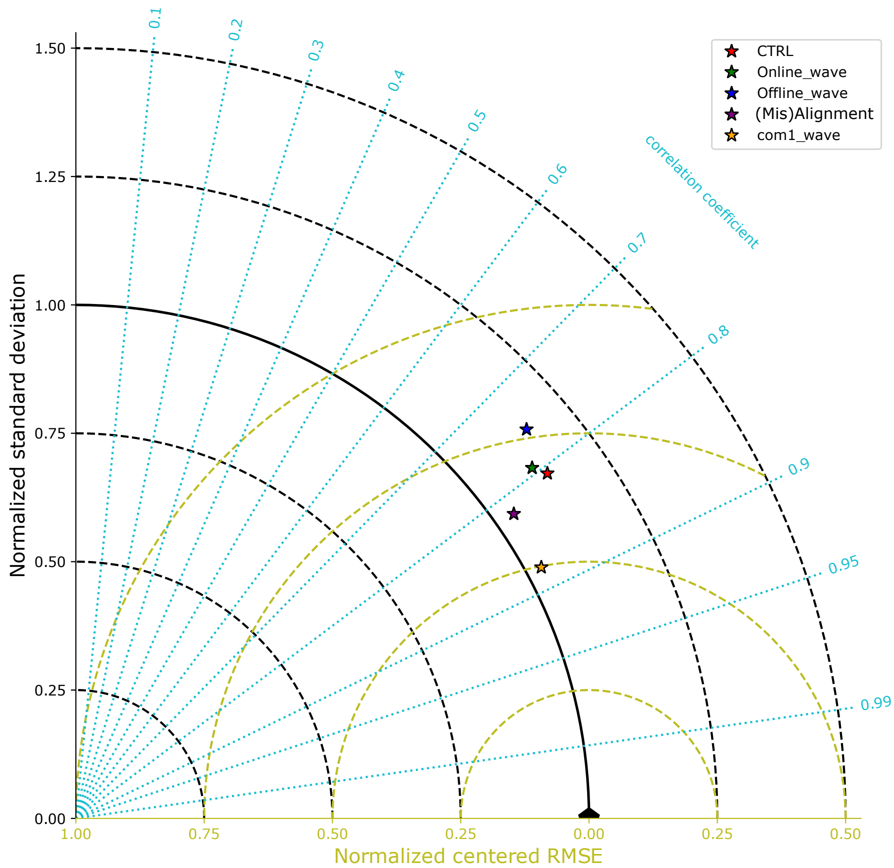

Figure 6.4: Taylor diagram of the simulated and the met-mast observed wind speeds at FINO1 station during $03 - 17$ September 2015.

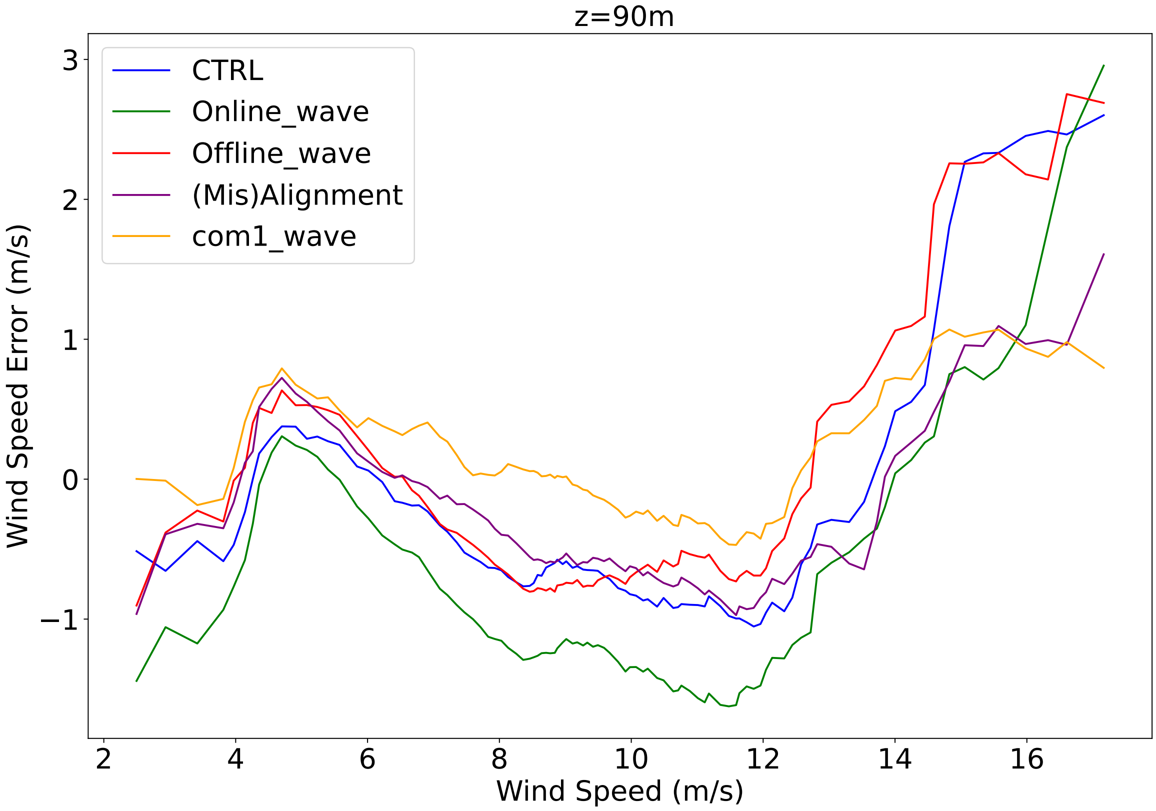

Figure 6.5: Simulated wind speed error (difference between the simulation result and the observation) (Percentile from 1% to 99%) versus the observed wind speed from the met-mast at FINO1 station for the period of $03 - 17$ September 2015.

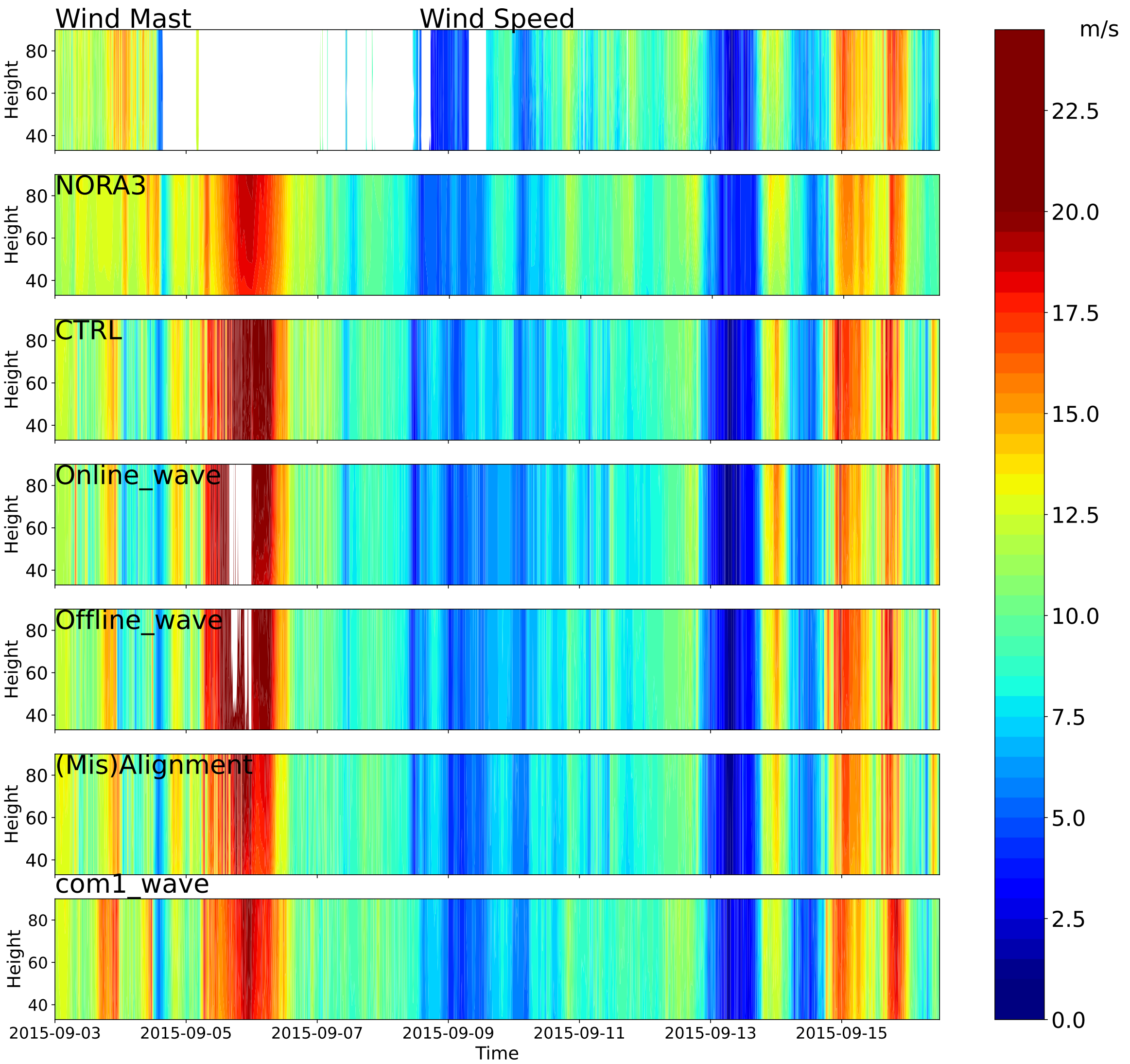

Figure 6.6: Time-height plots of the simulated wind, the observed and the NORA3 data for a duration between $03 - 17$ September 2015. White areas in wind mast data show the shadow zones or missing data.

it can also be seen that the simulations have good performance (accuracy) compared to the observational data.

Figure 6.7 shows the wind roses at three different levels 33 m, 50 m, and 90 m of the observed and simulated wind fields for the period of $03 - 17$ September 2015. The dominant wind direction from the observed data at a height of 33 m is about 110^o which slightly rotates counterclockwise to 100^o with a height of 90 m. All the simulated dominant wind directions are in reasonable agreement with the observed data with a maximum of 10^o differences. But simulated wind fields do not show any rotation with height. It could be because the differences between the plotted heights are too small, and we don't have enough vertical layers below 90 m in the model results.

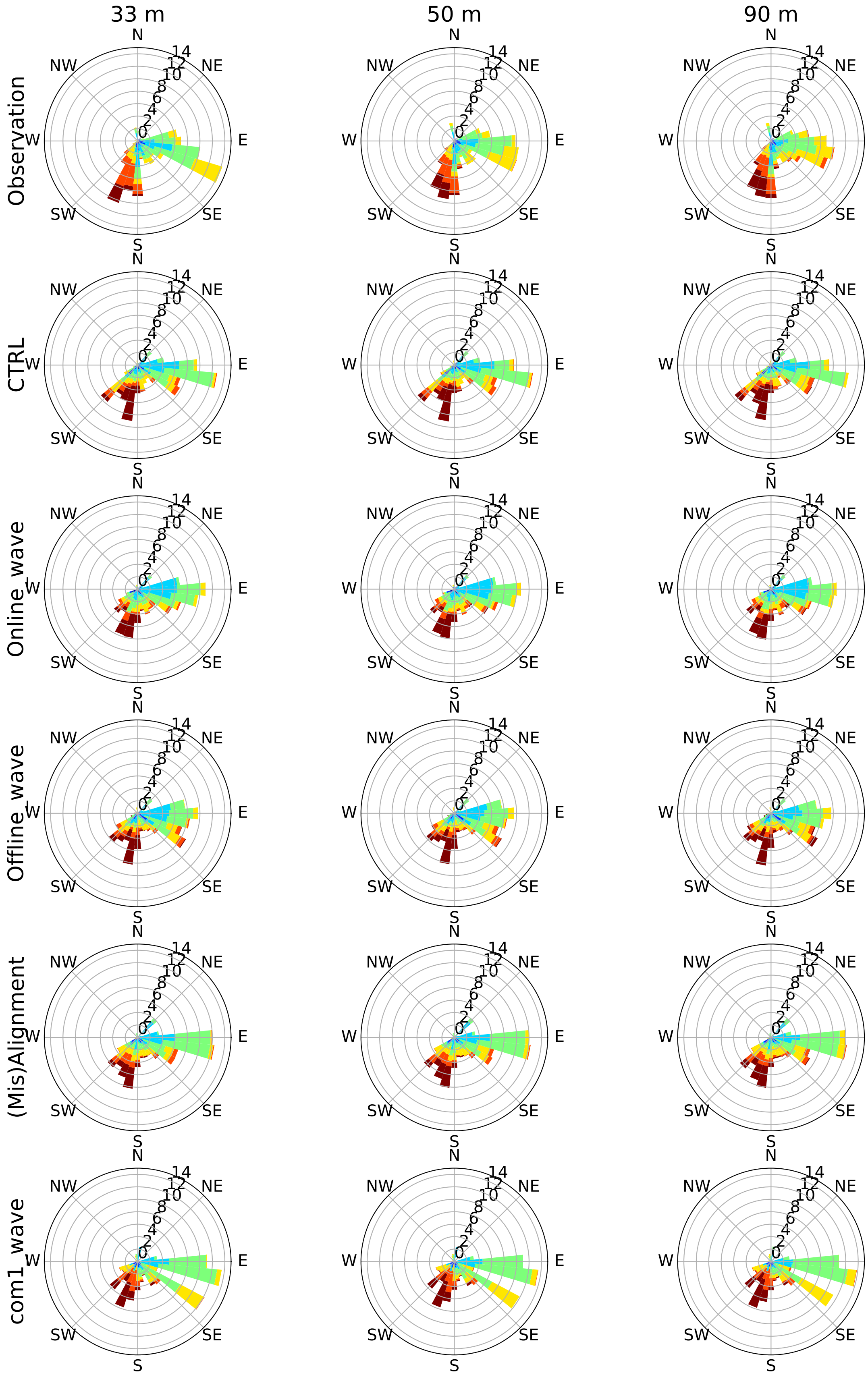

Figure 6.7: Wind roses at three different heights from observations and simulated results for $03 - 17$ September 2015.

6.1.3 Roughness length

Figure 6.8 shows the time series of wind speed and roughness length (i.e. ZNT as WRF variable) for the period of $03 - 17$ September 2015. As can be seen in this figure, changes in the roughness length in the CTRL experiment are directly related to the wind speed variations. But the relation does not hold for other experiments. When wind speed is less than 10 m/s, the online and offline experiments often show a minimum roughness length. As wind speed increases, there will be higher waves and the enhanced interaction between the wind and waves can cause higher roughness length.

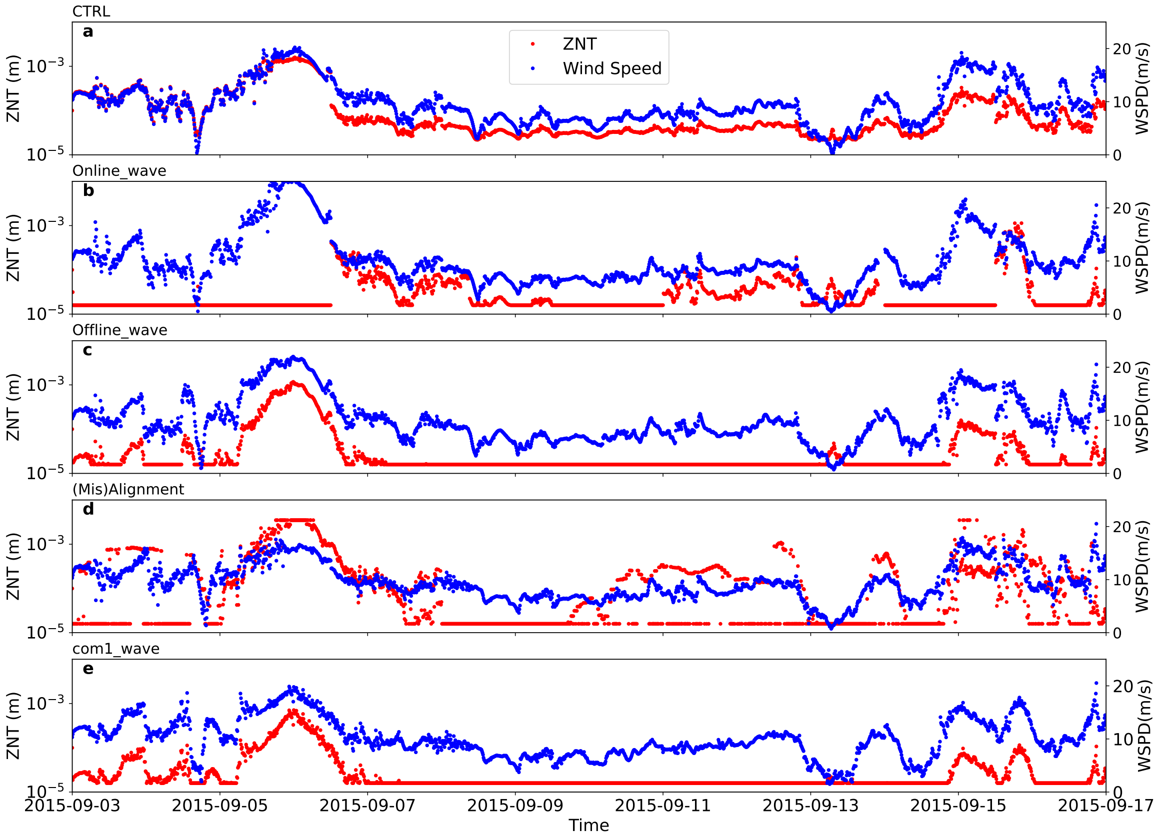

Figure 6.8: Time series of wind speed and roughness length (ZNT) at FINO1 station during $03 - 17$ September 2015 for (a) the CTRL; (b) the online_wave; (c) the offline_wave; (d) the (Mis)Alignment; and (e) the com1_wave experiments.

6.1.4 Wind energy

In this section, we present simulated wind power results from our different experiments and compare them with available observations in the FINO1 station. To calculate the wind power, the power and thrust curves of Adwen AD 5-116 wind turbine (which is installed close to FINO1 wind mast station) are used. The specifications of the wind turbine are given in Table 6.3. Mean wind power over the sea is often higher than those over land, and the com1_wave experiment shows higher mean wind power than other experiments.

Figure 6.11 shows the time series of simulated and observed wind power at FINO1 station for the period of $03 - 17$ September 2015. Due to the better performance of the com1_wave configuration at high wind speeds, it can also be seen that the best performance is also

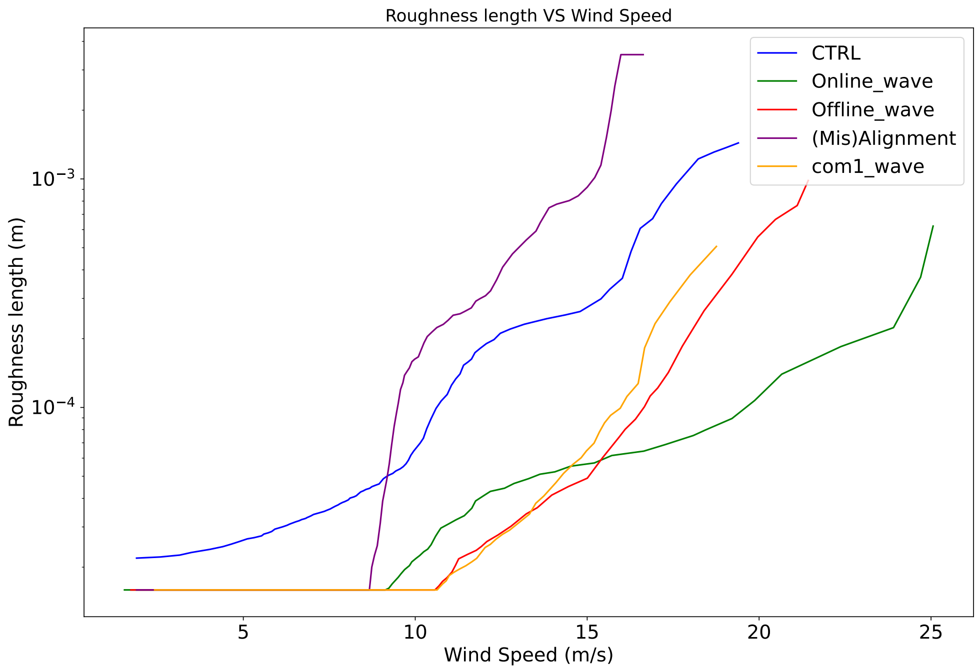

Figure 6.9: Roughness length versus wind speed for different simulations during $03-17$ September 2015.

related to the com1_wave experiment. The total extractable wind power from observation in this period is approximately 4145281 W/m^2 and the com1_wave with a difference of 14104 W/m^2 shows the smallest difference.

Table 6.3: Specification of wind turbines which are used for the calculations of the wind power in this study.

Turbine Name	Hub Height	Rotor Diameter	Cut-in speed	Cut-out speed	Rated speed
Adwen AD 5-116	90 m	116 m	4. m/s	25. m/s	12.5 m/s

6.2 Wind-wave misalignment

6.2.1 Validation of wind field

Figures 6.12 and 6.13 show the time series of wind speed and direction for the selected dates containing the misalignment between the wind and the wave directions (differences between the wind and wave directions are more than 120^o). As illustrated in these figures, the wind speed is lower in value than in the alignment cases. Wind speed changes from almost 0 m/s to a maximum value of 8 m/s during $10-12$ July 2015, and from 0 to about 15 m/s during $20-26$ July 2015. Previous studies indicate that misalignments are often found at low wind speeds but there are some studies that reported misalignments

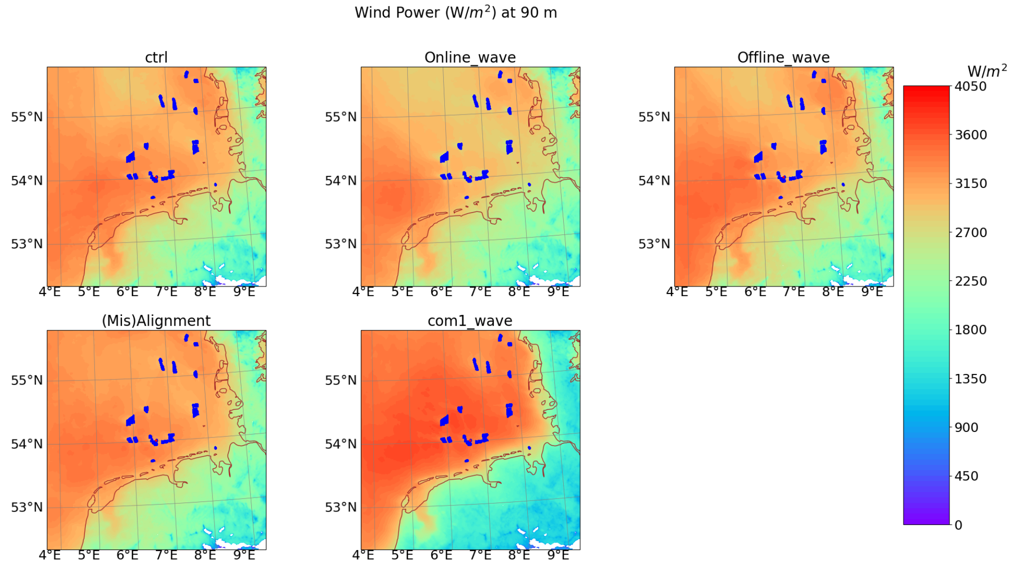

Figure 6.10: Spatial distribution of the mean wind power (W/m^2) at 90 m in the WRF model domain for the period of $03-17$ September 2015. Blue dots show the locations of the wind turbines installed in this area and the red dot shows the location of the FINO1 station.

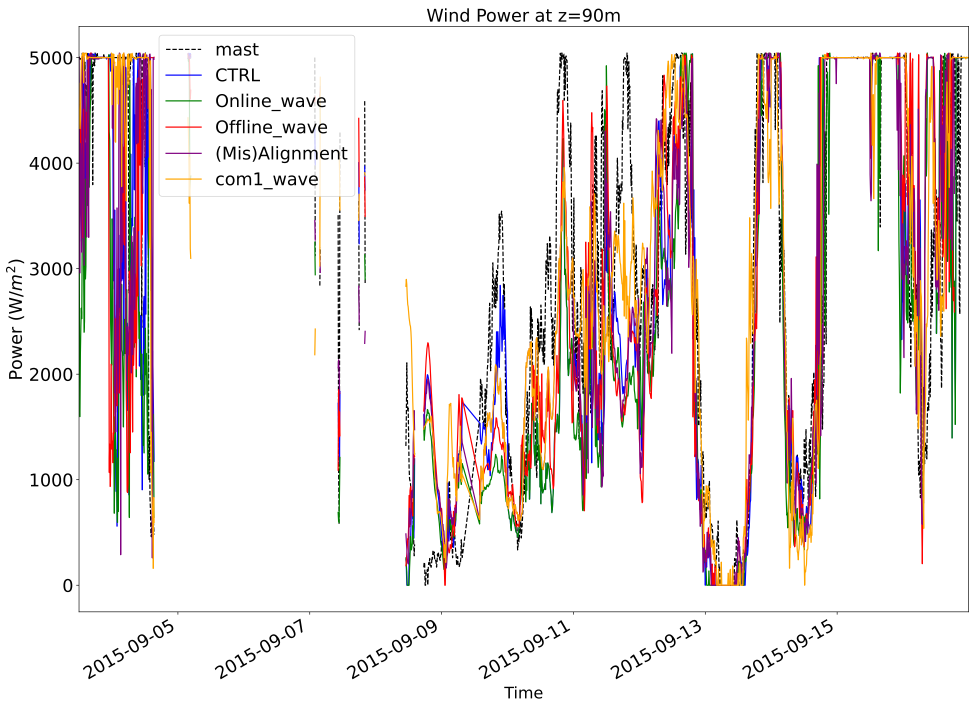

Figure 6.11: Time series of mean wind power (W/m^2) at FINO1 station for the period of $03-17$ September 2015.

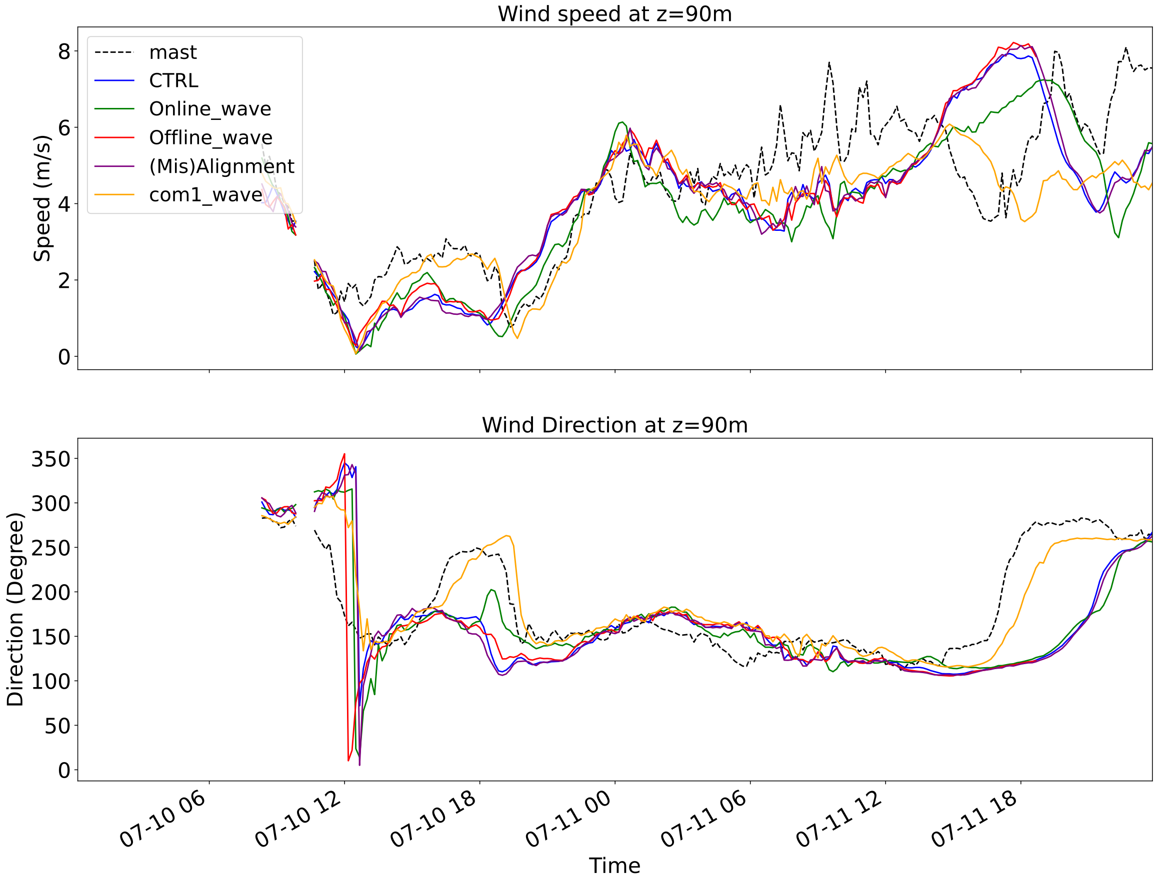

Figure 6.12: Time series of wind speed (top panel) and direction (bottom panel) at the FINO1 station at height of 90 m for a period between $10-12$ July 2015.

at high wind speeds (Bachynski et al. 2014 ; Li et al. 2015). For July $10-12$, the com1_wave experiment performes better compared with the observation, but there are not many discrepancies among different simulations for $20-26$ July.

Statistical comparison of simulations and observation data during the misalignment cases is presented in Table 6.4. The minimum, maximum, and standard deviation of the observational data are 0.3, 16.12, and 3.21, respectively. On average, all simulations underestimate the wind speed during these periods (with negative biases). The com1_wave shows minimum MBA and MAE and the offline_wave shows minimum RMSE. The CTRL and offline wave simulation show a better correlation compared with other simulations with a correlation of 0.83. In general, there are no significant differences among the simulations during these periods.

Figure 6.14 shows the wind rose for the misalignment periods. The observed prevailing wind direction is from west to southwest. Most of the experiments show a predominant wind direction from the west to the northwest except for the com1_wave experiment which shows a good agreement with respect to the observation.

Weibull distributions of observation and simulations at the FINO1 station for the misalignment periods are shown in Fig. 6.15. All the simulation curves show a shift to the left indicating that all simulations tend to underestimate the most frequent wind speed compared with observation. The corresponding scale and shape parameters are presented

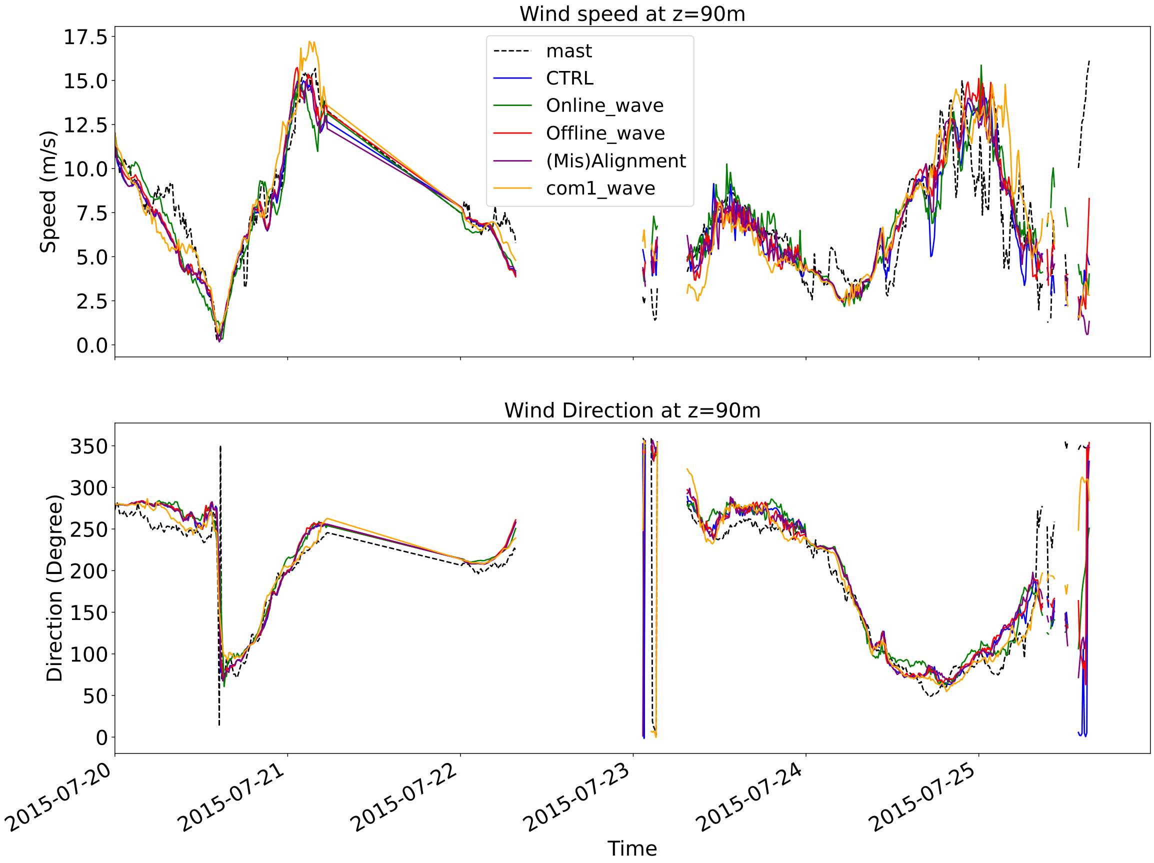

Figure 6.13: Time series of wind speed (top panel) and direction (bottom panel) at height of 90 m for FINO1 station during a period between $20-26$ July 2015).

Table 6.4: Statistical parameters of the observed and the simulated wind speeds at FINO1 station during the misalignment periods (i.e. $10-12$ July and $20-26$ July 2015)

Parameter	Observation	CTRL	Online_wave	Offline_wave	(Mis)Alignment	com1_wave
Min	0.3	0.18	0.06	0.21	0.14	0.07
Max	16.12	15.04	15.86	15.73	14.95	17.20
Std	3.21	3.21	3.34	3.33	3.22	3.52
Correlation		0.83	0.81	0.83	0.81	0.82
MBA		-0.35	-0.23	-0.23	-0.32	-0.17
MAE		1.30	1.35	1.31	1.33	1.28
RMSE		1.93	1.98	1.90	2.00	2.02

in Table 6.5. Weibull shape and scale parameters for observation data are 2.10 and 7.24 respectively. All simulations underestimate the shape and scale parameters, and minimum errors for the shape and the scale parameters are related to the online_wave and the com1_wave experiments respectively.

The Taylor diagram of all simulations during the misalignment period is shown in Fig. 6.16. As can be seen, the simulation results are almost similar. (Mis)Alignment, CTRL, and Online_wave experiments are very close to each other.

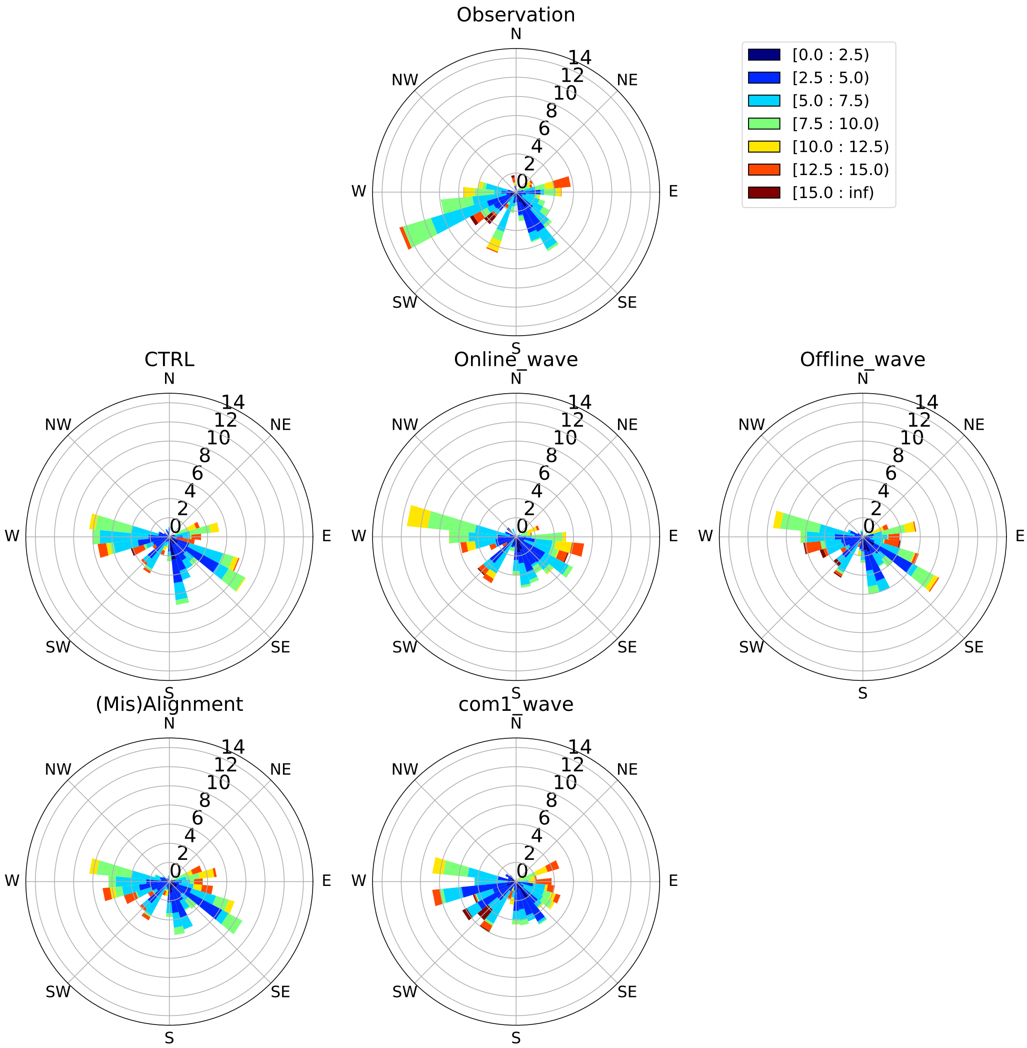

Figure 6.14: Wind rose comparisons between the observed (top) and simulated wind fields for the entire misalignment study periods (i.e. $10-12$ and $20-26$ July 2015)

6.2.2 Wind shear and Veer

Figure 6.17 shows the variation of wind speeds with height between $20-26$ July 2015. The predominant blue color in this figure indicates that the wind speed is often low during the study period. Most of the time, the model is able to simulate wind variations with height by a proper accuracy.

Figure 6.18 shows the variations of wind roses with height. For Observation data, the dominant wind direction shows a slight counterclockwise turning with a height from 33

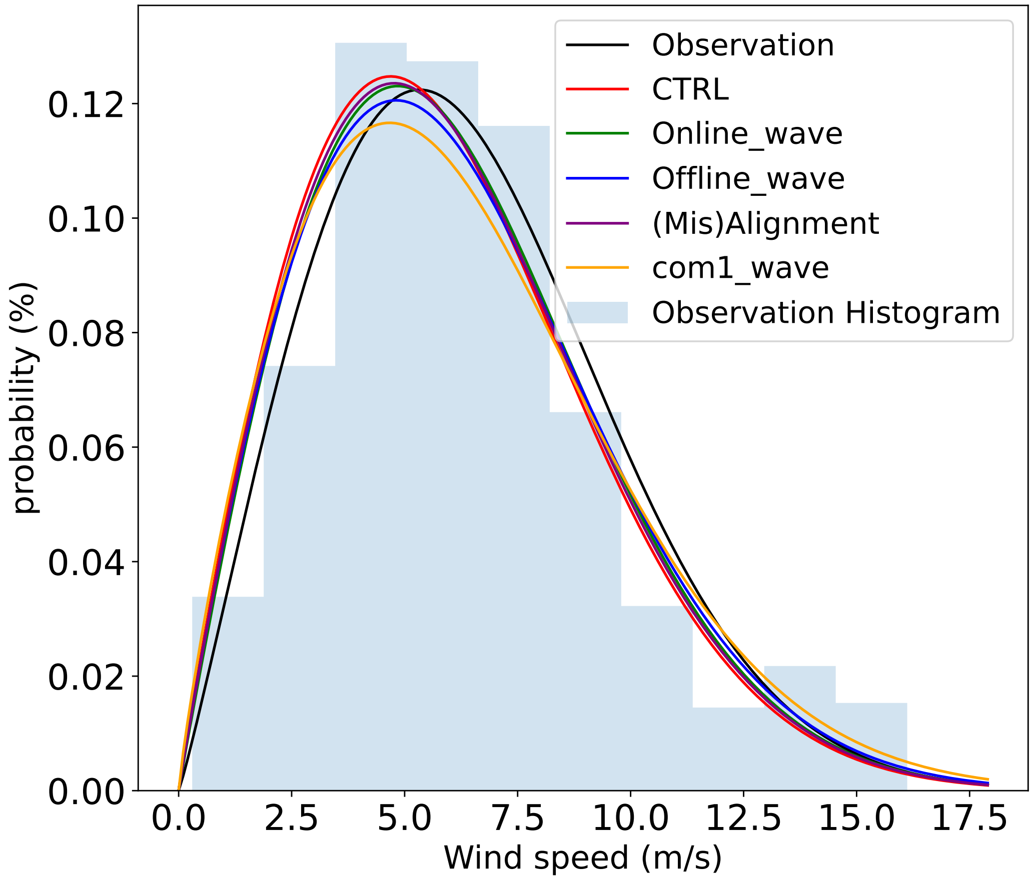

Figure 6.15: Comparing Weibull distribution functions of the observed and simulated wind speeds during the misalignment periods (i.e. $10-12$ and $20-26$ July 2015). Light blue bars show the histogram of the observation data.

Table 6.5: Weibull distribution parameters of observation and simulations during the misalignment periods at the FINO1.

Parameter	Observation	CTRL	Online_wave	Offline_wave	(Mis)Alignment	com1_wave
Shape	2.10	1.95	1.98	1.94	1.96	1.87
Scale	7.24	6.77	6.92	6.98	6.85	7.04

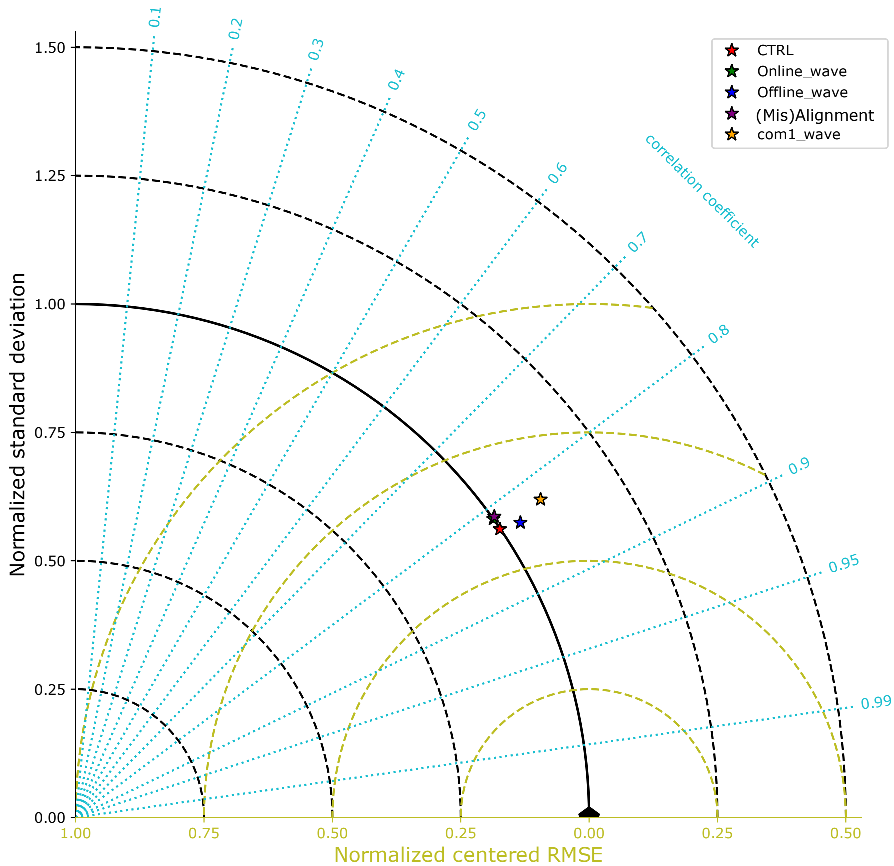

Figure 6.16: Taylor diagram comparing between the simulated and the met-mast observed data at the FINO1 station during the misalignment periods (i.e. $10-12$ and $20-26$ July 2015).

m to 90 m. But for simulated data, there aren't any changes with height regarding the dominant wind direction. As mentioned earlier, this could be due to the small differences between the levels' heights in the model.

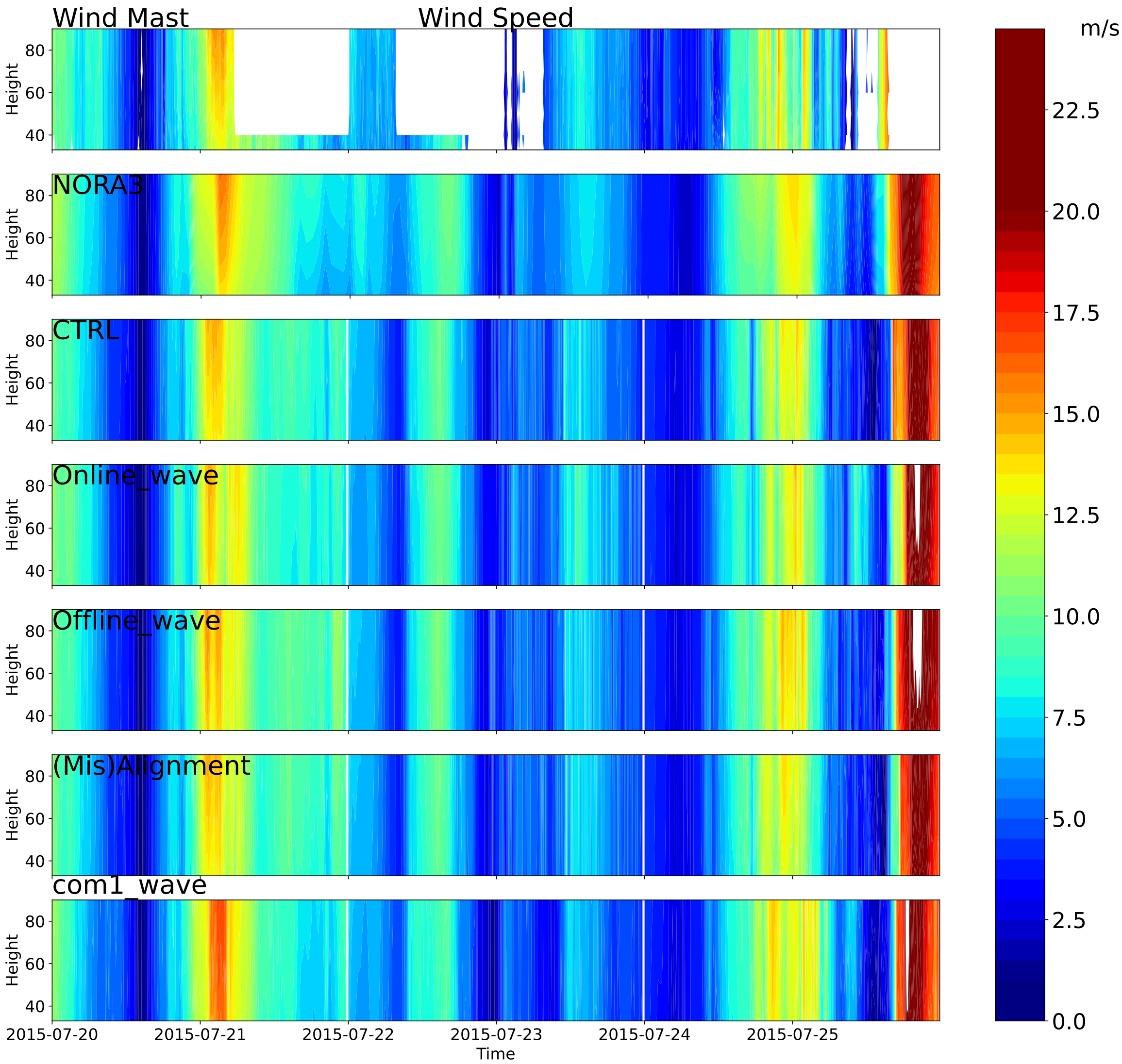

Figure 6.17: Time-height plots of thesimulated wind, the observed wind from FINO1, and the NORA3 wind data for a period between $20 - 26$ July 2015. White areas in the wind measured data indicates the shadow zones or missing data.

6.2.3 Roughness length

The time series of wind speed and roughness length during the misalignment period $(20-26$ July 2015) at FINO1 station are presented in Fig. 6.19. The variations of surface roughness are very small in most experiments except for the (Mis)Alignment and the CTRL runs. The roughness length in the CTRL experiment depends directly on the wind speed and the results of the (Mis)Alignment experiment show lots of fluctuations in time. Other simulations show small changes during high wind speeds.

Changes in roughness length with wind speed are shown in Fig. 6.20. The results of the CTRL run show an increasing trend as a function of wind speeds. In the (Mis)Alignment

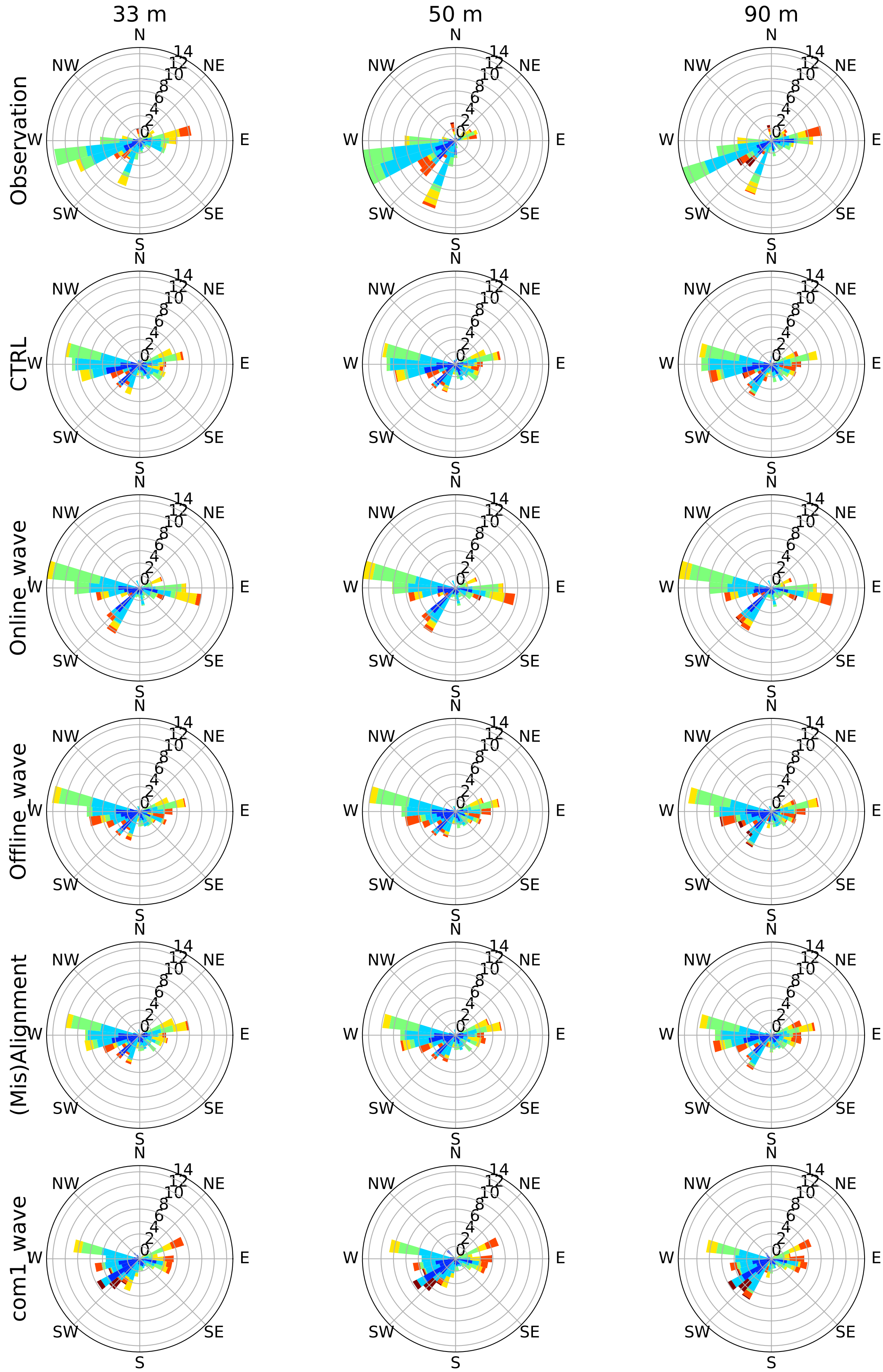

Figure 6.18: Wind roses at three different heights from observations and simulation results for $20-26$ July 2015.

experiment, the surface roughness increases with a steep slope for wind speeds over 7 m/s. The online_wave results show the same behavior as the observed roughness length, but with a lower slope and for the wind speeds more than 8 m/s.

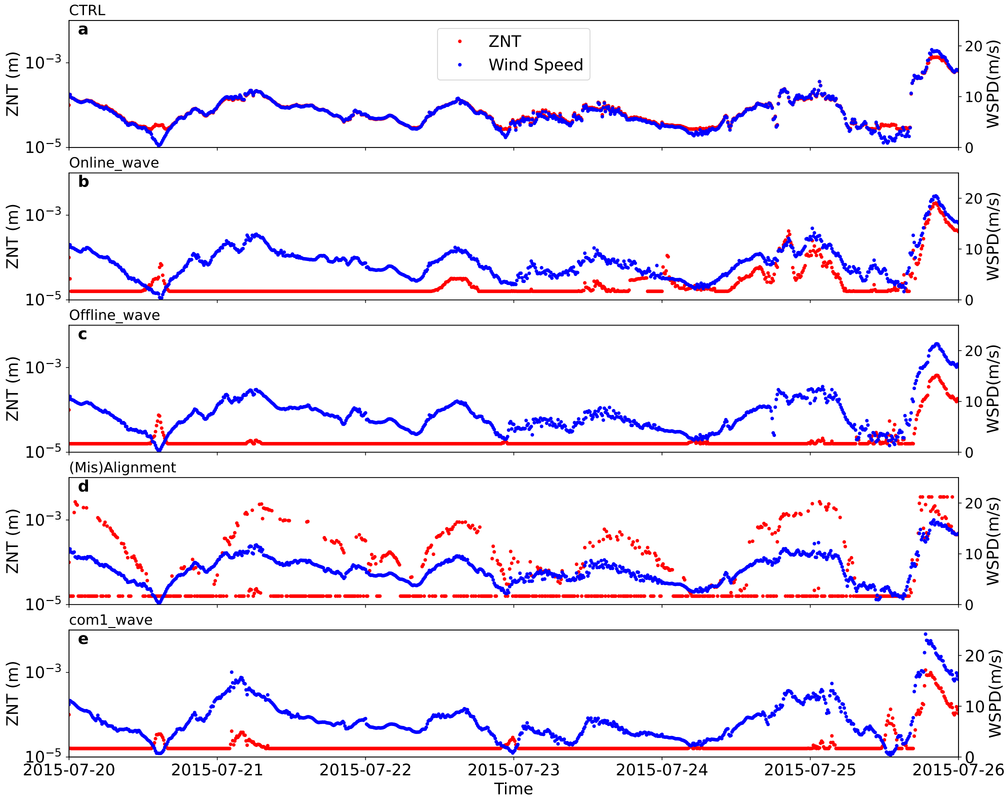

Figure 6.19: Changes of the wind speed and roughness length (ZNT) with time at FINO1 station during $20-26$ July 2015 for: (a) the CTRL run; (b) the online_wave experiment; (c) the offline_wave run; (d) the (Mis)Alignment run; and (e) the com1_wave experiment.

6.2.4 Wind energy

Figure 6.21 shows the distribution of the wind speed in the domain 3 of simulations for the period of $20-26$ July 2015. In the misalignment period (i.e. low wind speeds), we can see that the online_wave experiment predicts the maximum amount of energy within the model domain. The lowest energy estimation in this period is related to the com1_wave run. A comparison of the simulated wind power with the observations at the FINO1 is shown in Fig. 6.22. At low wind speeds, the model usually underestimates the wind energy compared with the observations. The total extractable wind power from the measurement is 979867 W/m^2 and the com1_wave run, by estimating the total wind power of 967747 W/m^2 in this period, has the least difference with respect to the observational data.

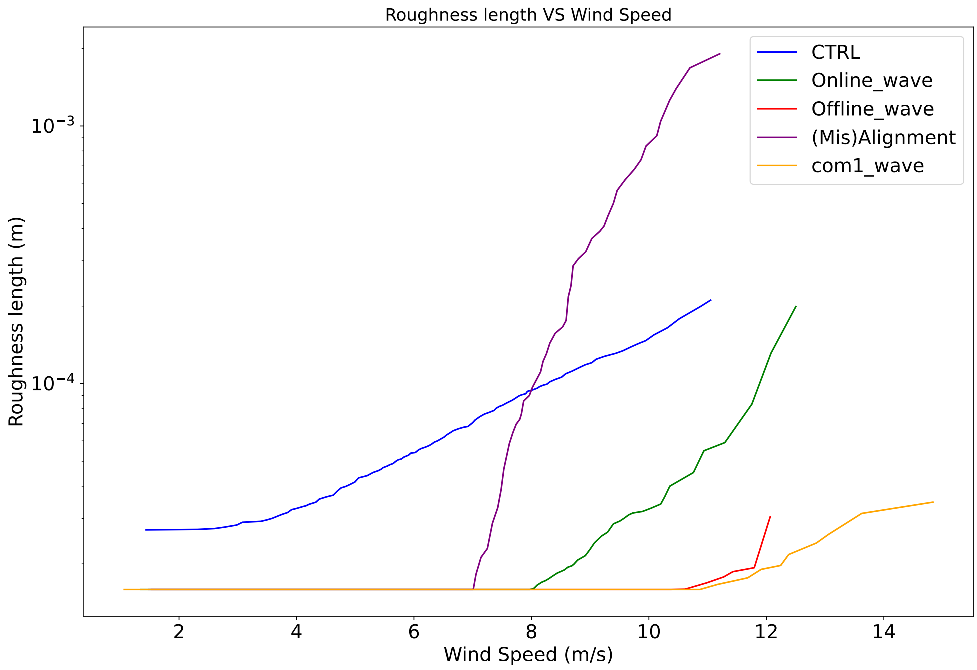

Figure 6.20: Roughness length versus wind speed for different simulations during $20 - 26$ July 2015.

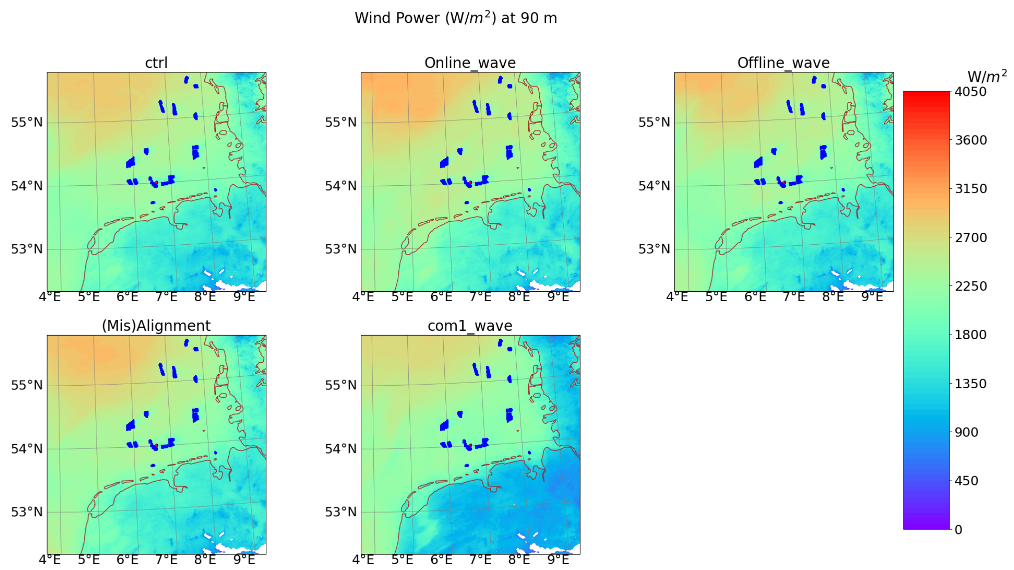

Figure 6.21: Spatial distribution of the mean wind power (W/m^2) at 90 m height in the WRF model domain for the period of $20 - 26$ July 2015. Blue dots show the locations of the wind turbines in the study area, and the red dot showed the location of the FINO1.

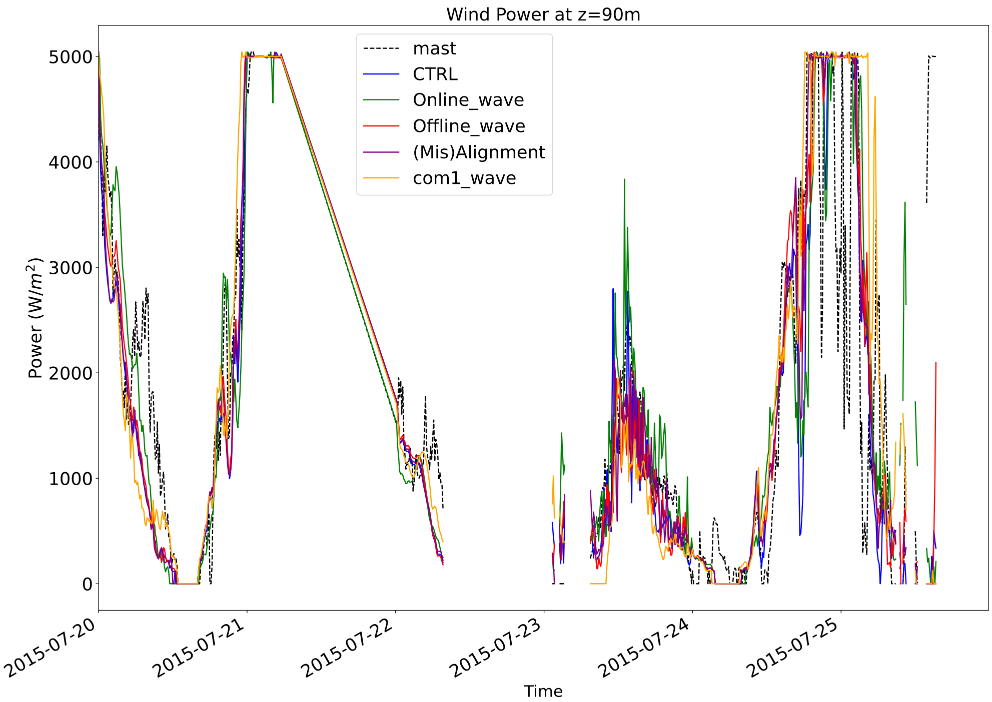

Figure 6.22: Time series of mean wind power (W/m^2) at the FINO1 station for the period of $20 - 26$ July 2015.

6.3 Wave boundary layer case study

Figure 6.23 shows the time variation of the wave age during June 2015. The blue-coloured area represents a favourite condition for the swell waves with a high likelihood of wind-wave interactions (we select this duration as the study period because it contains both the no-swell and the mixed wind-sea and swell conditions). The time series of the air-side friction velocity u_{*a} illustrates that several young sea state events create large surface roughness for the friction velocity above, approximately, 0.2 m/s. The largest values of u_{*a} occur during the lowest wave age episodes (there is an inverse relationship between the variation of the wave age and friction velocity). We use the high-frequency temperature and wind data (i.e. with a sampling frequency of 25 Hz) observed from the sonic anemometer at a height of 15 m to estimate the Monin–Obukhov stability parameter L, i.e. Eq. (5.1). During the swell events as shown in Fig. 6.23, the Monin-Obukhov (MO) theory fails in adjusting the wind profile within the marine atmospheric boundary layer. However, we use values of L to classify the stability regimes, particularly during the study period (i.e. with negative and positive values denoting the unstable and stable conditions). The magnitude of L indicates a distance that buoyancy production plays a dynamically important role in the turbulent kinetic energy budget with respect to surface shear production. Figure 6.23b shows during the study period when the wave age is large, the MABL tends to be stable, and the majority of high wind events occur during unstable conditions. Figure 6.23c represents the time-evolution of the power spectral density of the horizontal wind speed (i.e. u-component, the same characteristics are observed for the w-component) overlaid by the time series of the wave peak frequency, f_p, measured by the surface buoy operating in the close vicinity of the FINO1 met-mast (gray markers). There is a good agreement between the measured f_p and the spectral peak of u-component wind from sonic data at the wave frequency band (i.e. the frequencies within the coloured horizontal band) is consistent with an increase in the values of wave age. The agreement becomes better if the atmosphere is stable and is less pronounced in the presence of strong convective cells (i.e. unstable conditions before June 25).

Due to the focus of this study, we use the COAWST modeling system with activated WRF (allowing three nested domains as shown in Fig. 3.7) and SWAN (including only one domain). The WRF model with CTRL setup (see Table 3.3) downscales the reanalysis ERA5 for the coupling between atmosphere and wave at a grid resolution of 1 km in our study. Furthermore, the WRF model contains 60 vertical levels to assure a reasonable representation of wind turbines in the Southern North Sea area where turbines of different sizes and heights are operating. We use Fitch (2016) parameterization of wind turbines in the WRF by considering the proposed correction of Archer et al. (2020). For the wave conditions along the grid boundaries of the parent SWAN domain, we extract the two-dimension spectral information from the NORA3 hindcast with 3-hourly temporal resolution. The SWAN parent domain covers properly the area of FINO1 and Alpha Ventus wind park with a 1km horizontal grid resolution, in order to capture realistically the swell propagation (containing 241×426 grid points). For the SWAN model, we use the wind input and white-capping of Janssen (1991), hereafter Janssen, and ST6 source term formulations. To study the impacts of wave model resolution on wave propagation and statistics, we conduct additionally another WRF-SWAN experiment with two nested domains and use its result at a grid resolution of 3km (the parent outer domain with 453×417 grid points). Our overall objective is to compare two source term formulations in SWAN that account for the

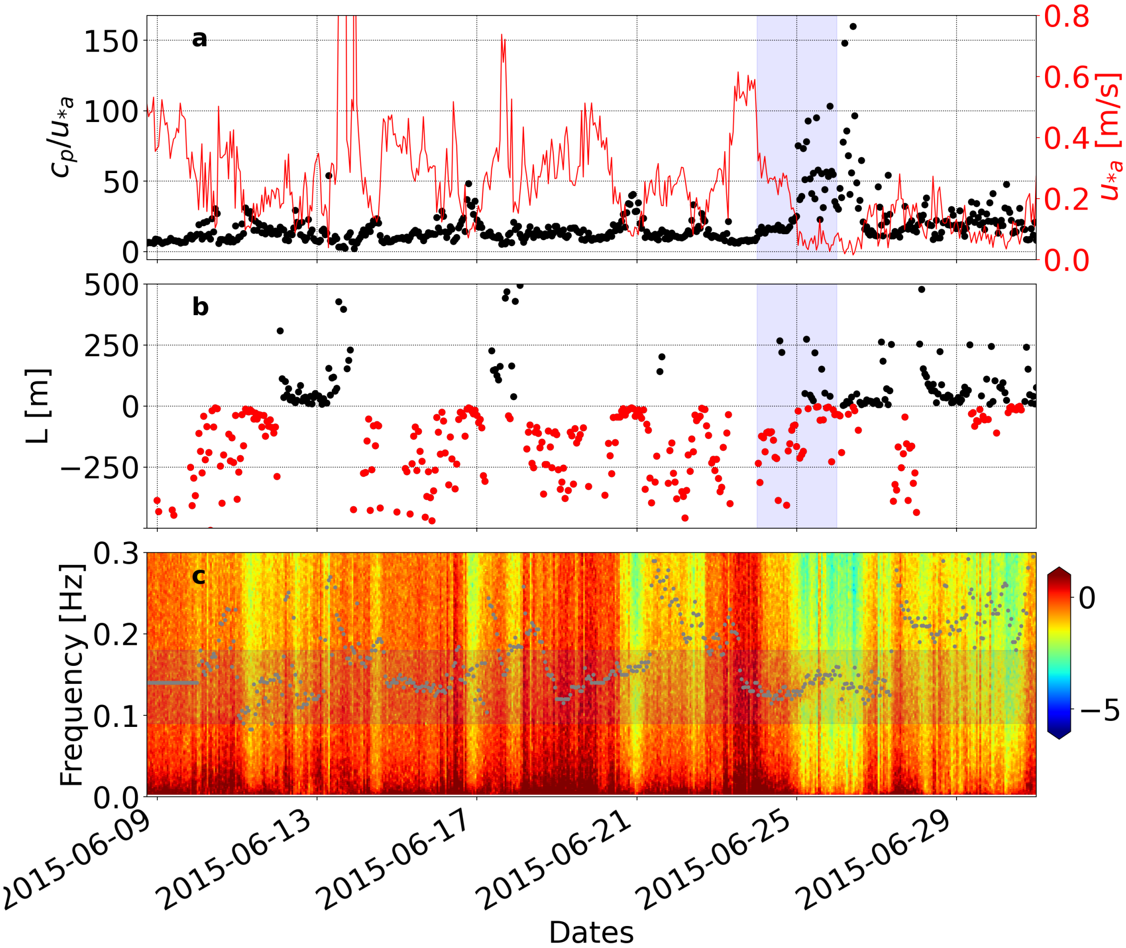

Figure 6.23: Time series of (a) wave age c_p/u_{*a} in which c_p denotes the phase speed estimated from the surface gravity wave dispersion relation based on observed values of the significant wave height, H_s and the wave peak period, T_p; (b) Monin–Obukhov stability parameter, L; and (c) energy spectral time evolution for the u-component of wind during June 2015 calculated from the 15 m height sonic anemometer with a sampling frequency of 25Hz. Blue coloured regions in (a) and (b) represent the study period. The shaded area in (c) denotes the wave-affected frequency band.

WBL during the selected study period. It is noted that the WBL modules implemented in SWAN do not account for the thermal effects on wind-wave interactions. Particularly, the ST6 uses an empirical drag coefficient that is dependent only on wind speed.

We show in Fig. 6.24 the synoptic situations during two representative dates corresponding to the unstable and stable conditions. At 24 June 2015 cases (Figs. 6.24a, b, and c), similar regions of high wind speeds are situated to the northeast of domains over the ocean, with peak wind speeds in the excess of 12m/s. While the wind speeds are higher in these regions for ST6 and Janssen experiments, they show slightly different spatial distribution compared with the ST6-NEST experiment (which shows more pronounced locally enhanced wind). In these three cases, the pressure contours are somewhat in perfect structural agreement and there is no synoptic feature in the study area. In Figs. 6.24d, e, and, f, the flow field with the highest wind speeds are established over the land (along the southeast boundary, most likely due to the interactions between the flow and topography). The highest wind speed belongs to the Janssen experiment on this date (June 25, 2015 12 UTC) followed by the ST6-NEST and the ST6. There is also evidence of localized regions of small wind speeds over the ocean in the area of FINO1 captured by the ST6 and the Janssen experiments. The spatial variation of the wind speed at 10 m shows very distinguished differences between different experiments along the northern (and southeast corner) of the domain mainly affected by the boundary conditions, particularly for the ST6-NEST case. The structure and size of the wind field in this experiment will have important impacts on the surface wave generation, propagation, and the spatiotemporal variability of the interactions between the atmosphere and ocean.

The spatial variabilities of the wind vertical velocity at 100 m height are compared for different wave physics under two stability regimes in Fig. 6.25, and at two different dates. Results in Figs. 6.25a, b, and c at June 24, 2015 08 UTC indicate that the model experiment with a two-domain nested SWAN setup provides slightly different spatial patterns while two other experiments result in close agreement. Beside the fact that the discrepancies between Fig. 6.25a and b are caused by the model resolution and different behaviour of the SWAN model across the boundaries of one- and two-nested domains, differences between Fig. 6.25b and c might be directly explained by the differences in the formulation of the wind input and white-capping, and indirectly through the effects of wind drag and forcing, and nonlinear (wave-wave and wave-wind) interactions. According to Fig. 6.23b, the unstable stratification and the increased turbulent mixing during this time modulate the flow field behavior and its interaction with the surface gravity waves (note that the wind shear is approximately constant in this period, not shown). Figures 6.25d and e further highlight the importance of atmospheric stability during the wind-wave episode on June 25, 2015 12 UTC (see Fig. 6.23b coloured area). Large discrepancies are observed between the ST6-NEST and the ST6 experiments both in coastal regions and the open ocean, and large values of w at 100 m in the ST6-NEST experiment are distributed more homogeneously over the open ocean than the ones from the ST6 experiment. Significant wave height, H_s, decreases to 1 m in this case while the interaction between the wind and wave enhances (see Fig. 6.23c), and Figs. 6.23e and f show somewhat similar and comparable spatial patterns (despite some differences, for instance, around 7°E and 54°N).

Vertical cross-sections over the middle of the domain passing through the FINO1 for heights below 1200 m at 24 June 08 UTC are shown in Fig. 6.26. The horizontal wind speeds, U_h, are characterized by an elevated unstable layer over the land, with moderately

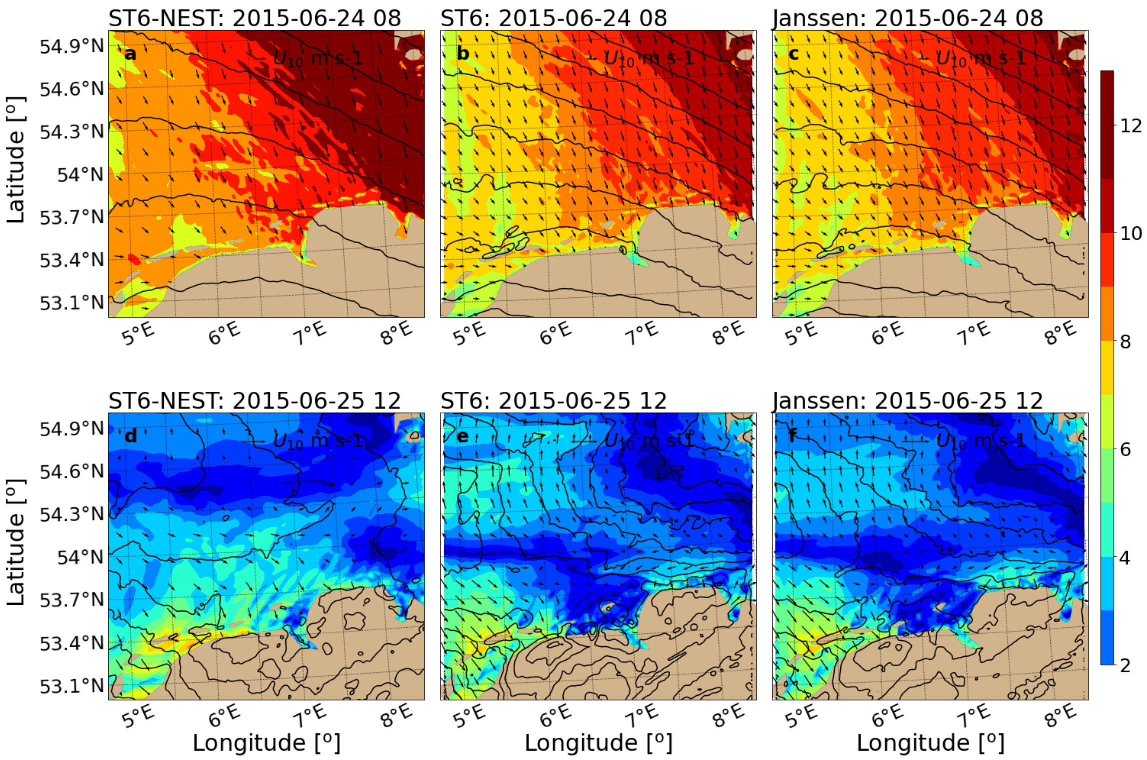

Figure 6.24: The 10 m wind speed overlaid with the sea-level pressure (contours—mb) from: (a,d) the ST6-NEST experiment; (b,e) the ST6 experiment; and (c,f) the Janssen experiment. Snapshot results in (a,b,c) are at June 24, 2015 08 UTC, and results in (d,e,f) are at June 25, 2015 12 UTC.

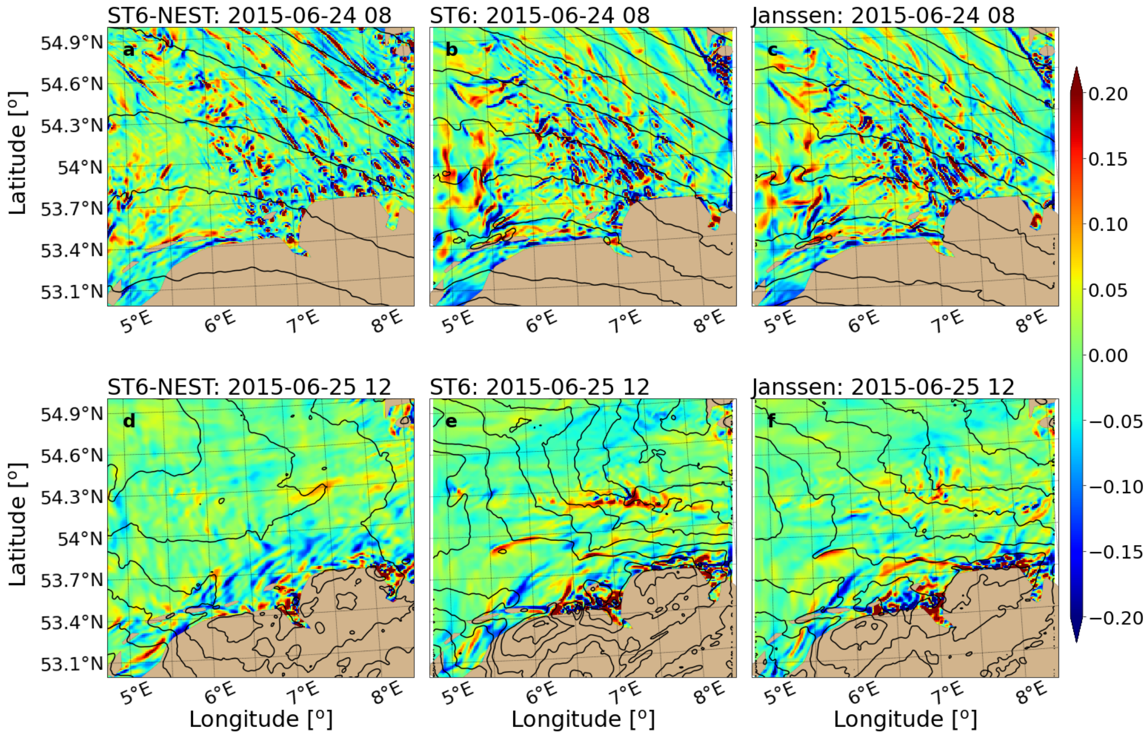

Figure 6.25: Snapshots of spatial variation of the vertical velocity w from different WRF-SWAN experiments: (a,d) SWAN with two nested domains with ST6 parameterization; (b,e) SWAN with only one domain and ST6 parameterization; and (c,f) SWAN with the same domain but Janssen parameterization. Results in (a,b,c) are at June 24, 2015 08 UTC, while results in (d,e,f) are at June 25, 2015 12 UTC.

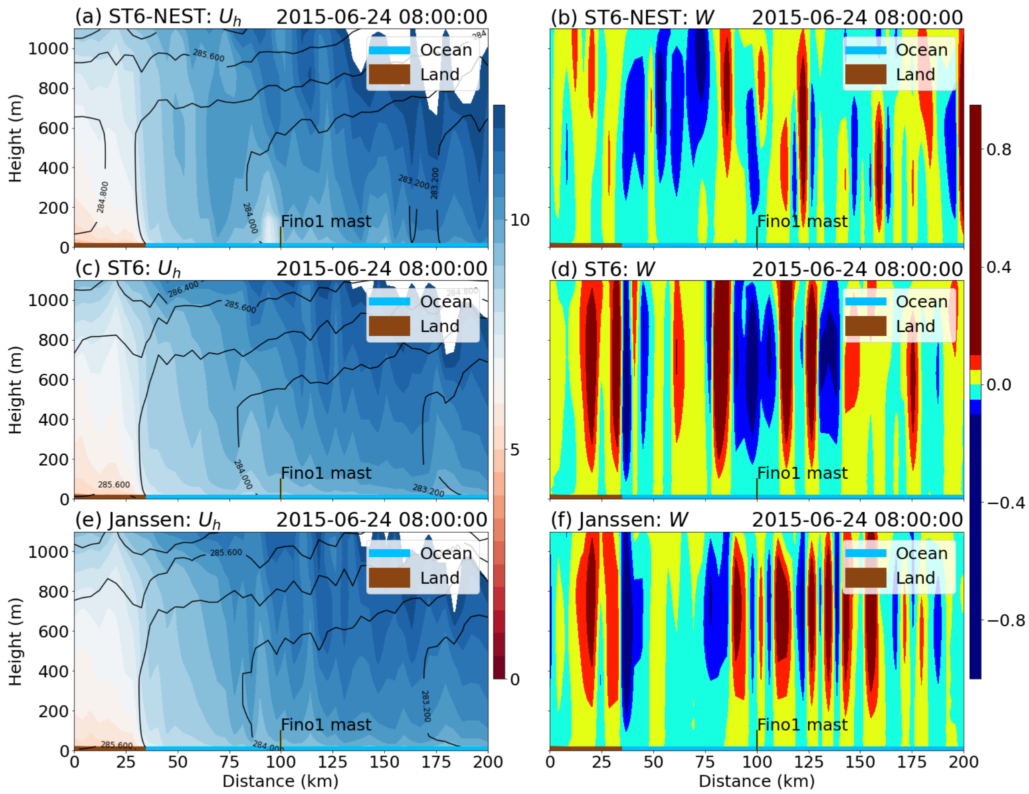

Figure 6.26: Vertical cross sections of WRF-SWAN simulations at 24 June 2015 08 UTC for: (a,c,e) horizontal wind speeds, U_h, corresponding to the ST6-NEST, the ST6, and the Janssen experiments (top-bottom), respectively; and (b,d,f) vertical velocities, w, corresponding to the ST6-NEST, the ST6, and the Janssen experiments (top-bottom), respectively. All plots of U_h are overlaid with potential temperature (contour gray lines).

strong horizontal winds (downstream of the FINO1) that very rapidly decrease towards the ocean (the land will be warmer than the ocean after 09:00 and this might be the reason for a week sea breeze at this time). A comparison of the ST6-NEST results (both U_h and w) with other simulations indicates that the ST6-NEST simulation provides a slightly different representation for the flow field, particularly in the area of FINO1. Figures 6.26b, d, and e show strong vertical upward (downward) movements, due to the surface heating (we overlaid the potential temperature to show the interconnection between the temperature and the wind speed over the land and ocean). In this case, the vertical motion over the land and offshore are considerably lower while both the ST6 and the Janssen experiments show the formation of convective cells at the boundary of the land-sea as well as over the ocean (particularly close to the location of FINO1). These cells are vertically expanded over, approximately, the entire study height.

Figure 6.27 shows the vertical cross-sections over the middle of the domain passing through the FINO1 for heights below 1200 m at 25 June 12 UTC. In Fig. 6.26, it was shown how the wind formed over the land early morning, and due to solar heating, a

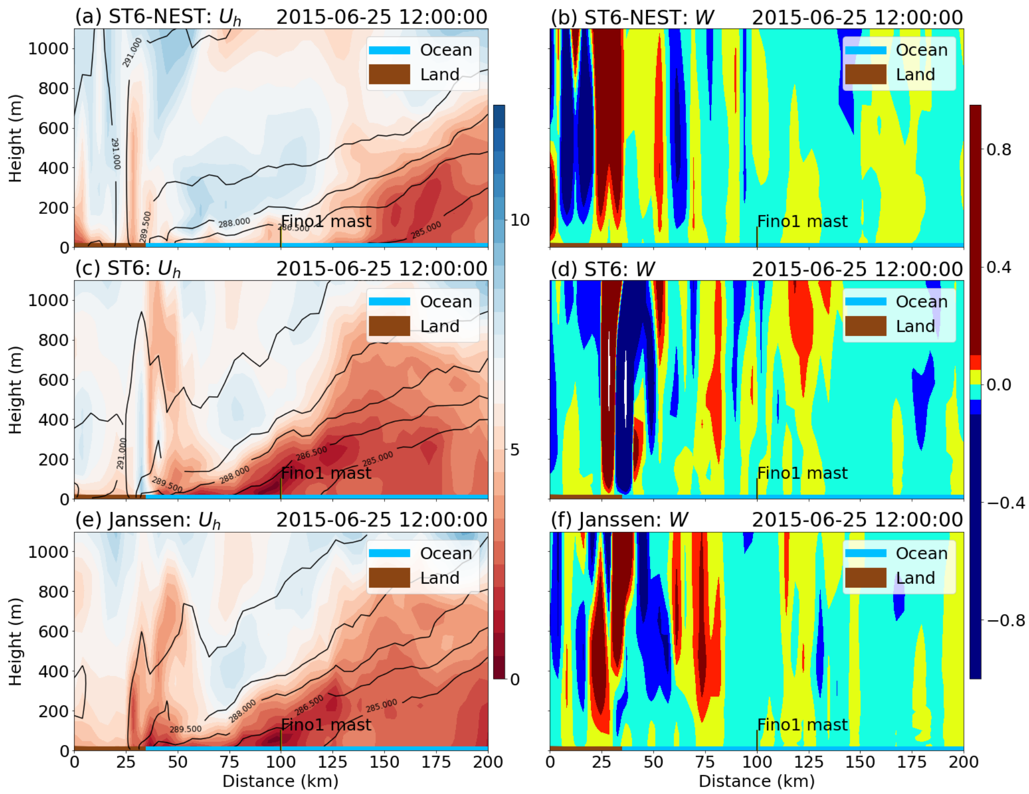

Figure 6.27: Vertical cross sections of the WRF-SWAN simulations at 25 June 2015 12 UTC for: (a,c,e) horizontal wind speeds, U_h, corresponding to the ST6-NEST, the ST6, and the Janssen experiments (top-bottom), respectively; and (b,d,f) vertical velocities, w, corresponding to the ST6-NEST, the ST6, and the Janssen experiments (top-bottom), respectively. All plots of U_h are overlaid with potential temperature (contour gray lines).

strong baroclinic zone evolves around noon. All model results show very strong upward (downward) vertical motions over the land which is now warm (see the temperature contour lines), and high wind over the ocean (and around the FINO1 area). While the ST6 and the Janssen simulations suggest similar distribution of U_h, the vertical velocities are not in good agreement. Close to the FINO1, the winds are approximately parallel to the coast (Fig. 6.24e and f), suggesting less likelihood for frictional decoupling. However, the ST6-NEST wind vectors at the coastal areas exhibit more tendency to cross the German Southern coast highlighting more chance for frictional decoupling. All model results show wind nearly everywhere, but there is a clear discrepancy in vertical/lateral distributions of wind at the boundary between land and sea.

Figures 6.28a, b, and c provide an overview of horizontal wind speeds corresponding to the wind-wave interaction case study between 24 and 26 June 2015 for heights below 250 m. These plots also highlight the influence of domain size and nesting boundary information on WRF-SWAN simulations in better representation of the flow field and its variations during the convective and (stable-unstable) mixed stability conditions. A qualitative look at these plots suggests that all runs reproduce the wind variation both during the convective conditions (early simulations at 24 June between 00 UTC and 06 UTC) and during the high wind speed event around 24 June at 15:00 UTC. Specifically, the variations are better captured using the higher resolution runs of the ST6 and the Janssen, whereas the coarser experiment overestimates the wind when the wind declines to the values below $2-3$ m/s. Even though all model runs produce qualitative similarities with the observational time series (i.e. Fig. 6.28d), the ST6-NEST leads to large errors during the low wind events.

Figure 6.29 gives an overview of wind direction for different model simulations. During the high wind event (at 24 June at 15 UTC), the wind direction decreases from approximately 300^o to 250^o for all runs, with a very good qualitative match with wind vane measurements at 90 m height (see Fig. 6.29d). For the first 6h at 25 June, the wind direction gradually reduces from 280^o to 180^o, and the ST6-NEST predicts with the highest accuracy the wind direction at 25 June between 00 UTC and 13 UTC. All models are not able to capture properly the variation of the wind direction after 13 UTC.

In Fig. 6.30, we compare the spatial variation of H_s against significant wave height data from ERA5 on June 24, 2015 18 UTC, when the wind speed reaches its peak during the study period. While the magnitudes of spatial variation of H_s show some similarities (particularly between the ST6 and Janssen runs), the spatial map of H_s from the ST6-NEST run demonstrates considerably higher values of H_s with a different spatial pattern, especially for the shallow water areas close to the Southern coastline. All maps are in good agreement in predicting the highest wave heights within the area located in the northeast of the domain (close to the eastern coast). In short, the ST6, the Janssen, and the ERA5 represent strong spatial similarities.

The spatial variations of mean wave period T_m from different WRF-SWAN experiments are compared with the one from the ERA5 in Fig. 6.31. Results show insignificant similarities between the Janssen run and the ERA5 (as expected), and the spatial distribution of T_m from ST6 at this time is in good agreement with ERA5 and Janssen runs, but with lower magnitudes (specifically on the northern side of the domain with a typical magnitude of 4 s compared with 6.5 s from the ERA5 and the Janssen experiments).

To test which SWAN configuration yields better results, we extract wave spectral and bulk information at the location of FINO1 and compare the model results to the nearby buoy measurements. The results of the SWAN simulations forced through the nested boundaries are shown in Fig. 6.32. It is observed that the wave conditions are almost energetic during the study period (i.e. $H_s > 0.5$ m, see grey markers in Fig. 6.32a). All modelled results of H_s, peak wave period (T_p), and D_p are generally in good agreement with the corresponding measurements, but T_p cannot be reproduced accurately before 24 June at 12 UTC, and the error in H_s from the ST6-NEST run increases when the wind speed decreases bellow 2 m/s towards the end of the study period. The high energy overestimation in the ST6-NEST results might be explained by the wind forcing for this configuration and the corresponding wind drag formulations. In general, different source term packages in SWAN runs show very similar performance, when compared with the observed values.

Figure 6.33a represents typical sea-state conditions during the study period (i.e. the wave condition from the surface buoy at 24 June 18 UTC is dominated by the north-northwesterly waves). This spectrum corresponds to a dominant energy peak (not fetch-limited condition) with a wide energy spread in direction and frequency. The spectrum is characterized as a

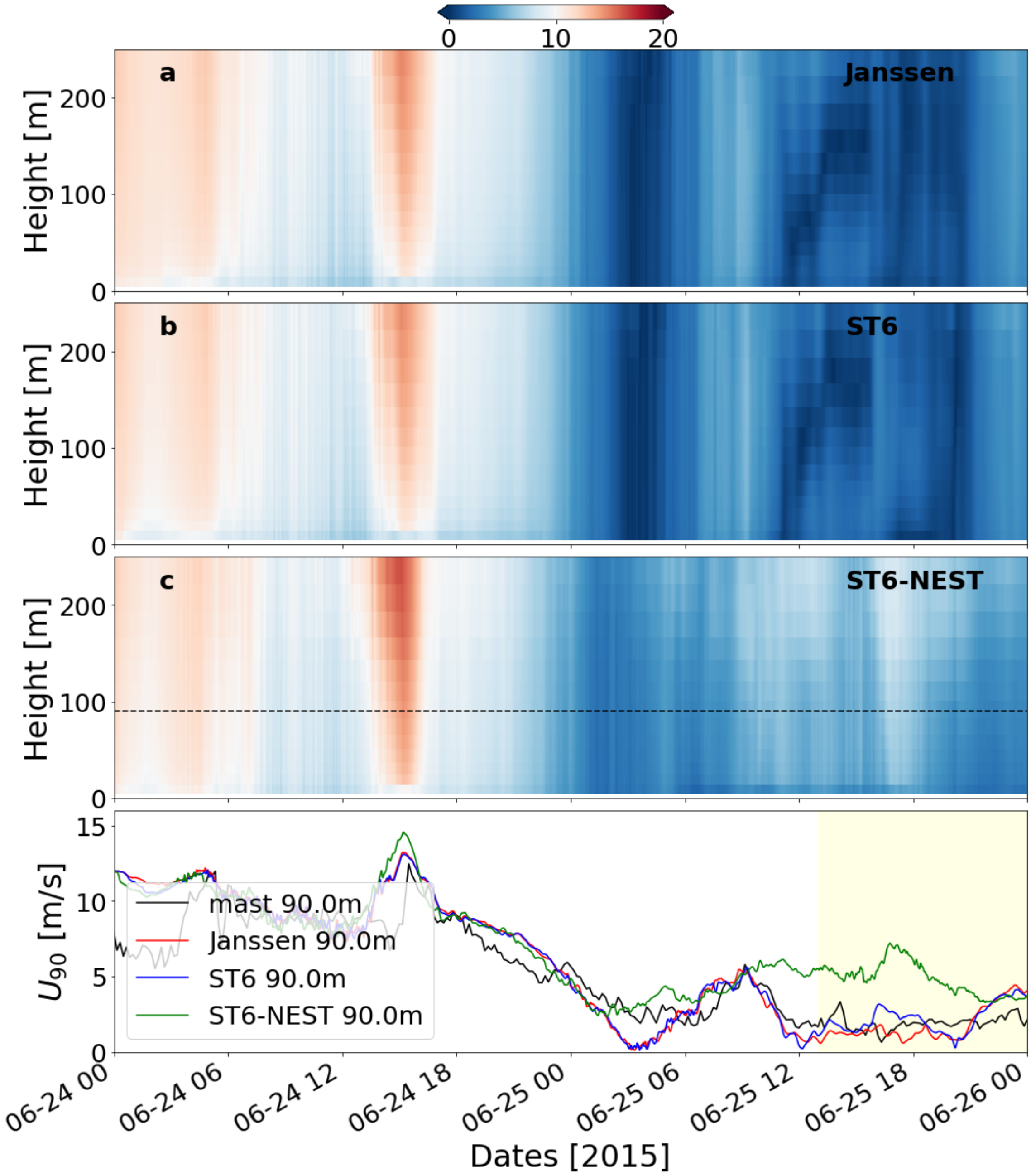

Figure 6.28: Time-height representations of the wind speed at geographical location of FINO1 between $24-26$ June 2015, from: (a) the Janssen simulation; (b) the ST6 experiment; and (c) the ST6-NEST experiment. Panel (d) shows the comparison between different WRF-SWAN experiments and observation from FINO1 mounted cup anemometer at 90 m height. The yellow shaded area in this subplot represents the time when the ST6-NEST time series deviate from measurement.

Wind direction
[Degree]

Figure 6.29: Time-height representations of the wind direction at geographical location of FINO1 between $24-26$ June 2015, from: (a) the Janssen simulation; (b) the ST6 run; and (c) the ST6-NEST experiment. The horizontal dashed line indicates 90 m height to be used in the time series comparisons hereafter. Panel (d) shows the comparison between different WRF-SWAN experiments and the observation from the FINO1 mounted cup anemometer at 90 m height. The yellow shaded area in this subplot represents the time when the ST6-NEST time series deviate from the measurement.

H_s [m]

Figure 6.30: Snapshots of spatial variation of H_s over the study area at June 24, 2015, at 15 UTC: (a,b,c,d) H_s from the Janssen, the ST6, the ST6-NEST, and the ERA5, respectively.

T_m [s]

Figure 6.31: Snapshots of spatial variation of the mean wave period T_m over the study area at June 24, 2015, at 15 UTC. (a,b,c,d) T_m from the Janssen, the ST6, the ST6-NEST, and the ERA5, respectively.

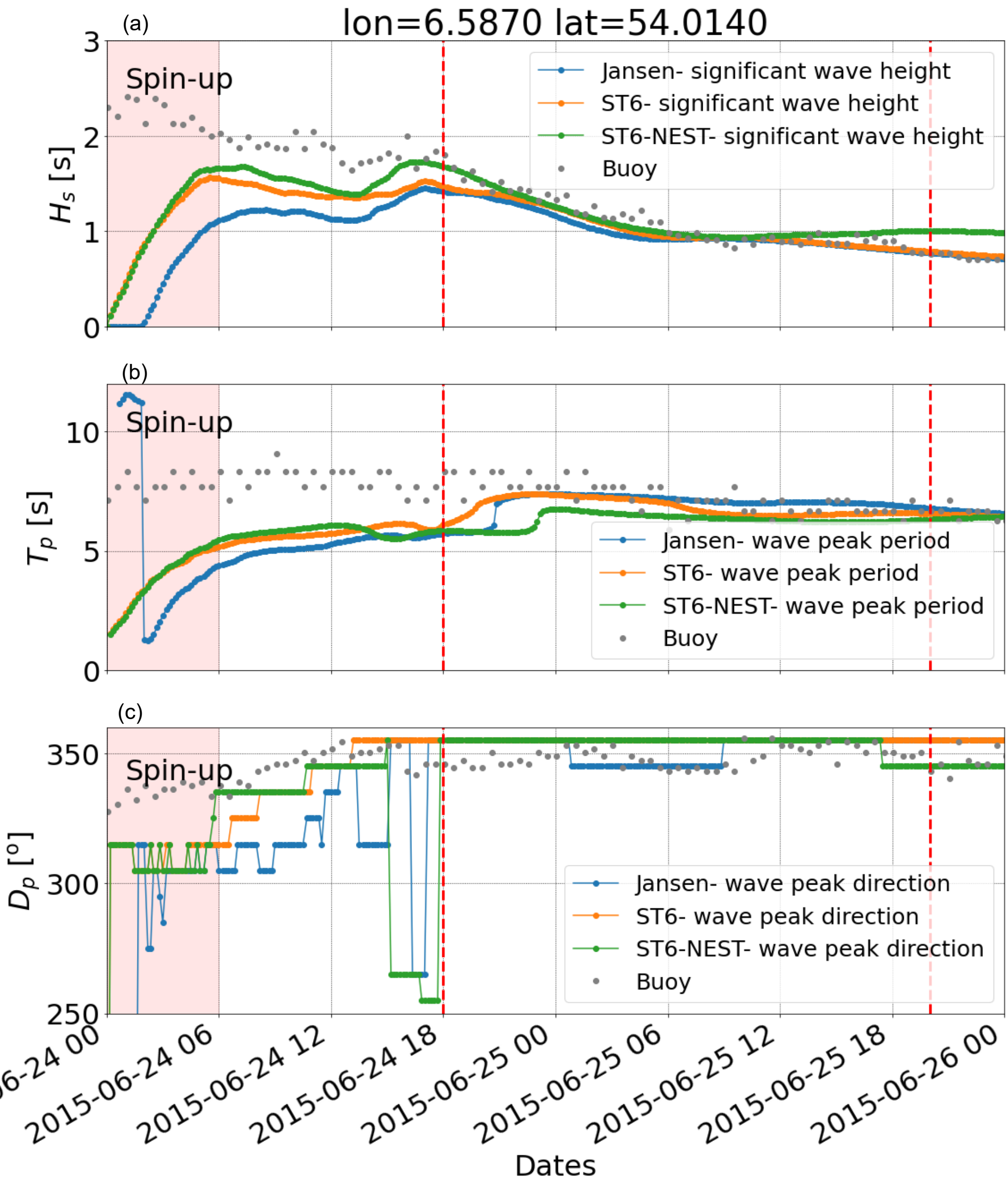

Figure 6.32: Time series of bulk wave parameters during the study period at the FINO1 location from three model experiments and surface buoy data. From top to bottom: (a) the significant wave height, H_s, (b) the mean wave period T_m; and (c) the peak wave direction, D_p. All plots overlaid with the corresponding buoy measurements of H_s, T_m, and D_p. Two vertical dashed lines show two analysis times (corresponding to the high- and low-wind events) to be used in coming figures.

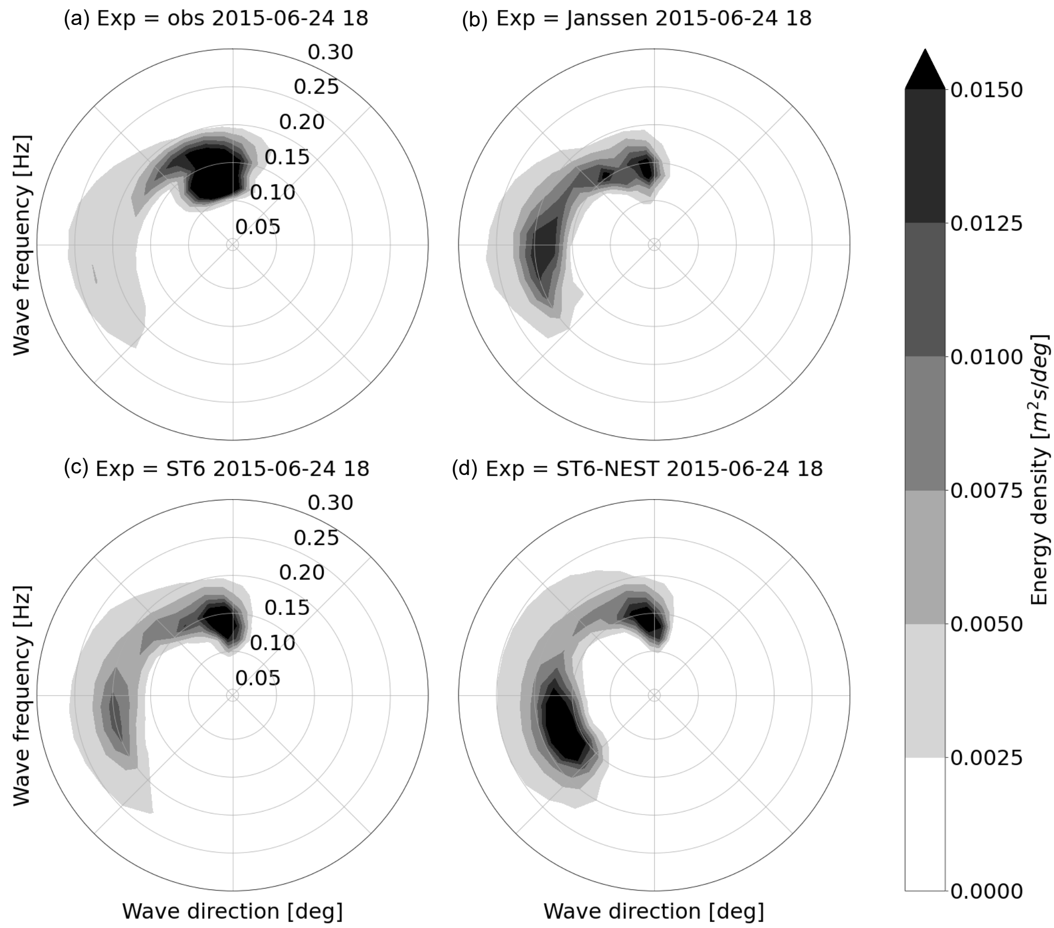

Figure 6.33: Modelled and measured 2D frequency-direction spectra for a northerly-northwesterly wave conditions at 24 June 2015 18:00 UTC): (a) the measured frequency-direction spectrum; and (b,c,d) the modelled 2D spectra by the Janssen, the ST6, and the ST6-NEST respectively.

mixed sea including both a well-developed sea (frequencies larger than 0.15 Hz) and swell waves (i.e. frequencies less than 0.15 Hz). Corresponding 2D spectra from the WRF-SWAN runs are shown in Figs. 6.33b, c, and d. There is a very satisfying qualitative agreement between the modelled and the measured spectra at this time. The energy at the (north-northwesterly) peak of the observed spectra decreases from the northern to the western part of the sector but this variation is specifically more erratic for all model spectra. The ST6 (and the Janssen run), however, gives a slightly better representation of these directional spreading but predicts also a local erratic westerly peak at 0.2 Hz. This secondary westerly energy overestimation, corresponding to the wind-sea component, is highest in the ST6-NEST experiment. In general, the swell component (in the north-northwesterly segment) is not only more energetic for the observed spectra than the modelled spectra, but also wider in direction. Contrarily, the wind sea component (in the westerly sector) is less energetic for the observed spectra than for the modelled ones.

While all models could capture effectively the dominant wave direction, we observe, however, slight discrepancies between the measured and the modelled wave directional data (i.e. Fig. 6.34). The ST6 and Janssen run at this time are in very good agreement with

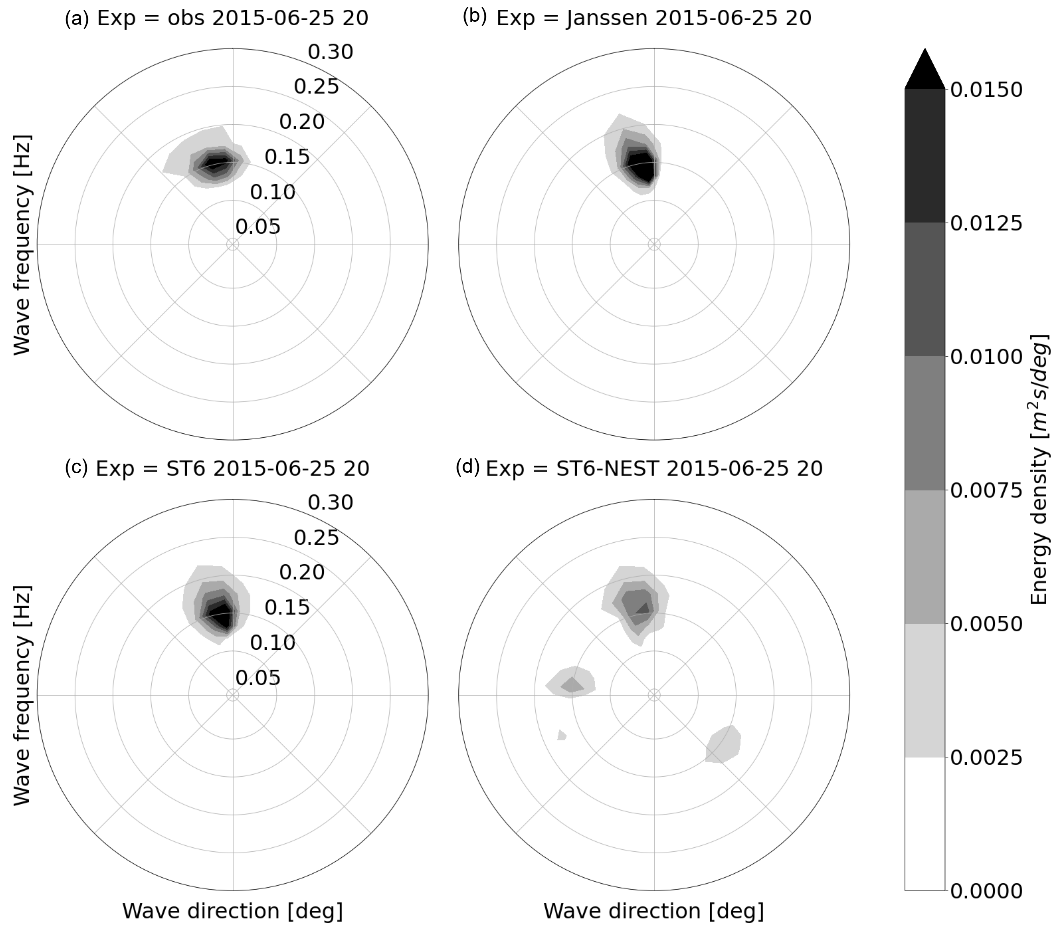

Figure 6.34: Modelled and measured 2D frequency-direction spectra for a northerly-northwesterly wave conditions at 25 June 2015 20:00 UTC): (a) the measured frequency-direction spectrum; and (b,c,d) the modelled 2D spectra by the Janssen, the ST6, and the ST6-NEST experiments respectively.

observation for north-northwesterly waves. The measured 2D spectrum shows a slightly wider energy distribution in direction. Furthermore, the ST6-NEST is lacking accuracy in capturing the magnitudes of dominant waves and it further produces non-realistic waves in different directions and frequencies.

In Fig. 6.35, we check qualitatively the ability of the ST6 and the Janssen experiments in capturing the spectral shapes of the wave energy spectra during the study period. Considering the coarse temporal outputs (i.e. 5-min), both model runs are in satisfying agreement with observation.

In Fig. 6.36, we compare how different source terms and WBL packages can model the shape and evolution of the wind energy source term $S_{in}(f)$, where f denotes the frequency in Hz. The frequency spectra of different WBL packages (in the logarithmic scale) at the location of FINO1 represent somewhat similar spectral variability (in both shape and magnitude). Some differences are observed both in the frequency of the peak value of $S_{in}(f)$ and its temporal variation (there is a forward lag in time when using Janssen setup). For frequencies between 0.3 Hz and 0.6 Hz before high wind event, the ST6 results are

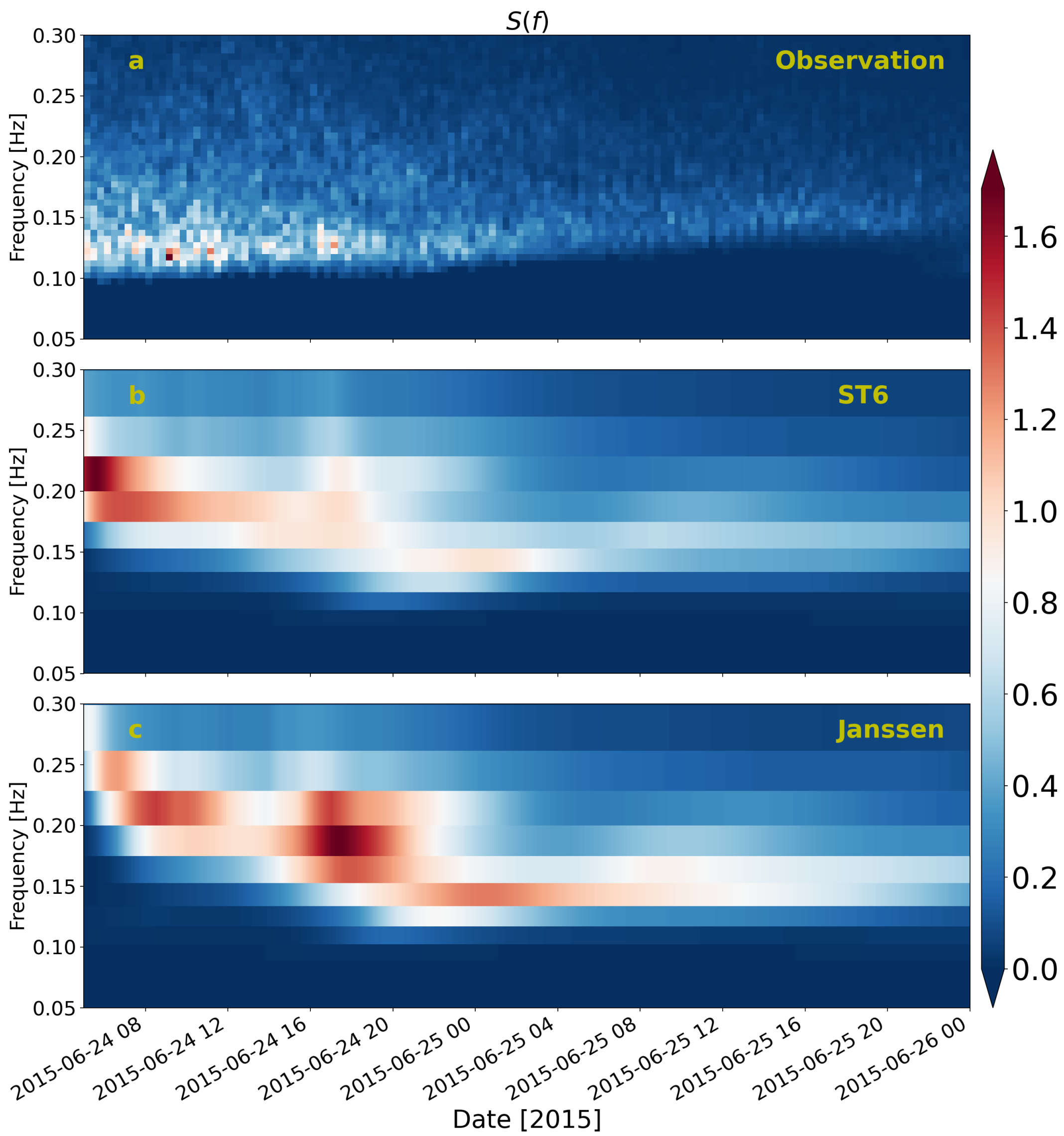

Figure 6.35: Time-frequency spectra of the wind energy $S(f)$ for: (a) observation; (b) the ST6 simulation; and (c) the Janssen run.

more energetic and the differences are further pronounced until 25 June at 00:00 UTC. This might be because the two packages perform similarly for frequencies below the tail frequencies (i.e. frequencies below 0.3 Hz) and behave differently at the high-frequency tail (i.e. frequencies beyond 0.3 Hz).

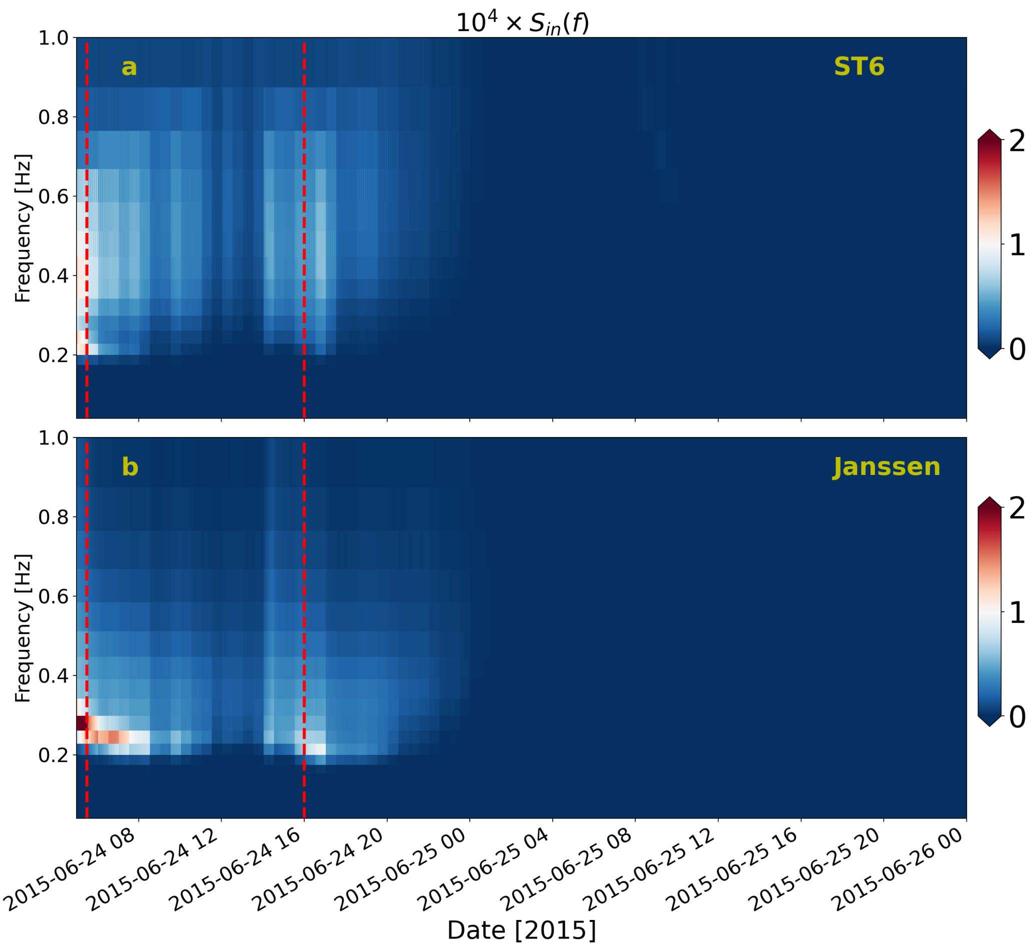

Figure 6.36: Time-frequency spectra of the wind energy input source term $S_{in}(f)$ for: (a) the ST6 simulation; and (b) the Janssen run. The vertical dashed lines denote times that wind input frequency spectra will be used for more detailed analysis in the next figure.

We investigate in Fig. 6.37, the shape variation of the source terms S_{in} and S_{ds} for two selected times at June 24 2015 04:00 UTC and June 24 2015 16:00 UTC (see also Fig. 6.36). Figure 6.37a shows that the wind input source term of ST6 is approximately an order of magnitude larger than the one from the Janssen simulation at the same time. The peaks in ST6 results are more pronounced and the dominant peak in the Janssen source term is shifted towards the higher frequencies. The dissipation source terms are somewhat similar and the ST6 gives lower values for the frequencies between 0.4 Hz and 0.7 Hz. In Fig. 6.37b, the Janssen model of S_{in} gives more energetic variation at lower frequencies than the ST6 wind input source term (that shows a smooth peak at higher frequencies). Dissipation source terms of both formulations have the same magnitude but with a lower peak frequencies for the Janssen results than the ST6 peak frequencies.

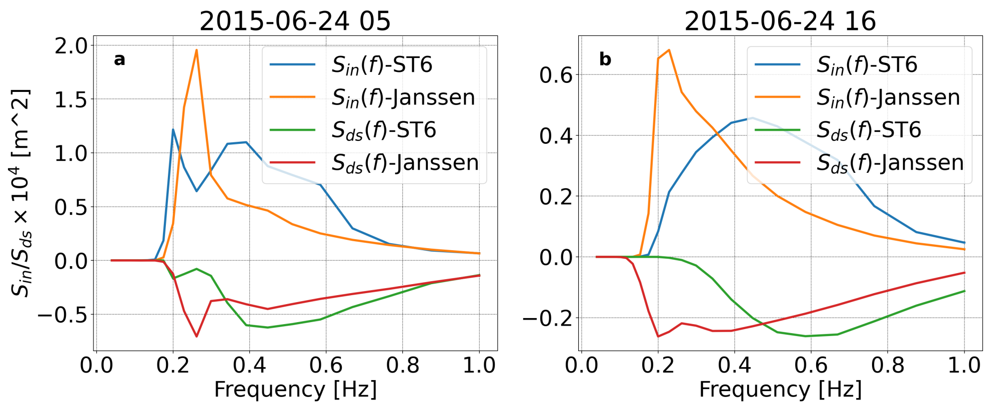

Figure 6.37: Spectral variation of the wind input source terms S_{in} (positive values) and dissipation source terms S_{ds} (negative values) as a function of frequency for two dates marked in the previous figure (vertical red dashed lines): (a) June 24, 2015 at 04:00 UTC (high wind); and (b) June 24, 2015 at 16:00 UTC.

6.4 Discussion

In this section, to consider the effects of wave-wind interactions on wind field and energy simulation, we developed some offline wave coupling system in the WRF model and compare it with online WRF-SWAN models. The offline wave-wind coupling can run stand-alone with the WRF and costs less computational resources compared to online wave-wind coupling models. Therefore, it can be used as a suitable method to consider the interactions between waves and winds. The offline coupled wave system results revealed good performance compared with online coupling system and the observations. The results showed that at high wind speeds (Alignment period), where the wave-wind interaction can increase, offline coupling systems perform well. But simulations didn't show significant differences in low wind speed (Misalignment period).

7 Towards the terra incognita: WRF-LES

7.1 Background

As discussed in previous sections, some small-scale processes cannot be captured using mesoscale models. For this purpose, a LES model can be used to simulate these scales. To close the model chain from meso- to micro-scale, we can use a dedicated LES model–the PALM model–with the forced boundary conditions from the output of the WRF, which will be presented in the next section. However, because the PALM's resolution is much higher than the WRF, in an order of ten meters compared to kilometers, there might be discontinuation of energy cascading from meso- to micro-scale. Also, the output frequency of the WRF cannot be too high because of the storage limitation. Thus, such sudden downscaling and low-frequency boundary forcing may cause a loss of spatial and temporal information.

A seamless approach is using an intermediate online coupling LES model, which fortunately can be done directly using the WRF with appropriate dynamics options, in other words, in WRF-LES model. This section will explore a few case studies using the WRF-LES to assess the ability of the WRF to simulate the turbulent properties of the atmospheric boundary layer.

Traditionally, idealized LES assumes a constant state of the background flow with a double-periodic lateral boundary condition so that the turbulent eddies have enough time to develop to reach their equilibrium state. However, for real-world applications, sometimes the real-data, time-dependent background conditions are critically important, for example, the change of the turbulent property during the passage of a front or an OCC event. Thus a nesting technique can be applied in these situations where the background information is simulated in real-time and passes to the LES domains through their lateral boundaries.

This section will discuss the application of the online nesting techniques where the WRF is run in a RANS mode and LES mode at the same time. In the RANS mode, 3 nested domains are used to downscale the ERA5 reanalysis data to 1 km resolution. In the LES mode, the simulated information continues to be passed down one or two further nesting levels with resolutions of 200 m and 40 m. First, we will examine an LES case using different dynamics options of diffusion mixing evaluation. Then we will discuss the turbulent spin-up issues in nesting of WRF-LES with the cell perturbation technique.

7.2 And OCC case study for Teesside region

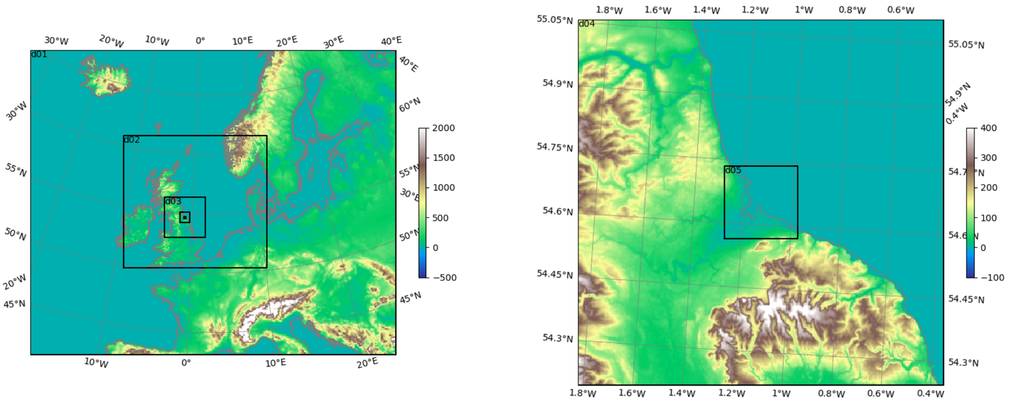

Figure 7.1: WRF-LES domains for the Teesside site. The first 3 domains (D01–D03, left) are used for in RANS mode, the finest 2 domains (D04–D05, right) are used for the LES mode.

First, we performed the experiments in Table 3.5 for the Teesside region during the OCC event explored in section 5.1. Figure 7.1 shows the WRF domains for the Teesside region. The first 3 RANS domains, D01, D02, and D03, are the same as the WRF simulation, with resolutions of 9 km, 3 km, and 1 km respectively. Both LES domains D04 and D05 have 481×481 grid points with resolutions of 200 m and 40 m, thus with domain widths of 96 km and 19.2 km, respectively.

Five experiments were designed (Table 3.5). The WRF_RANS domains are integrated from 00Z 21 Nov 2015 and run for 2 days. However, to save computational time, the LES domain D04 starts from 10Z and D05 starts from 11Z, 22 Nov until 16h00. The data time series at every time step at the Teesside mast locations are extracted for calculating the turbulent intensity. However, we use only 2.5 hours from 13:30 to 16:00 to discard the spin-up time of the WRF-LES simulations.

(a) LES_CTR
(b) LES_NBA
(c) LES_Smag
(c) LES_Smag_NBA
(e) LES_WENO

Figure 7.2: A snapshot of vertical velocity on the model level 20 (about 500m) of the WRF-LES domain D05 (40m) at 13:40 22 Nov 2015.

Figure 7.2 shows a snapshot of the vertical velocity of the experiment after the spin-up time. Except for the WENO experiment, the turbulence evolves fully in the experiments and there is a slight difference when the NBA option is turned on or off. At the current time slice, the turbulence is slightly stronger for the Smagorinsky options. On the other hand, the turbulence does not evolve fully for half of the domain.

Figure 7.3 shows the 50-m turbulent intensity for D03, D04, and D05 and its comparison with the Teeesside's mast observation. It is not surprising that the WRF-RANS (Fig. 7.3a) cannot capture the turbulent intensity compared to the observation. On the other hand, both 200-m and 40-m WRF-LES simulations can capture a turbulence level realistically. The WENO experiment perform the worst, probably due to the slowly evolved turbulence as shown above. Overall, the averaged turbulent intensity of NBA experiments is closer to the observation, and D05's TI is slightly larger than the one from D04 results.

The variance of the turbulence intensity is generally smaller than that of the observation and is not consistent across the two domains. For example, LES-NBA has the closest turbulent intensity variance compared to the observation for D04 but does not per well for D04.

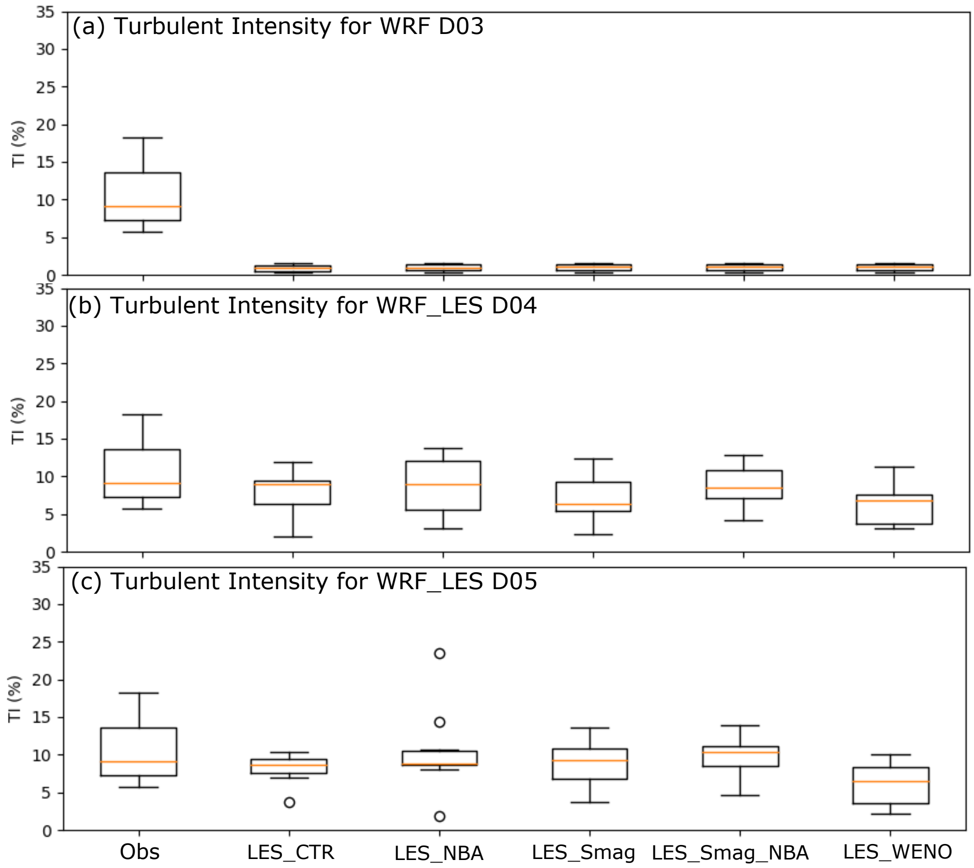

Figure 7.3: Turbulent Intensity for different WRF-LES experiment vs Teesside mast's anemometer.

7.3 Cell perturbation simulation

In section 7.2, the WRF-LES is effective in generating a reasonable level of turbulent intensity, even from a coarse LES resolution of 200 m, for an OCC event. Because of the availability of the high-frequency sonic anemometer data for the FINO1 site, we investigated another OCC event from 09–10 July 2015. The sonic anemometer data is measured at a height of 15 m with a frequency of 25 Hz and will be used in the energy spectral analysis. This OCC event is characterized by a strong wind speed of over 10 m/s, which may cause a problem for the WRF-LES simulation as the turbulent eddies do not have enough time to evolve. For this reason, we choose this event to assess the effectiveness of our cell perturbation implementation (see section 3.6.2).

We choose the experiment LES_NBA (Table 3.5) as the base experiment because of its good ability to reproduce the turbulent intensity for the Teesside region (Fig. 7.3). Because of the computation limitation, we use 4 domains for the experiment: three WRF-RANS domains with resolutions from 9 km down to 1 km, and one WRF-LES domain with a resolution of 200 m. For the cell perturbation, we consider the characteristic velocity of 10 m/s, so the perturbation time scale $T_s = 160$ seconds. Three cell perturbation strategies are designed (Table 7.1): LES_CP1 uses cell perturbation for horizontal grids only (point perturbation for vertical grids); LES_CP2 applies cell perturbation for both vertical and horizontal grids; and LES_CP3 changes the perturbation sign alternately.

The WRF-RANS domains start the simulation from 00Z, 9 Jul 2015, and produce the full 3D output every 1h. On the other hand, the WRF-LES starts later from 12Z and integrates for 12h, and has an output frequency every 10 minutes. The high-frequency time series at every time step is extracted at the FINO1 platform location for the spectral analysis.

Table 7.1: WRF-LES experiment design for FINO1 site from 9–10 Jul 2015

experiment	LES_NBA	LES_CP1	LES_CP2	LES_CP3
Horizontal cell perturbation	No	Yes	Yes	Yes
Vertical cell perturbation	No	No	**Yes**	No
Alternate sign	-	No	No	**Yes**

Figure 7.4 shows the wind speed at 90 m for the four 200-m WRF-LES simulations compared with the WRF-RANS (WRF D03), mast anemometer, and LiDAR data at the FINO1 mast station. After about 1 hour of the spin-up time for the information from the boundary to reach the mast location at the center of D04, the WRF-LES experiments have variations with much higher frequency compared to the 1-km WRF result and mast anemometer, which is 10-min averaged. There is a positive systematic difference of about 5 m/s between the WRF and WRF-LES wind speed compared to the mast data, which is identified as the shadow effect of the mast pole when the wind is from the NW direction (Fig. 4.2). On the other hand, the LiDAR data is close to both WRF and WRF-LES after the spin-up time of each experiment (about 6 h for WRF D03, and 1 h for WRF-LES). In general, the WRF-LES fluctuates around the WRF D03. However, around 21Z, 10 Jul 2015, the WRF-LES has a slight deviation from the WRF and is closer to the LiDAR observation.

In this study period, we have the 25-Hz frequency sonic anemometer at the height of 15

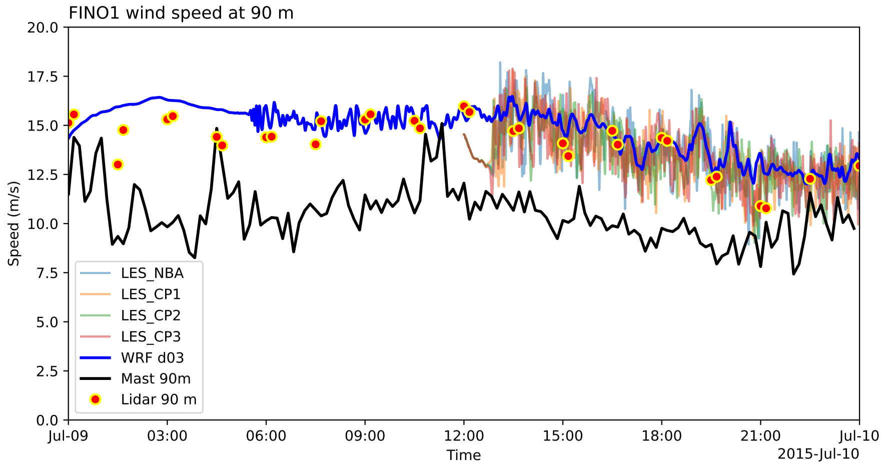

Figure 7.4: FINO1 90-m wind speed of WRF-LES experiments vs 1-km WRF, mast's anemometer and LiDAR observation.

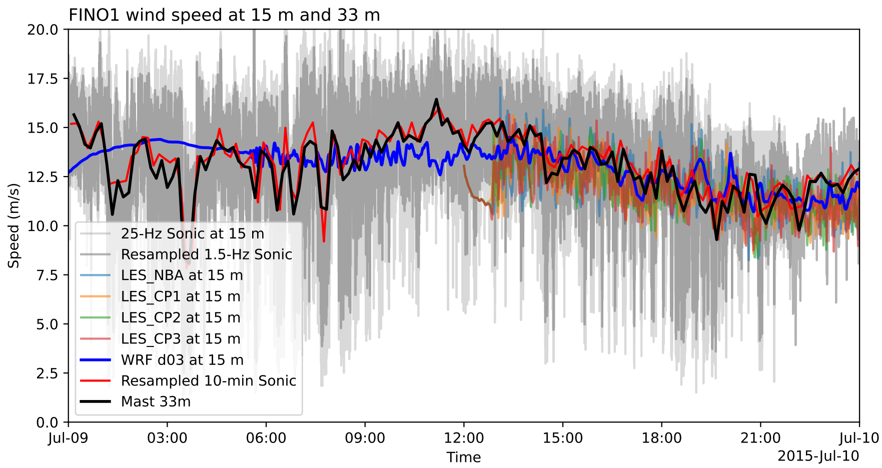

Figure 7.5: FINO1 15-m wind speed of different WRF-LES experiments vs 1-km WRF, Sonic observation and mast's anemometer at 33m.

m, which is shown as the light gray lines in Fig. 7.5. We also show the 10-min wind speed of the lowest cup anemometer at 33 m. The 10-min averaged sonic data fits surprisingly well with the 33-m cup wind speed, which means somehow the 33-m cup anemometer either does not suffer from the shadow effect as the 90-m one, or both the 15-m sonic anemometer and the 33-m cup anemometer are affected by almost the same shadow effect. The previous is likely to be true as the 33-m wind speeds are about 2 m/s stronger than that of the 90-m cup wind speed.

After being re-sampled to a 10-min average, the sonic data fits well with the WRF-RANS and WRF-LES 7.5. For the high-frequency fluctuation, the WRF-LES can capture some fluctuations with an amplitude that is much larger than the WRF-RANS. However, the amplitude is still much smaller than the 25-Hz sonic data. We also re-sample the sonic data to 1.5 Hz, which is the output of the WRF-LES, however, the re-sampled sonic's fluctuation is still much larger. There are a few possible reasons for this difference: a) the WRF-LES resolution is still not fine enough to capture such large-amplitude, high-frequency fluctuation; b) there is a lack of turbulence generation in the WRF-LES compared to the real data.For example, some of the turbulence sources not present in the WRF_LES are the obstacles of wind turbines and the mast station, as well as the roughness from the ocean wave.

The above time series of different WRF-LES experiments look similar. However, the snapshots of 90-m WRF-LES wind speed (Fig. 7.6) tell a different story. In the LES_NBA experiment (Fig. 7.6a), in almost three fourth of the domain—half the domain on each side, the turbulence is not fully developed. The reason for this is that the flow needs a certain amount of time for the turbulence to be evolved. Because the background wind speed is large, the region of under-developed turbulence expands.

In the cell perturbed experiments (Fig. 7.6b–d), the turbulence evolves much earlier. However, for the normal implementation of a single perturbation field (LES-CP1 and LES-CP2), there are line-like features extending from the boundaries. The effect of vertical cell perturbation is not clear as the turbulence features look similar for LES-CP1 and LES-CP2. When we alternate the sign of the perturbation field in LES-CP3, the turbulence feature looks more natural for most of the domain (Fig. 7.6d).

Figure 7.7 shows the power spectrum of the 15-m wind speed of the sonic anemometer and WRF/WRF-LES simulations. The 1-km WRF spectrum quickly drops for the sub-hour fluctuations. On the other hand, the WRF-LES simulations can capture a realistic spectrum until few-minute fluctuations before sharply dropping. Despite the boundary problems (Fig. 7.6), all WRF-LES experiments have a similar spectrum at the FINO1 location near the center of the domain where the turbulence has enough time and distance to evolve. However, in other situations, such as a smaller domain or a slower turbulence evolution, these boundary conditions may take a more important role.

7.4 Discussion

We have demonstrated that the online nesting WRF-LES has the capability to capture the turbulent intensity close to the observation to some extent. In some situations, WRF-LES simulation may lack turbulence near the inflow boundaries. This issue can be alleviated by using a simple cell perturbation on the potential temperature around the boundaries and an alternate change of sign can improve the representation of the turbulence.

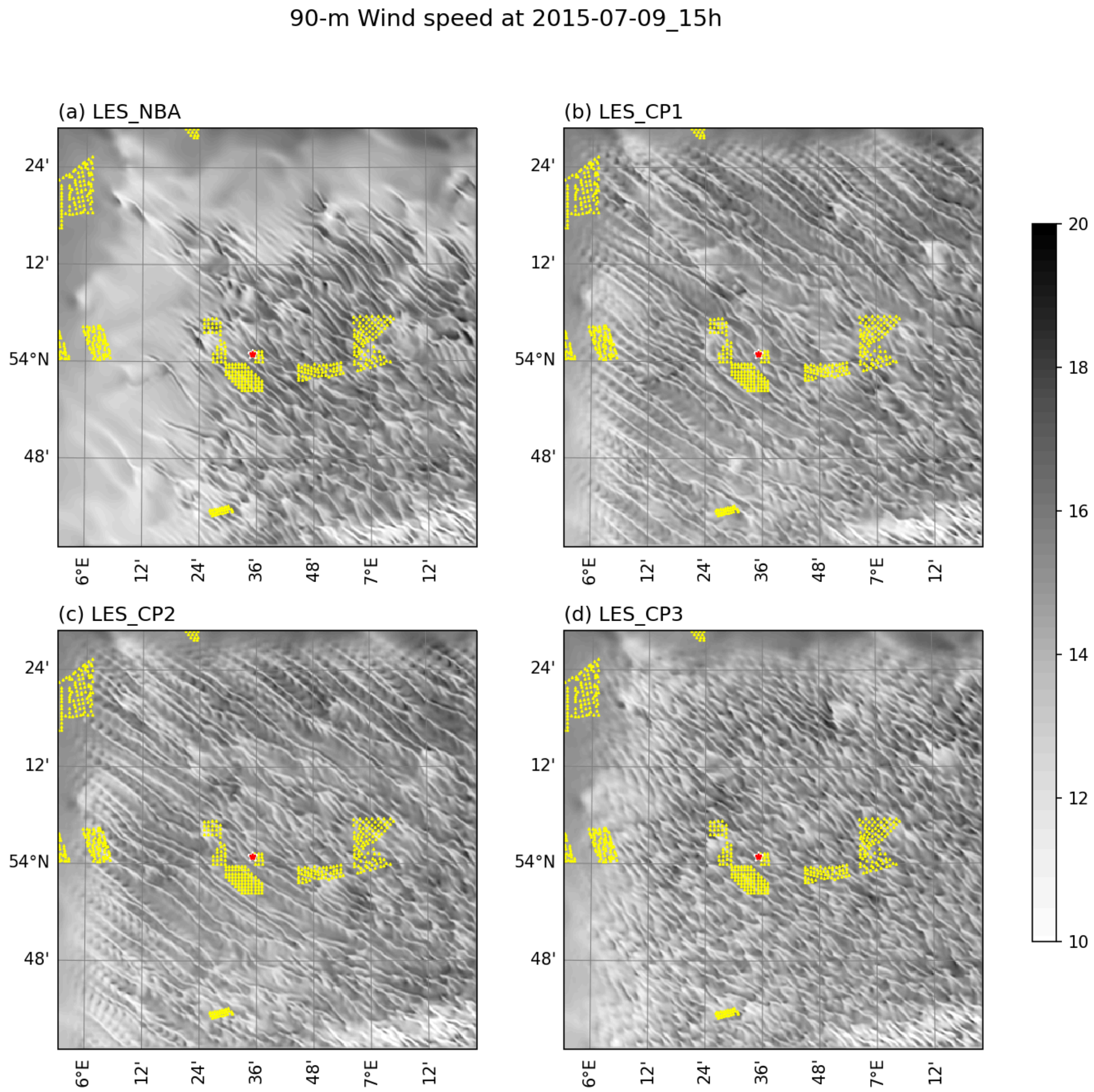

Figure 7.6: Snapshots of 90-m WRF-LES wind speed at 15Z, 9 Jul 2015. The yellow symbols show the locations of the surrounding wind turbines and the red star shows the location of the FINO1 platform.

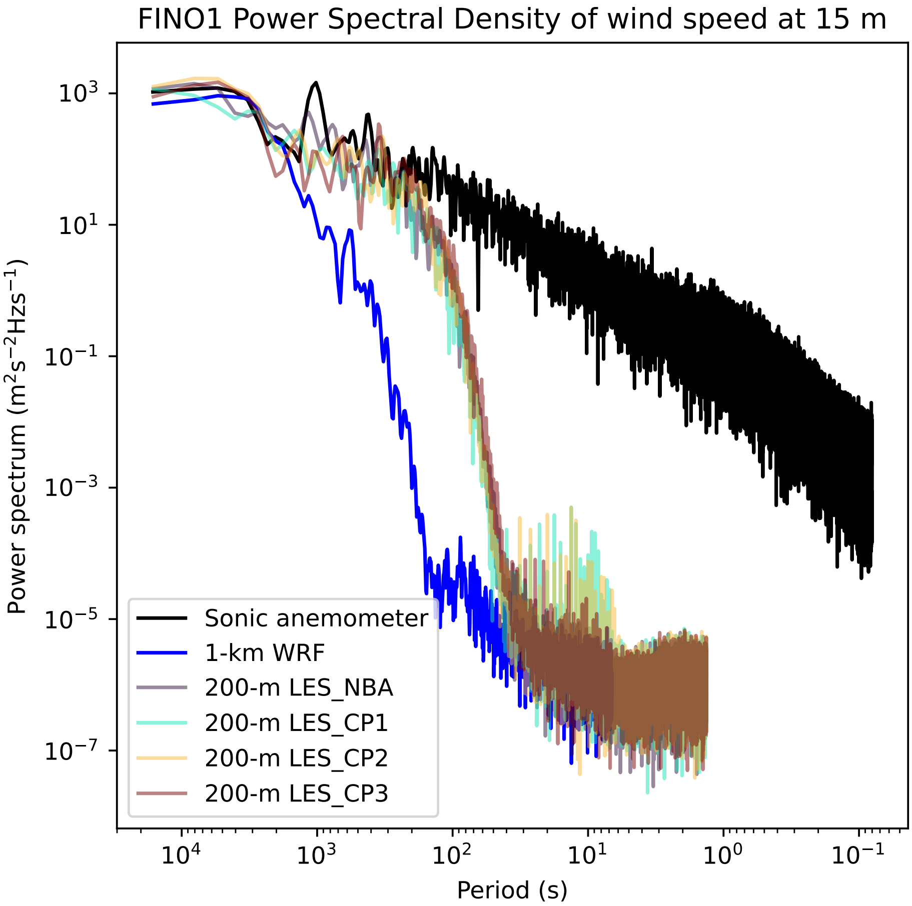

Figure 7.7: Power spectrum of wind speed at the FINO1's cup anemometer vs 1-km WRF and 200-m WRF-LES experiments vs 1-km WRF.

The coarse 200-m WRF-LES can also capture the spectra of the wind speed fluctuations near the surface with periods greater than a few minutes, while the 1-km WRF cannot. The amplitude of the 200-m WRF-LES can be also significantly smaller than the observation. A finer grid with wave-wind and turbine-wind interaction is recommended.

8 Offline meso-to-microscale modelling: WRF-PALM

8.1 Background and experiment design

As shown in the previous section, the WRF-LES is a powerful tool to seamlessly downscale the wind field from the mesoscale to the microscale with a horizontal resolution of a few dozen meters. However, because of the complexity of the WRF model, which is originally designed for the mesoscale purpose, a higher resolution of a few meters is not practical because of the computational cost. The official WRF distribution also does not include the wake effect from individual wind turbines (the wind farm parameterization can take only into account the collective effect), which is very essential for wind energy applications. For this reason, as a second model of the microscale component, we use the PALM model (see Section 3.7), a dedicated LES model which can simulate the large eddy turbulence more effectively. PALM also includes a wind turbine model that parameterizes the effect of individual wind turbines. In this section, we used the offline nesting technique with the forced boundary condition taken from a WRF simulation's output that is run separately.

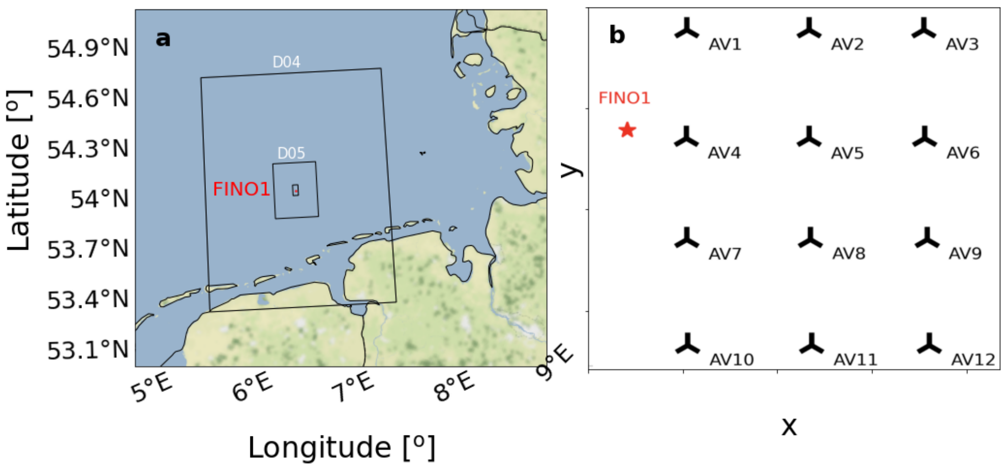

Figure 8.1: (a) The WRF inner domain (1 km) used in the WRF-PALM offline nesting over the North Sea covering the FINO1 offshore met-mast (red marker). The PALM model contains three subdomains (that we use only two in this report) with horizontal resolutions of 375 m (outer, D04) and 10 m (i.e. D05) respectively; and (b) the geographical locations of FINO1 and 12 turbines of the nearby Alpha Ventus wind park.

We use two nested domains for the PALM model (Fig. 8.1a). The parent domain of PALM simulations—which gets the information from the 1-km WRF domain from the lateral boundaries—covers the study site with its sizes of approximately 193 km (east–west)× 193 km (south–north) and the grid sizes $\Delta x = \Delta y = 375$ m and $\Delta z = 10$ m. The inner domain has the grid sizes of $\Delta x = \Delta y = \Delta z = 10$ m and contains 12 wind turbines of the Alpha Ventus wind farm (Fig. 8.1b).

8.2 Result

Figure 8.2a shows the observed 10-min averaged wind speed at 33-m height (from the FINO1-mounted cup anemometer) and the significant wave height, H_s, (measured at the surface buoy) between November 18 and December 1 2015 to highlight a range of wind speed variability attributed to several OCC events. The very close correlation of the winds and wave heights suggests a somewhat fully developed sea surface condition during the study duration. The first OCC event (determined by the temperature difference between the sea surface and the air temperature at 2 m height) is between 02–03Z, 22 Nov. 2015. Wave information is important when we are interested in investigating how wind turbines respond to the passage of the OCCs. It is obvious that the wind and waves are largely aligned (i.e. Fig. 8.2b). The second strong OCC event occurs between 20151123 06Z–20151124 00Z with more clear alignment between the wind and waves.

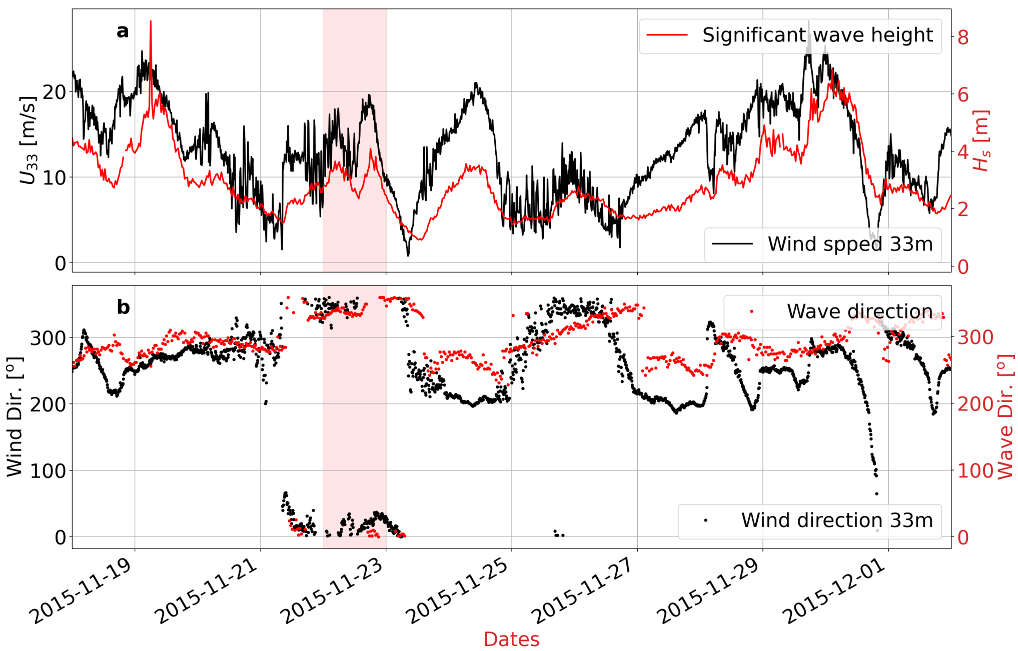

Figure 8.2: (a) Time series of wind speed measured at 33-m height from FINO1 for 12 days during November 2015 (black line) and significant wave height H_s (red line) measured at the surface buoy in the close vicinity of FINO1; and (b) times series comparisons of wind and wave directions at 33 m (black line) and the surface buoy (red line), respectively.

While more in-depth comparison will be given in the respected scientific paper, we briefly compare the wind speed and direction time series during the study period (i.e. during 22 November 2015, red-coloured areas in Fig. 8.2) using the results of models as well as observations. In Fig. 8.3, the time series of the PALM data have a temporal resolution of 2 minutes while the WRF result and observations are both in a temporal interval of 10 minutes. The closest PALM height of logged data to the height of operating wind turbines in the Alpha Ventus is 100 m and the highest wind measurements at FINO1 met-mast is 90 m. WRF winds are also at 90 m for the sake of comparing with the wind measurements (there is no LiDAR data available for this period). The time series of the wind speed and direction shows good agreement against the observational data in Fig. 8.3a and b (with a qualitatively better agreement between the PALM-calculated wind direction and the measured wind direction, i.e. Fig. 8.3b). The discrepancies between WRF and PALM results increase between 06:00 UTC and 13:00 UTC on 22 November 2015.

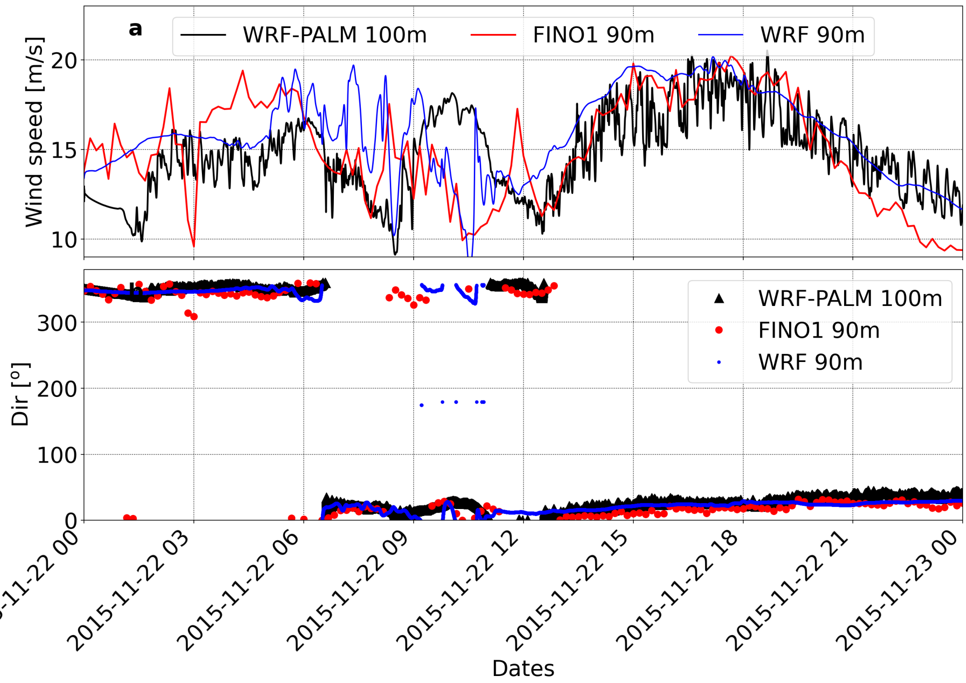

Figure 8.3: (a) Time series of wind speeds at the geographical location of FINO1 from WRF (blue line), measurement from cup anemometer at 90 m (red line), and from the WRF-PALM at 100 m (the closest recorded data from WRF-PALM to the hub-height is at 100 m and the maximum height of the wind sensor on FINO1 is 90 m in this figure); and (b) the same plot as (a) but for the time series of wind direction during 22 November 2015.

To further verify quantitatively how the offline nesting can accurately predict the flow field variability, the probability density prediction results of the wind speed and wind direction at the geographical location of FINO1 are shown in Fig. 8.4. Our analyses are based on the Kernel Density Estimation (KDE). The density of the predicted value of the WRF-PALM wind information against the respective met-mast observations, in the child domain D05, is more scattered almost for all winds with a correlation value of 0.51 as shown in Fig. 8.4a. The KDE of WRF results at the FINO1 location indicates better agreement for the wind speed (with a correlation value of 0.77). The KDE of the WRF-PALM wind direction shows, however, a better agreement with observational data (with a correlation of 0.75 compared with 0.63 in Fig. 8.4d). The marginal distributions in this figure further demonstrate that the wind speeds have widely varying distribution modes in Fig. 8.4a, and the KDE method in Fig. 8.4b agrees well with the probability distribution characteristics of the wind speed.

Based on comparing the SST and air temperature at 2 m, we can label the study period

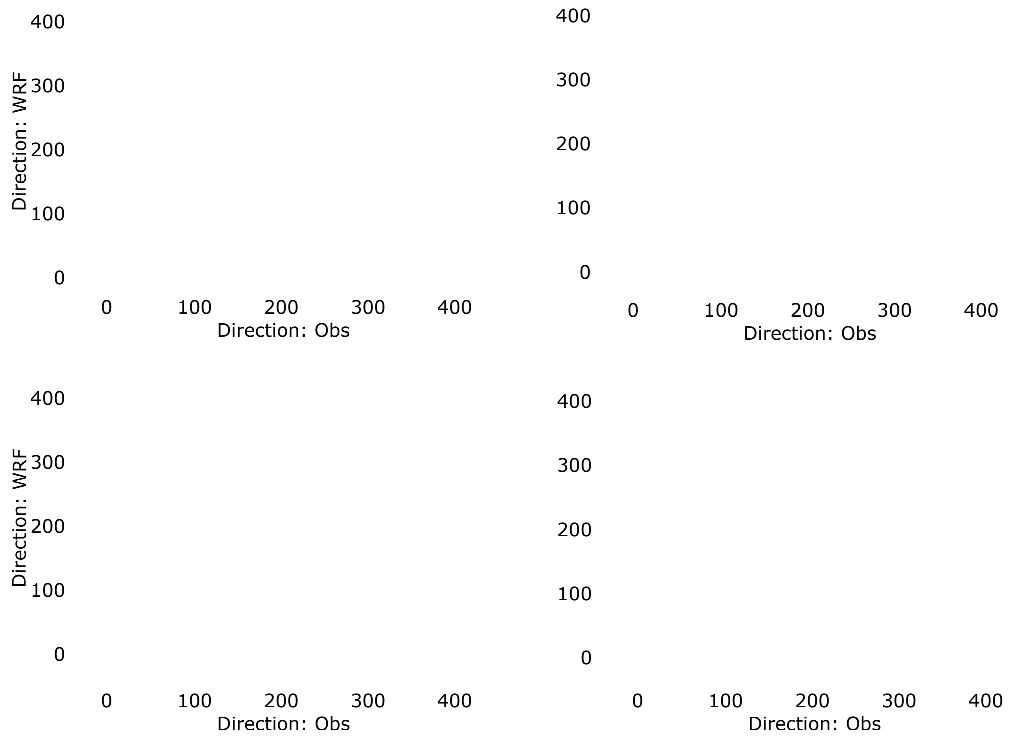

Figure 8.4: The Joint Probability Density (JPDF) of: (a) the PALM wind speed at 100 m height against the observational wind speed at 90 m height; (b) the WRF wind speed at 90 m height against the observational wind speed at 90 m height; (c) the PALM wind direction at 100 m height against the observational wind direction at 90 m height; and (d) the WRF wind direction at 100 m height against the observational wind direction at 90 m height.

as the period of OCC events of varying strengths. If we assume the passage of the strongest transient event, we can classify the variabilities of the wind speed into: (1) before the first frontal passage (starting from 00:00 UTC on November 22 for 20min); and (2) the onset of the first OCC event (starting from 01:40 UTC November 22 for 20min). We show in Fig. 8.5 how the mesoscale offline nesting system predicts the variability of the wind speed at height of 87.5 m (its magnitude and direction), and the spatiotemporal evolution of turbines' wakes before and during the passage of the main OCC event. Before the frontal passage, the wind is almost northerly (i.e. Figs. 8.5a and b) which then rotating gradually to the northwest (i.e. Fig. 8.5d) as the front enters into the farm region. It is observed that the yaw control of turbines leads to wake meandering (we do not investigate how well the modeled yawing results match with the observed SCADA data in this study).

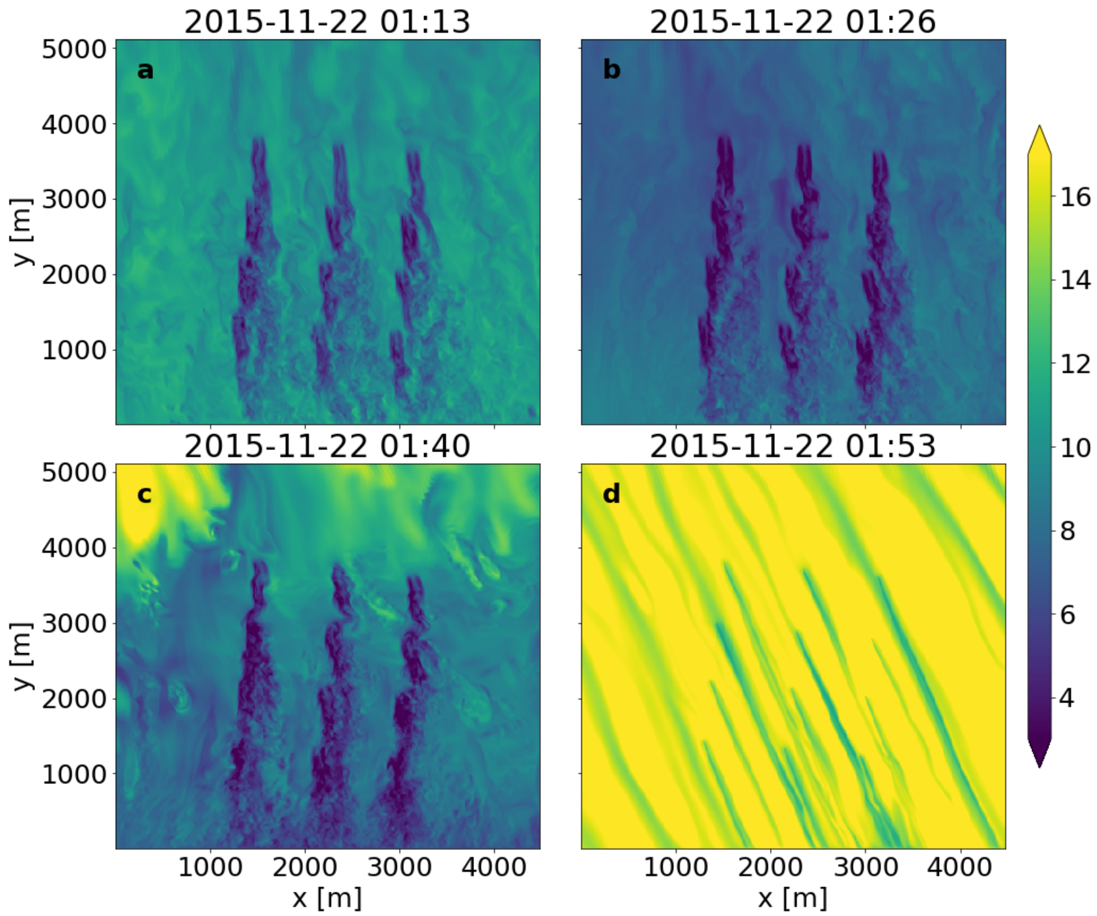

Figure 8.5: Wind speed comparison of PALM model results at domain D05 at the times: (a) before the main frontal passage; (b) close to the main OCC event but still before its passage; (c) when OCC is entering into the study region; and (d) during the OCC event. Within the PALM inner domain D05, we place 12 wind turbines (i.e. 5MW NREL turbines) at geographical locations of the Alpha Ventus turbines.

We have also recorded high-frequency outputs (i.e. sampling frequency of 25 Hz) at spatially separated points covering the rotor area of a turbine in the first row of the Alpha Ventus farm. This information can be used to study the non-Gaussian turbulence and generation of the Gaussian and constraint turbulent winds using tools like NREL TurbSim (Jonkman and Kilcher, 2012). Figure 8.6 shows the power spectra of the time series of three velocity components at two different heights (27 m in the left panels and 97 m in the right panels) respectively to examine how energy-containing and inertial subranges are affected as a result of the frontal passage. The (slight) variability in the wind energy (for the OCC cases) is observed across almost all frequencies, particularly close to the sea surface, and we will conduct more in-depth analyses in the corresponding publication.

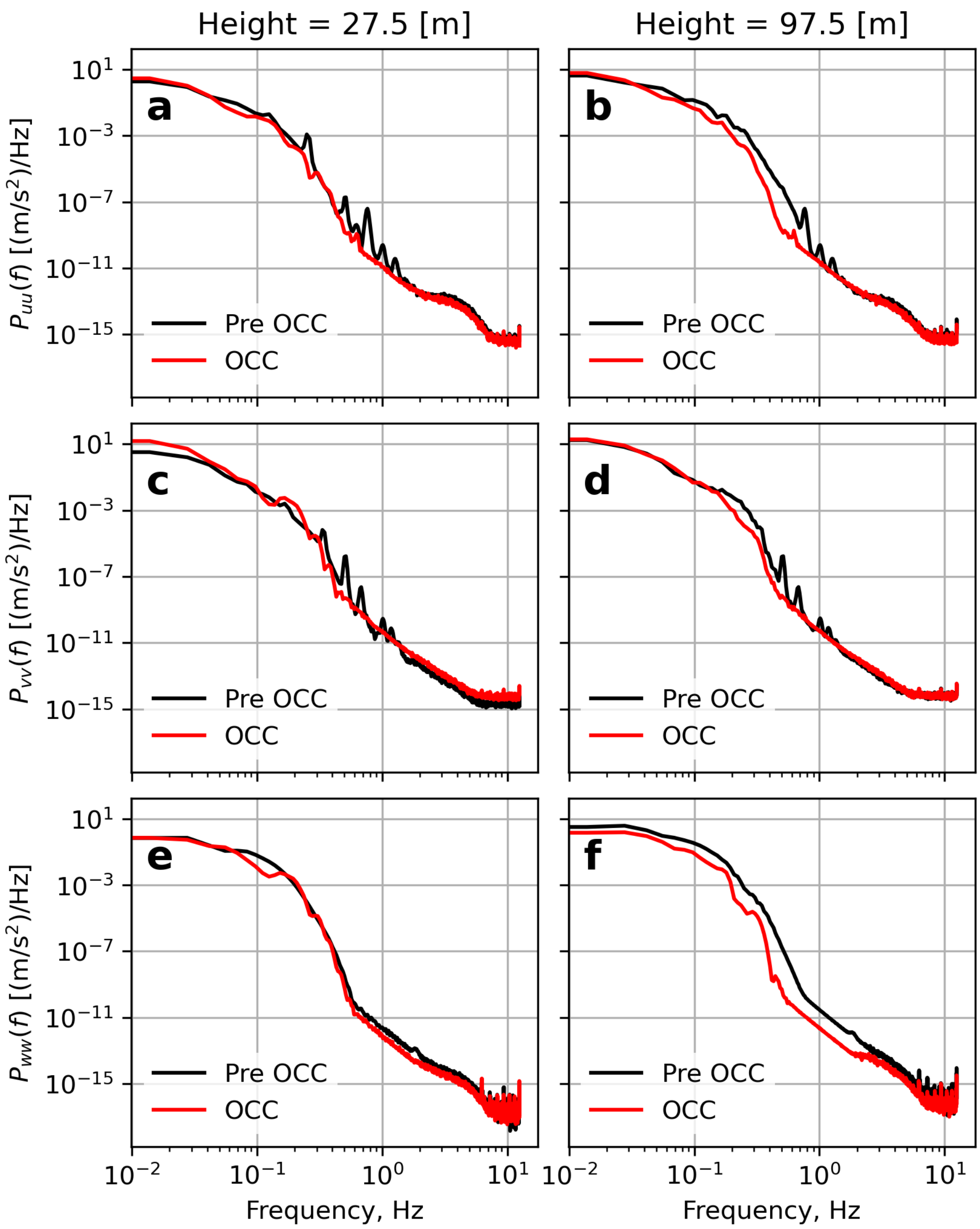

Figure 8.6: Comparisons of wind power spectra of three wind velocity components for the pre-OCC and the OCC at FINO1 location at heights of 27m (a,c,e) and 97m (b,d,f) above the surface.

Using the time series of PALM at the constraint points as input, we can generate stochastic winds by TurbSim on a 16×16 square grid with approximately 13 m width. The model uses a high-frequency time series of wind, wave information, and the wind mean profile. In Fig. 8.7, we generate two sets of wind fields before OCC (i.e. the PREOCC) and during OCC (i.e. OCC) generated by the TurbSim simulator. We assume the same decay parameters for both horizontal and vertical separation distances in the Davenport's TurbSim model.

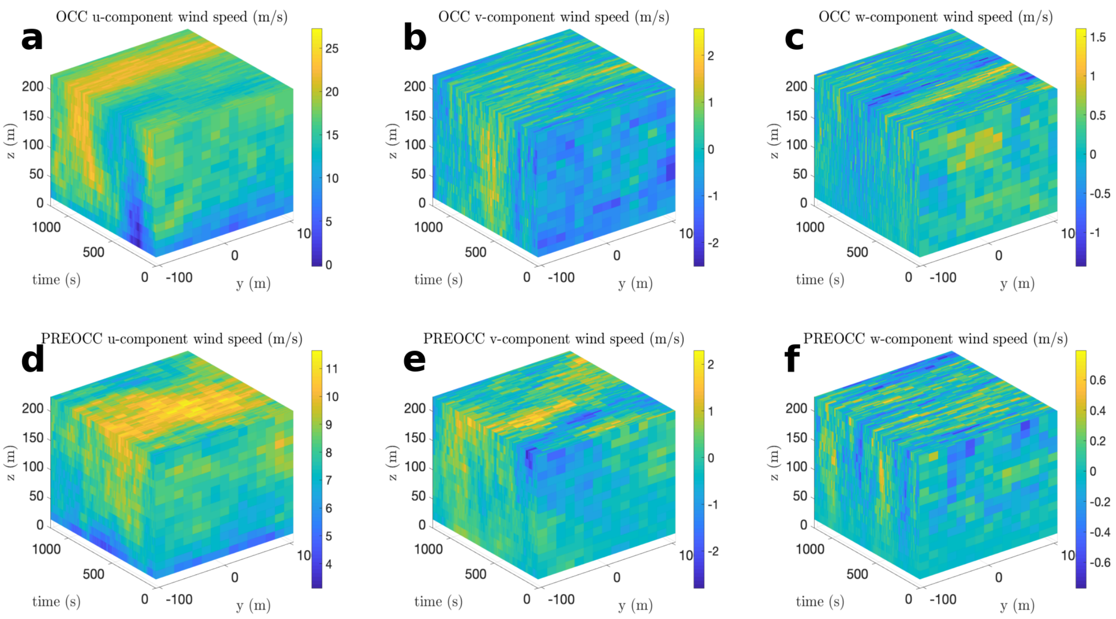

Figure 8.7: Three-dimensional turbulent wind fields generated by the TurbSim constrained by 30 vertical points at FINO1 during: (a,b,c) OCC event; and (d,e,f) PREOCC event.

We show tentatively in Fig. 8.8 the structural variability for a few quantities using the wind inflows for PREOCC and OCC cases. We use NREL FAST model (Jonkman et al., 2009) with a total temporal length of 600 s and a time step of 0.05 s. The first 200 s of simulations are discarded (due to the model spin-up time). We demonstrate the response spectra of "OopDefl1" representing the instantaneous out-of-plane tip deflections of blade 1 relative to the undeflected pitch axis; "BldPitch1" indicating the pitch angle of the first blade; and the "RotSpeed" representing the rotor speed. During the transient event, the variation of the wind inflows relative to the rotor induces oscillations in the rotor speed. The control system adjusts then the fluctuating power through the control of blade pitch angle (i.e. Fig. 8.8b red line). Spectra are somewhat different at low frequencies. The maximum OopDefl1 (of approximately 7 m) occurs when the wind speed declines during the zero pitch angle condition.

8.3 Discussion

We generated mesoscale forcing for the PALM model from WRF hourly output, and tentatively validated the model performance by a case study in the area of Alpha Ventus offshore wind park and FINO1 met-mast. Specifically, we focused on the real OCC weather event. Since the offline WRF-PALM nesting uses the non-cyclic boundary conditions, the inflow

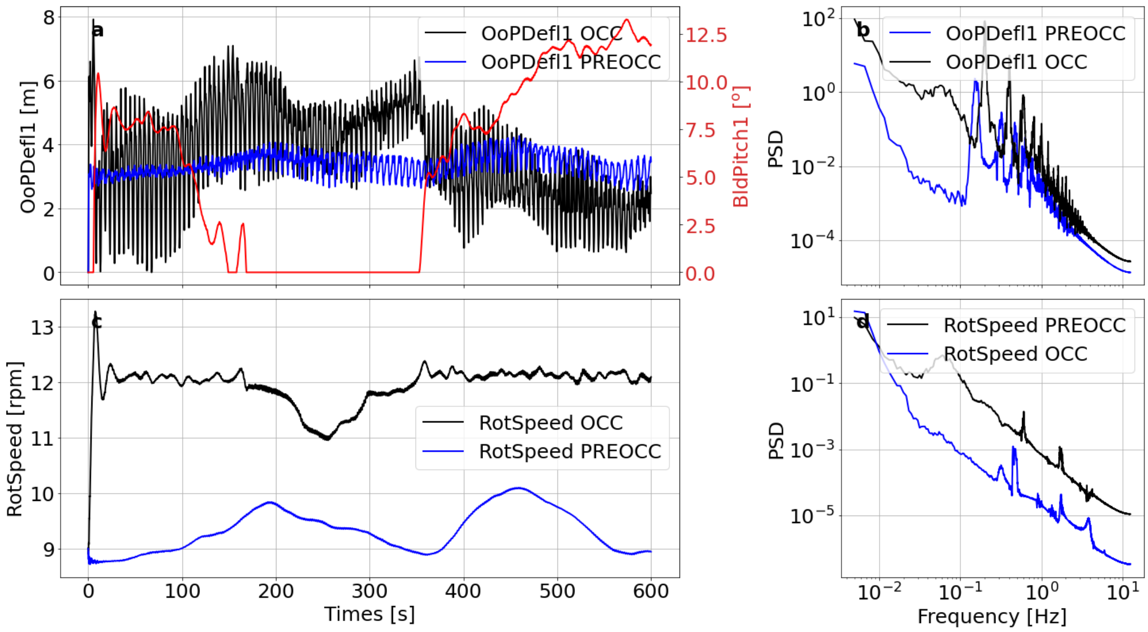

Figure 8.8: (a,c) Time series of turbine response from FASTv8 model; and (b,d) Power Density Spectra (PSDs) of the out-of-plane tip deflections of blade 1 and the rotor speeds before (PRECOCC) and during OCC events.

turbulence has been generated using a built-in Synthetic Turbulence Generator (STG) tool (we can alternatively accelerate the generation of turbulence, if we consider a large parent domain for the PALM to allow development of turbulence both in time and space). The interval for the STG adjustment set to 30 s, and we called the module every second. Furthermore, we set Rayleigh damping close to the top boundary to avoid/reduce propagation of gravity waves into the study domain.

The modelling framework was stable and able to properly predict the flow fields (with a satisfying agreement with respect to observations of wind speed and wind direction). We further applied the wind turbine parameterization in the WRF-PALM to capture the spatial-temporal variation of the wake produced by the wind turbines in the Alpha Ventus wind park, especially during the OCC transition condition. We also generated high frequency outputs of PALM model during OCC event and used NREL TurbSim software to generate turbulence box to be used in the NREL FASTv8. Tentative results, for instance, indicated that the turbulent fluxes during OCC event induced oscillations in the rotor speed.

9 Conclusions

In this report, we presented a multiscale modeling framework to simulate flow fields for offshore wind energy applications under different atmospheric stability conditions. The modelling systems had two model components: the mesoscale component downscales the flow field from the global reanalysis data, and the microscale component further downscales processes from the mesoscale component. The mesoscale component, with the core being the WRF model, can be coupled with the ocean wave model in an online or offline mode. The microscale component consists of an online nesting model, WRF-LES, and a standalone offline nesting model, PALM. Both used the WRF output as the forced lateral boundary conditions.

For the mesoscale component, we conducted different experiment to examine the sensitivity of the WRF to the simulation range and physics parameterization choices during different events, specifically stable conditions during low-level jet events and an unstable ones during the passage of convective cells. The verification against various observation sources (including cup anemometers, LiDAR, SCADA) shows that our model design can capture the key mesoscale processes. An optimal physics configuration is derived through one of our sensitivity experiment.

We developed and applied two-way (online) coupling and one-way (offline) coupling of ocean surface gravity waves with the multiscale modelling system. Comparing offline and online wave coupled systems showed that the offline coupled system could produce better results by considering the best physical configuration, especially during high wind speeds.

In order to reduce the site-specific uncertainty in wind predictions, we assimilated WRF with the available LiDAR measurements through the observation nudging (during an LLJ event). The results of the unnudged reference simulation and the nudged experiment were compared with the LiDAR measurements in terms of spatiotemporal variations in the wind speed and wind direction, as well as the vertical distribution of wind profiles at the geographical location of FINO1. We further studied the spatial effects of observation on the model simulation results. While the observation nudging could affect strongly the wind speed and directions at mid and high altitudes, its effects are marginal near the surface layers (this might be explained by either data availability as well as the reduced performance of the model at near-surface levels). The approach can then be helpful in the reduction of site-specific model uncertainty and for the resource assessment at certain heights relevant to offshore wind energy applications. We investigated the impact of observation nudging on the wind profiles during stable atmospheric stability conditions and the impacts might be different in the case of unstable atmospheric stability conditions.

The microscale component is used to resolve the small-scale processes that cannot be simulated using the mesoscale component, for example, the turbulent intensity and the wake effect from wind turbines. The microscale component consists of WRF-LES using the online nesting technique, and PALM with an offline nesting technique. Both LES strategies are practically oriented with the realistic output from the WRF as the lateral boundary forcing.

Although belonging to the same microscale component, WRF-LES and PALM have different purposes in our model framework. The WRF-LES model aims at a seamlessly downscaling from the mesoscale frameworks to a resolution of a few dozen meters, however, the wind turbine effects are not included. We examined several dynamics options for the WRF-LES and determined the suitable one for the simulation of turbulent intensity. To solve the problem of under-developed turbulence, which is common in the LES nesting strategy, we developed a fast and efficient cell perturbation method. The PALM model can simulate the turbulence eddies even with a higher resolution of a few meters and with turbine effects, however with a shorter duration. The PALM with realistic offline nesting can nicely resolve the wake effects, not only from a single wind turbine, but their interaction between multiple wind turbines in the FINO1 wind park.

In summary, we have developed a close model chain to seamlessly downscale the global-scale atmospheric conditions to the wind turbine-scale processes. Through the conducted experiments, we gained a better understanding of key processes, OCC and LLJ, as well as improved the model's ability to simulate them. The gained knowledge provides guidance for further study of wind energy applications in simulating wind conditions and in offshore wind turbine design.

Acknowledgement

The work is a part of the HIghly advanced Probabilistic design and Enhanced Reliability methods for the high-value, cost-efficient offshore WIND (HIPERWIND) project, which has received funding from the European Union's Horizon 2020 Research and Innovation Programme under Grant Agreement No. 101006689. The simulations were performed on resources provided by UNINETT Sigma2 - the National Infrastructure for High Performance Computing and Data Storage in Norway. Some data used in this study were gathered as part of the OBLEX-F1 field campaign that has been performed under the Norwegian Centre for Offshore Wind Energy (NORCOWE) funded by the Research Council of Norway (RCN 193821), the Offshore Boundary Layer Observatory (OBLO) project (project no. RCN 227777) and the Norwegian e-infrastructure NorStore (project no. RCN: NS9060K). OBLEX-F1 was coordinated in collaboration between the University of Bergen (Geophysical Institute) and NORCE Norwegian Research Centre (project executing organization). The Federal Maritime and Hydrographic Agency of Germany (BSH) is acknowledged for providing the FINO1 reference data through the FINO database at http://fino.bsh.de/. The FINO project (research platforms in the North Sea and Baltic Sea) is funded by the BMU, the German Federal Ministry for the Environment, Nature Conservation, Building and Nuclear Safety in collaboration with Project Management Jülich GmbH (project no. 0325321). The FINO1 meteorological reference data were provided by Deutsches Windenergi Institute (DEWI). We also thank the FINO1 platform operator Forschungs- und Entwicklungszentrum Fachhochschule Kiel GmbH (FuE Kiel GmbH) for their support (project no. 0329905E).

References

E. M. Agee, T. Chen, and K. Dowell. A review of mesoscale cellular convection. *Bull. Am. Meteorol. Soc.*, 54(10):1004–1012, 1973.

C. Archer, H. Simão, W. Kempton, W. B. Powell, and M. Dvorak. The challenge of integrating offshore wind power in the us electric grid. part i: Wind forecast error. *Renew. Energ.*, 103:346–360, 2017.

C. Archer, S. Wu, Y. Ma, and P. A. Jiménez. Two corrections for turbulent kinetic energy generated by wind farms in the wrf model. *Mon Weather Rev., https://doi.org/10.1175/MWR-D-20-0097*, 2020.

R. S. Arthur, J. D. Mirocha, N. Marjanovic, B. D. Hirth, J. L. Schroeder, S. Wharton, and F. K. Chow. Multi-scale simulation of wind farm performance during a frontal passage. *Atmosphere, https://doi.org/10.3390/atmos11030245*, 11:563–580, 2020.

B. Atkinson and J. Wu Zhang. Mesoscale shallow convection in the atmosphere. *Rev. Geophys.*, 34(4):403–431, 1996.

E. Avolio, S. Federico, M. Miglietta, T. L. Feudo, C. Calidonna, and A. M. Sempreviva. Sensitivity analysis of wrf model pbl schemes in simulating boundary-layer variables in southern italy: An experimental campaign. *Atmos. Res.*, 192:58–71, 2017.

E. E. Bachynski, M. I. Kvittem, C. Luan, and T. Moan. Wind-wave misalignment effects on floating wind turbines: motions and tower load effects. *Journal of Offshore Mechanics and Arctic Engineering*, 136(4), 2014.

P. Bai, Z. Ling, C. Liu, J. Wu, and L. Xie. Effects of tidal currents on winter wind waves in the qiongzhou strait: a numerical study. *Acta Oceanol. Sin.*, 39(11):33–43, 2020.

M. Bakhoday-Paskyabi and M. Flügge. Predictive capability of wrf cycling 3dvar: Lidar assimilation at fino1. *J. of Physics: Conference Series*, pages 1742–6596, 2021.

M. Bakhoday-Paskyabi, I. Fer, and A. D. Jenkins. Surface gravity wave effects on the upper ocean boundary layer: Modification of a one-dimensional vertical mixing model. *Cont. Shelf Res.*, 38:63–78, 2012.

R. F. Banks, J. Tiana-Alsina, J. M. Baldasano, F. Rocadenbosch, A. Papayannis, S. Solomos, and C. G. Tzanis. Sensitivity of boundary-layer variables to pbl schemes in the wrf model based on surface meteorological observations, lidar, and radiosondes during the hygra-cd campaign. *Atmos. Res.*, 176:185–201, 2016.

D. Barker, W. Huang, Y.-R. Guo, and A. Bourgeois. A three-dimensional variational (3dvar) data assimilation system for use with mm5. *NCAR Tech Note*, 68, 2003.

A. Benetazzo, S. Carniel, M. Sclavo, and A. Bergamasco. Wave–current interaction: effect on the wave field in a semi-enclosed basin. *Ocean Modelling*, 70:152–165, 2013.

A. K. Blackadar. Boundary layer wind maxima and their significance for the growth of nocturnal inversions. *Bull. Am. Meteorol. Soc.*, 38(5):283–290, 1957.

P. Bolgiani, C. Calvo-Sancho, J. Díaz-Fernández, L. Quitián-Hernández, M. Sastre, D. Santos-Muñoz, J. Farrán, J. J. González-Alemán, F. Valero, and M. L. Martín. Wind kinetic energy climatology and effective resolution for the era5 reanalysis. *Clim. Dyn.*, pages 1–16, 2022.

S. D. Burk and W. T. Thompson. The summertime low-level jet and marine boundary layer structure along the california coast. *Mon. Weather Rev.*, 124(4):668–686, 1996.

C. Calvino, T. Dabrowski, and F. Dias. A study of the wave effects on the current circulation in galway bay, using the numerical model coawst. *arXiv preprint arXiv:2109.12936*, 2021.

D. Carvalho, A. Rocha, M. Gómez-Gesteira, and C. S. Santos. Sensitivity of the wrf model wind simulation and wind energy production estimates to planetary boundary layer parameterizations for onshore and offshore areas in the iberian peninsula. *Appl. Energy*, 135:234–246, 2014.

H. Charnock. Wind stress on a water surface. *Q. J. R. Meteorol. Soc.*, 81:639–640, 1955. ISSN 0035-9009.

A. De Lange, M. Naidoo, R. M. Garland, and L. L. Dyson. Sensitivity of meteorological variables on planetary boundary layer parameterization schemes in the wrf-arw model. *Atmos. Res.*, 247:105214, 2021.

M. A. Donelan. The dependence of the aerodynamic drag coefficient on wave parameters. In *Proc. First Int. Conf. on Meteorol. and Air-Sea Interaction of the Coastal Zone*, pages 381–387. Amer. Meteor. Soc., 1982.

M. A. Donelan. Air-sea interaction. *The sea*, 9:239–292, 1990.

C. J. Donlon, M. Martin, J. Stark, J. Roberts-Jones, E. Fiedler, and W. Wimmer. The operational sea surface temperature and sea ice analysis (ostia) system. *Remote Sens. Environ.*, 116:140–158, 2012.

C. Draxl, A. N. Hahmann, A. Peña, and G. Giebel. Evaluating winds and vertical wind shear from weather research and forecasting model forecasts using seven planetary boundary layer schemes. *Wind Energy*, 17(1):39–55, 2014.

W. M. Drennan, K. K. Kahma, and M. A. Donelan. On momentum flux and velocity spectra over waves. *Bound.-Layer Meteorol.*, 92:489–515, 1999. ISSN 1573-1472.

W. M. Drennan, H. C. Graber, D. Hauser, and C. Quentin. On the wave age dependence of wind stress over pure wind seas. *J. Geophys. Res.: Oceans*, 108(C3), 2003.

J. Du, X. Larsén, M. Badger, and R. Bolaños. Impact of the interfaces for wind and wave modeling-interpretation using coawst, sar and point measurements. page 7358, 2017.

Y. Fan, I. Ginis, T. Hara, C. W. Wright, and E. J. Walsh. Numerical simulations and observations of surface wave fields under an extreme tropical cyclone. *J. Phys. Oceanogr.*, 39:2097–2116, 2009.

G. Fischer. Installation and operation of the research platform fino 1 in the north sea. In *Offshore Wind Energy*, pages 237–253. Springer, 2006.

A. C. Fitch. Notes on using the mesoscale wind farm parameterization of fitch et al.(2012). *Wind Energy*, 19:1757–1758, 2016.

T. Göçmen, X. G. Larsén, and M. Imberger. The effects of Open Cellular Convection on Wind Farm Operation and Wakes. *J. Phys. Conf. Ser.*, 1618(6):062014, sep 2020. ISSN 1742-6596. doi: 10.1088/1742-6596/1618/6/062014.

P. Gunwani and M. Mohan. Sensitivity of wrf model estimates to various pbl parameterizations in different climatic zones over india. *Atmos. Res.*, 194:43–65, 2017.

H. Haakenstad, Ø. Breivik, B. R. Furevik, M. Reistad, P. Bohlinger, and O. J. Aarnes. Nora3: A nonhydrostatic high-resolution hindcast of the north sea, the norwegian sea, and the barents sea. *J. Appl. Meteorol. Climatol.*, 60(10):1443–1464, 2021.

A. Hahmann, C. Vincent, A. Pena, J. Lange, and C. Hasager. Wind climate estimation using wrf model output: method and model sensitivities over the sea. *Int. J. Climatol.*, 35, 2015.

T. Hara and S. E. Belcher. Wind profile and drag coefficient over mature ocean surface wave spectra. *Journal of physical oceanography*, 34(11):2345–2358, 2004.

S. E. Haupt, B. Kosovic, W. Shaw, L. K. Berg, M. Churchfield, J. Cline, C. Draxl, B. Ennis, E. Koo, R. Kotamarthi, et al. On bridging a modeling scale gap: Mesoscale to microscale coupling for wind energy. *Bull. Am. Meteorol. Soc.*, 100(12):2533–2550, 2019.

Y. He, J. Fu, P. W. Chan, Q. Li, Z. Shu, and K. Zhou. Reduced sea-surface roughness length at a coastal site. *Atmosphere*, 12:991, 2021.

A. Hellsten, K. Ketelsen, M. Sühring, M. Auvinen, B. Maronga, C. Knigge, F. Barmpas, G. Tsegas, N. Moussiopoulos, and S. Raasch. A nested multi-scale system implemented in the large-eddy simulation model palm model system 6.0. *Geosci. Model Dev.*, 14: 3185–3214, 2021.

H. Hersbach, B. Bell, P. Berrisford, S. Hirahara, A. Horányi, J. Muñoz-Sabater, J. Nicolas, C. Peubey, R. Radu, D. Schepers, et al. The era5 global reanalysis. *Q. J. R. Meteorol. Soc.*, 146(730):1999–2049, 2020.

J. R. Holton. The diurnal boundary layer wind oscillation above sloping terrain. *Tellus*, 19 (2):200–205, 1967.

S.-A. Hsu. A dynamic roughness equation and its application to wind stress determination at the air-sea interface. *J. Phys. Oceanogr.*, 4(1):116–120, 1974.

P. A. Hwang and O. H. Shemdin. The dependence of sea surface slope on atmospheric stability and swell conditions. *J. Geophys. Res.: Oceans*, 93:13903–13912, 1988. ISSN 0148-0227.

M. J. Iacono, J. S. Delamere, E. J. Mlawer, M. W. Shephard, S. A. Clough, and W. D. Collins. Radiative forcing by long-lived greenhouse gases: Calculations with the aer radiative transfer models. *J. Geophys. Res.: Atmospheres*, 113(D13), 2008.

IEA-report. Wind power. *WindEurope, Paris https://www.iea.org/reports/wind-power*, 2021.

M. Imberger, X. G. Larsén, and N. Davis. Investigation of spatial and temporal wind-speed variability during open cellular convection with the model for prediction across scales in comparison with measurements. *Bound.-Layer Meteorol.*, 179(2):291–312, 2021.

P. Janssen, P. Lionello, and L. Zambresky. On the interaction of wind and waves. *Philosophical transactions of the royal society of London. Series A, Mathematical and Physical Sciences*, 329:289–301, 1989. ISSN 0080-4614.

P. A. E. M. Janssen. Quasi-linear theory of wind-wave generation applied to wave forecasting. *J. Phys. Oceanogr.*, 21:1631–1642, 1991. ISSN 0022-3670.

P. A. Jiménez and J. Dudhia. On the need to modify the sea surface roughness formulation over shallow waters. *J. Appl. Meteorol. Climatol.*, 57(5):1101–1110, 2018.

H. Johnson, J. Højstrup, H. Vested, and S. E. Larsen. On the dependence of sea surface roughness on wind waves. *J. Phys. Oceanogr.*, 28(9):1702–1716, 1998.

B. Jonkman and L. Kilcher. Turbsim user's guide: version 1.06. 00. *National Renewable Energy Laboratory: Golden, CO, USA*, 2012.

J. M. Jonkman, S. Butterfield, W. Musial, and G. Scott. Definition of a 5-mw reference wind turbine for offshore system development. *Technical Report NREL/TP-500-38060, National Renewable Energy Laboratory, 1617 Cole Boulevard, Golden, Colorado 80401-3393*, 2009.

Y. Kim, I. P. Castro, and Z. T. Xie. Divergence-free turbulence inflow conditions for large-eddy simulations with incompressible flow solvers. *Comput. Fluids.*, 84:56–68, 2013.

G. Komen, S. Hasselmann, and K. Hasselmann. On the existence of a fully developed wind-sea spectrum. *J. Phys. Oceanogr.*, 14(8):1271–1285, 1984.

S. Krüger, G. Steinfeld, M. Kraft, and L. J. Lukassen. Validation of a coupled atmospheric–aeroelastic model system for wind turbine power and load calculations. *Wind Energ. Sci.*, 7:323–344, 2022.

B. Lange, S. Larsen, J. Højstrup, and R. Barthelmie. Importance of thermal effects and sea surface roughness for offshore wind resource assessment. *J. Wind. Eng. Ind. Aerodyn.*, 92:959–988, 2004. ISSN 0167-6105.

L. Li, Z. Gao, and T. Moan. Joint distribution of environmental condition at five european offshore sites for design of combined wind and wave energy devices. *Journal of Offshore Mechanics and Arctic Engineering*, 137(3), 2015.

D. Lin, B. Khan, M. Katurji, L. Bird, R. Faria, and L. E. Revell. Wrf4palm v1.0: a mesoscale dynamical driver for the microscale palm model system 6.0. *Geosci. Model Dev.*, 14:2503–2524, 2021.

E. N. Lorenz. The predictability of a flow which possesses many scales of motion. *Tellus*, 21(3):289–307, 1969.

B. Maronga, M. Gryschka, R. Heinze, F. Hoffmann, F. Kanani-Sühring, M. Keck, K. Ketelsen, M. O. Letzel, M. Sühring, and S. Raasch. The parallelized large-eddy simulation model (palm) version 4.0 for atmospheric and oceanic flows: model formulation, recent developments, and future perspectives. *Geosci. Model Dev.*, 8(8):2515–2551, 2015.

B. Maronga, S. Banzhaf, C. Burmeister, T. Esch, R. Forkel, D. Fröhlich, V. Fuka, K. F. Gehrke, J. Geletič, S. Giersch, et al. Overview of the palm model system 6.0. *Geosci. Model Dev.*, 13(3):1335–1372, 2020.

D. Medici, S. Ivanell, J.-Å. Dahlberg, and P. H. Alfredsson. The upstream flow of a wind turbine: blockage effect. *Wind Energy*, 14(5):691–697, 2011.

N. Mukul Tewari, M. Tewari, F. Chen, W. Wang, J. Dudhia, M. LeMone, K. Mitchell, M. Ek, G. Gayno, J. Wegiel, et al. Implementation and verification of the unified noah land surface model in the wrf model (formerly paper number 17.5). In *Proceedings of the 20th Conference on Weather Analysis and Forecasting/16th Conference on Numerical Weather Prediction, Seattle, WA, USA*, volume 14, 2004.

D. Muñoz-Esparza, B. Kosović, J. Mirocha, and J. van Beeck. Bridging the transition from mesoscale to microscale turbulence in numerical weather prediction models. *Bound.-Layer Meteorol.*, 153(3):409–440, 2014.

D. Muñoz-Esparza, B. Kosović, J. Van Beeck, and J. Mirocha. A stochastic perturbation method to generate inflow turbulence in large-eddy simulation models: Application to neutrally stratified atmospheric boundary layers. *Phys. Fluids*, 27(3):035102, 2015.

W. Musial. Overview of floating offshore wind. in proceedings of the webinar hosted by national renewable energy laboratory. *Proceedings of the Webinar Hosted by National Renewable Energy Laboratory, Golden, CO, USA, 26 February 2020*, 2020.

M. Nakanishi and H. Niino. An improved mellor–yamada level-3 model: Its numerical stability and application to a regional prediction of advection fog. *Bound.-Layer Meteorol.*, 119(2):397–407, 2006.

M. Olabarrieta, J. C. Warner, B. Armstrong, J. B. Zambon, and R. He. Ocean–atmosphere dynamics during hurricane ida and nor'ida: An application of the coupled ocean–atmosphere–wave–sediment transport (coawst) modeling system. *Ocean Modelling*, 43: 112–137, 2012.

W. Oost, G. Komen, C. Jacobs, and C. Van Oort. New evidence for a relation between wind stress and wave age from measurements during asgamage. *Bound.-Layer Meteorol.*, 103(3):409–438, 2002.

E. Patton, B. Kosovic, P. Sullivan, J. Dudhia, L. Mahrt, M. Zagar, and L. Gulstad. Impacts of stratification and nonequilibrium winds and waves on hub-height winds. Technical report, Final Technical Report, University Corporation for Atmospheric Research . . . , 2015.

V. Pettas, M. Kretschmer, A. Clifton, and P. W. Cheng. On the effects of inter-farm interactions at the offshore wind farm alpha ventus. *Wind Energ. Sci.*, 6:1455–1472, 2021.

A. Peña, S. E. Gryning, and C. B. Hasager. Measurements and modelling of the wind speed profile in the marine atmospheric boundary layer. *Bound.-Layer Meteorol.*, 129:479–495, 2008.

S. Porchetta, O. Temel, D. Muñoz-Esparza, J. Reuder, J. Monbaliu, J. van Beeck, and N. van Lipzig. A new roughness length parameterization accounting for wind–wave (mis) alignment. *Atmos. Chem. Phys.*, 19:6681–6700, 2019. ISSN 1680-7316.

S. Porchetta, D. Muñoz-Esparza, W. Munters, J. van Beeck, and N. van Lipzig. Impact of ocean waves on offshore wind farm power production. *Renew. Energ.*, 180:1179–1193, 2021a. ISSN 0960-1481.

S. Porchetta, O. Temel, J. C. Warner, D. Muñoz-Esparza, J. Monbaliu, J. van Beeck, and N. van Lipzig. Evaluation of a roughness length parametrization accounting for wind–wave alignment in a coupled atmosphere–wave model. *Q. J. R. Meteorol. Soc.*, 147(735): 825–846, 2021b.

W. E. Rogers, A. V. Babanin, and D. W. Wang. Observation-based source terms in the third-generation wave model wavewatch. *J. Atmos. Ocean. Technol.*, 29:1329–1346, 2012.

C.-W. Shu. Essentially non-oscillatory and weighted essentially non-oscillatory schemes for hyperbolic conservation laws. *Advanced numerical approximation of nonlinear hyperbolic equations*, pages 325–432, 1998.

W. C. Skamarock, J. B. Klemp, J. Dudhia, D. O. Gill, Z. Liu, J. Berner, W. Wang, J. G. Powers, M. G. Duda, D. M. Barker, et al. A description of the advanced research wrf model version 4. *National Center for Atmospheric Research: Boulder, CO, USA*, 145: 145, 2019.

A. Smedman, U. Högström, H. Bergström, A. Rutgersson, K. K. Kahma, and H. Pettersson. A case study of air-sea interaction during swell conditions. *J. Geophys. Res.: Oceans*, 104:25833–25851, 1999. ISSN 0148-0227.

S. D. Smith, R. J. Anderson, W. A. Oost, C. Kraan, N. Maat, J. De Cosmo, K. B. Katsaros, K. L. Davidson, K. Bumke, L. Hasse, et al. Sea surface wind stress and drag coefficients: The hexos results. *Bound.-Layer Meteorol.*, 60(1):109–142, 1992.

M. Sommerfeld, M. Dörenkämper, G. Steinfeld, and C. Crawford. Improving mesoscale wind speed forecasts using lidar-based observation nudging for airborne wind energy systems. *Wind Energ. Sci.*, 4:563–580, 2019.

J. D. Stark, C. J. Donlon, M. J. Martin, and M. E. McCulloch. Ostia: An operational, high resolution, real time, global sea surface temperature analysis system. In *Oceans 2007-europe*, pages 1–4. IEEE, 2007.

H. F. Stockdon and R. A. Holman. Estimation of wave phase speed and nearshore bathymetry from video imagery. *J. Geophys. Res.: Oceans*, 105(C9):22015–22033, 2000.

H. Sun, X. Gao, and H. Yang. A review of full-scale wind-field measurements of the wind-turbine wake effect and a measurement of the wake-interaction effect. *Renew. Sustain. Energy Rev.*, 132:110042, 2020.

P. K. Taylor and M. J. Yelland. The dependence of sea surface roughness on the height and steepness of the waves. *J. Phys. Oceanogr.*, 31:572–590, 2001. ISSN 1520-0485.

G. Thompson, P. R. Field, R. M. Rasmussen, and W. D. Hall. Explicit forecasts of winter precipitation using an improved bulk microphysics scheme. part ii: Implementation of a new snow parameterization. *Mon. Weather Rev.*, 136(12):5095–5115, 2008.

C. Trust. Offshore wind industry review of gbs: Identifying the key barriers to large scale commercialization of gravity-based structures in the offshore wind industry. *The Carbon Trust: London, UK, 2015*, 2015.

K. N. Tsagareli, A. V. Babanin, D. J. Walker, and I. R. Young. Numerical investigation of spectral evolution of wind waves. part i: Wind-input source function. *J. Phys. Oceanogr.*, 40:656–666, 2010.

P. Veers and et al. Grand challenges in the science of wind energy. *Science*, 336, 2019.

C. L. Vincent, A. N. Hahmann, and M. C. Kelly. Idealized mesoscale model simulations of open cellular convection over the sea. *Boundary-layer meteorology*, 142(1):103–121, 2012.

D. Wagner, G. Steinfeld, B. Witha, H. Wurps, and J. Reuder. Low level jets over the southern north sea. *Meteorologische Zeitschrift*, 28(5):389–415, 12 2019. doi: 10.1127/metz/2019/0948.

C. Walsh. Wind energy in europe 2020 statistics and the outlook for 2021- 2025. *WindEurope*, 2020.

W. Wang, C. Bruyere, M. Duda, J. Dudhia, D. Gill, M. Kavulich, K. Keene, H.-C. Lin, J. Michalakes, S. Rizvi, et al. User's guides for the advanced research wrf (arw) modeling system. *Version 4*, 2021.

J. C. Warner, B. Armstrong, R. He, and J. B. Zambon. Development of a coupled ocean–atmosphere–wave–sediment transport (coawst) modeling system. *Ocean modelling*, 35 (3):230–244, 2010.

A. S. Wise, J. M. T. Neher, R. S. Arthur, J. D. Mirocha, J. K. Lundquist, and F. K. Chow. Meso- to micro-scale modeling of atmospheric stability effects on wind turbine wake behavior in complex terrain. *Wind Energ. Sci.*, pages 1–36, 2021.

B. Witha, G. Steinfeld, and D. Heinemann. High-resolution offshore wake simulations with the les model palm. In *Wind energy-impact of turbulence*, pages 175–181. Springer, 2014.

L. Wu, A. Rutgersson, and E. Nilsson. Atmospheric boundary layer turbulence closure scheme for wind-following swell conditions. *J. Atmos. Sci.*, 74(7):2363–2382, 2017.

J. C. Wyngaard. Toward numerical modeling in the "terra incognita". *Journal of the atmospheric sciences*, 61(14):1816–1826, 2004.

C. Zhang, Y. Wang, and K. Hamilton. Improved representation of boundary layer clouds over the southeast pacific in arw-wrf using a modified tiedtke cumulus parameterization scheme. *Mon. Weather Rev.*, 139(11):3489–3513, 2011.

S. Zieger, A. V. Babanin, W. E. Rogers, and R. I. Young. Observation-based source terms in the third-generation wave model wavewatch. *Ocean Modelling*, 96:2–25, 2015.